MODEL VALIDATIONS, COMPARISONS, AND ISSUES OF THE NEXT GENERATION ATTENUATION (NGA) RELATIONS FOR PREDICTING EARTHQUAKE GROUND MOTIONS

A thesis

submitted by

James Kaklamanos

In partial fulfillment of the requirements for the degree of

Master of Science

in

Civil and Environmental Engineering

TUFTS UNIVERSITY

February 2010

© 2010, James Kaklamanos

ADVISOR: Dr. Laurie G. Baise

UMI Number: 1474461

All rights reserved

INFORMATION TO ALL USERS
The quality of this reproduction is dependent upon the quality of the copy submitted.

In the unlikely event that the author did not send a complete manuscript
and there are missing pages, these will be noted. Also, if material had to be removed,
a note will indicate the deletion.

UMI 1474461
Copyright 2010 by ProQuest LLC.
All rights reserved. This edition of the work is protected against
unauthorized copying under Title 17, United States Code.

ProQuest LLC
789 East Eisenhower Parkway
P.O. Box 1346
Ann Arbor, MI 48106-1346

Abstract

Model Validations, Comparisons, and Issues of the Next Generation Attenuation (NGA) Relations for Predicting Earthquake Ground Motions

by

James Kaklamanos

Recent earthquake ground motion prediction equations, such as those developed from the Next Generation Attenuation of Ground Motions (NGA) project in 2008, have established a new baseline for the estimation of ground motion parameters such as peak ground acceleration (*PGA*), peak ground velocity (*PGV*), and spectral acceleration (*Sa*). When these relations were published, very little was written about model validation or prediction accuracy. We perform statistical goodness-of-fit analyses to quantitatively compare the predictive abilities of these recent models, using several testing subsets of the master database used to develop the NGA models. In addition, we perform a blind comparison of the new models with previous simpler models, using ground motion records from the two most recent earthquakes of magnitude 6.0 or greater to strike mainland California. A model validation framework is introduced to assess the prediction accuracy of ground motion prediction equations and aid in their future development.

To my mother, Cindy; father, James; sisters, Christie and Alexa; my grandparents Evelyn, Flo, and Nick, who are here today; and my grandfather Charles, who is not. I would not be where I am today without your guidance, support, and love.

Acknowledgements

On Wednesday, September 1, 2004, I officially began my career as a Tufts University undergraduate. During a brief break in my schedule on that balmy late-summer day, I decided to explore my new home and take a walk across campus. When I arrived at the roof of Tisch Library, with the Boston skyline glimmering in the afternoon sunlight, I wondered where the next chapter of my life would take me. Isak Dinesen once wrote, "God made the world round so we would never be able to see too far down the road." At the start of my college career, I never thought that I would eventually pursue graduate study in civil engineering. Five-and-a-half years later, having completed my B.S. and M.S. in civil engineering, I could not possibly be happier with my decision to obtain my undergraduate and graduate degrees in civil engineering at Tufts. My experience here has been challenging, enjoyable, and truly rewarding. I have been fortunate to meet and work with some of the most intelligent, charismatic, and good-natured individuals that I will likely meet in my entire life.

First, I would like to thank my research advisor, Professor Laurie Baise, for accepting me as a student and giving me the opportunity to pursue research in geotechnical earthquake engineering. Through her positive support and guidance, she has given me the freedom to shape my own projects, develop skills to pursue unsolved problems, and mature intellectually as a researcher. Ultimately, through my work with Professor Baise, I have become deeply intrigued with the field of geotechnical earthquake engineering, and I hope to make important contributions to this field for years to come. In addition to Professor Baise, I would also like to acknowledge the other members of my thesis committee: Dean Lewis Edgers, Professor Chris Swan, and Professor Richard

Vogel. Their advice helped me formulate various aspects of my research, and their written comments improved the quality of the final document. Additionally, Dr. Eric Thompson has served as an invaluable resource to me throughout the research process, from mentoring me in the idiosyncrasies of the *R* statistical language, to offering fruitful suggestions on research directions and results.

I am grateful to the members of the Department of Civil and Environmental Engineering at Tufts University for providing me with a teaching assistantship, and for my teaching advisor, Professor Lee Minardi, for his countless hours of dedication. My experience working as a teaching assistant for two introductory engineering courses has allowed me to develop my abilities to convey information effectively, organize and synthesize the presentation of course material, and discover that I have a passion for teaching. Finally, I would like to acknowledge the first person at Tufts who truly encouraged me to study engineering: Dean Kim Knox. Her upbeat enthusiasm and unwavering optimism have inspired me to follow my dreams.

Most importantly, I have been blessed with a loving family for which I am deeply indebted and grateful. My parents, James and Cindy; sisters, Christie and Alexa; and grandparents Charles, Evelyn, Nick, and Flo, have guided and supported me throughout my entire life, and I know for certain that I would not be where I am today without their affection and encouragement. On my first day at Tufts, gazing at the view from the Tisch Library roof, I never would have dreamed of the road down which I would eventually travel. Five-and-a-half years later, I could not be more thankful for where life has taken me, and I look forward with unbridled enthusiasm to the gifts that the future holds.

Table of Contents

Appendices

List of Tables

List of Figures

List of Symbols

Acronyms

AS08	Abrahamson and Silva (2008) ground motion prediction equation
AS97	Abrahamson and Silva (1997) ground motion prediction equation
BA08	Boore and Atkinson (2008) ground motion prediction equation
BDSN	Berkeley Digital Seismic Network
BJF97	Boore *et al.* (1997) ground motion prediction equation
BSSC	Building Seismic Safety Council
C97	Campbell (1997) ground motion prediction equation
CB08	Campbell and Bozorgnia (2008) ground motion prediction equation
CESMD	Center for Engineering Strong Ground Motion Data
CGS	California Geological Survey
COSMOS	Consortium of Organizations for Strong-Motion Observation Systems
CSMIP	California Strong Motion Instrumentation Program
CY08	Chiou and Youngs (2008) ground motion prediction equation
GMPE	ground motion prediction equation
I08	Idriss (2008) ground motion prediction equation
I91	Idriss (1991) ground motion prediction equation
LSRL	least-squares regression line
MASW	multichannel analysis of surface waves method
NCSN	Northern California Seismic Network
NEHRP	National Earthquake Hazards Reduction Program
NGA	Next Generation Attenuation (of Ground Motions)
NSMP	National Strong Motion Program
PEER	Pacific Earthquake Engineering Research Center
PSHA	probabilistic seismic hazard analysis
ReMi	refraction microtremor method
SASW	spectral analysis of surface waves method
SCE97	Sadigh *et al.* (1997) ground motion prediction equation

SDOF	single degree-of-freedom
UCB	University of California, Berkeley
USGS	United States Geological Survey
UTM	Universal Transverse Mercator

Upper-Case Symbols

A	side length for Law of Sines (Figure 2.7)
A_{1100}	*PGA* on rock site; baseline for nonlinear site response (CB08)
ALL	unspecified style-of-faulting dummy variable (BJF97)
AS	aftershock dummy variable (CY08)
B	side length for Law of Sines (Figure 2.7)
C	side length for Law of Sines (Figure 2.7)
D	depth to basement rock; also, averaging depth for shear wave velocity
E	Nash-Sutcliffe model efficiency coefficient
F	reverse style-of-faulting dummy variable (AS97, C97, I91, and I08)
F_{AS}	aftershock dummy variable (AS08)
F_{HW}	hanging wall dummy variable (AS08 and CY08)
F_{NM}	normal style-of-faulting dummy variable (AS08, CB08, and CY08)
F_{RV}	reverse style-of-faulting dummy variable (AS08, CB08, and CY08)
GM_{xy}	geometric mean of the as-recorded horizontal components (the response variable for the previous generation of GMPEs)
GMRotI50	geometric mean horizontal component, independent of the sensor orientation of the two as-recorded horizontal components (the response variable for the NGA models)
H	hypotenuse, used in derivation of R_X (Figure 2.6)
H_{SEIS}	depth to seismogenic sediments, which contribute to seismic energy release ("seismogenic depth")
HW	hanging wall dummy variable (AS97)
K	deposits from the Cretaceous geologic period (see Table 2.4 for modifiers)
L	fault rupture length (along strike)
M	earthquake magnitude (generic); most commonly, moment magnitude

M_W	moment magnitude
N	number of observations over which goodness-of-fit statistics are calculated; $N = n$ for a single-period analysis, and $N = mn$ for a multiple-period analysis
NM	normal faulting mechanism (Table 2.6)
NS	normal style-of-faulting dummy variable (BA08)
PB	percent bias
PGA	peak ground acceleration
$\hat{PGA}_{1100}$	PGA on rock site, baseline for nonlinear site response (AS08)
$\hat{PGA}_{rock}$	PGA on rock site, baseline for nonlinear site response (AS97)
PGD	peak ground displacement
PGV	peak ground velocity
$PRMSE$	percent root mean square error
Q	deposits from the Quaternary geologic period (see Table 2.4 for modifiers)
R	source-to-site distance (generic); also, the open-source statistical language and environment utilized for most of the calculations in this thesis
R_{EPI}	epicentral distance
R_{HYP}	hypocentral distance
R_{JB}	horizontal distance to the surface projection of the rupture plane ("Joyner-Boore distance")
R_{RUP}	closest distance to the rupture plane ("rupture distance")
R_{SEIS}	closest distance to the rupture plane within the zone of seismogenic rupture ("seismogenic distance")
R_X	horizontal distance to the surface projection of the top edge of the rupture plane, measured perpendicular to the strike ("site coordinate")
$RMSE$	root mean square error
RS	reverse style-of-faulting dummy variable (BA08 and BJF97)
RV	reverse faulting mechanism (Table 2.6)
S	site class dummy variable (AS97)
S_{HR}	hard rock dummy variable (C97)
S_{SR}	soft rock dummy variable (C97)

Sa	5% damped elastic pseudo-response spectral acceleration
SS	strike-slip style-of-faulting dummy variable (BA08 and BJF97); also, strike-slip faulting mechanism (Table 2.6)
T	spectral period; also, deposits from the Tertiary geologic period (see Table 2.4 for modifiers)
T_{high}	maximum useable spectral period
U	unspecified style-of-faulting dummy variable (BA08)
V_S	shear wave velocity
V_{S30}	time-averaged shear wave velocity over a subsurface depth of 30 meters
$V_{S,D}$	time-averaged shear wave velocity over a subsurface depth of D
W	down-dip fault rupture width
Y	observed response variable (generic)
$\hat{Y}$	predicted response variable (generic)
$\overline{Y}$	mean of the observed values
$\overline{\hat{Y}}$	mean of the predicted values
$Z_{1.0}$	depth to V_S = 1.0 km/sec
$Z_{1.5}$	depth to V_S = 1.5 km/sec
$Z_{2.5}$	depth to V_S = 2.5 km/sec
Z_{HYP}	hypocentral depth
Z_{TOR}	depth to top of rupture plane

Lower-Case Symbols

a	angle for Law of Sines (Figure 2.7)
b	angle for Law of Sines (Figure 2.7)
c	angle for Law of Sines (Figure 2.7)
d	distance used in the derivation of R_X (Figure 2.3)
f_c	high-pass corner frequency of the seismic recording instrument
g	acceleration due to gravity (981 cm/s^2)
m	number of ground motion parameters selected for analysis (m = 7 in this study)
n	number of observations (ground motion records)

pga4nl	*PGA* on rock site; baseline for nonlinear site response (BA08)
r	Pearson's correlation coefficient
r^2	coefficient of determination
x	horizontal component of ground motion
y	horizontal component of ground motion
$y_{ref}(T)$	*Sa* on rock site; baseline for nonlinear site response (CY08)
z	depth; also, vertical component of ground motion

Greek Symbols

α	source-to-site azimuth angle
β	angle used in derivation of R_X (Figure 2.6)
γ	angle used in derivation of R_X (Figure 2.6)
δ	fault dip angle
ξ	damping ratio
λ	rake angle

MODEL VALIDATIONS, COMPARISONS, AND ISSUES OF THE NEXT GENERATION ATTENUATION (NGA) RELATIONS FOR PREDICTING EARTHQUAKE GROUND MOTIONS

Chapter 1:
INTRODUCTION

1.1 Probabilistic Seismic Hazard Analyses

1.1.1 Purpose and Consequences

In August 2005, America watched as Hurricane Katrina destroyed the city of New Orleans. Few people in this country were alive the last time a major American city was so vastly affected by a natural disaster—that time, it was not by a hurricane, but by an earthquake. The Great San Francisco Earthquake of 1906 goes down in history as the deadliest and most destructive earthquake to strike America. Many people do not realize that the "Big One" *will* happen again—it is just a matter of when and where. There is greater than a 99% probability of at least a magnitude 6.7 earthquake occurring in California in the next 30 years, and a 46% probability of at least a magnitude 7.5 earthquake occurring during that same period (Field *et al.*, 2008). In addition, other locations in the country have considerable seismic hazards to which many people are oblivious. Earthquakes can have devastating effects—through loss of life, property, and livelihood—on families, communities, and societies as a whole. Scientists and engineers are faced with the challenge of developing methods by which seismic hazards can be understood, quantified, and incorporated into seismic design.

To quantify the seismic hazard at a given location, a *seismic hazard analysis* is performed. There exist two general categories of seismic hazard analyses: (1) *deterministic*, which assumes a "worst-case scenario" earthquake, and (2) *probabilistic*, which incorporates the uncertainties of earthquake size, location, recurrence rate, and level of ground motion (Kramer, 1996). Probabilistic seismic hazard analyses (PSHAs), which were introduced to the field of earthquake engineering by Cornell (1968), have the powerful advantage of realistically incorporating hazard contributions and uncertainties from multiple seismic sources. As a result, PSHAs have largely surpassed deterministic seismic hazard analyses as the preferred method of quantifying seismic hazard. However, deterministic seismic hazard analyses are still occasionally used in tandem with PSHAs for specific projects, such as the seismic design of critical structures such as dams and power plants.

The output of a probabilistic seismic hazard analysis is a *seismic hazard curve*, which is a relationship between the values of a ground motion parameter and the mean annual rate of exceedance of those values (Kramer, 1996). Individual seismic hazard curves are drawn for specific locations. To assess seismic hazards across broad areas, site-specific hazard curves are conglomerated into *seismic hazard maps*, which are drawn for a particular rate of exceedance (*e.g.*, 5% probability of exceedance in 50 years). Given this rate of exceedance, the corresponding seismic hazard map would display the level of ground motion that we would expect to be surpassed with a 5% probability over a period of 50 years, and how this level of ground motion varies spatially. Seismic hazard maps govern the preliminary seismic design of structures, and they are used in post-earthquake emergency response to determine the locations where first responders should

be dispatched. Through seismic design and emergency response, seismic hazard maps (and therefore PSHAs) can greatly influence the extent of earthquake-induced fatalities and damage, and thus their development has significant consequences.

1.1.2 Procedure

A simple probabilistic seismic hazard analysis can be described in four steps (Kramer, 1996; Reiter, 1990):

1. Identify all earthquake sources and their uncertainties.
2. Characterize the temporal distribution of earthquake recurrence, by considering the uncertainties of earthquake size and rate of recurrence.
3. Using *ground motion prediction equations* (*GMPEs*), determine the expected level of ground motion for each potential earthquake, as well as the uncertainties in the estimates.
4. Combine the uncertainties in earthquake location, size, and ground motion level to develop a seismic hazard curve.

For this thesis, the most relevant portion of the seismic hazard calculations is step 3, which involves the use of ground motion prediction equations to quantify the expected level of ground motion.

1.1.3 Influence of Ground Motion Prediction Equations

For the purposes of this discussion, we will assume a greatly simplified probabilistic seismic hazard analysis. Suppose that the earthquake hazard at a given site can be disaggregated into two possible magnitudes (M_1 = 5 and M_2 = 6), and two possible

source-to-site distances (R_1 = 10 km and R_2 = 50 km). More advanced PSHAs, such as those involved in generating the national seismic hazard maps released by the United States Geological Survey (USGS), incorporate many more combinations and variables than discussed in this simple example (Petersen *et al.*, 2008). In order to carry out step 3 of the PSHA, we need a method by which we can characterize the expected level of ground motion—and the uncertainty of the estimate—for each of the four possible earthquakes resulting from the combinations (M_1 = 5, R_1 = 10 km), (M_1 = 5, R_2 = 50 km), (M_2 = 6, R_1 = 10 km), and (M_2 = 6, R_2 = 50 km). Ground motion prediction equations are precisely the tools by which we can estimate an expected level of ground motion at a specific location, as a function of magnitude, distance, and other variables (to be introduced later). Because they serve such an integral role in PSHAs, it is of great importance that we properly understand and develop ground motion prediction equations.

1.2 Ground Motion Prediction Equations (GMPEs)

The purpose of ground motion prediction equations (also called "ground motion prediction relations" or "attenuation relationships") is to predict the ground motion at a given location as a function of earthquake magnitude, distance from the earthquake source, and other source, path, and site characteristics. The usual response variables in ground motion prediction relations are peak ground acceleration (*PGA*), peak ground velocity (*PGV*), and 5%-damped elastic pseudo-response spectral acceleration (*Sa*).

A typical ground motion prediction relation has the form

$$\ln \hat{Y} = f(M, R, \sum Source_i, \sum Site_i), \tag{1.1}$$

where $\ln \hat{Y}$ is the prediction of the natural logarithm of the ground motion parameter of interest, M is the magnitude of the earthquake, R is a measure of distance representing the path of seismic energy from the earthquake source to the site of interest, $\sum Source_i$ are other variables relating to the earthquake source (such as type of faulting, rupture width and depth, and fault dip), and $\sum Site_i$ are variables relating to the site of interest (such as average shear wave velocity, geologic characteristics, or depth to bedrock) (Kramer, 1996; Douglas, 2003; Abrahamson *et al*., 2008). Source parameters are constant for a given earthquake and do not vary from location to location; site parameters are constant for a given location and do not vary from earthquake to earthquake.

Peak values of ground motion parameters are assumed to follow a lognormal distribution; therefore, the logarithms of the ground motion parameters follow a normal distribution. As a result, regression is typically performed on the logarithm of the ground motion parameter of interest. Ground motion prediction relations are developed for specific tectonic environments using multivariate regression on ground motion databases, and the relationships are updated as more earthquake data are obtained (Kramer, 1996; Abrahamson and Shedlock, 1997).

1.3 Response Variables in GMPEs

As explained in section 1.2, the typical response variables in ground motion prediction relations are peak ground acceleration (*PGA*), peak ground velocity (*PGV*), and 5% damped elastic pseudo-response spectral acceleration (*Sa*). Peak ground acceleration and peak ground velocity represent the maximum recorded ground motion during an

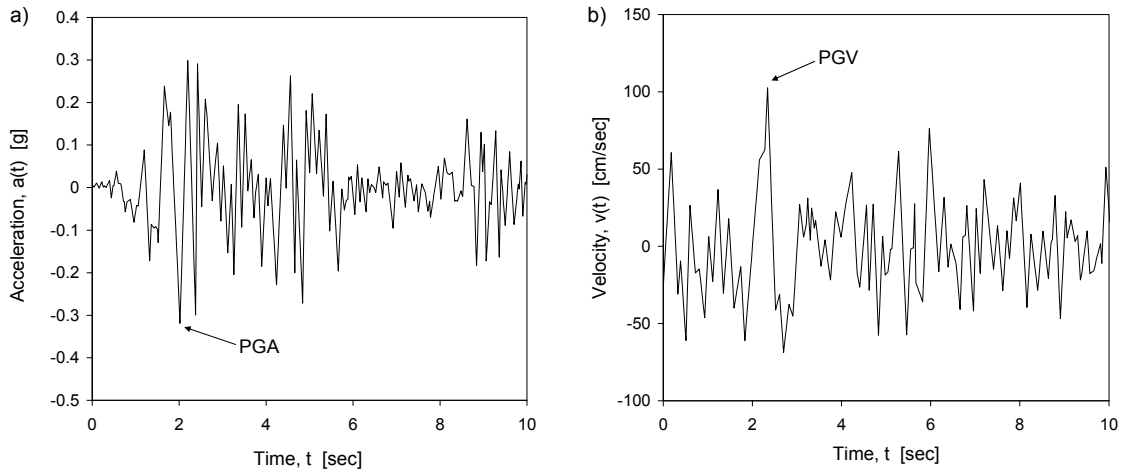

Figure 1.1. Example (a) acceleration and (b) velocity time histories, with the illustration of *PGA* and *PGV*.

earthquake, and are determined from ground motion time histories at specific locations. An acceleration time history is a plot of recorded ground acceleration versus time, and a velocity time history is a plot of recorded ground velocity versus time. Given an acceleration time history, *PGA* is simply the absolute maximum value of acceleration; *PGV* is similarly defined for velocity. Typical units for *PGA* are *g*'s, where *g* is the acceleration due to gravity (981 cm/s^2), and *PGV* is often expressed in cm/sec. Example acceleration and velocity time histories, as well as the determination of *PGA* and *PGV*, are shown in Figure 1.1.

A *response spectrum* describes the maximum response (spectral acceleration, *Sa*) of a single-degree-of-freedom (SDOF) structure to a particular input motion as a function of the natural period (T) and damping ratio (ξ) of the SDOF system. For the purposes of GMPEs, structural materials are assumed to exhibit a constant damping ratio of 5% (Kramer, 1996). In graphical form (Figure 1.2), a response spectrum is a plot of spectral acceleration *Sa* (the response of the structure) on the vertical axis, and period T (the frequency content of the vibration) on the horizontal axis. Response spectra have

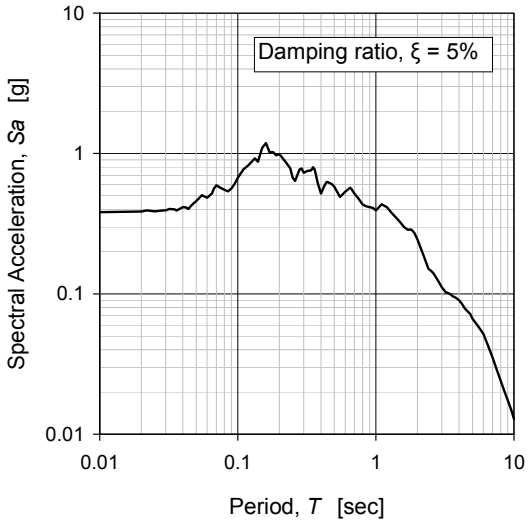

Figure 1.2. An example response spectrum, displaying spectral acceleration (*Sa*) versus period *T* for a constant damping ratio of $\xi = 5\%$.

important implications, as they are used by structural engineers for seismic design. Developers of GMPEs define relationships for the spectral acceleration at various periods, in addition to *PGA* and *PGV*. Units for spectral acceleration are *g*'s (like *PGA*).

1.4 Explanatory Variables in GMPEs

Early ground motion prediction equations generally included only magnitude and distance as explanatory variables (Douglas, 2003). Over the past 20 years, however, many GMPEs have become increasingly complex in terms of the number of explanatory variables and in the complexity of the functional forms. However, Douglas (2003) and Strasser *et al.* (2009) show that although GMPEs have become increasingly more complex over time, there has not been a marked improvement in the uncertainty of the ground motion prediction estimates.

1.4.1 Source Parameters

Source parameters, which are constant for a given earthquake, capture the effects of earthquake size and characteristics of rupture. The fundamental source parameter present in all GMPEs is earthquake magnitude, M. As the earthquake magnitude increases, so does the level of ground shaking. Most ground motion prediction equations have adopted moment magnitude (M_W) as the preferred measure of magnitude because it is based on seismic moment, which is fundamentally linked to the characteristics of the fault rupture and the energy released during the earthquake (Kanamori, 1977; Hanks and Kanamori, 1979). Other characteristics of fault rupture that have entered recent GMPEs include depth to top of rupture (Z_{TOR}), down-dip rupture width (W), and fault dip (δ), which are illustrated in Figure 1.3.

Other source characteristics often manifest themselves in GMPEs in the form of *dummy variables* (or "flags"), which take on a value of 1 when a certain condition is met and 0 otherwise. A common dummy variable that enters most GMPEs is the style of faulting, which allows for different ground motion predictions to be made for earthquakes

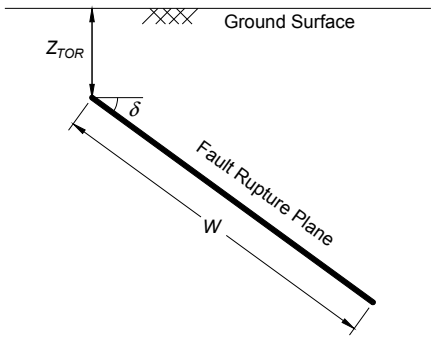

Figure 1.3. Vertical cross-section through a fault rupture plane, illustrating the depth to top of rupture (Z_{TOR}), down-dip rupture width (W), and fault dip (δ). The length of the fault rupture plane (L) is measured along the strike (perpendicular to the plane of the page).

characterized by normal faulting, strike-slip faulting, or reverse faulting. For a given set of magnitude and distance parameters, ground motion data generally show that normal-faulting earthquakes produce lower ground motions than reverse-faulting earthquakes, and that strike-slip earthquakes provide intermediate levels of ground motion (Spudich *et al.*, 1999; Bommer *et al.*, 2003; Ambraseys *et al.*, 2005). By the use of a dummy variable, the ground motion estimate may be increased or decreased according to the style of faulting (which may be classified according to the rake angle of fault movement, λ).

1.4.2 Path Parameters

Path parameters represent the propagation of the seismic energy from the earthquake source to the site of interest. The fundamental path parameter present in all relations is source-to-site distance, R. As the distance from the earthquake source increases, seismic energy is attenuated (dissipated) and the level of ground shaking decreases. Several different definitions of source-to-site distance are used in ground motion prediction equations. The most common measure in current GMPEs is the distance from the site to the closest point on the rupture plane (the *rupture distance*, R_{RUP}) (Abrahamson *et al.*, 2008). Another frequently used measure is the horizontal distance to the surface projection of the rupture, also known as the *Joyner-Boore distance* (R_{JB}) (Boore and Atkinson, 2008). Some scientists argue that fault rupture within softer near-surface sediments is non-seismogenic, and thus does not contribute significantly to seismic energy release during earthquakes. The seismogenic depth (H_{SEIS}) is the depth to sediments that contribute to seismic energy release, and often ranges from 2 to 4 km; for sites in California, a reasonable value of 3 km may be assumed. Under these

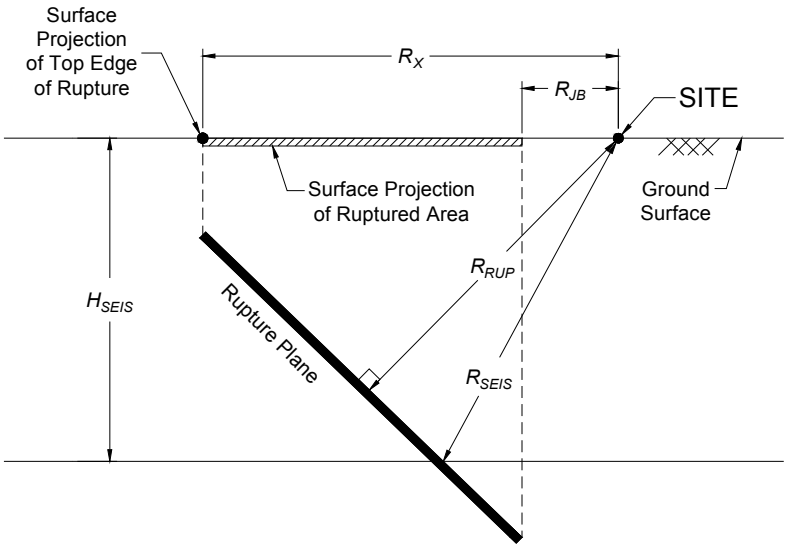

Figure 1.4. Comparison of different distance measures found in ground motion prediction equations, using a vertical cross-section through a fault rupture plane. The rupture distance (R_{RUP}), Joyner-Boore distance (R_{JB}), site coordinate (R_X), and seismogenic distance (R_{SEIS}) are illustrated for a hypothetical site. Note that if the site were located directly over the ruptured area, R_{JB} would be equal to zero.

assumptions, the *seismogenic distance* (R_{SEIS}) is the distance from the site to the closest point on the rupture plane at or below a depth of H_{SEIS} (Campbell, 1997). Finally, a new distance parameter found in some recent GMPEs is the *site coordinate* (R_X), which is the horizontal distance to the vertical projection of the top edge of the rupture measured perpendicular to the strike (Abrahamson and Silva, 2008; Chiou and Youngs, 2008a). These distance measures are illustrated for a hypothetical site in Figure 1.4. As we will explain later, there is a geometrical interdependence between these distance measures.

The four distance measures discussed above are linked to the characteristics of the fault rupture plane, which is assumed to be the source of seismic energy in an earthquake. Two other distance measures—the epicentral distance (R_{EPI}) and the hypocentral distance (R_{HYP})—are easier to calculate, but they are not directly related to energy release. Older relations often use R_{EPI} or R_{HYP} as the measure of distance, but it has become common

practice to use one or more of the distance measures that are directly related to fault rupture (Douglas, 2003). One additional path parameter included in some relations is the hanging wall flag. Somerville *et al.* (1995) and Abrahamson and Somerville (1996) defined the *hanging-wall effect* as a systematic increase in ground motion for sites located on the hanging wall versus the footwall of a fault. To account for this, some GMPEs use a dummy variable that increases the estimated ground motion for locations on the hanging wall side of the fault.

1.4.3 Site Parameters

Site parameters quantify the influence of site geology on ground motion amplification. Based on the composition of the subsurface, different locations will experience different ground motions during earthquakes. Sites underlain by soft soil will experience greater amplification of ground motions than sites underlain by rock. In recent years, there has been a greater emphasis on the incorporation of site parameters in GMPEs. Previous GMPEs either excluded site parameters altogether, or included simple dummy variables indicating whether a site was on soil or rock (Douglas, 2003). The manner in which site parameters are incorporated into most current ground motion prediction relations is by using V_{S30}, the time-averaged shear wave velocity over the top 30 meters of the subsurface (Power *et al*., 2008). Another site characteristic that has important implications for site amplification is the depth to bedrock at the site. Unfortunately, this value is difficult to obtain. However, if a shear wave velocity (V_S) profile is available at a site, then the depth at which a certain value of shear wave velocity is reached (such as 1.0 km/s or 2.5 km/s) can be used as a corollary for depth to bedrock. Several recent

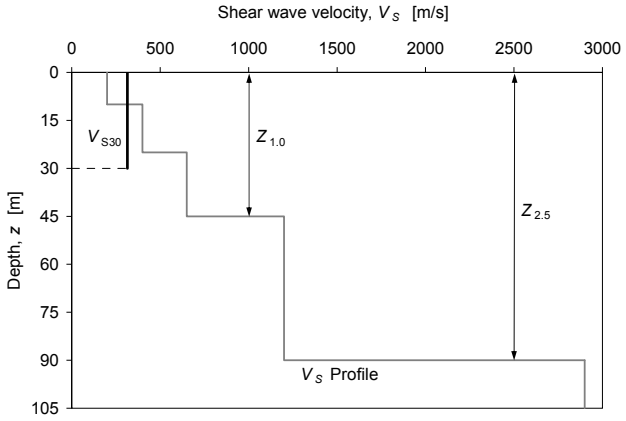

Figure 1.5. An example shear wave velocity profile, illustrating site parameters commonly found in ground motion prediction equations: V_{S30} (time-averaged shear wave velocity over the top 30 meters of the subsurface), $Z_{1.0}$ (depth to V_S = 1 km/sec), and $Z_{2.5}$ (depth to V_S = 2.5 km/sec).

relationships (to be discussed later) utilize $Z_{1.0}$ (the depth to V_S = 1.0 km/s, approximately where soil is assumed to change to soft rock) or $Z_{2.5}$ (the depth to V_S = 2.5 km/s, approximately where soft rock is assumed to change to hard rock) as site characteristics in ground motion prediction relations (Abrahamson and Silva, 2008; Chiou and Youngs, 2008a; Campbell and Bozorgnia, 2008). A schematic of a shear wave velocity profile with V_{S30}, $Z_{1.0}$, and $Z_{2.5}$ is presented in Figure 1.5.

All of the site parameters discussed above are constant for a given location; they do not change from earthquake to earthquake. The nonlinear site response term, however, varies from earthquake to earthquake because it is dependent on the expected level of ground motion and the values of the other site parameters. Nonlinearity results in a de-amplification of ground motions because of the shear softening of soil under large applied cyclic loads (Kramer, 1996). Abrahamson and Silva (1997) were the first team to include nonlinear site effects in a widely used GMPE, and many current GMPEs include

nonlinear site effects. When models include nonlinear site effects, two calculations are required:

1. Calculation of the expected *PGA* on a baseline rock site (where nonlinear effects are assumed to be zero).
2. Calculation of the expected ground motion parameter on the site of interest, using the expected *PGA* on the baseline rock site as an input parameter for the calculation of nonlinear site effects.

1.5 The Next Generation Attenuation (NGA) Project

After a five-year effort, the Next Generation Attenuation of Ground Motions (NGA) project was completed in 2008. The project, sponsored by the Pacific Earthquake Engineering Research Center (PEER), established five new GMPEs that predict ground motion parameters for shallow crustal earthquakes in active tectonic regions (such as California). These models are the first large-scale update of GMPEs for this tectonic environment since 1997, when the previous generation of GMPEs was released. Table 1.1 lists the new NGA models and each model's predecessor, as well as the abbreviations for all models (Abrahamson and Silva, 1997; Abrahamson and Silva, 2008; Boore *et al*., 1997; Boore and Atkinson, 2008; Campbell, 1997; Campbell and Bozorgnia, 2003; Campbell and Bozorgnia, 2008; Chiou and Youngs, 2008a; Idriss, 1991; Idriss, 2002; Idriss, 2008; Sadigh *et al.*, 1997). "NGA East," a similar GMPE development project for central and eastern North America, a stable continental tectonic environment of moderate seismicity, is currently in its beginning stages (Cramer *et al.*, 2009).

Table 1.1. GMPEs tested in this study

NGA models			Previous models		
Team	Year	Abbrev.	Team	Year	Abbrev.
Abrahamson and Silva	2008	AS08	Abrahamson and Silva	1997	AS97
Boore and Atkinson	2008	BA08	Boore, Joyner, and Fumal	1997	BJF97
Campbell and Bozorgnia	2008	CB08	Campbell	1997	C97*
Chiou and Youngs	2008	CY08	Sadigh, Chang, Egan, Makdisi, and Youngs	1997	SCE97
Idriss	2008	I08	Idriss	1991	I91*

NOTE:
* In the early 2000s, Campbell and Bozorgnia released an update to Campbell's 1997 model (Campbell and Bozorgnia, 2003) and Idriss developed an unpublished update to his 1991 model (Idriss, 2002). However, to maintain consistency in the comparison between the set of new and old models, we use all the GMPEs from the 1990s as the baseline for comparison.

The NGA models will have serious consequences, as they are beginning to serve as the basis for seismic hazard assessment in many applicable regions. In the most recent update to the national seismic hazard maps released by the United States Geological Survey (USGS), the NGA models are included in the hazard calculations (Petersen *et al.*, 2008). However, there have not been many published quantitative comparisons of the NGA models, and the few existing comparisons tend to focus on specific regions or scenarios. Ghasemi *et al.* (2008) compare and rank several GMPEs for seismic hazard analysis in Iran. Stafford *et al.* (2008) compare the NGA models with European models for seismic hazard analysis in the Euro-Mediterranean region. Star *et al.* (2008) and Stewart *et al*. (2008) compare the NGA models for simulated ground motions for various scenarios in southern California. Due to the lack of a comprehensive comparison of the

NGA models in the literature, we became intrigued to perform an NGA model validation ourselves.

1.6 Scope of Thesis

In this thesis, we attempt to make a contribution to the geotechnical earthquake engineering community by objectively comparing the NGA models using a statistical validation framework. First, we present a detailed discussion of the decisions the model teams made when selecting their databases of ground motions to be used in regression during model development. As we will illustrate, the decisions that model developers make during the selection of their regression datasets, such as the inclusion of aftershocks and determination of distance cutoffs, can greatly affect the models' predictive capabilities. We then present a detailed discussion of the explanatory and response variables found in the NGA relations and how they differ from previous GMPEs.

From the master database used to develop the five NGA models, we develop testing databases of ground motion records that meet the requirements of the models. By calculating objective goodness-of-fit statistics, we compare the model predictions to the actual ground motion records to assess the predictive capabilities of the models. The Nash-Sutcliffe model efficiency coefficient (E), a commonly used statistic used in hydrology, is selected as the primary goodness-of-fit measure. We also report Pearson's correlation coefficient (r), percent root mean square error ($PRMSE$), and percent bias (PB) as additional goodness-of-fit measures. We test the models under different conditions, for soil and rock sites at various distances for both mainshocks and

aftershocks. Based on the results, we discuss which GMPEs offer the most successful predictions in various situations, and the manner in which model development decisions influence model performance.

In addition, to assess the level of improvement that has occurred over time, we compare the new models with the previous generation of models. We perform blind comparative tests by implementing the new and old models on recent earthquakes that were not present in any of the databases used to develop the models. In our comparisons, we utilize ground motion records from the two most recent earthquakes of magnitude 6.0 or greater to strike mainland California: (1) the *M* 6.0 Parkfield earthquake of 28 September 2004, and (2) the *M* 6.5 San Simeon earthquake of 22 December 2003. The results of these two tests are examples of how these GMPEs may perform when predicting ground motion for future earthquakes.

The focus of this thesis is on ground motion prediction equations for peak ground acceleration, peak ground velocity, and spectral acceleration, because these are the ground motion parameters explored during the NGA project. Although we do not specifically analyze relationships for predicting other earthquake-related phenomena, we develop a statistical validation methodology that could be used as a framework for comparing other earthquake parameters. The effect of earthquake-induced ground motions on structures is also outside the scope of this thesis, although GMPEs certainly have an influence in how these structures are designed.

By comparing the explanatory variables and performance of different models, we discuss the sources of uncertainty in the estimates of ground motion parameters and offer recommendations for model development. Ultimately, we present a model validation

framework for assessing the prediction accuracy of ground motion prediction equations. Through detailed comparisons and analyses of the issues surrounding the Next Generation Attenuation models, our suggestions may be useful in the development of future ground motion prediction equations.

Chapter 2:
DATA

2.1 The NGA Database

In order to develop the NGA models, researchers compiled an extensive data set of 3551 ground motion records from 173 shallow crustal earthquakes (Chiou *et al.*, 2008). A spreadsheet of the entire database, called the "NGA flatfile" (Pacific Earthquake Engineering Research Center, 2008a), is publicly available on the PEER NGA project web site (Pacific Earthquake Engineering Research Center, 2008b). The researchers utilized subsets of this database in their regressions for model development. The research teams generally excluded records that were not representative of free-field conditions (*e.g.*, records from basements, tall structures, or dam crests), records from locations outside of the models' range of applicability, and records lacking key information, although the specific decisions of each team varied (Power *et al.*, 2008).

The teams made various assumptions in selecting their final datasets for regression. One of the most significant decisions for the researchers was whether to include aftershocks in their regression subsets. Three teams (AS08, CY08, and I08) opted to include aftershocks (Abrahamson *et al*., 2008). Chiou and Youngs (2008a) only included records within 70 km of the earthquake source, while the other teams included

records within 200 km, the maximum source-to-site distance to which the NGA models are applicable. Chiou and Youngs (2008a) claim that a distance cutoff larger than 70 km would generate a bias in the dataset; to extend their model to distances greater than 70 km, they make assumptions on physical attenuation characteristics. Idriss (2008) only included rock sites (assumed to be locations with $V_{S30} \geq 450$ m/s) in his model; this significant difference isolates the I08 model from the others because it can only be applied to rock sites. As we will demonstrate, these dataset selection decisions greatly influence the models' prediction accuracy.

2.2 Explanatory Variables

A summary of the explanatory variables used in the GMPEs is presented in Table 2.1. There is a wide range of model complexity, but as a whole, the NGA models are much more complicated than their previous counterparts are. Based on the number of input parameters, I08 has the simplest formulation of the NGA models, followed by BA08, CB08, CY08, and AS08. Three of the NGA models (AS08, CB08, and CY08) include two or three different distance measures in the same model, whereas previous GMPEs incorporated just one per model. Four of the NGA models utilize the time-averaged shear wave velocity over the top 30 meters of the subsurface (V_{S30}) as the primary site characteristic; Idriss (2008) does not quantitatively incorporate site characteristics into his model, although he provides separate coefficients for soft and hard rock sites (assuming a boundary of V_{S30} = 900 m/s between soft and hard rock). Boore *et al.* (1997) were the first to include V_{S30} in a GMPE. Other previous models utilize dummy variables to incorporate site conditions (Abrahamson and Silva, 1997; Campbell, 1997), or provide

completely different sets of regression equations for soil and rock sites (Sadigh *et al.*, 1997). Furthermore, three of the NGA relations (AS08, CB08, and CY08) incorporate a depth parameter ($Z_{1.0}$ or $Z_{2.5}$) as a secondary site characteristic in addition to V_{S30}. One of the previous models (Campbell, 1997) includes a parameter D for depth to basement rock. Appendix A contains explicit details of the explanatory variables for each of the ten GMPEs explored in this study.

Table 2.1. Explanatory variables of the GMPEs in this study

		NGA models					Previous models				
	Parameter	AS08	BA08	CB08	CY08	I08	AS97	BJF97	C97	SCE97	I91
Source parameters	Moment magnitude, M	●	●	●	●	●	●	●	●	●	●
	Depth to top of rupture, Z_{TOR}	●		●	●						
	Down-dip rupture width, W	●									
	Fault dip, δ	●		●	●						
	Style-of-faulting flag (function of rake angle, λ)	●	●	●	●	●	●	●	●	●	●
	Aftershock flag	●			●						
Distance and path parameters	Closest distance to the rupture plane, R_{RUP}	●		●	●	●	●			●	●
	Horizontal distance to the surface projection of the rupture (Joyner-Boore distance), R_{JB}	●	●	●	●			●			
	Horizontal distance to the top edge of the rupture measured perpendicular to the strike, R_X	●			●						
	Closest distance to the rupture plane within the zone of seismogenic rupture (seismogenic distance), R_{SEIS}								●		
	Hypocentral distance, R_{HYP}										●
	Hanging wall flag	●			●		●				
Site parameters	Time-averaged shear wave velocity over the top 30 meters of the subsurface, V_{S30}	●	●	●	●			●			
	Depth to bedrock or specific shear wave velocity horizon ($Z_{1.0}$, $Z_{2.5}$, or D) [1]	●		●	●				●		
	Site conditions flag [2]						●		●	●	
	PGA (or *Sa*) on rock, as baseline for nonlinear site response	●	●	●	●		●				

NOTES:
1. AS08 and CY08 use depth to V_S = 1.0 km/s ($Z_{1.0}$), CB08 uses depth to V_S = 2.5 km/s ($Z_{2.5}$), and C97 uses depth to basement rock (D).
2. AS97 and SCE97 differentiate deep soil sites from sites composed of rock or shallow soil. C97 has separate categories for soil, soft rock, and hard rock.

2.2.1 Calculation of Site Coordinate

An extensive set of explanatory variables is necessary to implement the ten GMPEs in this study. For the records in the NGA flatfile, many of the necessary parameters are explicitly included as columns, whereas others (such as R_X) needed to be calculated from the available information in the flatfile. The horizontal distance to the top edge of the rupture, measured perpendicular to the fault strike (also known as the *site coordinate*, R_X) enters the hanging wall scaling terms of the Abrahamson and Silva (2008) and Chiou and Youngs (2008a) NGA relations. However, there is not a clear published description on how to calculate R_X from the values available in the NGA flatfile. A generalized definition of R_X for a multi-segment fault is given in Spudich and Chiou (2008), but it is complicated and involves values that are not explicitly present in the NGA flatfile. Using geometric and trigonometric principles, we derive a simple formulation for R_X as a function of the other distance and source parameters.

In order to obtain an equation for R_X, we must define an important location measure, the *source-to-site azimuth* (α). Figure 2.1 is a plan view of the surface projection of the ruptured area, and the surface projection of the top edge of rupture, which aligns with the fault strike. We assume that the fault rupture may be modeled by a single plane, which is a reasonable proposition for most earthquakes. The positive y-axis is directed along the fault strike such that the ruptured area is to the right. The positive x-axis is in the direction of the ruptured area (the hanging wall side of the fault). The source-to-site azimuth (α) for a given site is the angle between the positive fault strike direction and line connecting a site to the closest point on the surface projection of the top edge of rupture, with clockwise angles assumed positive (Chiou, 2005). Sites located on

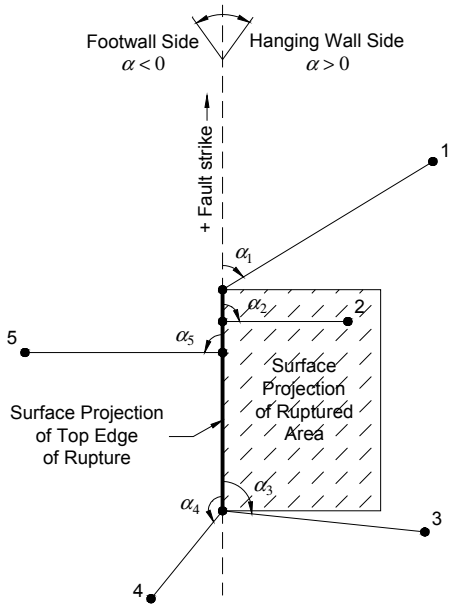

Figure 2.1. Plan view of a fault rupture, giving the definition and sign convention of the source-to-site azimuth (α). Also illustrated are five example sites and their source-to-site azimuths. Sites 1 to 3, which are located on the hanging wall side of the fault, have positive azimuths; sites 4 and 5, which are located on the footwall side of the fault, have negative azimuths.

the hanging wall have positive azimuths (ranging from 0° to 180°), and sites located on the footwall have negative azimuths (ranging from −180° to 0°). R_X is defined to be positive for sites on the hanging wall side of the fault and negative for sites on the footwall side of the fault (Chiou and Youngs, 2008a). As Figure 2.2 illustrates, a site can be categorized into one of nine cases, based (1) on the value of α, and for sites on the hanging wall side of the fault, (2) on how the site is oriented with respect to the ruptured area. The cases are numbered starting with the ruptured area and proceeding clockwise. These nine cases are important for the derivation of the equations for R_X and for all distance measures in general.

We derive the following equations for the site coordinate R_X, which are for various groupings of α:

(a) For $\alpha = 90°$ (cases 1 and 4 in Figure 2.2; location on the hanging wall side of the fault, in line with the ruptured area in the *x*-direction):

$$R_X = \begin{cases} \dfrac{R_{RUP}}{\sin\delta} - \dfrac{Z_{TOR}}{\tan\delta} & for\ R_{JB} = 0 \quad (2.1a) \\ R_{JB} + W\cos\delta & for\ R_{JB} > 0. \quad (2.1b) \end{cases}$$

(b) For $0 \le \alpha < 180°$, $\alpha \ne 90°$ (cases 2, 3, 5, and 6; location on the hanging wall side of the fault, not in line with the ruptured area in the *x*-direction):

$$R_X = \begin{cases} R_{JB}\,|\tan\alpha| & for\ \dfrac{W\cos\delta}{R_{JB}\,|\tan\alpha|} \ge 1 \quad (2.2a) \\ R_{JB}\tan\alpha\,\cos\left[\alpha - \sin^{-1}\left(\dfrac{W\cos\delta\cos\alpha}{R_{JB}}\right)\right] & for\ \dfrac{W\cos\delta}{R_{JB}\,|\tan\alpha|} < 1. \quad (2.2b) \end{cases}$$

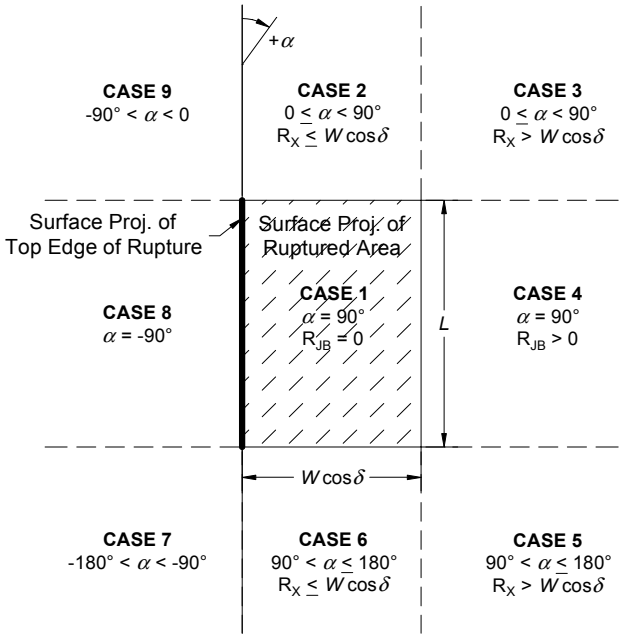

Figure 2.2. Plan view of the nine geometric cases for the location of a site with respect to the fault strike and surface projection of ruptured area, used in the calculation of R_X.

(c) For $\alpha = -90°$ (case 8; location on the footwall side of the fault, in line with the ruptured area in the *x*-direction):

$$R_X = -R_{JB}. \tag{2.3}$$

(d) For $-180° < \alpha < -90°$, $\alpha \neq -90°$ (cases 7 and 9; location on the footwall side of the fault, not in line with the ruptured area in the *x*-direction):

$$R_X = R_{JB} \sin\alpha. \tag{2.4}$$

We will now describe the geometric and trigonometric derivations for the various cases. Case 1, where R_X is given by Equation 2.1a, occurs when the site is directly above the rupture plane. Figure 2.3 displays a vertical cross-section directly through the rupture plane, with the distance measures for a hypothetical site located above the rupture surface ($R_{JB} = 0$). Using trigonometry on the large triangle formed by R_{RUP} and $R_X + d$, we have

$$\sin\delta = \frac{R_{RUP}}{R_X + d}. \tag{2.5}$$

Similarly, for the small triangle formed by Z_{TOR} and d, we have

$$\tan\delta = \frac{Z_{TOR}}{d}. \tag{2.6}$$

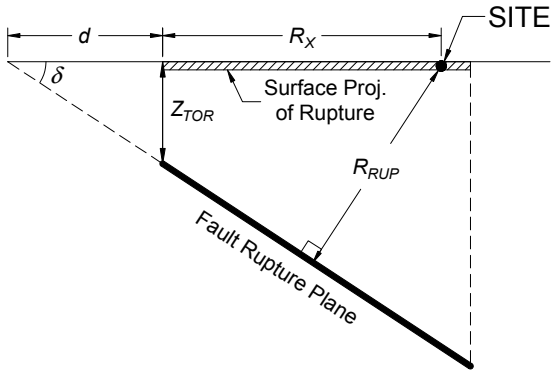

Figure 2.3. Vertical cross-section at a site located directly over the ruptured area (case 1 in Figure 2.2; $R_{JB} = 0$).

Performing some algebraic manipulations to eliminate d, the resulting equation for R_X is:

$$R_X = \frac{R_{RUP}}{\sin\delta} - \frac{Z_{TOR}}{\tan\delta}, \tag{2.7}$$

which is the result given in Equation 2.1a.

The geometries for cases 2, 4, and 6 are shown in the plan view in Figure 2.4. Equation 2.1b for case 4, when the site is located in line with the ruptured area in the x-direction (α = 90°) but not directly over the ruptured area ($R_{JB} > 0$), is immediately apparent from the figure. For case 2 ($0 \le \alpha < 90°$), the equation is developed from right-triangle trigonometry:

$$R_X = R_{JB} \tan\alpha . \tag{2.8}$$

The equation for case 6 ($90 < \alpha \le 180°$), is slightly different:

$$R_X = R_{JB} \tan(180° - \alpha). \tag{2.9}$$

The trigonometric identity for the tangent of a difference of two angles x and y,

$$\tan(x - y) = \frac{\tan x - \tan y}{1 + \tan x \tan y}, \tag{2.10}$$

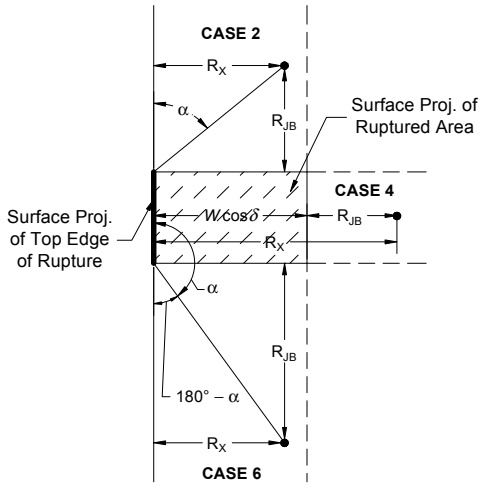

Figure 2.4. Plan view for locations on the hanging wall side of the fault having cases 2, 4, and 6 in the calculation of R_X.

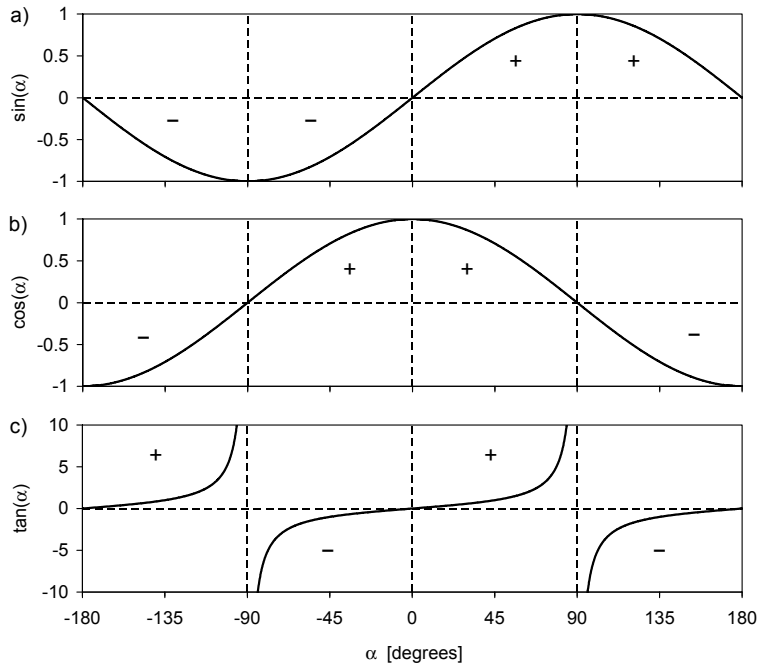

Figure 2.5. Graphs of trigonometric functions used in the derivations: (a) sine, (b) cosine, and (c) tangent. In particular, note that tan(α) is positive for α on the interval (0°, 90°) and negative on the interval (90°, 180°), and that sin(α) is negative for α on the interval (−180°, 0°).

leads to

$$\tan(180° - \alpha) = -\tan\alpha \,. \tag{2.11}$$

A graph of tan(α) and other trigonometric functions for $-180° \le \alpha \le 180°$ is provided in Figure 2.5. Since the tangent function is negative for angles between 90° and 180°, the term "–tan(α)" becomes positive. Thus, Equation 2.9 can be written as

$$R_X = R_{JB} \,|\tan\alpha\,| \tag{2.12}$$

for case 6. Since tan(α) = |tan(α)| when tan(α) ≥ 0, such as for case 2, the expression for R_X for both case 2 and case 6 may be given by Equation 2.12 and Equation 2.2a.

The equation for case 3 is derived by considering the two triangles shown in the plan view of Figure 2.6. The derivation is more difficult because R_{JB} is no longer orthogonal to the surface projection of the ruptured area. The known quantities are R_{JB},

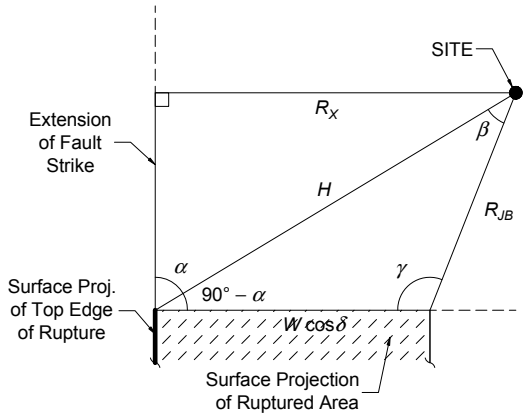

Figure 2.6. Plan view for case 3 on the hanging wall side of the fault, where R_{JB} is not orthogonal to the surface projection of the ruptured area.

W, δ, and α; and the unknown quantities are R_X, H, β, and γ. An expression for R_X can be developed using the Law of Sines, given by

$$\frac{\sin a}{A} = \frac{\sin b}{B} = \frac{\sin c}{C} \tag{2.13}$$

for the arbitrary triangle in Figure 2.7, with angles a, b, and c, and side lengths A, B, and C, where A defines the length of the side across from angle a, etc. Knowing that β is acute and γ is obtuse, the Law of Sines can be applied on the bottom triangle to derive an unambiguous equation for β in terms of the known quantities. Since the sums of the angles in a triangle must equal 180°, the value of γ can then be determined from α and β. The Law of Sines can then be used again on the bottom triangle to solve for the length H.

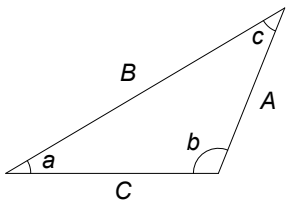

Figure 2.7. Triangle used in the formulation of the Law of Sines.

Knowing H, the value of R_X can be found by using right-triangle trigonometry on the top triangle. Trigonometric identities lead to the simplified Equation 2.2b. When a similar analysis is performed for case 5, the resulting final equation is the same as for case 3.

The plan view in Figure 2.8 describes the geometry for cases 7, 8, and 9, in which the site is located on the footwall side of the fault. R_X is defined to be negative for sites on the footwall, and α is also negative, so the derivations must take this into account. The formulation of R_X for case 8 ($\alpha = -90°$) is trivial (Equation 2.3). Using trigonometry, we obtain the formulas

$$R_X = R_{JB} \sin(180° - \alpha) \tag{2.14}$$

for case 7 ($-180° < \alpha < 90°$), and

$$R_X = R_{JB} \sin \alpha \tag{2.15}$$

for case 9 ($-90° < \alpha < 0°$). The trigonometric identity for the sine of a difference of two

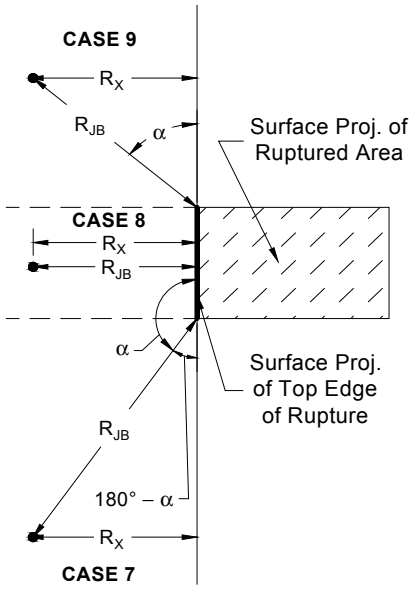

Figure 2.8. Plan view for locations on the footwall side of the fault; cases 7, 8, and 9 in the calculation of R_X. The source-to-site azimuth (α) and R_X are negative for each of these cases.

angles x and y,

$$\sin(x - y) = \sin x \cos y - \sin y \cos x , \tag{2.16}$$

leads to

$$\sin(180° - \alpha) = \sin \alpha . \tag{2.17}$$

Therefore, cases 7 and 9 may both be represented by the same formula (Equation 2.15, or Equation 2.4 above). Knowing that $\sin(\alpha)$ is negative for $-180° < \alpha < 0°$ (Figure 2.5), the use of this formula correctly gives a negative value for R_X. Although R_X can be calculated for sites on the footwall side of the fault, the hanging wall flag (F_{HW}) in the AS08 and CY08 models is equal to zero and thus the hanging wall term, which contains R_X, does not enter the ground motion calculation at all.

2.2.2 Calculation of Depth Parameters

Although V_{S30} is included for nearly every record in the flatfile, the depth parameters $Z_{1.0}$ (used in AS08 and CY08) and $Z_{2.5}$ (used in CB08) are not present for many records. The preferred method of determining the depth parameters is using a site-specific measured V_S profile that extends to the 1.0 km/sec and 2.5 km/sec horizons. Unfortunately, only 54 sites in the NGA flatfile have measured V_S profiles that reach 1.0 km/sec (Chiou and Youngs, 2008a), and even fewer reach 2.5 km/sec. If the site is located in an area where a regional velocity model is available (such as San Francisco or Los Angeles), then the depth parameters may be determined from the regional velocity model. If a measured V_S profile or regional velocity model is unavailable (which is the most common case), the depth parameters are determined by the recommendations of the model developers

(Abrahamson and Silva, 2008; Chiou and Youngs, 2008a; Campbell and Bozorgnia, 2007). The recommendations for the estimation of $Z_{1.0}$ and $Z_{2.5}$ will be summarized here.

Abrahamson and Silva (2008) recommend using the following median relationship to estimate $Z_{1.0}$ from V_{S30}:

$$Z_{1.0} = \begin{cases} \exp(6.745) & \text{for } V_{S30} < 180\ m/s \\ \exp\left[6.745 - 1.35 \cdot \ln\left(\frac{V_{S30}}{180}\right)\right] & \text{for } 180 \le V_{S30} \le 500\ m/s \\ \exp\left[5.394 - 4.48 \cdot \ln\left(\frac{V_{S30}}{500}\right)\right] & \text{for } V_{S30} > 500\ m/s\ . \end{cases} \quad (2.18)$$

Chiou and Youngs (2008a) recommend using the following median relationship to estimate $Z_{1.0}$ from V_{S30}:

$$Z_{1.0} = \exp\left[28.5 - \frac{3.82}{8} \cdot \ln\left(V_{S30}{}^{8} + 378.7^{8}\right)\right]\ . \quad (2.19)$$

Graphs of the two median relationships for $Z_{1.0}$ are presented in Figure 2.9, along with

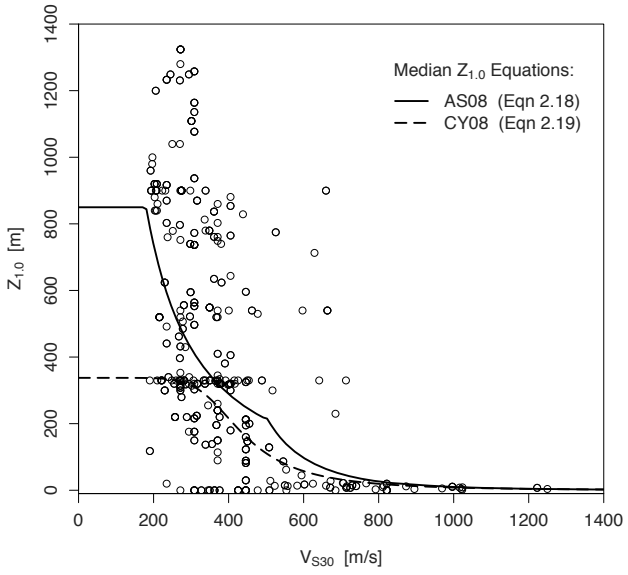

Figure 2.9. $Z_{1.0}$ versus V_{S30} for records in the NGA flatfile having specified values of $Z_{1.0}$. Also shown are the median equations employed by the AS08 and CY08 models for estimating $Z_{1.0}$ as a function of V_{S30}.

data from the 448 sites in the NGA flatfile with specified values of $Z_{1.0}$. Note that the majority of this data is from regional velocity models and not from boreholes. The large amount of scatter on this plot and its implications will be discussed later.

In order to estimate $Z_{2.5}$, Campbell and Bozorgnia (2007) offer guidelines for extrapolating the estimates of $Z_{1.0}$ or $Z_{1.5}$ (depth to V_S = 1.5 km/s) if these values are available. The depth parameters are in units of meters for the AS08 and CY08 models (as well as in the NGA flatfile), and in units of kilometers for the CB08 model. If $Z_{1.5}$ is known, then the following equation may be used to estimate $Z_{2.5}$, where all depths are in meters:

$$Z_{2.5} = 636 + 1.549 Z_{1.5} \,. \tag{2.20}$$

If $Z_{1.0}$ is known (but not $Z_{1.5}$), then $Z_{2.5}$ may be estimated by the following extrapolation:

$$Z_{2.5} = 519 + 3.595 Z_{1.0} \,. \tag{2.21}$$

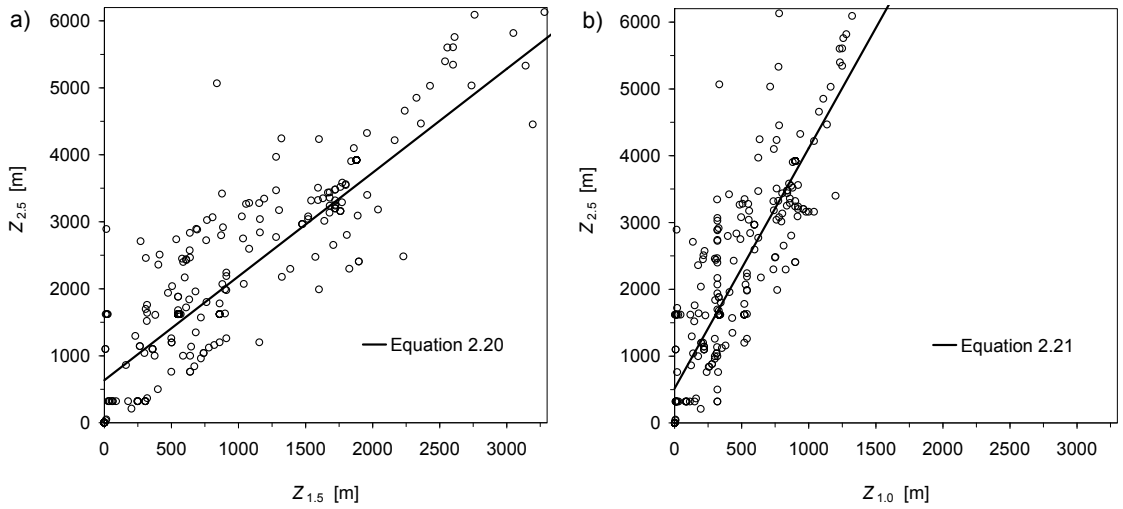

Figure 2.10. Plots of (a) $Z_{2.5}$ versus $Z_{1.5}$ and (b) $Z_{2.5}$ versus $Z_{1.0}$, using data from sites in the NGA flatfile used in our analyses with populated depth parameter columns. Also shown are the functions defined by Campbell and Bozorgnia (2007) for estimating $Z_{2.5}$ from $Z_{1.5}$ (Equation 2.20) and $Z_{2.5}$ from $Z_{1.0}$ (Equation 2.21).

Figure 2.10 contains plots of Equations 2.20 and 2.21, along with data from sites in the NGA flatfile used in our analyses with populated depth parameter columns. In general, if $Z_{2.5}$ is not listed in the database, then neither $Z_{1.0}$ nor $Z_{1.5}$ is listed. If neither $Z_{1.0}$ nor $Z_{1.5}$ is known, and the basin is not known to be particularly shallow or particularly deep, then Campbell and Bozorgnia (2007) recommend assigning $Z_{2.5}$ to be the "default value" of 2 km. In this case, the basin response term will equal zero, and V_{S30} will solely represent the site characteristics in the ground motion calculation.

The Campbell (1997) relationship includes depth to basement rock D as an explanatory variable for modeling long-period site response. "Basement rock" may be considered to be pre-Tertiary sedimentary rock and hard volcanic deposits, high-grade metamorphic rock, or crystalline rock (Chiou, 2005). When no other information is available, Campbell (2000) recommends setting $D = 0$ for hard rock sites, $D = 1$ km for soft rock ("generic rock") sites, and $D = 5$ km for generic soil sites.

2.2.3 Classification of Aftershocks

There is no column in the NGA flatfile that indicates whether a ground motion record is a mainshock or an aftershock, which is necessary for determining the appropriate value of the aftershock flag variable (0 or 1) in the AS08 and CY08 models. Fortunately, Abrahamson and Silva (2008) and Boore and Atkinson (2007) include tables that indicate which earthquakes are classified as mainshocks and which earthquakes are classified as aftershocks. Abrahamson and Silva (2008) group mainshocks, foreshocks, and swarms into one category. However, this assumption does not affect a large number of ground motion records in the NGA flatfile.

Table 2.2. Source parameters for the Parkfield and San Simeon earthquakes

	Parkfield	San Simeon
Date	28 Sept. 2004	22 Dec. 2003
Moment Magnitude, M	6.0	6.5
Hypocenter latitude [deg]	35.815	35.706
Hypocenter longitude [deg]	−120.374	−121.102
Hypocentral depth, Z_{HYP} [km]	7.9	4.7
Depth to top of rupture, Z_{TOR} [km]	0.12	0.00
Down-dip rupture width, W [km]	15.5	22.0
Fault rupture length (along strike), L [km]	34.0	44.0
Fault strike [deg]	137	303
Fault dip, δ [deg]	80	56
Rake angle, λ [deg]	180	76
Classification based on rake angle	Strike-slip	Reverse
Finite fault model utilized	Dreger (2004)	Rolandone *et al.* (2004)

2.2.4 Determination of Explanatory Variables for Blind Comparison Tests

For the Parkfield and San Simeon earthquakes, which are not present in the NGA flatfile, we determined the explanatory variables from a variety of sources. Source characteristics such as depth to top of rupture, down-dip rupture width, and fault dip were determined by selecting a finite fault model for the Parkfield (Dreger, 2004) and San Simeon (Rolandone *et al.*, 2004) earthquakes, as seen in Table 2.2. The required distance measures were calculated from the source-to-site geometry for each location. Given the latitude and longitude of a station with recorded ground motion for either earthquake, we first converted the latitude and longitude to more useful Universal Transverse Mercator (UTM) coordinates (in units of kilometers) using a series of projection equations (Snyder, 1987). Now, the problem is reduced to finding the closest distance from a point to a

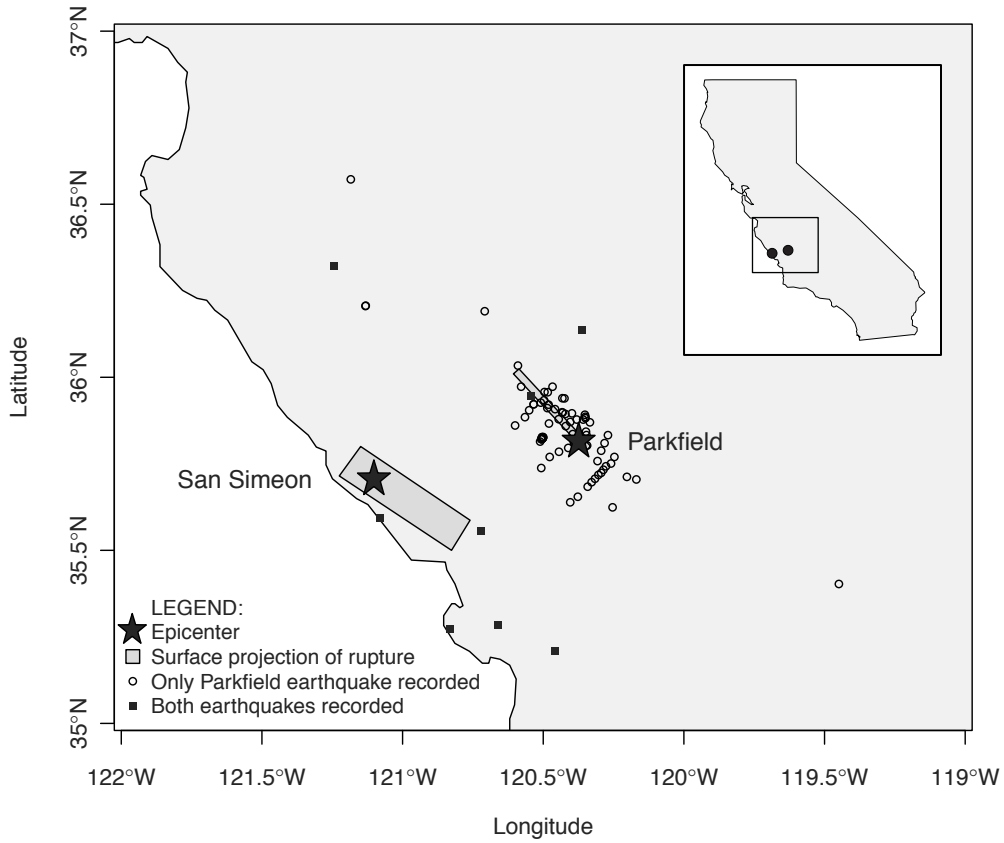

Figure 2.11. Map of ground motion recording stations for the Parkfield and San Simeon earthquakes evaluated in this study, along with the earthquake epicenters and surface projections of the ruptured areas.

plane in three-dimensional space. A seismogenic depth of 3 km was assumed when calculating R_{SEIS} for the C97 model.

For the Parkfield and San Simeon earthquakes, we analyzed a total of 93 ground motion records from 85 stations. Seventy-seven stations recorded just the Parkfield earthquake, and eight stations recorded both the Parkfield and San Simeon earthquakes (the epicenters of the two earthquakes were only 67 km apart, and thus some records are located at common stations). Our methodology for selecting ground motion records will be discussed in section 2.5. A map of the 85 stations and the rupture zones of the Parkfield and San Simeon earthquakes is presented in Figure 2.11. The stations are

owned and operated by various organizations, including the Berkeley Digital Seismic Network [BDSN] (2004), California Strong Motion Instrumentation Program [CSMIP] (2004), Northern California Seismic Network [NCSN] (2004), and United States Geological Survey [USGS] (2004). Table 2.3 is a list of the owners and operators of the seismic recording stations we used in this study, as well as the number of stations we used. Data for each of the stations are available on the individual websites of the organizations, as well as on the following online databases: (1) the Consortium of Organizations for Strong-Motion Observation Systems [COSMOS] (2004); (2) the National Strong Motion Program [NSMP] (2004), which is run by the USGS and only has data from USGS-owned stations (including the station from NCSN); and (3) the Center for Engineering Strong Motion Data [CESMD] (2004).

The site characteristics for the 85 stations were obtained from a variety of sources, depending on the availability of information. First, some of the stations that recorded the Parkfield and San Simeon earthquakes also recorded other earthquakes in the NGA flatfile, such as the *M* 6.2 Parkfield earthquake of 1966 and the *M* 6.4 Coalinga earthquake of 1983; site characteristics for these stations were determined directly from

Table 2.3. Owners of the seismic recording stations used in this study

Owner of seismic station		Operating organization		
Name	Abbreviation	Name	Abbreviation	No. of stations used
Berkeley Digital Seismic Network	BDSN	University of California, Berkeley	UCB	1
California Strong Motion Instrumentation Program	CSMIP	California Geological Survey	CGS	58
Northern California Seismic Network	NCSN	United States Geological Survey	USGS	1
United States Geological Survey	USGS	United States Geological Survey	USGS	25

the flatfile. For stations that were not present in the flatfile, and for stations in the flatfile without measured shear wave velocity profiles, we determined the site characteristics from measured V_S data, if available. Shear wave velocity profiles at 52 ground motion recording stations in the Parkfield area were collected by Kayen (2007) using the spectral analysis of surface waves (SASW) test, a geophysical method that produces Rayleigh waves by an electro-mechanical shaker (Stokoe *et al.*, 1994). Sixteen of these profiles surpassed the V_S = 1.0 km/s horizon, so estimates of $Z_{1.0}$ in addition to V_{S30} could be made for these stations. Furthermore, V_S profiles at two stations in the Turkey Flat Strong-Motion Array in Parkfield were published by Real (1988).

To an arbitrary averaging depth of D, the average shear wave velocity $V_{S,D}$ is computed as a weighted harmonic mean of the shear wave velocity $V_S(z)$ in the upper D meters of the subsurface:

$$V_{S,D} = \frac{D}{\int_0^D \frac{dz}{V_S(z)}} \quad . \tag{2.22}$$

The denominator of Equation 2.22 is the travel time of the wave to propagate through the upper D meters of the subsurface. Calculation of the shear wave velocity in this manner preserves the travel time, which represents the true wave behavior during its upward propagation. The shear wave velocity function $V_S(z)$ is usually modeled as a step function with constant V_S for each individual layer in the subsurface. For a discrete profile with n layers between the ground surface and the averaging depth D, each with thickness z_i and constant shear wave velocity V_{Si}, as illustrated in Figure 2.12, Equation 2.22 simplifies to:

$$V_{S,D} = \frac{D}{\sum_{i=1}^{n}\left(\frac{z_i}{V_{Si}}\right)} \ , \tag{2.23}$$

where

$$D = \sum_{i=1}^{n} z_i \ . \tag{2.24}$$

By convention, the time-averaged shear wave velocity over the upper 30 meters of subsurface depth (V_{S30}) is used as the basis for site classification. The National Earthquake Hazards Reduction Program (NEHRP) made this change to the seismic design code provisions in 1997 (Building Seismic Safety Council [BSSC], 1998).

For locations without measured V_S profiles, site characteristics were inferred from surficial geologic units using the classification scheme of Wills and Clahan (2006), which the NGA research team also used to estimate V_{S30} for many records in the flatfile (Chiou *et al.*, 2008). The surface geology of the stations was determined from the NGA flatfile, the respective web pages of the station owners, and geologic maps of California (California Geological Survey, 2007; Shakal *et al.*, 2005; Jennings, 1977). Once the surficial geologic unit was identified, the site was assigned the median V_{S30}

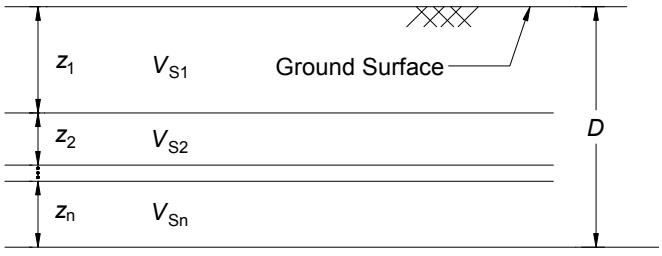

Figure 2.12. Example soil profile for the calculation of average shear wave velocity, over a total averaging depth D, across n sublayers each with thickness z_i and shear wave velocity V_{Si}.

Table 2.4. Inferring V_{S30} from surficial geology

Symbol	Surficial geologic unit description	Median V_{S30} [m/sec]	Number of stations in this study
Qal, deep	Quaternary (Holocene) alluvium in areas where the alluvium is more than 30 m thick, often much deeper	271.44	2
Qal, thin	Quaternary (Holocene) alluvium in narrow valleys, small basins, and adjacent to the edges of basins where the alluvium would be expected to be underlain by contrasting material within 30 m	338.54	26
Qoa	Quaternary (Pleistocene) alluvium	370.79	7
Tsh	Tertiary (mostly Miocene and Pliocene) shale and siltstone units	376.07	16
QT	Quaternary to Tertiary (Pleistocene—Pliocene) alluvial deposits	438.34	26
Tss	Tertiary (mostly Miocene, Oligocene, and Eocene) sandstone units	477.65	3
Tv	Tertiary volcanic units	597.12	1
serpentine	Serpentine rock	641.56	1
Kgr	Cretaceous granitic rock	684.94	1
KJf	Franciscan complex rock, including mélange, sandstone, shale, chert, and greenstone	712.82	2

Modified from Wills and Clahan (2006) and Chiou *et al.* (2008).

corresponding to the geologic unit, as presented in Table 2.4. For each surficial geologic unit, Wills and Clahan (2006) use the mean of the natural logarithm of V_{S30} from a set of profiles in the Pacific Engineering database as an estimator of the median V_{S30} at unsampled locations in California.

Appendix B contains detailed tables of the explanatory and response variables we gathered and calculated for our blind comparison tests on the 2004 M 6.0 Parkfield earthquake and the 2003 M 6.5 San Simeon earthquake. For each of the 85 records from the Parkfield earthquake and the 8 records from the San Simeon earthquake, the appendix contains information on the ground motion recording stations, location parameters, and site parameters. The source parameters—which are constant for a given earthquake—

were summarized in Table 2.2. Taken together with Table 2.2, Appendix B can be thought of as a mini-flatfile for the Parkfield and San Simeon earthquakes.

2.3 Response Variables

The response variables for the GMPEs are peak ground acceleration (*PGA*), peak ground velocity (*PGV*), and 5%-damped elastic pseudo-response spectral acceleration (*Sa*). All models have equations for *PGA* and *Sa*, although the spectral periods with defined coefficients vary from model to model, especially for the older models, as seen in Table 2.5. One of the NGA models (CB08) includes a model for peak ground displacement (*PGD*). We consider *PGA* to be part of the acceleration response spectrum with a period of 0.01 sec, because most of the NGA models (CB08, CY08, and I08) have identical coefficients for *PGA* and *Sa*(0.01 sec). Idriss (2008) notes that the observed values of *PGA* and *Sa*(0.01 sec) in the flatfile are generally within 2% of each other. Four of the NGA models (AS08, BA08, CB08, and CY08) and one of the previous models (C97) have equations for *PGV*. In this study, we analyze *PGA* and *Sa* for the six spectral periods represented most comprehensively in the USGS national seismic hazard maps: 0.1, 0.2, 0.3, 0.5, 1.0, and 2.0 seconds (Petersen *et al*., 2008). Being represented in the national seismic hazard maps, these spectral periods have significant engineering consequences. Furthermore, all ten GMPEs have defined coefficients for these periods, so cross-comparisons can easily be made between the models. The subset of periods we analyze is highlighted in Table 2.5. The previous GMPEs offer predictions for *Sa* to maximum periods of 2 to 5 seconds, whereas the new GMPEs offer predictions up to 10

Table 2.5. Response variables of the GMPEs in this study

		NGA models					Previous models				
Parameter	Period [sec]	AS08	BA08	CB08	CY08	I08	AS97	BJF97	C97	SCE97	I91
PGA	–	●	●	●	●	●	●	●	●	●	●
PGV	–	●	●	●	●				●		
PGD	–			●							
Sa	0.01	●	●	●	●	●	●				
	0.02	●	●	●	●	●	●				
	0.03	●	●	●	●	●	●				●
	0.04	●			●	●	●				
	0.05	●	●	●	●	●	●		●		●
	0.06					●	●				
	0.07									●*	
	0.075	●	●	●	●		●		●	●*	●
	0.08					●					
	0.09						●				
	0.10	●	●	●	●	●	●	●	●	●	●
	0.11							●			●
	0.12						●	●			
	0.13							●			●
	0.14							●			
	0.15	●	●	●	●	●	●	●	●		●
	0.16							●			
	0.17						●	●			
	0.18							●			
	0.19							●			
	0.20	●	●	●	●	●	●	●	●	●	●
	0.22							●			
	0.24						●	●			
	0.25	●	●	●	●	●					●
	0.26							●			
	0.28							●			
	0.30	●	●	●	●	●	●	●	●	●	●
	0.32							●			
	0.34							●			
	0.35					●					●
	0.36						●	●			
	0.38							●			
	0.40	●	●	●	●	●	●	●		●	●
	0.42							●			
	0.44							●			
	0.45					●					
	0.46						●	●			
	0.48							●			
	0.50	●	●	●	●	●	●	●	●	●	●
	0.55							●			
	0.60					●	●	●			●

Table 2.5 Continued. Response variables of the GMPEs in this study

		NGA models					Previous models				
Parameter	Period [sec]	AS08	BA08	CB08	CY08	I08	AS97	BJF97	C97	SCE97	I91
Sa	0.65							●			
	0.70					●		●			●
	0.75	●	●	●	●		●	●	●	●	
	0.80					●		●			●
	0.85						●	●			
	0.90					●		●			●
	0.95							●			
	1.00	●	●	●	●	●	●	●	●	●	●
	1.10							●			
	1.20							●			
	1.30							●			
	1.40							●			
	1.50	●	●	●	●	●	●	●	●	●	●
	1.60							●			
	1.70							●			
	1.80							●			
	1.90							●			
	2.00	●	●	●	●	●	●	●	●	●	●
	3.00	●	●	●	●	●	●		●	●	●
	4.00	●	●	●	●	●	●		●	●	●
	5.00	●	●	●	●	●	●				●
	6.00					●					
	7.00					●					
	7.50	●	●	●	●						
	8.00					●					
	9.00					●					
	10.00	●	●	●	●	●					

NOTE:
* SCE97 provides coefficients at $T = 0.07$ sec for rock sites and $T = 0.075$ sec for deep soil sites.

seconds. Although the new GMPEs can predict *Sa* at long periods up to 10 seconds, the database of ground motions at long periods is small (Abrahamson and Silva, 2008), and the computed values of *Sa* for long periods are more sensitive to noise (Boore and Atkinson, 2007). Accordingly, in this paper, we focus our analysis on spectral periods of 2 seconds and smaller.

The observed ground motions for records in the NGA database were obtained directly from the flatfile. To calculate the observed ground motions for the Parkfield and San Simeon earthquakes, which are not present in the flatfile, we first obtained the acceleration time histories and response spectra from earthquake ground motion databases (Consortium of Organizations for Strong Motion Observation Systems, 2004; National Strong Motion Program, 2004; Center for Engineering Strong Motion Data, 2004). To ensure that the filtering process of the acceleration record does not affect the values of the response spectra, we only considered spectral accelerations for periods less than

$$T_{high} = \frac{1}{1.25 f_c}, \tag{2.25}$$

where f_c is the high-pass corner frequency of the instrument (used in the filtering of the initial ground motion record to obtain the processed accelerograms). The buffer of 1.25 is similar to the standard employed in the processing of the NGA data (Pacific Earthquake Engineering Research Center, 2008a) and in some previous GMPEs (Abrahamson and Silva, 1997). However, since we have limited our analysis to periods of 2 seconds or less, the requirement of Equation 2.25 actually does not eliminate any observations from the stations in our set.

An important distinction between the new and old GMPEs is how the two horizontal, orthogonal components of ground motion are combined to obtain a single value for a location. Typically, seismic stations record three mutually orthogonal components of ground motion: two horizontal, orthogonal components (x and y) and one vertical component (z). Horizontal acceleration is often of greater engineering significance than vertical acceleration because horizontal accelerations tend to be larger

than vertical accelerations, and structures are usually less equipped to handle lateral loads than gravity loads. As a result, most recent GMPEs focus on horizontal acceleration instead of vertical acceleration. Because there are two orthogonal components of horizontal acceleration, the question arises as to how these two horizontal components are combined. Douglas (2003) and Beyer and Bommer (2006) provide a summary of the different methods of combining the horizontal components into a single value. The methods include computing the arithmetic mean, geometric mean, both components separately, larger component, random component, resultant of the two components, and the component obtained by vectorial addition. The geometric mean is the most commonly used method of combining the two horizontal components. The models in the previous generation of GMPEs in this study combine the two horizontal components by utilizing the geometric mean of the as-recorded components, or GM_{xy} (Abrahamson and Shedlock, 1997). For a single component, as illustrated in Figure 1.1, the observed peak ground motion parameter Y_{max} for a ground motion record is obtained by the absolute maximum value of the ground motion parameter over the time interval of the record, or

$$Y_{\max} = \max | Y(t) |, \tag{2.26}$$

where Y is PGA, PGV, Sa, etc. When the as-recorded x and y components are combined by the simple geometric mean, the maximum combined component Y_{GMxy} is given by

$$Y_{GMxy} = \sqrt{\max | Y_x(t) | \cdot \max | Y_y(t) |} \tag{2.27}$$

(Douglas, 2003).

One of the disadvantages of combining the as-recorded x and y components in this manner is that the resulting value depends on the orientation of the orthogonal sensors as installed the field. To overcome this issue, Boore *et al*. (2006) introduced *GMRotI50*, a

new method of combining the two horizontal components, which is the geometric mean independent of the orientation of the instruments used to record the horizontal motion The NGA relations use *GMRotI50* for the calculation of the response variables (Chiou *et al.*, 2008). The orientation-independent geometric mean is calculated by an algorithm that involves rotating the as-recorded horizontal orthogonal motions through the set of angles from 0 to 90°, computing the geometric mean of the components for each of these rotations, and then selecting the 50th percentile (i.e., the median) of this set of geometric means. Boore *et al.* (2006) describe this algorithm in detail. In the abbreviation "GMRotI50," "GM" refers to "geometric mean," "Rot" means that the ground motions are rotated over all non-redundant angles (0 to 90°), "I" indicates that the rotation is independent of the ground motion period T, and "50" refers to the fact that the 50th percentile (median) is selected from the set of geometric means. Theoretically, the fundamental advantage of the new measure is that sensor orientation is removed as a contributor to uncertainty. However, the practical significance of this reduction in uncertainty has yet to be proven; Beyer and Bommer (2006) suggest that the reduction in uncertainty is negligible for most GMPEs, except possibly at longer periods of ground motion. Usually, the numerical values of GM_{xy} and *GMRotI50* are similar (Boore and Atkinson, 2008); however, comparisons of *GMRotI50* (the "new" geometric mean) with GM_{xy} (the "old" geometric mean) indicate that *GMRotI50* is systematically larger than GM_{xy}, but by less than 3% (Boore *et al.*, 2006).

In this study, the main implication of the difference between GM_{xy} and *GMRotI50* is that GM_{xy} is the response variable with which we must compare the model predictions from the old GMPEs, and that *GMRotI50* is the response variable with which we must

compare the model predictions from the new GMPEs. The calculation of *GMRotI50* is more intensive than the simple calculation required for GM_{xy} (Equation 2.27). We utilized a FORTRAN procedure provided by Boore (2008) to compute *GMRotI50* from the recorded acceleration time histories for the Parkfield and San Simeon earthquakes. The NGA flatfile contains the values of *GMRotI50* for each ground motion record, so we did not have to perform additional computations for the records in the flatfile. As explained in section 2.5, the models in the previous generation are only implemented in the blind comparison test, so we did not need to compute GM_{xy} (the old geometric mean) for values in the NGA flatfile. For the records involved in the blind comparison test, which are not present in the flatfile, we computed GM_{xy} and *GMRotI50* from the acceleration time histories obtained from the seismic databases. The corresponding ground motion parameters for the 93 records from the Parkfield and San Simeon earthquakes, calculated using both the new and old geometric mean, are presented in Appendix B.

2.4 Ranges of Applicability of the Models

Each model is applicable only within specific ranges of magnitude, distance, and other variables. Table 2.6 presents the ranges of applicability of the five NGA models, which have specific requirements for magnitude, distance, and V_{S30}. Campbell and Bozorgnia (2008) specify some additional quantitative requirements regarding the depth parameter $Z_{2.5}$, depth to top of rupture Z_{TOR}, and fault dip δ. At the bottom of Table 2.6 is a summary of the requirements that an earthquake ground motion record must meet in

Table 2.6. Ranges of applicability of the NGA models

Model	Magnitude	Distance [km]	V_{S30} [m/sec]	Additional requirements
AS08	$5.0 \leq M \leq 8.5$	$R_{RUP} \leq 200$	No specification	–
BA08	$5.0 \leq M \leq 8.0$	$R_{JB} \leq 200$	$180 \leq V_{S30} \leq 1300$	–
CB08	$4.0 \leq M \leq 7.5$ (NM*), 8.0 (RV), 8.5 (SS)	$R_{RUP} \leq 200$	$150 \leq V_{S30} \leq 1500$	$Z_{2.5} \leq 10$ km $Z_{TOR} \leq 15$ km $15° \leq \delta \leq 90°$
CY08	$4.0 \leq M \leq 8.0$ (NM and RV), 8.5 (SS)	$R_{RUP} \leq 200$	$150 \leq V_{S30} \leq 1500$	–
I08	$4.5 \leq M \leq 8.0$	$R_{RUP} \leq 200$	$V_{S30} \geq 450$	–
ALL	*Normal faulting:* $5.0 \leq M \leq 7.5$ *Reverse and strike-slip faulting:* $5.0 \leq M \leq 8.0$	$R_{RUP} \leq 200$ and $R_{JB} \leq 200$	*Excluding I08:* $180 \leq V_{S30} \leq 1300$ *Including I08:* $450 \leq V_{S30} \leq 1300$	$Z_{2.5} \leq 10$ km $Z_{TOR} \leq 15$ km $15° \leq \delta \leq 90°$

NOTE:
* For CB08 and CY08, different maximum magnitudes are specified for normal (NM), reverse (RV), and strike-slip (SS) faulting mechanisms.

order to be applicable to all five NGA models; we followed these requirements when developing our testing subsets. The NGA database contains many records that do not meet the criteria specified in Table 2.6. As a result, we needed to generate testing subsets of the NGA database containing records that met the requirements of all the models.

Table 2.7 presents the ranges of applicability of the five previous models. In addition to the smaller range of spectral periods with defined coefficients, the most notable difference between the previous models and the new models is the smaller range of distances to which the previous models may be applied. Although some of the previous models do not specify maximum distances explicitly, 100 km is generally

viewed as a reasonable limit. Campbell and Bozorgnia (2003) suggest that even the models with specific distance limits less than 100 km (such as BJF97 and C97) may be reasonably extrapolated to 100 km.

Table 2.7. Ranges of applicability of the previous models

Model	Magnitude		Distance [km]		Spectral Period [sec]	
	Min	Max	Type	Max	Min	Max
AS97	–[1]	8.5	R_{RUP}	–	0.01	5.0
BJF97	5.5	7.5	R_{JB}	80	0.10	2.0
C97	5.0	–	R_{SEIS}	60	0.05	4.0
SCE97	4.0	–	R_{RUP}	100	0.07	4.0
I91	–	–	R_{RUP}, R_{HYP}[2]	–	0.03	5.0

NOTES:
1. An en dash (–) means that the model does not specify a minimum or maximum.
2. I91 specifies R_{HYP} for $M \leq 6$ and R_{RUP} for $M > 6$.

2.5 Testing Subsets

In order to perform a quantitative comparison of the predictive abilities of the NGA models, the first logical step is to test the models on the NGA database, upon which the new models were developed. Figure 2.13 is a flowchart illustrating the testing subsets and the number of ground motion records in each of the subsets. To explore the implications of the developers' modeling decisions, we assess the prediction accuracy of the models in various situations, including (1) mainshocks versus aftershocks, (2) soil sites versus rock sites, and (3) at small, medium, and large distances. One of the most significant decisions for the NGA model teams was whether to include aftershocks in

their regression subsets. To assess the effect of this decision, we divide the records in the NGA database into mainshocks and aftershocks, and compare the prediction accuracy of the models in each category. Boore and Atkinson (2008) and Campbell and Bozorgnia (2008) did not include aftershocks in their regression databases. Thus, the testing of the BA08 and CB08 on the aftershocks subset serves as a blind test for these models. In order to test the I08 model, each subset was further subdivided into soil sites ($180 \leq V_{S30} < 450$ m/sec) and rock sites ($450 \leq V_{S30} \leq 1300$ m/sec, where I08 is applicable). The boundary between soil and rock in our subdivision corresponds to the I08 lower limit of $V_{S30} = 450$ m/s. Because of the differing assumptions made by the developers, the final testing subsets do not perfectly match the regression datasets of any of the developers, but they provide a useful basis for comparison.

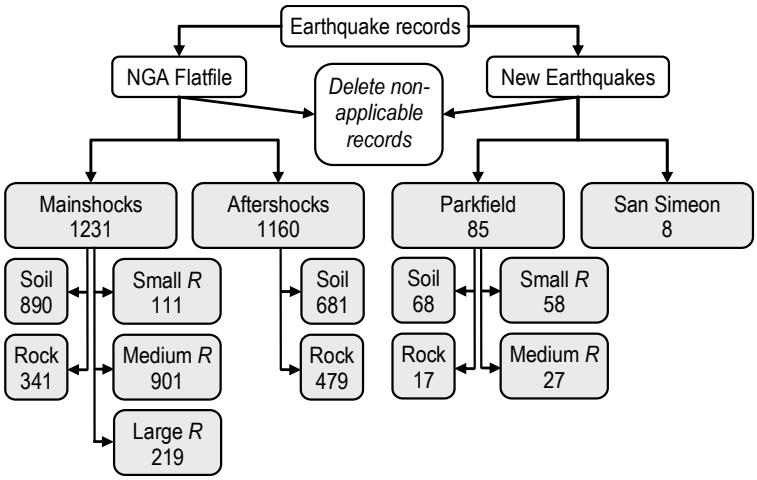

Figure 2.13. Flowchart of the subset delineation process, along with the sample size of each final subset. Datasets with sufficient data in each category are subdivided into (a) soil sites ($180 \leq V_{S30} < 450$ m/s) and rock sites ($450 \leq V_{S30} \leq 1300$ m/s), and (b) small distance ($R_{RUP} \leq 10$ km), medium distance ($10 < R_{RUP} \leq 100$ km), and large distance ($100 < R_{RUP} \leq 200$ km).

In addition to comparing the prediction accuracy for mainshocks versus aftershocks, and soil sites versus rock sites, we also compare the effect of distance on prediction accuracy. We utilize subdivisions of small ($R_{RUP} \leq 10$ km), medium ($10 < R_{RUP} \leq 100$ km), and large distances ($100 < R_{RUP} \leq 200$ km) for subsets with sufficient data in each category. Ground motion often displays little attenuation at distances less than 10 km (hence the first boundary), and the 100 km boundary separates the ranges of applicability of the previous and new models. We chose not to subdivide the aftershocks dataset by distance because there was an uneven distance distribution; only 10 of the 1160 aftershocks records could be classified as small distance.

The blind comparison using the new and old models was performed using the database of new earthquakes, distinct from the NGA flatfile. In order to test both the new and old models on the Parkfield and San Simeon earthquakes, we restricted records to distances no greater than 100 km from the earthquake source. Most of the available records for the Parkfield earthquake are near-source, but most of the records for the San Simeon earthquake are at distances greater than 100 km. Because the database for the San Simeon earthquake was reduced to only eight records, we did not subdivide this dataset. Furthermore, we did not compare the previous models with the new models using the NGA testing subsets. Because the NGA models were exposed to larger portions of these testing subsets during model development, the NGA models would have an unfair advantage over the previous models. The previous and current models are tested together in the blind datasets, in which none of the ground motion records influenced the regressions of any of the ten models.

In developing the final testing subsets, we deleted non-applicable records from the NGA flatfile if they did not meet the criteria in Table 2.6 (since only the new models are tested), and we deleted records from the database of new earthquakes if they did not meet the combined criteria in Tables 2.6 and 2.7 (since both the new and old models are tested). We also deleted records not representative of free-field conditions, records without finite fault models (which did not have values for R_{RUP}, R_{JB}, W, or Z_{TOR}), records missing other important information (such as V_{S30} or Sa), and records with identified problems. Boore and Atkinson (2007) provide a useful record-by-record summary of reasons for excluding records from the NGA flatfile. Lists of the aftershocks and mainshocks we analyzed, as well as the corresponding numbers of records in each subdivision, are presented in Tables 2.8 and 2.9, respectively.

Table 2.8. List of aftershocks in NGA testing subsets

Earthquake ID No. in NGA flatfile	Name	Year	Magnitude	Number of records		
				Total no. of records	Subdivision	
					Soil	Rock
43	Friuli, Italy-02	1976	5.91	4	3	1
69	Irpinia, Italy-02	1980	6.20	10	2	8
138	Duzce, Turkey	1999	7.14	21	14	7
171	Chi-Chi, Taiwan-02	1999	5.90	290	163	127
173	Chi-Chi, Taiwan-04	1999	6.20	237	146	91
174	Chi-Chi, Taiwan-05	1999	6.20	314	184	130
175	Chi-Chi, Taiwan-06	1999	6.30	284	169	115

Table 2.9. List of mainshocks in NGA testing subsets

EQ ID No. in NGA flatfile	Name	Year	Magnitude	Number of records					
				Total no. of records	Subdivision 1		Subdivision 2		
					Soil	Rock	Small *R*	Med. *R*	Large *R*
12	Kern County	1952	7.36	1	1	0	0	0	1
25	Parkfield	1966	6.19	5	3	2	1	4	0
28	Borrego Mtn	1968	6.63	1	1	0	0	0	1
30	San Fernando	1971	6.61	30	19	11	0	21	9
31	Managua, Nicaragua-01	1972	6.24	1	1	0	1	0	0
41	Gazli, USSR	1976	6.80	1	0	1	1	0	0
46	Tabas, Iran	1978	7.35	7	5	2	1	3	3
48	Coyote Lake	1979	5.74	6	5	1	4	2	0
50	Imperial Valley-06	1979	6.53	32	31	1	15	17	0
56	Mammoth Lakes-01	1980	6.06	2	2	0	2	0	0
57	Mammoth Lakes-02	1980	5.69	2	2	0	2	0	0
64	Victoria, Mexico	1980	6.33	4	3	1	1	3	0
68	Irpinia, Italy-01	1980	6.90	12	2	10	2	10	0
72	Corinth, Greece	1981	6.60	1	1	0	0	1	0
73	Westmorland	1981	5.90	6	6	0	2	4	0
76	Coalinga-01	1983	6.36	44	43	1	0	44	0
83	Ierissos, Greece	1983	6.70	1	1	0	0	1	0
87	Borah Peak, ID-01	1983	6.88	6	3	3	0	4	2
90	Morgan Hill	1984	6.19	22	17	5	3	19	0
91	Lazio-Abruzzo, Italy	1984	5.80	5	4	1	0	5	0
96	Drama, Greece	1985	5.20	1	0	1	0	1	0
97	Nahanni, Canada	1985	6.76	3	0	3	3	0	0
101	N. Palm Springs	1986	6.06	30	24	6	4	26	0
102	Chalfant Valley-01	1986	5.77	5	5	0	1	4	0
103	Chalfant Valley-02	1986	6.19	10	10	0	1	9	0
108	San Salvador	1986	5.80	2	1	1	2	0	0
111	New Zealand-02	1987	6.60	2	2	0	0	2	0
113	Whittier Narrows-01	1987	5.99	109	96	13	0	108	1
115	Superstition Hills-01	1987	6.22	1	1	0	0	1	0
116	Superstition Hills-02	1987	6.54	11	11	0	2	9	0
118	Loma Prieta	1989	6.93	67	42	25	5	61	1
119	Griva, Greece	1990	6.10	2	2	0	0	2	0
121	Erzican, Turkey	1992	6.69	1	1	0	1	0	0
125	Landers	1992	7.28	68	65	3	1	20	47
127	Northridge-01	1994	6.69	154	122	32	12	134	8
128	Double Springs	1994	5.90	1	1	0	0	1	0
129	Kobe, Japan	1995	6.90	12	8	4	4	6	2
130	Kozani, Greece-01	1995	6.40	7	4	3	0	7	0
134	Dinar, Turkey	1995	6.40	4	4	0	1	3	0
135	Gulf of Aqaba	1995	7.20	1	1	0	0	1	0
136	Kocaeli, Turkey	1999	7.51	22	15	7	2	15	5
137	Chi-Chi, Taiwan	1999	7.62	410	229	181	36	299	75
140	Sitka, Alaska	1972	7.68	2	0	2	0	1	1
141	Caldiran, Turkey	1976	7.21	1	1	0	0	1	0
144	Manjil, Iran	1990	7.37	7	6	1	0	5	2
145	Sierra Madre	1991	5.61	8	6	2	0	8	0
152	Little Skull Mtn, NV	1992	5.65	8	5	3	0	7	1
158	Hector Mine	1999	7.13	79	67	12	0	29	50
168	Nenana Mountain, Alaska	2002	6.70	5	4	1	0	0	5
169	Denali, Alaska	2002	7.90	9	7	2	1	3	5

Chapter 3:
METHODS

3.1 Numerical Implementation of the Models

For each earthquake ground motion record in each of the testing subsets, we computed median estimates of *PGA* and *Sa* at periods of 0.1, 0.2, 0.3, 0.5, 1.0, and 2.0 sec. When using a GMPE, a median prediction will give a model's closest estimate of the observed ground motion at a site. Thus, a comparison of different models' median ground motion estimates with the observed values allows us to quantify the various models' goodness of fit. To perform our computations, we utilized the open-source statistical language and environment *R* (R Development Core Team, 2009). The *R* code we have developed for the numerical implementation of the five NGA models is presented in Appendix C, along with basic instructions on how to use *R* to obtain ground motion predictions with our code.

On the PEER web site, the model development teams provide varying amounts of guidance for users attempting to implement their models (Pacific Earthquake Engineering Research Center, 2008b). In addition to the papers in *Earthquake Spectra* (Abrahamson and Silva, 2008; Boore and Atkinson, 2008; Campbell and Bozorgnia, 2008; Chiou and Youngs, 2008a; Idriss, 2008), four of the teams (BA08, CB08, CY08, and I08) have

posted their detailed final project reports on the project web site (Boore and Atkinson, 2007; Campbell and Bozorgnia, 2007; Chiou and Youngs, 2008b; Idriss, 2007). These reports provided additional clarification and example calculations so users can verify that they have properly implemented the models. On the NGA project web site, PEER recently released a single Excel spreadsheet that implements all five NGA models. Furthermore, three of the teams (CB08, CY08, and I08) have released other Microsoft Excel spreadsheets to aid researchers and practicing engineers in executing the models. In addition, three of the teams (AS08, BA08, and CB08) have posted code on the PEER web site to allow individuals to implement the models in FORTRAN (Pacific Earthquake Engineering Research Center, 2008b).

Some of the functional forms in the NGA models are exceedingly complex, and the definitions and descriptions in the *Earthquake Spectra* papers are oftentimes unclear. The implementation of the AS08 model, the most complicated of the five NGA models, was particularly difficult. The additional reports, spreadsheets, and code presented on the NGA web site clarified some of the confusion, but also raised new issues for some of the models regarding the computations in the posted code (Abrahamson, 2009; Chiou, 2009). Because of the complexity of the NGA relationships, a detailed verification process was necessary to validate our numerical implementation in *R*. In addition to using the aforementioned resources available on the NGA project web site, we utilized comprehensive test data provided by Campbell (2009). Campbell's test data for each of the NGA relationships contain ground motion predictions for an exhaustive range of input parameters. With the exception of roundoff errors, our ground motion predictions were identical to the predictions offered by this independent set of resources.

3.2 Goodness-of-Fit Measures

Goodness-of-fit statistics are utilized to quantify the comparison of the model predictions with the observed ground motion records. Given a set of n observed ground motion records, we generate ground motion predictions using a model. As explained in section 2.3, we have chosen to analyze the models' predictive capabilities for m = 7 ground motion parameters: *PGA* (which may be represented by *Sa*(0.01 s)), *Sa*(0.1 s), *Sa*(0.2 s), *Sa*(0.3 s), *Sa*(0.5 s), *Sa*(1.0 s), and *Sa*(2.0 s). We can visualize the set of observed ground motions as an $n \times m$ matrix with n ground motion records and m ground motion parameters for each record, as displayed in Figure 3.1. Similarly, we can visualize the set of predictions from a model as another $n \times m$ matrix. The purpose of goodness-of-fit statistics is to quantitatively compare the observed and predicted values.

We can compute goodness-of-fit statistics in two ways: (1) for a single ground motion parameter, and (2) across the group of seven ground motion parameters. With the ultimate goal of performing a composite, comprehensive analysis, we wish to compare

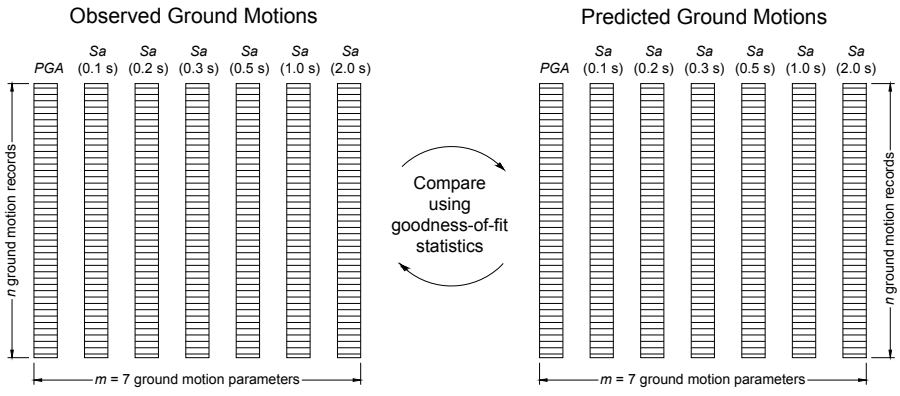

Figure 3.1. Schematic illustrating the role of goodness-of-fit statistics in comparing the observed ground motion parameters to the predicted values using a model.

the models' performance over multiple periods of interest, not just at a single period; thus, the second method (the "total" method) is preferable. To do this, we convert each $n \times m$ matrix into a single column vector of length mn (= $7n$), where entries 1 to n correspond to *PGA*, entries $n+1$ to $2n$ correspond to *Sa*(0.1 s), entries $2n+1$ to $3n$ correspond to *Sa*(0.2 s), and so on. This calculation scheme weights the contributions from each of the seven ground motion parameters equally. To analyze the performance at single periods, the comparison can be performed on the corresponding individual columns of the original $n \times m$ matrix; that is, only comparing the n observed values for *PGA* with the n predicted values of *PGA*. We focus our comparisons and rankings on the total analyses (when the set of seven ground motion parameters is combined), but in Appendix D we also present the results for the seven individual ground motion parameters in order to establish a record of model performance for the individual ground motion parameters. A more detailed comparison of single-period versus multiple-period analyses is presented in Appendix D.

The primary statistic we use as our basis of comparison is the Nash-Sutcliffe model efficiency coefficient (E), a commonly used statistic in hydrology (Nash and Sutcliffe, 1970). The coefficient of efficiency is calculated by the equation

$$E = \left[1 - \frac{\sum_{i=1}^{N} \left(Y_i - \hat{Y}_i \right)^2}{\sum_{i=1}^{N} \left(Y_i - \bar{Y} \right)^2} \right] \cdot 100\% , \qquad (3.1)$$

where N is the number of ground motion records in the vector ($N = n$ for a single-period analysis, and $N = mn = 7n$ for a multiple-period analysis), the observed values (*PGA*, *Sa*, etc.) are denoted by Y_i, predicted values are denoted by $\hat{Y}_i$, and the mean of the observed

values is denoted by $\overline{Y}$. The value of E may vary between $-\infty$ and 100%, with higher values indicating better agreement. When E is less than 0, the arithmetic mean of the observed values has greater prediction accuracy than the model itself. The coefficient of efficiency has some important advantages over other commonly used goodness of fit statistics, such as Pearson's correlation coefficient (r), percent root mean square error (*PRMSE*), and percent bias (*PB*).

Another common goodness-of-fit statistic presented in the literature is Pearson's correlation coefficient (r), or its square, the coefficient of determination (r^2). The correlation coefficient is calculated by the equation

$$r = \left[\frac{N\sum_{i=1}^{N}\left(Y_i \hat{Y}_i\right) - \sum_{i=1}^{N} Y_i \sum_{i=1}^{N} \hat{Y}_i}{\sqrt{N\sum_{i=1}^{N} Y_i^2 - \left(\sum_{i=1}^{N} Y_i\right)^2}\sqrt{N\sum_{i=1}^{N} \hat{Y}_i^2 - \left(\sum_{i=1}^{N} \hat{Y}_i\right)^2}} \right] \cdot 100\,\% \,. \tag{3.2}$$

If a model is perfect, a plot of observed versus predicted values will follow a line with a slope of 1. Figure 3.2 displays the observed and predicted *PGA* using the CB08 relationship on the aftershocks subset. Since the predicted values are generally larger than the observed values, the model is clearly over-predicting the actual ground motion. The correlation coefficient, which measures the dispersion about the least-squares regression line (LSRL), will not detect this problem. However, the coefficient of efficiency, which measures the dispersion about the 1-to-1 line, will penalize the model for consistently over-predicting. Compared to r, the Nash-Sutcliffe model efficiency coefficient is more sensitive to additive and multiplicative differences between the model predictions and observations, and thus is a better indicator of goodness of fit (Legates and McCabe, 1999).

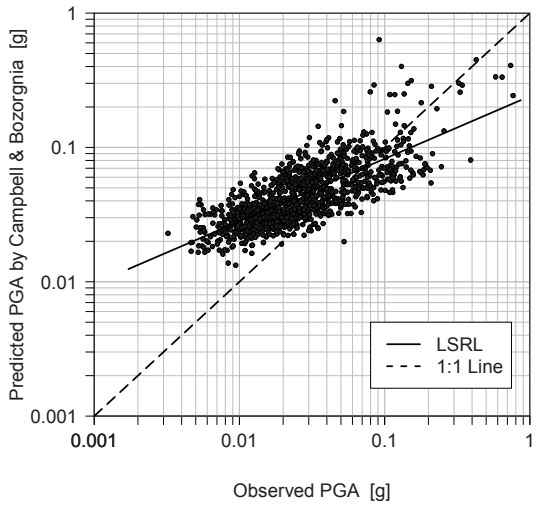

Figure 3.2. Advantages of the efficiency coefficient over the correlation coefficient. The observed versus predicted *PGA* using the CB08 relationship is plotted for the aftershocks dataset, along with the least-squares regression line (LSRL) and the ideal 1-to-1 line. The model is systematically over-predicting the actual ground motion, a phenomenon that the coefficient of efficiency—but not the coefficient of correlation—would capture.

The percent root mean square error (*PRMSE*) is a good measure of the total error of a model, but not the relationship about the 1-to-1 line of observed versus predicted values. The percent root mean square error is equal to the root mean square error (*RMSE*) normalized by the mean of the observed values:

$$PRMSE = \frac{RMSE}{\overline{Y}} = \left[\frac{\sqrt{\frac{1}{N}\sum_{i=1}^{N}\left(Y_i - \hat{Y}_i\right)^2}}{\frac{1}{N}\sum_{i=1}^{N} Y_i} \right] \cdot 100\% . \qquad (3.3)$$

The square in the numerator converts the mean square error into the original units of the ground motion parameter (*g*'s), and normalizing by the mean of the observed values converts the statistic to a percent, like the other goodness-of-fit measures in this study.

The final goodness-of-fit statistic we calculated is percent bias (*PB*), which is useful for identifying whether a model is systematically overpredicting or

underpredicting the true ground motion, but is not as useful for quantifying the scatter between the observed and predicted values. The percent bias is derived by normalizing the bias by the mean of the observed values:

$$PB = \left[\frac{\overline{\hat{Y}} - \overline{Y}}{\overline{Y}} \right] \cdot 100\%, \tag{3.4}$$

where $\overline{\hat{Y}}$ is the mean of the predicted values, and $\overline{Y}$ is the mean of the observed values, as previously defined. When the means are written in sigma notation, we have

$$PB = \left[\frac{\frac{1}{N}\sum_{i=1}^{N} \hat{Y}_i - \frac{1}{N}\sum_{i=1}^{N} Y_i}{\frac{1}{N}\sum_{i=1}^{N} Y_i} \right] \cdot 100\%. \tag{3.5}$$

Simplifying by factoring and canceling out the $1/N$ term, the computational formula for *PB* may be written as:

$$PB = \left[\frac{\sum_{i=1}^{N} \hat{Y}_i - \sum_{i=1}^{N} Y_i}{\sum_{i=1}^{N} Y_i} \right] \cdot 100\%. \tag{3.6}$$

We computed all goodness-of-fit statistics using the observed and predicted values in real space (as opposed to logarithmic space, in which the models were developed), since seismic hazard assessment is concerned with the real values of the response variables (not the logarithms of the values).

Chapter 4:
RESULTS

4.1 Example Response Spectra

Qualitative visual comparisons of several predicted and observed response spectra indicate that there is general agreement between the NGA models. The GMPEs often provide reasonable predictions of the ground motions, but they often overpredict or underpredict ground motions in unison. Four sample response spectra from the widely recorded *M* 6.7 Northridge earthquake of 1994 are displayed in Figure 4.1. The corresponding site information, rupture distance, and observed *PGA* is presented in Table 4.1; the data is from the NGA flatfile (Pacific Earthquake Engineering Research Center, 2008a). The sites compose a variety of distances and site categories; site A is the only location of the four where I08 is applicable, since $V_{S30} > 450$ m/s. The models give good predictions over all spectral periods for site A; underpredict the near-source ground motion for site B, especially at short periods (although BA08 offers a good prediction at long periods); and offer slight overpredictions for site C at short periods and for site D at long periods. Site B, one of the closest stations to the earthquake source, experienced the greatest ground motion of any station that recorded the Northridge earthquake. The models all have difficulty predicting this highly variable near-source ground motion. The

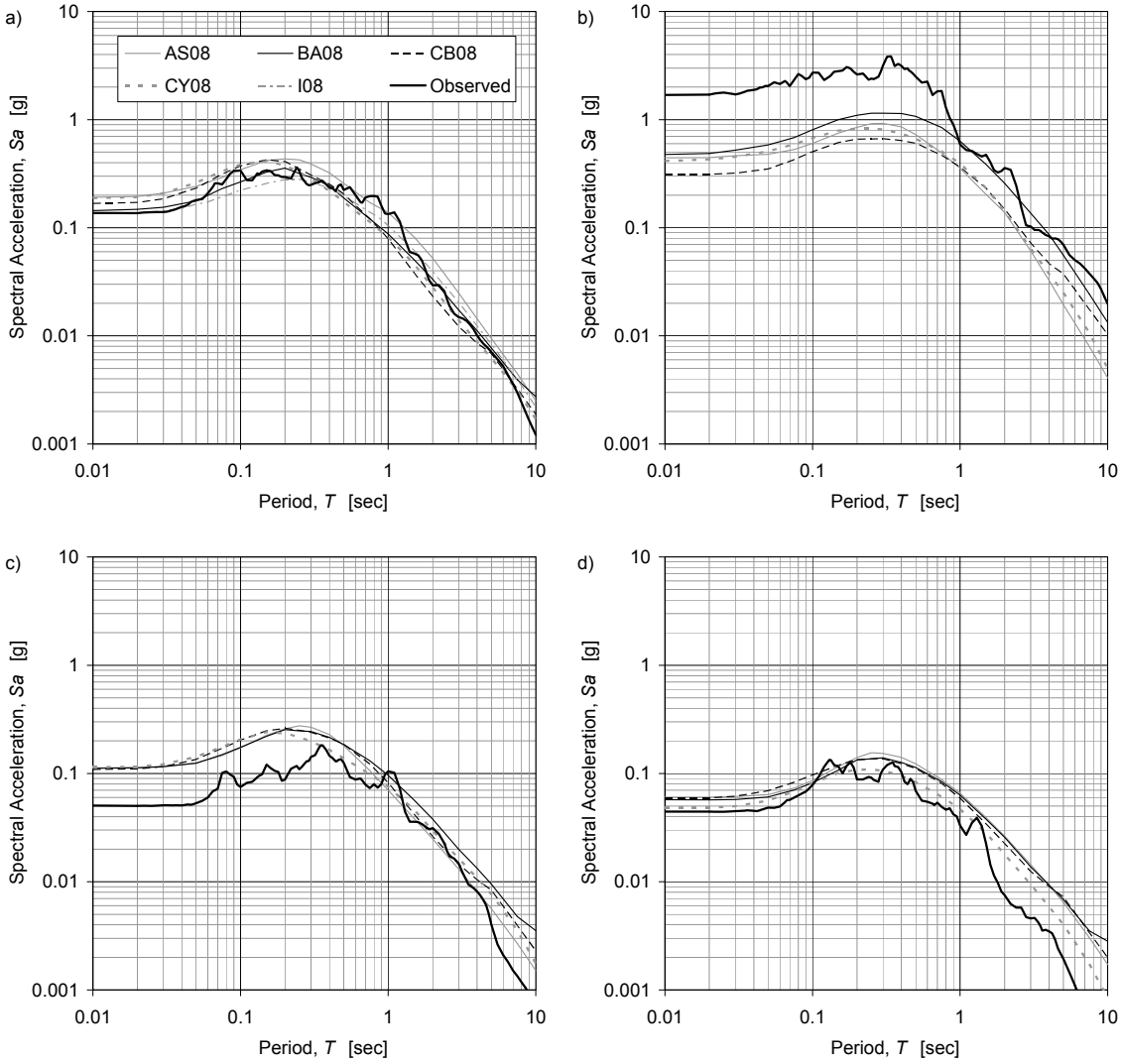

Figure 4.1. Example response spectra from the Northridge earthquake of 1994, for the sites in Table 4.1.

Table 4.1. Characteristics of example response spectra from the Northridge earthquake

	Record No. in NGA Flatfile	Station Name	R_{RUP} [km]	V_{S30} [m/s]	$PGA_{observed}$ [g]
A	1011	L.A. - Wonderland Avenue	20.3	1222.5	0.134
B	1087	Tarzana - Cedar Hill Nursery A	15.6	257.2	1.662
C	945	Anaverde Valley - City Ranch	38.0	446.0	0.050
D	1097	Wrightwood - Nielson Ranch	81.7	345.2	0.044

four plots in Figure 4.1 illustrate common patterns in the models' predictions—that the various models' estimates are generally close to one-another, although there may be systematic overprediction or underprediction at some periods. These qualitative comparisons are instructive for the purposes of identifying general patterns in the model predictions of specific ground motion records, but quantitative goodness-of-fit analyses are necessary in order to perform a more rigorous comparison.

As previously explained, because of the superiority of E over the other goodness-of-fit statistics, we utilize E as our primary measure of comparison. All the tables of results report the coefficient of efficiency in the body of this thesis. However, we present comprehensive tables and figures of the other goodness-of-fit statistics in Appendix D. When the models are compared according to other goodness-of-fit statistics, the model rankings are similar to those when the comparison is based upon E.

4.2 Mainshocks

The mainshocks dataset, with 1231 ground motion records from the NGA flatfile, is the most comprehensive dataset in this study. Figure 4.2 displays each model's coefficient of efficiency calculated at individual periods across the entire response spectrum, from 0.01 to 10 seconds. Note that most of the models suffer a decrease in prediction accuracy for the longer periods, probably due to the smaller available regression datasets for long periods. Between periods of 0.1 and 0.3 seconds, some of the models (especially CY08) also have decreased coefficients of efficiency. For the observed response spectra, the maximum spectral acceleration often occurs in the range of 0.1 to 0.3 seconds. The

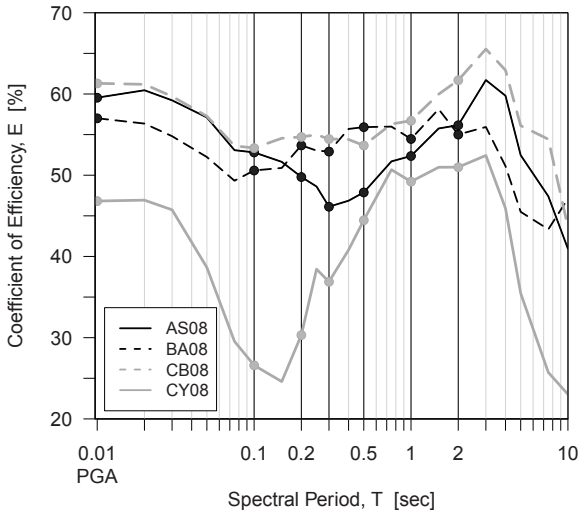

Figure 4.2. Coefficient of efficiency calculated at each period across the response spectrum for four NGA models using the mainshocks dataset, with points marking the set of periods upon which we focus our comparisons: *PGA* (*Sa* at 0.01 sec), and *Sa* at 0.1, 0.2, 0.3, 0.5, 1.0, and 2.0 sec.

values of spectral acceleration near the peak of the spectrum often show greater variability than smaller values, thus explaining the decrease in prediction accuracy for some of the models.

The points on the figure mark the set of periods upon which we focus our comparisons, with *PGA* represented by a spectral period of 0.01 seconds. One of the benefits of calculating *E* as a summation over the seven periods of interest is that a model's prediction accuracy across the response spectrum can be represented by a single number. In some cases, the value of *E* calculated for a set of observations and predictions will be greater than each value of *E* when the set is subdivided into groups. The "whole is greater than the sum of the parts" phenomenon, which occurs occasionally in our analyses, can be explained by the relative influence of extreme observations, and the fact that *E* compares alternative models to the mean of the observed values. Despite this phenomenon, the relative performances of the models in subdivided datasets may still be

compared reasonably using E. A detailed description of this phenomenon, as well as a brief numerical example, is presented in Appendix D.

In Table 4.2, we present the NGA models' prediction accuracies for the entire mainshocks dataset, as well as for the subdivisions by site classification and distance. In the total sense, the values of E are between 40 and 60 percent. All models perform more poorly at small and large distances than at intermediate distances. In two cases (CY08 for small distances and AS08 for large distances), we find E to be less than zero, indicating that the mean of the observed motions is a better predictor than the GMPEs in these cases. In their model, Abrahamson and Silva (2008) include a "large distance" term that is constrained by broadband recordings from three small California earthquakes not present in the NGA flatfile. Abrahamson and Silva (2008) justify their large distance term, which slightly decreases the ground motion estimate when $R_{RUP} \geq 100$ km, because there is a data deficiency in the NGA flatfile for large distances and small magnitudes. However, the data for their large distance term is not based upon data in the NGA flatfile, and this may partially explain why their model predictions for the large distance dataset

Table 4.2. Coefficients of efficiency for mainshocks in NGA database

		NGA models				
		AS08	BA08	CB08	CY08	I08
Subdivision 1	Soil	57.7	59.5	60.4	53.7	–
	Rock	49.7	55.6	57.2	23.5	43.4
Subdivision 2	Small R	22.6	34.8	35.4	−11.8	–
	Medium R	46.4	46.9	48.9	38.4	–
	Large R	−6.5	15.3	23.8	3.5	–
Total E		54.8	58.1	59.3	42.7	–
Model rankings based on total E		3	2	1	4	–

do not match the data in the NGA flatfile as well as the predictions by the other models. Quite interestingly, the two models with the highest overall prediction accuracy, BA08 and CB08, are two of the simpler NGA models. The more complicated models, AS08 and CY08, do not perform as well. When included in the testing subset for rock sites, the I08 model ranks fourth of five.

Table 4.3. Coefficients of efficiency for aftershocks in NGA database

		NGA models				
		AS08	BA08	CB08	CY08	I08
Subdivisions	Soil	51.2	49.8	44.6	45.8	–
	Rock	25.6	39.2	28.6	30.9	37.4
Total *E*		47.9	47.6	41.2	43.1	–
Model rankings based on total *E*		1	2	4	3	–

4.3 Aftershocks

The models' prediction accuracy for aftershocks is less than that of mainshocks, as seen in Table 4.3. The ranges of *E* are in the 40- to 50-percent range when the whole subset is analyzed. Most models suffer a considerable decrease in *E* from soil to rock, most noticeably the AS08 model. Only the AS08, CY08, and I08 model teams included aftershocks in their regression datasets. As explained in Figure 3.2, the CB08 model tends to over-predict ground motion for aftershocks, and thus has a lower coefficient of efficiency. However, the BA08 model, having not been influenced by any of the values in this subset during model development, performs surprisingly well.

4.4 Blind Comparison Tests

4.4.1 Parkfield Earthquake

The *M* 6.0 Parkfield earthquake of 2004 generated an unprecedented amount of near-source ground motion records. Of the 85 records with $R_{RUP} \leq 100$ km that we tested, 58 records (68%) are located within 10 km of the rupture plane. As noted by Shakal *et al*. (2005), the ground motions near the fault were highly variable during the Parkfield earthquake. Figure 4.3 is a plot of *PGA* versus rupture distance for the Parkfield dataset, along with the median relationships using the ten GMPEs in this study (drawn for the average value of V_{S30} across all sites the dataset, 403.2 m/sec, which corresponds

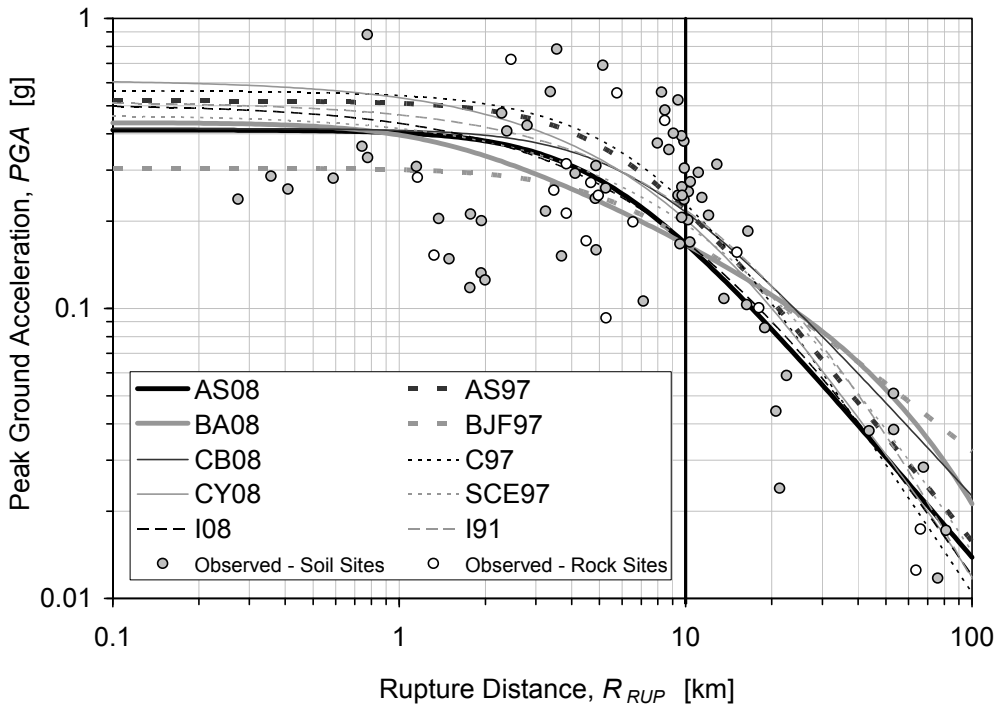

Figure 4.3. Plot of *PGA* versus R_{RUP} for the Parkfield dataset, along with the predicted ground motion using the average site characteristic among the 85 stations, V_{S30} = 403.2 m/s. Graphically, the models have similar patterns of attenuation with distance. The increase in ground motion variability at distances less than 10 km is clearly observed. Points are separated into the categories of soil sites ($180 \leq V_{S30} < 450$ m/s) and rock sites ($450 \leq V_{S30} \leq 1300$ m/s).

Table 4.4. Coefficients of efficiency for the Parkfield dataset

		NGA models					Previous models				
		AS08	BA08	CB08	CY08	I08	AS97	BJF97	C97	SCE97	I91
Subdivision 1	Soil	36.6	34.7	42.0	24.3	–	34.7	40.0	32.7	31.6	–
	Rock	43.1	44.7	41.1	30.3	40.9	8.7	44.4	19.1	15.1	26.8
Subdivision 2	Small *R*	23.0	20.7	26.7	5.2	–	11.6	25.6	11.4	9.1	–
	Medium *R*	65.0	70.5	74.9	75.9	–	75.2	75.6	73.8	74.3	–
Total *E*		38.1	36.9	42.0	25.8	–	30.4	41.1	30.1	28.4	–
Model rankings based on total *E*		3	4	1	8	–	5	2	6	7	–

approximately to dense soil or soft rock). Graphically, the models have similar patterns of attenuation with distance. The increased ground motion variability at rupture distances of less than 10 km is clearly observed. The high near-source variability in the observed ground motions is manifested in the models' relatively low prediction accuracy for this earthquake, presented in Table 4.4. When the analysis is separated into categories by distance, the coefficients of efficiency for the NGA models at small distances are similar to the small-distance values in mainshocks subset (*E* less than 30%). At medium distances, all models—new and old—have relatively high values of *E* (above 65%), with the CY08 model performing best. The models' good predictions at medium distances suggest that the lower values of *E* in the total Parkfield dataset are likely the result of the high near-source variability in the observed ground motions, rather than the inability of the models to offer reasonable predictions in blind cases. When the analysis is separated by V_{S30}, some models perform better on soil and other models perform better on rock. Figure 4.3, in which the observed ground motions are differentiated by V_{S30}, displays similar amounts of scatter for soil and rock sites, although there are fewer rock sites than soil sites.

Directivity effects, which characterize the rupture direction of the fault, are a significant contributor to the variability of near-source ground motions. When an earthquake occurs, the rupture starts at the hypocenter and proceeds along the fault in either one direction (*unilateral* rupture) or both directions (*bilateral* rupture). A site located in the direction of rupture progression has "forward directivity." Due to constructive interference of waves, these locations can potentially experience greater shaking than locations that are not within the zone(s) of forward directivity (Kramer, 1996). The rupture during the Parkfield earthquake was primarily unilateral (to the northwest), with a small component to the southeast (Shakal *et al.*, 2006). Generally, before an earthquake occurs, it is difficult to predict the rupture direction. However, Somerville *et al.* (1997) offer suggestions for modifications to GMPEs that allow for the incorporation of directivity effects by considering fault-parallel and fault-normal ground motions. One of the original objectives of the NGA project was to develop predictions for fault-parallel and fault-normal ground motions, but this was not completed (Power *et al.*, 2008). Although no current GMPEs incorporate directivity effects, they are likely to be explored in the future.

For some—but not all—of the cases, the NGA models outperform their previous counterparts. When comparing the total dataset, the CB08 relationship has the highest coefficient of efficiency, followed by the BJF97 model, and then two of the NGA models (AS08 and BA08). Interestingly, the BJF97 model performs at a level similar to that of to its contemporary (BA08), and noticeably better than the other models in the previous generation. One difference between BJF97 and the other previous models is that Boore

et al. (1997) were the first team to quantitatively incorporate site characteristics into a GMPE, perhaps giving the model greater prediction accuracy.

4.4.2 San Simeon Earthquake

As Table 4.5 illustrates, the prediction accuracy of the models is much better for the San Simeon earthquake than for the Parkfield earthquake, most likely because highly variable near-source ground motions no longer dominate the database. The coefficients of efficiency are within a narrow range for the four NGA models (hovering near 70%), with the CY08 model performing best. Unlike the Parkfield earthquake, there is a clear difference between the new and previous models for the San Simeon earthquake. The newer models have values of *E* in the 60's and 70's, and the older models have values of *E* in the 30's to 50's. All four NGA models have higher values of *E* than their previous counterparts do, with an average increase of 17.2%.

Table 4.5. Coefficients of efficiency for the San Simeon dataset

	NGA models					Previous models				
	AS08	BA08	CB08	CY08	I08	AS97	BJF97	C97	SCE97	I91
Total *E*	66.2	67.0	66.2	70.3	–	55.5	58.8	49.2	34.0	–
Model rankings based on total *E*	3 (tie)	2	3 (tie)	1	–	6	5	7	8	–

Chapter 5:
DISCUSSION

5.1 Incorporation of Aftershocks in Model Development

As we already explained, each NGA modeling team made different decisions when selecting their regression datasets from the NGA flatfile, but one of the most significant decisions was whether to include aftershocks. The aftershock records of the 1999 *M* 7.6 Chi-Chi, Taiwan, earthquake sequence comprise 83% of the aftershock records in the flatfile and 97% of the aftershock records in our aftershock dataset. (The reason why the proportion in our subset is so large is that finite fault models were only developed for seven aftershocks in the NGA flatfile, four of which were aftershocks of the widely recorded Chi-Chi earthquake. We excluded earthquakes without finite fault models from our testing subsets because these records did not have values for R_{RUP}, R_{JB}, W, or Z_{TOR}, which are necessary for implementing the NGA relationships.) The AS08, CY08, and I08 model teams included aftershocks in their regression datasets, most of which were from the Chi-Chi sequence. One potential problem with including such a high proportion of records from a single event is that the model may become over-fit toward the characteristics of that event, and the model's ability to generalize to other situations is

lowered. This could be one reason why the BA08 and CB08 models outperformed the AS08, CY08, and I08 models on the mainshocks subset, which is comprised of more earthquakes (50) than any other subset in this study.

In assessing seismic hazards, the greatest hazard contribution comes from mainshocks, not aftershocks. For a given magnitude, aftershocks tend to generate smaller ground motions than mainshocks of the same magnitude, and the spectral scaling is different (Boore and Atkinson, 2008; Boore and Atkinson, 1989; Atkinson, 1993). Mainshocks are more likely to generate greater ground motions at a site. We do not intend to discount the importance of aftershocks, as aftershocks generate potentially devastating stresses and strains on already-fatigued systems. However, we argue that mainshocks are more important from the point of view of seismic hazard calculations; structural effects are beyond the scope of this thesis. Thus, the most important testing subset in this study is the mainshocks subset.

The AS08, CY08, and I08 model teams included aftershocks in their regression datasets, but only the AS08 and CY08 models include an aftershock dummy variable that reduces the ground motion estimate when the earthquake is an aftershock. Because aftershocks are associated with smaller ground motions than mainshocks for a given magnitude, the AS08 and CY08 teams utilize the aftershock dummy variable to alert the model to decrease its estimated ground motion when the GMPE is being used for an aftershock. The inclusion of aftershocks in the regression subset for the I08 model without an appropriate dummy variable effectively treats aftershocks as equivalent to mainshocks, even though the ground motion and spectral scaling is known to differ. As a result, the ground motion predictions for mainshocks are more prone to underprediction.

In summary, current probabilistic seismic hazard analyses incorporate mainshocks and not aftershocks; therefore, ground motion predictions for mainshocks have the most significant consequences. When aftershocks are included in the regression dataset for a model, there is a decrease in the prediction accuracy of mainshocks. Thus, our results suggest that aftershocks should not even be included in the regression database for GMPE development. However, if model developers choose to include aftershocks in their regression datasets, we highly recommend that an aftershock dummy variable be included in the model.

5.2 Uncertainty of Site Parameters

Of the model parameters, the greatest contribution to epistemic uncertainty comes from V_{S30} (Abrahamson and Silva, 2008). One of the major problems of shear wave velocity data is that actual measurements are sparse. Only about 30% of the stations in the NGA database have measured values of V_{S30} (Power *et al.*, 2008); the remaining V_{S30} values are inferred using correlations of V_{S30} with surficial geology, such as those published by Wills and Clahan (2006), presented in Table 2.4. However, Scott *et al.* (2006) find that shear wave velocity correlates poorly with geologic units.

In Figure 5.1, we explore the accuracy of inferring V_{S30} from surficial geology. For the 258 California stations in the flatfile with measured V_S profiles, we utilize the correlations in Wills and Clahan (2006) to estimate V_{S30} from surficial geology. In addition to the measured stations in the flatfile, we include 55 stations in the Parkfield, California, vicinity with measured V_S profiles provided by Kayen (2007). We then plot

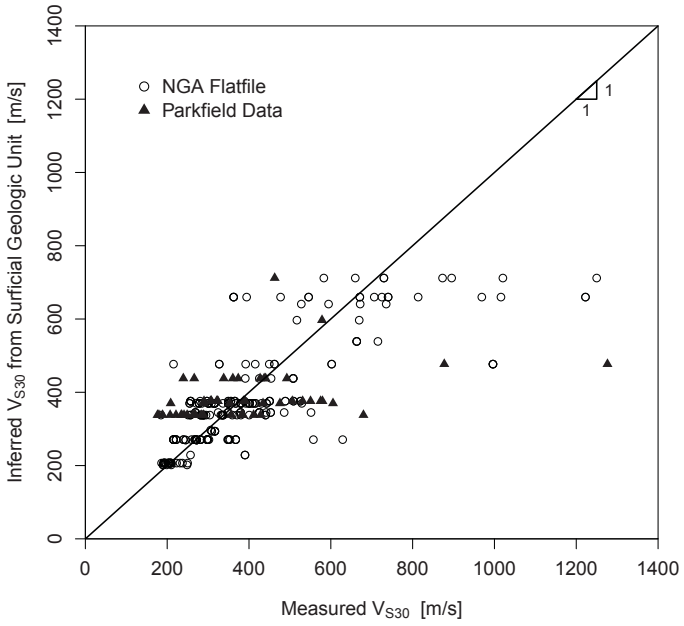

Figure 5.1. Measured V_{S30} versus the corresponding values of V_{S30} inferred from surficial geology using Wills and Clahan (2006), for sites in California with measured V_S profiles.

the value of V_{S30} inferred from surficial geology (which would be used as an input parameter if there were no measurement at the site) against the known, measured value of V_{S30}. If the classification scheme based upon surficial geology were perfect, the plot would follow the 1-to-1 line; unfortunately, there is a substantial amount of scatter in this plot. In addition, the discrete categories based on surficial geologic unit are visible as horizontal groupings. The coefficient of efficiency for this V_{S30} estimation procedure is 52.9%. Although the NGA flatfile has estimated values of V_{S30} for almost every recording station, we suspect that many of the V_{S30} estimates based upon surficial geology are inaccurate.

Even more difficult to estimate than V_{S30} are the depth parameters, $Z_{1.0}$ and $Z_{2.5}$. In section 2.2.2, we described the procedures for estimating the depth parameters when site-specific boreholes or regional velocity models are not available. Figure 2.9 presented

a graph of the median relationships provided by the AS08 (Equation 2.18) and CY08 (Equation 2.19) models for estimating $Z_{1.0}$ from V_{S30}, along with data from the 448 sites in the NGA flatfile with specified values of $Z_{1.0}$. The considerable amount of scatter in Figure 2.9 is even more apparent when comparing plots of measured versus calculated $Z_{1.0}$, as seen in Figure 5.2. For each of the 448 sites in the flatfile with specified values of $Z_{1.0}$, we calculate $Z_{1.0}$ from V_{S30} using Equations 2.18 and 2.19, and then plot the calculated values of $Z_{1.0}$ versus the values of $Z_{1.0}$ specified in the NGA flatfile. The plots deviate greatly from the ideal 1-to-1 line. The coefficients of efficiency are only 25.6% for the AS08 equation and −7.7% for the CY08 equation, indicating that the median equations suggested by Abrahamson and Silva (2008) and Chiou and Youngs (2008a) fare poorly when estimating $Z_{1.0}$ from the flatfile. Moreover, the $Z_{1.0}$ estimates are

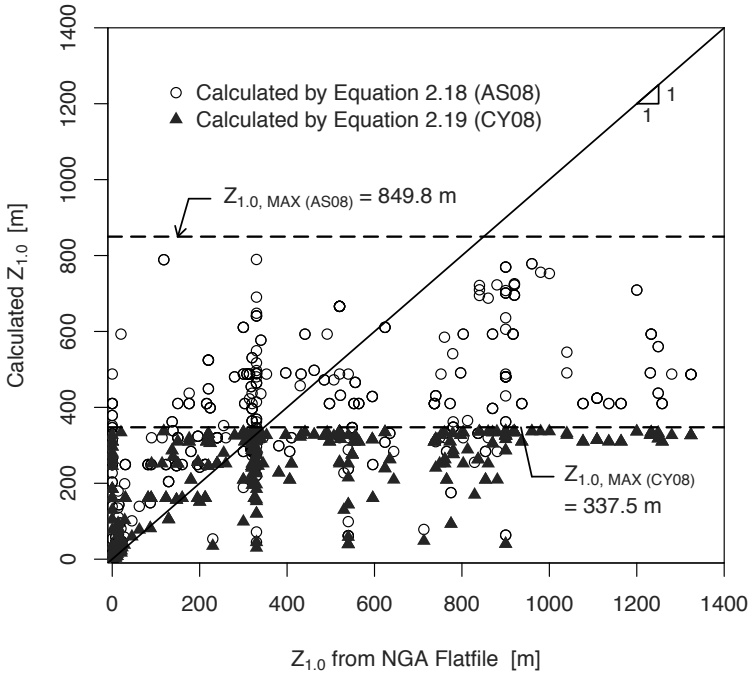

Figure 5.2. Comparison of $Z_{1.0}$ calculated from V_{S30} using the median equations versus the corresponding values of $Z_{1.0}$ from the flatfile, for Equation 2.18 (AS08) and Equation 2.19 (CY08).

numerically bounded at maximums of 849.8 m for Equation 2.18 and 337.5 m for Equation 2.19. Abrahamson and Silva (2008) developed Equation 2.18 from analytical site response models. Chiou and Youngs (2008b) utilized an updated velocity model for southern California when they developed Equation 2.19, which has smaller depth parameters than the previous velocity model reflected in the flatfile. Therefore, it is not surprising that there is some disagreement between Equations 2.18 and 2.19 and the values in the flatfile, but the discrepancies demonstrate that the depth parameters and their methods of estimation are fraught with uncertainty.

Campbell (1989) finds that the inclusion of depth parameters in GMPEs can improve their predictive capabilities. However, all the research teams who include depth parameters acknowledge that the depth parameters are correlated with V_{S30}. If the depth parameters were strongly correlated with V_{S30}, then it would most likely not be necessary to include them as separate explanatory variables, since they would not be contributing additional information to the model (a phenomenon known as "multicollinearity"). *Multicollinearity*, which occurs when two or more explanatory variables in a model are highly correlated, can have several undesirable consequences on the resulting model. The regression coefficients may become unstable and unrealistic in sign, and inferences on the different explanatory variables may be problematic (Helsel and Hirsch, 2002). A prime example of multicollinearity occurs when one explanatory variable is calculated from another explanatory variable, such as when $Z_{1.0}$ is calculated from V_{S30} for the AS08 and CY08 models. The issue of multicollinearity is the reason that BA08 did not use depth parameters in their model (Boore and Atkinson, 2008), although the other research teams decided that the depth parameters made a worthwhile contribution.

The key problem with site characteristics in GMPEs is a lack of measurements. For the majority of cases, site-specific V_{S30} measurements are unavailable; therefore, V_{S30} is inferred from surficial geology or site conditions. Then, the depth parameters are estimated from V_{S30}. When this happens, information about the ground surface (i.e., surficial geology) is being used to estimate a parameter that involves 30 m of depth (V_{S30}), which in turn is used to estimate a parameter that typically involves depths much greater than 30 m ($Z_{1.0}$ or $Z_{2.5}$). The entire decision process is based upon weak correlations of shear wave velocity with surficial geology. Clearly, there are problems with using surficial geology to estimate parameters that involve considerable subsurface depths. Surficial geologic maps provide no information about how the geologic units change with depth, and therefore are questionable for estimating V_{S30}. It is widely agreed that site characteristics should be incorporated into GMPEs. In our results, we find that models with quantitative site parameters (*i.e.*, AS08, BA08, CB08, CY08, BJF97, and C97) generally perform better than models that do not include site parameters or models that only include a dummy variable. However, to improve the prediction accuracy of GMPEs, we argue that there must be a greater emphasis on site-specific data collection. Recently-developed non-intrusive geophysical methods, such as the spectral analysis of surface waves (SASW), multichannel analysis of surface waves (MASW), and refraction microtremor (ReMi) methods, allow for large amounts of seismic data to be obtained efficiently and economically (Stokoe *et al.*, 1994; Park *et al.*, 1999; Louie, 2001). An increased database of site characteristics would reduce the scatter in Figures 5.1 and 5.2, and would ultimately lead to more reliable ground motion predictions.

For developing more reliable ground motion predictions, another issue (in addition to the lack of data) is determining which site parameters are the best predictors of amplification. The choice of a 30-meter averaging depth for V_S as a representation of site characteristics is somewhat arbitrary. One explanation is that 30 meters (approximately 100 feet) is a standard depth to which engineering site investigations and borings are performed, and that V_S data at greater depths is limited (Anderson *et al.*, 1996). However, the use of V_{S30} as a corollary for site amplification is a matter of debate; some researchers have questioned the accuracy of the correlation of V_{S30} and site amplification, and that such correlations have been repeatedly overstated (Castellaro *et al.*, 2008). Within the past 15 years, there has been a growing emphasis in the literature on the use of V_{S30}, when there is not enough research to support that an averaging depth of 30 meters is the most effective manner of representing the conditions at a site. When Boore *et al.* (1997) first introduced V_{S30} as an explanatory variable in a GMPE, they emphasized that the ideal averaging depth corresponds to one-quarter wavelength for the period of interest (Joyner and Fumal, 1984), and that 30 m is a choice limited by the lack of data at greater depths. Rather than perpetuating the use of V_{S30} as the predominant site parameter, we should be attempting to do better than V_{S30}. The incorporation of depth parameters in the NGA models may be a step in the right direction in terms of incorporating data from greater depths, but more data needs to be collected and more analysis needs to be performed before they are seriously pursued as high-quality site parameters. Obtaining more V_S data would provide a gateway for more effective site parameters to be used in prediction of earthquake ground motion.

5.3 Selection of Distance Measures and Cutoffs

5.3.1 Physical Interdependence of Distance Measures

Three distance measures are present in the NGA relations: the rupture distance (R_{RUP}), Joyner-Boore distance (R_{JB}), and site coordinate (R_X). These three distance parameters are *not* independent of each other—one can derive geometrical relationships that connect the parameters. As seen by Equations 2.1 through 2.4, R_X is not an independent distance parameter because it can be calculated directly from other input variables. Using geometry and trigonometry, we performed calculations to show that given one distance parameter in the set $\{R_{RUP}, R_{JB}, R_X\}$, the two other distance parameters are constrained by the first distance parameter, the source-to-site azimuth α, and the assumed values for the source parameters W, Z_{TOR}, and δ. The one situation in which two of the three distance measures are not constrained by the first distance parameter is in the special case of $R_{JB} = 0$, when the site is located directly above the ruptured area. If one specifies R_X or R_{RUP}, then the other two distance parameters follow. However, if only $R_{JB} = 0$ is specified, then an additional assumption must be made for either R_X or R_{RUP}. The remaining distance measure can then be easily calculated from the other parameters.

The geometrical interdependence of distance parameters is an issue because several of the NGA relations (AS08, CB08, and CY08) involve more than one distance parameter. Boore and Atkinson (2008) use R_{JB} as the primary distance parameter, and the other four models use R_{RUP} as the primary distance parameter. AS08, CB08, and CY08 also use a second distance parameter, R_{JB}, as part of the hanging wall term, and AS08 and CY08 use a third distance parameter, R_X, to also model the hanging wall effect. By using R_{JB} as the primary distance parameter, Boore and Atkinson (2008) implicitly

incorporate a hanging wall factor because R_{JB} is smaller for sites on the hanging wall than on the footwall, thus resulting in slightly increased ground motion predictions (Abrahamson *et al.*, 2008). An added benefit is that only one distance parameter is used in the model.

When different explanatory variables in the same model can be physically related by a formula, such as the distance parameters and site parameters for some models, the issue of multicollinearity arises. Moreover, users of the models must realize that the input parameters are not independent. Many current implementations of the NGA relations (such as the Excel and FORTRAN files on the PEER project web site) require the user to input each explanatory variable independently (Pacific Earthquake Engineering Research Center, 2008b). Without understanding the physical relationship between R_{RUP}, R_{JB}, and R_X, the user may enter inappropriate values for models with multiple distance measures. When the parameters are entered independently, the terms may be geometrically inconsistent with each other, and a ground motion estimate would be calculated for a physically impossible combination of input parameters. For example, a user may make the simple assumption that the three distance measures are equal, *i.e.* $R_{RUP} = R_{JB} = R_X$. However, this assumption is only valid in the special case of a site located on the hanging-wall side of a vertical strike-slip fault ($\delta = 90°$) with surface rupture ($Z_{TOR} = 0$). Previous GMPEs generally included just one type of distance parameter per model, so the issues of multicollinearity and geometrical consistency are not an issue for these models. The interdependence of distance parameters is a phenomenon that needs to be considered in model implementation.

5.3.2 Effect of Distance on Prediction Accuracy

As seen in Tables 4.2 and 4.4, the GMPEs perform best at intermediate distances, where most data is available. In addition to the lack of data, ground motion is highly variable at small distances, and the estimation of ground motion at large distances raises other complications, such as Moho bounce effects (Atkinson and Boore, 2006). As a result, ground motions at small and large distances are more difficult to predict than ground motions at intermediate distances. The CY08 model performs poorly in several of the subsets, but performs superiorly in the blind comparison tests in the intermediate distance range. One of the key differences in model development is that Chiou and Youngs (2008a) only included sites within 70 km of rupture in their regression dataset, while the other NGA research teams included sites within 200 km. Perhaps the over-fitting of the CY08 model to intermediate distances gives it increased predictive capabilities within that range, and decreased predictive capabilities outside of that range.

5.4 Improving Prediction Accuracy

In this thesis, we have focused our comparisons on the models' median estimates of *PGA* and *Sa*. The median equations are the models' closest estimates of the observed ground motion, and they are the key focus of the model development efforts. However, we must emphasize the importance of the uncertainties of the median estimates. Ground motion variability has often been disregarded or discounted in the application of GMPEs (Bommer and Abrahamson, 2006). Strasser *et al.* (2009) present a good discussion of the contributions to uncertainty and the challenges in reducing them. They claim that

Table 5.1. Summary of model rankings

		NGA models					Previous models				
		AS08	BA08	CB08	CY08	I08	AS97	BJF97	C97	SCE97	I91
NGA flatfile	Mainshocks	3	2	1	4	–	–	–	–	–	–
	Aftershocks	1	2	4	3	–	–	–	–	–	–
Blind test	Parkfield	3	4	1	8	–	5	2	6	7	–
	San Simeon	3	2	3	1	–	6	5	7	8	–

reductions in uncertainty are not necessarily brought by increasing the number of explanatory variables in the models or by increasing the quantity of ground motion records in the regression datasets. Kuehn *et al.* (2009) warn about the dangers of over-fitting using the current approaches to model development, and propose an alternative method for the development of GMPEs that uses generalization error minimization techniques.

Table 5.1 is a summary of the model rankings for all the testing subsets. The excellent performance of the simpler models (BA08 and CB08) on the mainshocks subset and their generally high rankings on the blind comparison subsets lends credence to the suggestion that more complicated models do not necessarily offer more accurate predictions. The more complicated models with greater numbers of input parameters require more assumptions on variables that are difficult to predict before an earthquake actually happens. A higher-quality regression dataset (not necessarily higher-*quantity*) with greater measurements of site characteristics, coupled with simple functional forms in the GMPEs, may yield the best solution.

Chapter 6:
CONCLUSIONS

Using the Nash-Sutcliffe model efficiency coefficient (*E*) as the primary goodness-of-fit statistic, we have compared the prediction accuracy of the five ground motion prediction equations released as part of the Next Generation Attenuation of Ground Motions project. The coefficient of efficiency, commonly used in hydrology, is a superior goodness-of-fit statistic to many other statistics found in the literature, and it works well as a framework for validating alternative models. First, we tested the NGA models on subsets of the database upon which they were developed. Then, we compared the performance of the new models with the previous generation of models by implementing a blind comparison test on two recent California earthquakes (the 2004 *M* 6.0 Parkfield earthquake, and the 2003 *M* 6.5 San Simeon earthquake), for which ground motion records were not present in any of the databases used to develop the models. The newer models generally perform better than their previous counterparts do in these blind tests, but all models have difficulty predicting the highly variable near-source ground motions of the Parkfield earthquake. For seismic hazard assessment in active tectonic regions susceptible to shallow crustal earthquakes, the five previous GMPEs are generally considered to be obsolete. Even though some of the older models (such as BJF97) perform well in some cases, the new NGA relations, which were developed from a much richer database of ground motion data, are intended to be used in place of the previous GMPEs.

We find that the decisions that model developers make when selecting their regression datasets greatly influence the models' predictive capabilities. Allowing a model to be extrapolated to distances far beyond the range found in the regression dataset may be detrimental from a prediction standpoint. Especially on the blind comparison test, the CY08 model (developed only with data from distances no greater than 70 km from the earthquake source) performs relatively well at intermediate distances, but it performs more poorly than the other models at small and large distances. Including large numbers of records from single earthquakes (such as the high number of records from the Chi-Chi mainshock and aftershocks) can result in over-fitting the data to those particular scenarios, thus reducing the models' ability to generalize to other situations. In addition, including aftershocks in the regression dataset may lead to unconservative ground motion predictions if they are not properly handled by using an aftershock dummy variable. In general, however, aftershocks do not appear to help with model prediction accuracy.

High model complexity, whether through large numbers of explanatory variables or convoluted functional forms, can also lead to over-fitting. We find that two of the models with simpler functional forms and explanatory variables, BA08 and CB08, have the highest prediction accuracy when tested on a comprehensive subset of mainshocks from the NGA database, and also perform well in blind situations. These results suggest that increasing the complexity of GMPEs does not necessarily increase their prediction accuracy. Instead of increasing the models' complexity, an increased emphasis on the measurement of site parameters would lead to a higher-quality regression dataset and better ground motion predictions. The development of better site characteristics than V_{S30} would also improve the prediction accuracy of GMPEs.

In this study, we have quantitatively compared the predictive capabilities of the five ground motion prediction equations developed from the NGA project. However, we do not wish to suggest that specific NGA models should be utilized more than others in general practice, or that other models should not be used at all. Even though some models generally outrank others, each model has positive and negative characteristics. In a seismic hazard analysis, it is advantageous to diversify the calculations and consider the estimates from multiple models. As we have seen in this study, when the analysis is broken into subsets and subdivisions, there are certain situations in which each NGA model performs superiorly.

Rather than promoting the ubiquitous use of one model over another, we hope that the results of this study may be considered from a model development point of view. When future ground motion prediction equations are created, researchers need to consider the implications of their regression and modeling decisions on the ultimate prediction accuracy of the final model. Developers need to carefully consider decisions relating to model complexity, selection of input parameters, inclusion of aftershocks in the regression database, and allowing the regression database to be monopolized by single events or distance ranges. Finally, in implementing the NGA relations, we found that certain aspects of some of the models were very unclear. The proper sharing of modeling information, as well as clear descriptions, for new GMPEs will allow these models to be correctly applied for ground motion prediction in the future. We do not know exactly when or where the next Big One will strike, but we can utilize ground motion prediction equations to better quantify, evaluate, and mitigate seismic hazards, and ultimately save lives when that day comes.

Appendix A:
EXPLANATORY VARIABLES FOR EACH MODEL

In this appendix, we present tables with explicit details of how we determined the explanatory variables when implementing each of the GMPEs in this study. For the five new models (AS08, BA08, CB08, CY08, and I08), we identify exactly how we determined the values of the explanatory variables from the NGA flatfile. For the five previous models (AS97, BJF97, C97, SCE97, and I91), we offer detailed descriptions of the explanatory variables and how we determined their values from the source, path, and site data (not from the NGA flatfile). As explained in section 2.5, the previous models are only tested on blind data from the Parkfield and San Simeon earthquakes (which are not present in the NGA flatfile). Further information on the obtainment of explanatory variables for the blind comparison tests is available in section 2.2.4.

Table A.1. Relevant columns for explanatory variables in the NGA flatfile (v7.2)

Column letter	Column title	Symbol	Unit
J	Earthquake magnitude	M	—
R	Dip	δ	deg
S	Rake angle	λ	deg
AF	Dept [sic] to top of fault rupture model	Z_{TOR}	km
AH	Fault rupture width	W	km
AX	Joyner-Boore Dist.	R_{JB}	km
BA	ClstD	R_{RUP}	km
BC	Source-to-site azimuth	α	deg
CB	Preferred Vs30	V_{S30}	m/s
CT	Z1	$Z_{1.0}$	m
CU	Z1.5	$Z_{1.5}$	m
CV	Z2.5	$Z_{2.5}$	m

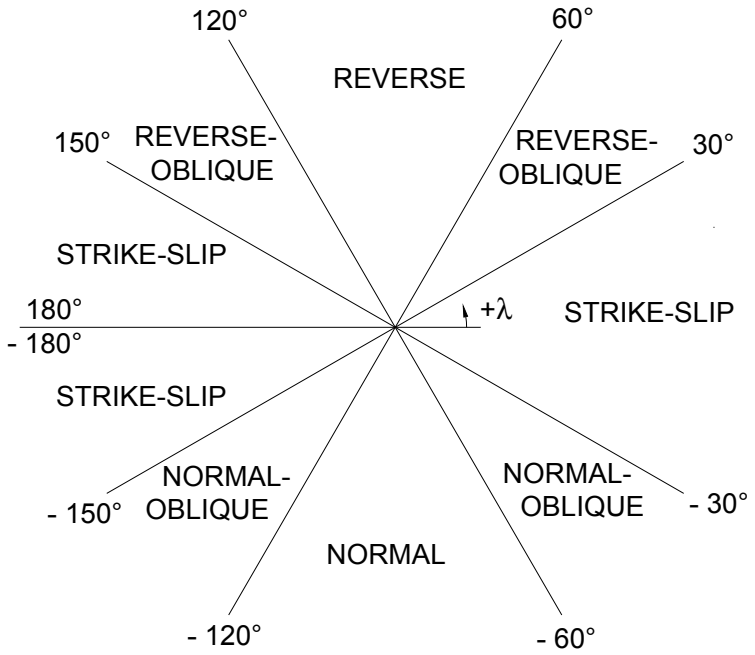

Figure A.1. Standard convention for rake angle (λ) in the NGA database. Classifications of fault mechanism as a function of λ vary from model to model, as explained in this appendix.

Table A.2. Determination of explanatory variables for the AS08 model

Symbol	Parameter Definition	Method of Determination
M	Moment magnitude	Directly from flatfile
R_{RUP}	Closest distance to the rupture plane [km]	Directly from flatfile
R_{JB}	Horizontal distance to the surface projection of the rupture [km]	Directly from flatfile
R_X	Horizontal distance to the surface projection of the top edge of the rupture plane, measured perpendicular to the strike [km]	Calculated from R_{RUP}, R_{JB}, Z_{TOR}, W, δ and α (see section 2.2.1)
Z_{TOR}	Depth to top of rupture [km]	Directly from flatfile
W	Down-dip fault rupture width [km]	Directly from flatfile
δ	Fault dip [degrees]	Directly from flatfile
F_{RV}	Reverse style-of-faulting flag	$F_{RV} = 1$ if $30° \leq \lambda \leq 150°$
F_{NM}	Normal style-of-faulting flag	$F_{NM} = 1$ if $-120° \leq \lambda \leq -60°$
F_{HW}	Hanging wall flag	$F_{HW} = 1$ if $0 < \alpha < 180°$ and $\delta \neq 90°$
F_{AS}	Aftershock flag	Assumptions explained in section 2.2.3
V_{S30}	Time-averaged shear wave velocity over a subsurface depth of 30 meters [m/s]	Directly from flatfile
$Z_{1.0}$	Depth to $V_S = 1.0$ km/s [m]	$Z_{1.0}$ is obtained directly from flatfile if Column CT is populated; if the column is empty, then $Z_{1.0}$ is calculated from V_{S30} using Equation 2.18 (Equation 17 in Abrahamson and Silva (2008)).
$P\hat{G}A_{1100}$	PGA on rock site; baseline for nonlinear site response [g]	Evaluate PGA using $V_{S30} = 1100$ m/s and $Z_{1.0} = 6.43$ m (the value using obtained using Equation 2.18 with $V_{S30} = 1100$ m/s)

Table A.3. Determination of explanatory variables for the BA08 model

Symbol	Parameter Definition	Method of Determination
M	Moment magnitude	Directly from flatfile
R_{JB}	Horizontal distance to the surface projection of the rupture [km]	Directly from flatfile
RS	Reverse style-of-faulting flag	$RS = 1$ if $30° \leq \lambda \leq 150°$
NS	Normal style-of-faulting flag	$NS = 1$ if $-150° \leq \lambda \leq -30°$
SS	Strike-slip style-of-faulting flag	$SS = 1$ if λ is not in either of the ranges specified for RS or NS
U	Unspecified style-of-faulting flag	All faulting mechanisms are specified in the NGA flatfile and in our blind comparisons; however, the user may use $U = 1$ (and $RS = NS = SS = 0$) if he/she wishes to estimate ground motion parameters when the style of faulting is unspecified.
V_{S30}	Time-averaged shear wave velocity over a subsurface depth of 30 meters [m/s]	Directly from flatfile
pga4nl	*PGA* on rock site; baseline for nonlinear site response [*g*]	Evaluate *PGA* using $V_{S30} = 760$ m/s

Table A.4. Determination of explanatory variables for the CB08 model

Symbol	Parameter Definition	Method of Determination
M	Moment magnitude	Directly from flatfile
R_{RUP}	Closest distance to the rupture plane [km]	Directly from flatfile
R_{JB}	Horizontal distance to the surface projection of the rupture [km]	Directly from flatfile
Z_{TOR}	Depth to top of rupture [km]	Directly from flatfile
δ	Fault dip [degrees]	Directly from flatfile
F_{RV}	Reverse style-of-faulting flag	$F_{RV} = 1$ if $30° \leq \lambda \leq 150°$
F_{NM}	Normal style-of-faulting flag	$F_{NM} = 1$ if $-150° \leq \lambda \leq -30°$
V_{S30}	Time-averaged shear wave velocity over a subsurface depth of 30 meters [m/s]	Directly from flatfile
$Z_{2.5}$	Depth to $V_S = 2.5$ km/s [km]	$Z_{2.5}$ is calculated in the following manner, in order of preference depending on the availability of information: 1. If $Z_{2.5}$ is available, divide the value in the flatfile by 1000 (CB08 uses $Z_{2.5}$ in km, but $Z_{2.5}$ is presented in meters in the flatfile); 2. Using Equation 2.20 if $Z_{1.5}$ is available; 3. Using Equation 2.21 if $Z_{1.0}$ is available; 4. If the basin depth is not known to be particularly deep or shallow, use the "default value" of 2 km.
A_{1100}	*PGA* on rock site; baseline for nonlinear site response [*g*]	Evaluate *PGA* using $V_{S30} = 1100$ m/s

Table A.5. Determination of explanatory variables for the CY08 model

Symbol	Parameter Definition	Method of Determination
M	Moment magnitude	Directly from flatfile
R_{RUP}	Closest distance to the rupture plane [km]	Directly from flatfile
R_{JB}	Horizontal distance to the surface projection of the rupture [km]	Directly from flatfile
R_X	Horizontal distance to the surface projection of the top edge of the rupture plane, measured perpendicular to the strike [km]	Calculated from R_{RUP}, R_{JB}, Z_{TOR}, W, δ and α (see section 2.2.1)
Z_{TOR}	Depth to top of rupture [km]	Directly from flatfile
δ	Fault dip [degrees]	Directly from flatfile
F_{RV}	Reverse style-of-faulting flag	$F_{RV} = 1$ if $30° \leq \lambda \leq 150°$
F_{NM}	Normal style-of-faulting flag	$F_{NM} = 1$ if $-120° \leq \lambda \leq -60°$
F_{HW}	Hanging wall flag	$F_{HW} = 1$ if $0 < \alpha < 180°$
AS	Aftershock flag	Assumptions explained in section 2.2.3
V_{S30}	Time-averaged shear wave velocity over a subsurface depth of 30 meters [m/s]	Directly from flatfile
$Z_{1.0}$	Depth to $V_S = 1.0$ km/s [m]	$Z_{1.0}$ is obtained directly from flatfile if Column CT is populated; if the column is empty, then $Z_{1.0}$ is calculated from V_{S30} using Equation 2.19.
$y_{ref}(T)$	*Sa* on rock site; baseline for nonlinear site response [*g*]	Equations 13a and 13b in Chiou and Youngs (2008a)

Table A.6. Determination of explanatory variables for the I08 model

Symbol	Parameter Definition	Method of Determination
M	Moment magnitude	Directly from flatfile
R_{RUP}	Closest distance to the rupture plane [km]	Directly from flatfile
F	Reverse style-of-faulting flag	$F = 1$ if $30° \leq \lambda \leq 150°$

Table A.7. Determination of explanatory variables for the AS97 model

Symbol	Parameter Definition	Method of Determination
M	Moment magnitude	Constant for earthquake
R_{RUP}	Closest distance to the rupture plane [km]	From source-to-site geometry
F	Reverse style-of-faulting flag	No specifications are provided in Abrahamson and Silva (1997) for the rake angles to use for reverse, reverse-oblique, and strike-slip; thus, we assume the standard conventions in the NGA database (Figure A.1): set $F = 1$ if $60° \leq \lambda \leq 120°$ (reverse), $F = 0.5$ if $30° \leq \lambda \leq 60°$ or $120° \leq \lambda \leq 150°$ (reverse-oblique), and $F = 0$ otherwise.
HW	Hanging wall flag	$HW = 1$ if $0 < \alpha < 180°$. As stated in Abrahamson and Silva (2008), the AS97 model does not clearly define where to apply the cutoff of HW for steeply dipping faults. However, the AS97 hanging wall function includes a distance taper so that the hanging wall function is zero for sites with $R_{RUP} >$ 24 km (Abrahamson and Silva, 1997). Thus, we follow the convention of F_{HW} (like AS08) for HW and assume that the distance taper implicitly incorporates the cutoff.
S	Site class dummy variable	*Deep soil* sites ($S = 1$) have at least 20 m of soil overlying the bedrock (Geomatrix site classes C and D). *Rock / shallow soil* sites ($S = 0$) are located either directly on rock ($V_S >$ 600 m/s), or on less than 20 m of soil (Geomatrix site classes A and B). (Chiou *et al.*, 2008).
$\hat{PGA}_{rock}$	PGA on rock site; baseline for nonlinear site response [g]	Evaluate PGA using $S = 0$

Table A.8. Determination of explanatory variables for the BJF97 model

Symbol	Parameter Definition	Method of Determination
M	Moment magnitude	Constant for earthquake
R_{JB}	Horizontal distance to the surface projection of the rupture [km]	From source-to-site geometry
RS	Reverse style-of-faulting flag	$RS = 1$ if $30° < \lambda < 150°$
SS	Strike-slip style-of-faulting flag	$SS = 1$ if $-180° \leq \lambda \leq -150°$, $-30° \leq \lambda \leq 30°$, or $150° \leq \lambda \leq 180°$
ALL	Unspecified style-of-faulting flag	Use $ALL = 1$ (and $RS = SS = 0$) to estimate ground motion parameters when the style of faulting is unspecified. Note that the BJF97 model is *not* applicable to normal-faulting earthquakes (Boore *et al.*, 1997).
V_{S30}	Time-averaged shear wave velocity over a subsurface depth of 30 meters [m/s]	From seismic recording station data (see section 2.2.4)

Table A.9. Determination of explanatory variables for the C97 model

Symbol	Parameter Definition	Method of Determination
M	Moment magnitude	Constant for earthquake
R_{SEIS}	Closest distance to the rupture plane within the zone of seismogenic rupture [km]	Campbell (1997) assumes that the fault rupture above a seismogenic depth H_{SEIS} (often assumed to be 3 km in California) is non-seismogenic and does not release significant seismic energy during earthquakes. The seismogenic depth R_{SEIS} is the distance from the site to the closest point on the rupture plane at a depth no less than H_{SEIS}.
D	Depth to basement rock	Depth to Cretaceous or older deposits, or depth to V_S = 3 km/s where shear wave velocity data is available. When no other information is available, Campbell (2000) suggests using D = 5 km for generic soil sites, D = 1 km for generic [soft] rock sites, and D = 0 km when the site is known to be on hard rock.
F	Reverse style-of-faulting flag	F = 1 if 22.5° < λ < 150° (reverse), F = 0.5 if the fault mechanism is unspecified, and F = 0 for strike-slip and normal events (i.e., when λ is not in the reverse-faulting range)
S_{HR}	Hard rock flag *	S_{HR} = 1 when the site is located on hard rock (Cretaceous or older sedimentary deposits, metamorphic rock, crystalline rock, or hard volcanic rock)
S_{SR}	Soft rock flag *	S_{SR} = 1 when the site is located on soft rock (such as Tertiary sedimentary deposits or soft volcanic deposits)

* When at least 10 m of soil overlie the bedrock, use $S_{HR} = S_{SR} = 0$.

Table A.10. Determination of explanatory variables for the SCE97 model

Symbol	Parameter Definition	Method of Determination
M	Moment magnitude	Constant for earthquake
R_{RUP}	Closest distance to the rupture plane [km]	From source-to-site geometry
–	Style of faulting [1, 2]	Sites are classified as reverse if $45° \leq \lambda \leq 145°$, and as strike-slip if λ falls outside of this range. Strike-slip and normal earthquakes are grouped into the same category.
–	Site category [3]	The site categories for SCE97 mimic those of AS97 (i.e., "deep soil" and "rock / shallow soil"). We assume that deep soil sites have at least 20 m of soil overlying the bedrock (Geomatrix site classes C and D). Rock sites (including "shallow soil" sites) are located either directly on rock ($V_S > 600$ m/s), or on less than 20 m of soil (Geomatrix site classes A and B) (Chiou *et al.*, 2008).

NOTES:

1. For deep soil sites, the functional forms are the same for reverse and strike-slip earthquakes, but there are different constant terms for reverse and strike-slip events.
2. For rock sites, the baseline equations are for strike-slip earthquakes. To adjust for reverse earthquakes, multiply the strike-slip amplitudes by 1.2. That is, $(Sa)_{\text{reverse}} = 1.2(Sa)_{\text{strike-slip}}$.
3. Different equations with slightly different functional forms are provided for deep soil sites and for rock sites.

Table A.11. Determination of explanatory variables for the I91 model

Symbol	Parameter Definition	Method of Determination
M	Moment magnitude	Constant for earthquake
R	Source-to-site distance	For $M > 6$, $R = R_{RUP}$ (closest distance to the rupture plane); for $M \leq 6$, $R = R_{HYP}$ (hypocentral distance).
F	Reverse style-of-faulting flag	No specifications are provided for the rake angles to use for reverse, reverse-oblique, and strike-slip; thus, we assume the standard conventions in the NGA database (Figure A.1): set $F = 1$ if $60° \leq \lambda \leq 120°$ (reverse), $F = 0.5$ if $30° \leq \lambda \leq 60°$ or $120° \leq \lambda \leq 150°$ (reverse-oblique), and $F = 0$ otherwise.

Appendix B:
DATA FOR THE PARKFIELD AND SAN SIMEON EARTHQUAKES

Appendix B contains detailed tables of the explanatory and response variables we gathered and calculated for our blind comparison tests on the 2004 *M* 6.0 Parkfield earthquake and the 2003 *M* 6.5 San Simeon earthquake. The sources of data and our methodology for obtaining the explanatory and response variables are explained in sections 2.2.4 and 2.3, respectively; this appendix contains the raw numbers for each of the 85 sites for the Parkfield earthquake and the 8 sites for the San Simeon earthquake. The source parameters, which are constant for each earthquake, were presented in Table 2.2 and are not replicated here. Tables B.1 and B.2 list the explanatory variables for the Parkfield and San Simeon earthquakes, respectively, with information on the ground motion recording stations, location parameters, and site parameters. Tables B.3 and B.4 list the response variables (*PGA* and *Sa*) for the two earthquakes, which we calculated from the observed acceleration time series and response spectra, at each recording station. We only calculated *Sa* up to the maximum useable period (T_{high}) based on the processed frequency band for each station. The ground motion parameters are presented in terms of GM_{xy} (used in the previous generation of GMPEs) and *GMRotI50* (used in the new generation of GMPEs). Taken together with Table 2.2, Appendix B can be thought of as a mini-flatfile for the Parkfield and San Simeon earthquakes.

Table B.1. Explanatory variables for the Parkfield earthquake (Page 1 of 11)

	1	2	3	4	5	6	7	8
Station information								
Station number / code	1083	1747	35219	36138	36153	36176	36177	36227
Owner	USGS	USGS	CSMIP	CSMIP	CSMIP	CSMIP	CSMIP	CSMIP
Station location and name	San Luis Obispo – Rec Center	Coalinga – Fire Station 39	Buttonwillow – Hwy 58 & Wasco	Parkfield – Fault Zone 12	San Luis Obispo – Lopez Lake Grounds	Parkfield – Vineyard Canyon 3W	Parkfield – Vineyard Canyon 2E	Parkfield – Cholame 5W
Location parameters								
Latitude [deg]	35.285	36.137	35.403	35.899	35.208	35.922	35.973	35.697
Longitude [deg]	–120.661	–120.363	–119.449	–120.433	–120.457	–120.534	–120.467	–120.328
Elevation [m]	52	89	84	465	168	791	725	338
Epicentral distance, R_{EPI} [km]	64.32	35.75	95.52	10.74	67.79	18.71	19.44	13.74
Hypocentral distance, R_{HYP} [km]	64.76	36.55	95.82	13.38	68.22	20.47	21.12	15.83
Joyner-Boore distance, R_{JB} [km]	62.07	22.52	91.26	0.29	64.65	2.15	3.44	9.93
Rupture distance, R_{RUP} [km]	63.69	22.52	91.26	0.36	66.10	4.86	3.47	11.40
Site coordinate, R_X [km]	60.38	–22.52	–31.08	–0.29	52.16	4.84	–3.44	7.44
Seismogenic distance, R_{SEIS} [km]	63.69	23.18	91.47	3.18	66.10	5.51	5.17	11.53
Source-to-site azimuth, α [deg]	69.23	–90.00	–19.91	–90.00	51.42	90.00	–90.00	40.45
Hanging wall indicator, F_{HW}	1	0	0	0	1	1	0	1
Site parameters								
Geologic symbol	KJf	Qal, thin	Qal, deep	Qal, thin	Tss	Tsh	KJf	Qal, thin
V_{S30} [m/sec]	712.82	338.54	271.44	268.99	477.00	307.85	462.78	241.21
V_{S30} data measured (0) or inferred (1)	1	1	1	0	1	0	0	0
$Z_{1.0}$ [m] (if available)	–	–	–	–	–	–	–	120
$Z_{1.5}$ [m] (if available)	–	–	–	–	–	–	–	–
Site class dummy variable, S (AS97, SCE97)	0	1	1	1	0	0	0	0
Soft rock dummy variable, S_{SR} (C97)	0	0	0	0	1	1	1	0
Hard rock dummy variable, S_{HR} (C97)	1	0	0	0	0	0	0	0

Table B.1 Continued. Explanatory variables for the Parkfield earthquake (Page 2 of 11)

	9	10	11	12	13	14	15	16
Station information								
Station number / code	36228	36229	36230	36407	36408	36410	36411	36412
Owner	CSMIP	CSMIP	CSMIP	CSMIP	CSMIP	CSMIP	CSMIP	CSMIP
Station location and name	Parkfield – Cholame 2WA	Parkfield – Cholame 12W	Parkfield – Cholame 2E	Parkfield – Fault Zone 1	Parkfield – Fault Zone 3	Parkfield – Cholame 3W	Parkfield – Cholame 4W	Parkfield – Cholame 4AW
Location parameters								
Latitude [deg]	35.733	35.639	35.751	35.758	35.803	35.724	35.718	35.707
Longitude [deg]	–120.286	–120.404	–120.259	–120.307	–120.344	–120.294	–120.304	–120.316
Elevation [m]	345	338	425	347	365	350	379	342
Epicentral distance, R_{EPI} [km]	12.09	19.72	12.59	8.76	3.02	12.42	12.49	13.08
Hypocentral distance, R_{HYP} [km]	14.42	21.23	14.89	11.77	8.44	14.70	14.77	15.26
Joyner-Boore distance, R_{JB} [km]	8.24	16.78	8.45	4.91	0.00	8.53	8.56	9.19
Rupture distance, R_{RUP} [km]	8.47	18.89	8.45	5.14	0.74	9.07	9.41	10.39
Site coordinate, R_X [km]	1.94	16.86	–1.21	1.53	0.74	3.15	4.27	5.89
Seismogenic distance, R_{SEIS} [km]	8.88	18.89	9.06	5.82	2.99	9.39	9.69	10.58
Source-to-site azimuth, α [deg]	13.26	61.93	–8.24	17.34	90.00	20.28	26.88	34.36
Hanging wall indicator, F_{HW}	1	1	0	1	1	1	1	1
Site parameters								
Geologic symbol	Qal, thin	Qoa	Tsh	Qal, thin	Qoa	Qal, thin	QT	Qal, thin
V_{S30} [m/sec]	176.34	353.32	505.92	179.78	208.54	234.22	437.14	283.28
V_{S30} data measured (0) or inferred (1)	0	0	0	0	0	0	0	0
$Z_{1.0}$ [m] (if available)	110	–	80	–	–	–	–	–
$Z_{1.5}$ [m] (if available)	–	–	–	–	–	–	–	–
Site class dummy variable, S (AS97, SCE97)	1	1	0	1	1	1	0	1
Soft rock dummy variable, S_{SR} (C97)	0	0	1	0	0	0	0	0
Hard rock dummy variable, S_{HR} (C97)	0	0	0	0	0	0	0	0

Table B.1 Continued. Explanatory variables for the Parkfield earthquake (Page 3 of 11)

	17	18	19	20	21	22	23	24
Station information								
Station number / code	36414	36415	36416	36419	36420	36421	36422	36427
Owner	CSMIP	CSMIP	CSMIP	CSMIP	CSMIP	CSMIP	CSMIP	CSMIP
Station location and name	Parkfield – Fault Zone 4	Parkfield – Gold Hill 1W	Parkfield – Gold Hill 2W	Parkfield – Stone Corral 1E	Parkfield – Gold Hill 3W	Parkfield – Gold Hill 2E	Parkfield – Stone Corral 2E	Point Buchon – Los Osos
Location parameters								
Latitude [deg]	35.836	35.818	35.812	35.788	35.796	35.843	35.810	35.274
Longitude [deg]	–120.395	–120.378	–120.391	–120.294	–120.411	–120.348	–120.282	–120.885
Elevation [m]	417	386	451	394	610	416	463	25
Epicentral distance, R_{EPI} [km]	3.01	0.49	1.57	7.83	3.95	3.90	8.34	75.84
Hypocentral distance, R_{HYP} [km]	8.48	7.92	8.12	11.13	9.04	8.84	11.54	76.22
Joyner-Boore distance, R_{JB} [km]	0.00	0.00	0.57	3.55	3.10	1.93	4.49	74.42
Rupture distance, R_{RUP} [km]	1.77	1.93	3.24	3.55	5.76	1.94	4.49	75.90
Site coordinate, R_X [km]	1.77	1.94	3.26	–1.55	5.79	–1.93	–3.98	76.41
Seismogenic distance, R_{SEIS} [km]	3.28	3.32	4.12	4.84	6.19	3.89	5.82	75.90
Source-to-site azimuth, α [deg]	90.00	90.00	90.00	–25.97	90.00	–90.00	–62.49	82.36
Hanging wall indicator, F_{HW}	1	1	1	0	1	0	0	1
Site parameters								
Geologic symbol	Qal, thin	Qal, thin	Tsh	Qal, thin	QT	Qal, thin	Tsh	QT
V_{S30} [m/sec]	221.51	207.21	323.79	266.10	492.50	357.12	550.41	438.34
V_{S30} data measured (0) or inferred (1)	0	0	0	0	0	0	0	1
$Z_{1.0}$ [m] (if available)	–	–	–	–	–	–	–	–
$Z_{1.5}$ [m] (if available)	–	–	–	–	–	–	–	–
Site class dummy variable, S (AS97, SCE97)	0	1	0	1	0	0	0	1
Soft rock dummy variable, S_{SR} (C97)	1	0	1	0	0	0	1	0
Hard rock dummy variable, S_{HR} (C97)	0	0	0	0	0	0	0	0

Table B.1 Continued. Explanatory variables for the Parkfield earthquake (Page 4 of 11)

	25	26	27	28	29	30	31	32
Station information								
Station number / code	36431	36432	36433	36434	36437	36439	36440	36441
Owner	CSMIP	CSMIP	CSMIP	CSMIP	CSMIP	CSMIP	CSMIP	CSMIP
Station location and name	Parkfield – Fault Zone 7	Parkfield – Gold Hill 6W	Parkfield – Gold Hill 4W	Parkfield – Gold Hill 5W	Parkfield – Stone Corral 3E	Parkfield – Gold Hill 3E	Parkfield – Vineyard Canyon 5W	Parkfield – Vineyard Canyon 6W
Location parameters								
Latitude [deg]	35.871	35.738	35.785	35.770	35.833	35.870	35.885	35.861
Longitude [deg]	–120.404	–120.507	–120.444	–120.477	–120.270	–120.334	–120.565	–120.600
Elevation [m]	453	361	561	472	528	487	498	398
Epicentral distance, R_{EPI} [km]	6.78	14.76	7.15	10.57	9.61	7.09	18.93	21.05
Hypocentral distance, R_{HYP} [km]	10.46	16.73	10.79	13.25	12.53	10.69	20.55	22.49
Joyner-Boore distance, R_{JB} [km]	0.20	13.87	6.14	9.48	6.54	4.86	6.97	11.10
Rupture distance, R_{RUP} [km]	0.27	16.32	8.75	12.02	6.55	4.87	9.55	13.61
Site coordinate, R_X [km]	–0.20	16.56	8.83	12.17	–6.48	–4.86	9.66	13.79
Seismogenic distance, R_{SEIS} [km]	3.15	16.32	8.91	12.07	7.71	6.20	9.67	13.62
Source-to-site azimuth, α [deg]	–90.00	90.00	90.00	90.00	–82.30	–90.00	90.00	90.00
Hanging wall indicator, F_{HW}	0	1	1	1	0	0	1	1
Site parameters								
Geologic symbol	Qoa	QT	QT	QT	Tsh	Qoa	Tsh	QT
V_{S30} [m/sec]	290.68	438.34	438.34	438.34	579.61	434.28	320.97	438.34
V_{S30} data measured (0) or inferred (1)	0	1	1	1	0	0	0	1
$Z_{1.0}$ [m] (if available)	–	–	–	–	20	30	–	–
$Z_{1.5}$ [m] (if available)	–	–	–	–	90	–	–	–
Site class dummy variable, S (AS97, SCE97)	1	1	0	0	0	0	0	1
Soft rock dummy variable, S_{SR} (C97)	0	0	0	0	1	0	1	1
Hard rock dummy variable, S_{HR} (C97)	0	0	0	0	0	0	0	0

Table B.1 Continued. Explanatory variables for the Parkfield earthquake (Page 5 of 11)

	33	34	35	36	37	38	39	40
Station information								
Station number / code	36443	36445	36446	36447	36448	36449	36450	36451
Owner	CSMIP	CSMIP	CSMIP	CSMIP	CSMIP	CSMIP	CSMIP	CSMIP
Station location and name	Parkfield – Fault Zone 9	Parkfield – Fault Zone 15	Parkfield – Vineyard Canyon 4W	Parkfield – Vineyard Canyon 2W	Parkfield – Vineyard Canyon 1W	Parkfield – Fault Zone 8	Parkfield – Cholame 3E	Parkfield – Cholame 6W
Location parameters								
Latitude [deg]	35.879	35.921	35.905	35.927	35.934	35.878	35.770	35.684
Longitude [deg]	–120.445	–120.481	–120.550	–120.509	–120.497	–120.381	–120.247	–120.342
Elevation [m]	480	602	585	572	591	464	455	330
Epicentral distance, R_{EPI} [km]	9.57	15.23	18.78	17.41	17.26	7.02	12.52	14.82
Hypocentral distance, R_{HYP} [km]	12.47	17.25	20.45	19.20	19.07	10.63	14.84	16.77
Joyner-Boore distance, R_{JB} [km]	0.00	0.00	4.48	0.09	0.00	2.27	8.24	11.16
Rupture distance, R_{RUP} [km]	2.00	1.38	7.12	2.79	1.49	2.28	8.24	12.86
Site coordinate, R_X [km]	1.99	1.33	7.17	2.78	1.46	–2.27	–3.42	9.34
Seismogenic distance, R_{SEIS} [km]	3.43	3.32	7.39	3.92	3.34	4.15	9.00	12.93
Source-to-site azimuth, α [deg]	90.00	90.00	90.00	90.00	90.00	–90.00	–24.52	46.18
Hanging wall indicator, F_{HW}	1	1	1	1	1	0	0	1
Site parameters								
Geologic symbol	QT	Tsh	Tsh	Qal, thin	Tsh	Tsh	Tsh	Qal, thin
V_{S30} [m/sec]	373.71	305.83	390.58	411.21	290.03	323.45	386.52	263.06
V_{S30} data measured (0) or inferred (1)	0	0	0	0	0	0	0	0
$Z_{1.0}$ [m] (if available)	140	–	100	–	–	40	100	–
$Z_{1.5}$ [m] (if available)	–	–	–	–	–	–	–	–
Site class dummy variable, S (AS97, SCE97)	0	1	0	0	1	0	0	1
Soft rock dummy variable, S_{SR} (C97)	1	0	1	1	1	1	1	0
Hard rock dummy variable, S_{HR} (C97)	0	0	0	0	0	0	0	0

Table B.1 Continued. Explanatory variables for the Parkfield earthquake (Page 6 of 11)

	41	42	43	44	45	46	47	48
Station information								
Station number / code	36452	36453	36454	36455	36456	36510	36518	36519
Owner	CSMIP	CSMIP	CSMIP	CSMIP	CSMIP	CSMIP	CSMIP	CSMIP
Station location and name	Parkfield – Cholame 1E	Parkfield – Fault Zone 11	Parkfield – Fault Zone 6	Parkfield – Vineyard Canyon 1E	Parkfield – Fault Zone 14	Parkfield – Temblor	Parkfield – Turkey Flat 4	Parkfield – Turkey Flat 3
Location parameters								
Latitude [deg]	35.743	35.896	35.859	35.957	35.908	35.705	35.892	35.886
Longitude [deg]	–120.277	–120.398	–120.420	–120.484	–120.458	–120.169	–120.352	–120.350
Elevation [m]	349	508	450	552	509	397	571	516
Epicentral distance, R_{EPI} [km]	11.87	9.25	6.41	18.63	12.81	22.20	8.77	8.17
Hypocentral distance, R_{HYP} [km]	14.24	12.24	10.23	20.30	15.12	23.57	11.93	11.46
Joyner-Boore distance, R_{JB} [km]	7.95	2.44	0.00	1.11	0.00	18.01	5.26	4.96
Rupture distance, R_{RUP} [km]	7.97	2.45	1.77	1.15	0.77	18.02	5.27	4.96
Site coordinate, R_X [km]	0.60	–2.44	1.77	–1.11	0.73	–3.95	–5.26	–4.96
Seismogenic distance, R_{SEIS} [km]	8.48	4.29	3.31	3.56	3.13	18.38	6.59	6.30
Source-to-site azimuth, α [deg]	4.30	–90.00	90.00	–90.00	90.00	–12.66	–90.00	–90.00
Hanging wall indicator, F_{HW}	1	0	1	0	1	0	0	0
Site parameters								
Geologic symbol	Qal, thin	Tsh	QT	Qal, thin	Qal, thin	serpentine	Tss	Qoa
V_{S30} [m/sec]	188.81	531.10	266.11	385.25	248.73	641.00	1276.26	605.34
V_{S30} data measured (0) or inferred (1)	0	0	0	0	0	1	0	0
$Z_{1.0}$ [m] (if available)	60	120	–	–	–	–	–	–
$Z_{1.5}$ [m] (if available)	–	–	–	–	–	–	–	–
Site class dummy variable, S (AS97, SCE97)	1	1	0	1	1	0	0	0
Soft rock dummy variable, S_{SR} (C97)	0	1	0	1	0	0	1	0
Hard rock dummy variable, S_{HR} (C97)	0	0	0	0	0	1	0	0

Table B.1 Continued. Explanatory variables for the Parkfield earthquake (Page 7 of 11)

	49	50	51	52	53	54	55	56
Station information								
Station number / code	36520	36529	36531	36535	36712	37737	46174	46175
Owner	CSMIP	CSMIP	CSMIP	CSMIP	CSMIP	CSMIP	CSMIP	CSMIP
Station location and name	Parkfield – Turkey Flat 2	Parkfield – Turkey Flat 1	Parkfield – 1-Story School Building	Shandon – 1-Story High School Bldg.	Templeton – Hospital Grounds	Cambria – Hwy 1 Caltrans Bridge Grnds	Coalinga – Priest Valley	Coalinga – Slack Canyon
Location parameters								
Latitude [deg]	35.882	35.878	35.898	35.655	35.556	35.593	36.191	36.034
Longitude [deg]	–120.350	–120.358	–120.431	–120.377	–120.720	–121.124	–120.708	–120.590
Elevation [m]	505	491	465	316	264	7	702	776
Epicentral distance, R_{EPI} [km]	7.75	7.14	10.55	17.76	42.51	72.21	51.46	31.16
Hypocentral distance, R_{HYP} [km]	11.15	10.73	13.23	19.41	43.22	72.60	52.12	32.24
Joyner-Boore distance, R_{JB} [km]	4.66	3.83	0.36	14.51	41.70	66.27	21.30	0.97
Rupture distance, R_{RUP} [km]	4.67	3.83	0.41	16.50	43.72	67.87	21.31	1.16
Site coordinate, R_X [km]	–4.66	–3.83	–0.36	13.85	44.40	68.96	–3.25	0.37
Seismogenic distance, R_{SEIS} [km]	6.04	5.33	3.20	16.51	43.72	67.87	21.64	3.53
Source-to-site azimuth, α [deg]	–90.00	–90.00	–90.00	56.17	90.00	90.00	–171.21	158.97
Hanging wall indicator, F_{HW}	0	0	0	1	1	1	0	1
Site parameters								
Geologic symbol	Qoa	Tss	Qal, thin	Qoa	QT	Qal, thin	Qal, thin	Kgr
V_{S30} [m/sec]	475.60	877.37	266.25	370.79	438.34	338.54	338.54	684.94
V_{S30} data measured (0) or inferred (1)	0	0	0	1	1	1	1	1
$Z_{1.0}$ [m] (if available)	40	–	–	–	–	–	–	–
$Z_{1.5}$ [m] (if available)	–	–	–	–	–	–	–	–
Site class dummy variable, S (AS97, SCE97)	1	0	1	1	1	1	1	0
Soft rock dummy variable, S_{SR} (C97)	0	1	0	0	0	0	0	0
Hard rock dummy variable, S_{HR} (C97)	0	0	0	0	0	0	0	1

Table B.1 Continued. Explanatory variables for the Parkfield earthquake (Page 8 of 11)

	57	58	59	60	61	62	63	64
Station information								
Station number / code	47231	47232	47236	47460	61022	DFU	EFU	FFU
Owner	CSMIP	CSMIP	CSMIP	CSMIP	BDSN	USGS	USGS	USGS
Station location and name	King City – 2-Story Hospital	King City – Canal & Reich	San Benito – Bear Valley CDF	Greenfield – Police Station	Parkfield – Bear Valley Ranch	Parkfield – Donna Lee	Parkfield – Eades	Parkfield – Froelich
Location parameters								
Latitude [deg]	36.206	36.207	36.572	36.321	35.945	35.9392	35.8942	35.9111
Longitude [deg]	–121.132	–121.131	–121.184	–121.243	–120.542	–120.4245	–120.4212	–120.4855
Elevation [m]	91	91	444	85	583	517	498	546
Epicentral distance, R_{EPI} [km]	80.95	80.94	111.20	96.35	20.94	14.52	9.77	14.67
Hypocentral distance, R_{HYP} [km]	81.31	81.29	111.49	96.64	22.45	16.59	12.64	16.74
Joyner-Boore distance, R_{JB} [km]	52.27	52.24	81.04	67.00	1.00	3.83	0.74	0.00
Rupture distance, R_{RUP} [km]	53.25	53.21	81.04	67.73	3.69	3.83	0.78	2.38
Site coordinate, R_X [km]	24.08	23.94	0.43	22.97	3.69	–3.83	–0.74	2.37
Seismogenic distance, R_{SEIS} [km]	53.25	53.21	81.10	67.73	4.51	5.35	3.35	3.67
Source-to-site azimuth, α [deg]	153.22	153.36	179.70	160.21	90.00	–90.00	–90.00	90.00
Hanging wall indicator, F_{HW}	1	1	1	1	1	0	0	1
Site parameters								
Geologic symbol	Qal, thin	Qal, thin	QT	Qal, deep	Tsh	Qal, thin	Qal, thin	Qal, thin
V_{S30} [m/sec]	338.54	338.54	438.34	271.44	376.07	679.78	382.11	235.64
V_{S30} data measured (0) or inferred (1)	1	1	1	1	1	0	0	0
$Z_{1.0}$ [m] (if available)	–	–	–	–	–	15	–	–
$Z_{1.5}$ [m] (if available)	–	–	–	–	–	–	–	–
Site class dummy variable, S (AS97, SCE97)	1	1	1	1	0	0	1	1
Soft rock dummy variable, S_{SR} (C97)	0	0	0	0	1	0	0	0
Hard rock dummy variable, S_{HR} (C97)	0	0	0	0	0	0	0	0

Table B.1 Continued. Explanatory variables for the Parkfield earthquake (Page 9 of 11)

	65	66	67	68	69	70	71
Station information							
Station number / code	GFU	JFU	KFU	MFU	PHOB	RFU	SFU
Owner	USGS	USGS	USGS	USGS	NCSN	USGS	USGS
Station location and name	Parkfield – Gold Hill	Parkfield – Joaquin Canyon	Parkfield – Jack Canyon	Parkfield – Middle Mountain	Hog Canyon	Parkfield – Red Hills	Parkfield – Stockdale Mtn
Location parameters							
Latitude [deg]	35.8331	35.9397	35.7125	35.9576	35.8666	35.6244	35.973
Longitude [deg]	–120.3464	–120.4319	–120.2025	–120.4956	–120.480	–120.2535	–120.5786
Elevation [m]	424	546	477	719	796	578	728
Epicentral distance, R_{EPI} [km]	3.20	14.80	19.24	19.26	11.13	23.80	25.47
Hypocentral distance, R_{HYP} [km]	8.56	16.85	20.83	20.95	13.89	25.14	26.77
Joyner-Boore distance, R_{JB} [km]	1.31	3.36	15.11	0.37	2.55	19.87	1.41
Rupture distance, R_{RUP} [km]	1.32	3.37	15.11	0.59	5.25	20.70	4.12
Site coordinate, R_X [km]	–1.31	–3.36	–2.22	–0.37	5.24	7.71	4.10
Seismogenic distance, R_{SEIS} [km]	3.54	5.00	15.51	3.45	5.83	20.78	4.90
Source-to-site azimuth, α [deg]	–90.00	–90.00	–8.46	–90.00	90.00	21.84	90.00
Hanging wall indicator, F_{HW}	0	0	0	0	1	1	1
Site parameters							
Geologic symbol	Tv	Qal, thin	Tsh	Qal, thin	QT	QT	Tsh
V_{S30} [m/sec]	578.50	384.99	575.04	428.35	438.34	239.44	376.07
V_{S30} data measured (0) or inferred (1)	0	0	0	0	1	0	1
$Z_{1.0}$ [m] (if available)	15	–	20	40	–	–	–
$Z_{1.5}$ [m] (if available)	55	–	80	–	–	–	–
Site class dummy variable, S (AS97, SCE97)	0	1	0	1	1	1	0
Soft rock dummy variable, S_{SR} (C97)	1	0	1	0	0	0	1
Hard rock dummy variable, S_{HR} (C97)	0	0	0	0	0	0	0

Table B.1 Continued. Explanatory variables for the Parkfield earthquake (Page 10 of 11)

	72	73	74	75	76	77	78
Station information							
Station number / code	UPSAR01	UPSAR02	UPSAR03	UPSAR05	UPSAR06	UPSAR07	UPSAR08
Owner	USGS	USGS	USGS	USGS	USGS	USGS	USGS
Station location and name	Parkfield – USGS Parkfield Dense Seismograph Array 01	Parkfield – USGS Parkfield Dense Seismograph Array 02	Parkfield – USGS Parkfield Dense Seismograph Array 03	Parkfield – USGS Parkfield Dense Seismograph Array 05	Parkfield – USGS Parkfield Dense Seismograph Array 06	Parkfield – USGS Parkfield Dense Seismograph Array 07	Parkfield – USGS Parkfield Dense Seismograph Array 08
Location parameters							
Latitude [deg]	35.8212	35.8221	35.8214	35.8238	35.8239	35.8238	35.8248
Longitude [deg]	–120.5072	–120.5064	–120.5052	–120.5033	–120.5031	–120.5028	–120.5011
Elevation [m]	576	577	585	597	601	603	619
Epicentral distance, R_{EPI} [km]	12.06	11.99	11.88	11.73	11.71	11.68	11.54
Hypocentral distance, R_{HYP} [km]	14.52	14.47	14.38	14.26	14.25	14.23	14.12
Joyner-Boore distance, R_{JB} [km]	7.76	7.64	7.61	7.30	7.28	7.27	7.08
Rupture distance, R_{RUP} [km]	10.34	10.23	10.20	9.90	9.88	9.87	9.68
Site coordinate, R_X [km]	10.45	10.33	10.30	9.99	9.97	9.96	9.77
Seismogenic distance, R_{SEIS} [km]	10.44	10.33	10.30	10.01	10.00	9.98	9.81
Source-to-site azimuth, α [deg]	90.00	90.00	90.00	90.00	90.00	90.00	90.00
Hanging wall indicator, F_{HW}	1	1	1	1	1	1	1
Site parameters							
Geologic symbol	QT	QT	QT	QT	QT	QT	QT
V_{S30} [m/sec]	438.34	438.34	360.55	438.34	438.34	427.14	438.34
V_{S30} data measured (0) or inferred (1)	1	1	0	1	1	0	1
$Z_{1.0}$ [m] (if available)	–	–	–	–	–	–	–
$Z_{1.5}$ [m] (if available)	–	–	–	–	–	–	–
Site class dummy variable, S (AS97, SCE97)	1	1	1	1	1	1	1
Soft rock dummy variable, S_{SR} (C97)	0	0	0	0	0	0	0
Hard rock dummy variable, S_{HR} (C97)	0	0	0	0	0	0	0

Table B.1 Continued. Explanatory variables for the Parkfield earthquake (Page 11 of 11)

	79	80	81	82	83	84	85
Station information							
Station number / code	UPSAR09	UPSAR10	UPSAR11	UPSAR12	UPSAR13	VFU	WFU
Owner	USGS	USGS	USGS	USGS	USGS	USGS	USGS
Station location and name	Parkfield – USGS Parkfield Dense Seismograph Array 09	Parkfield – USGS Parkfield Dense Seismograph Array 10	Parkfield – USGS Parkfield Dense Seismograph Array 11	Parkfield – USGS Parkfield Dense Seismograph Array 12	Parkfield – USGS Parkfield Dense Seismograph Array 13	Parkfield – Vineyard Canyon	Parkfield – Work Ranch
Location parameters							
Latitude [deg]	35.826	35.8276	35.8258	35.8269	35.8274	35.9225	35.8145
Longitude [deg]	–120.5007	–120.500	–120.502	–120.5039	–120.5045	–120.5342	–120.5111
Elevation [m]	613	604	600	585	597	786	503
Epicentral distance, R_{EPI} [km]	11.52	11.49	11.63	11.82	11.88	18.76	12.39
Hypocentral distance, R_{HYP} [km]	14.10	14.07	14.18	14.33	14.38	20.51	14.76
Joyner-Boore distance, R_{JB} [km]	6.96	6.81	7.07	7.11	7.12	2.13	8.51
Rupture distance, R_{RUP} [km]	9.57	9.42	9.67	9.71	9.72	4.83	11.08
Site coordinate, R_X [km]	9.66	9.50	9.76	9.81	9.81	4.82	11.21
Seismogenic distance, R_{SEIS} [km]	9.70	9.55	9.79	9.83	9.84	5.49	11.14
Source-to-site azimuth, α [deg]	90.00	90.00	90.00	90.00	90.00	90.00	90.00
Hanging wall indicator, F_{HW}	1	1	1	1	1	1	1
Site parameters							
Geologic symbol	QT	QT	QT	QT	QT	Tsh	QT
V_{S30} [m/sec]	438.34	338.16	438.34	438.34	438.34	307.85	440.66
V_{S30} data measured (0) or inferred (1)	1	0	1	1	1	0	0
$Z_{1.0}$ [m] (if available)	–	–	–	–	–	–	–
$Z_{1.5}$ [m] (if available)	–	–	–	–	–	–	–
Site class dummy variable, S (AS97, SCE97)	1	1	1	1	1	0	1
Soft rock dummy variable, S_{SR} (C97)	0	0	0	0	0	1	0
Hard rock dummy variable, S_{HR} (C97)	0	0	0	0	0	0	0

Table B.2. Explanatory variables for the San Simeon earthquake

	1	2	3	4	5	6	7	8
Station information								
Station number / code	1083	1747	36153	36427	36695	37737	47460	61022
Owner	USGS	USGS	CSMIP	CSMIP	CSMIP	CSMIP	CSMIP	BDSN
Station location and name	San Luis Obispo – Rec Center	Coalinga – Fire Station 39	San Luis Obispo – Lopez Lake Grounds	Point Buchon – Los Osos	Templeton – 1 Story Hospital	Cambria – Hwy 1 Caltrans Bridge Grnds	Greenfield – Police Station	Parkfield – Bear Valley Ranch
Location parameters								
Latitude [deg]	35.285	36.137	35.208	35.274	35.556	35.593	36.321	35.945
Longitude [deg]	−120.661	−120.363	−120.457	−120.885	−120.719	−121.124	−121.243	−120.542
Elevation [m]	52	89	168	25	264	7	85	583
Epicentral distance, R_{EPI} [km]	61.51	82.08	80.51	51.82	38.48	12.69	69.41	57.13
Hypocentral distance, R_{HYP} [km]	61.98	82.43	80.87	52.37	39.22	14.80	69.82	57.64
Joyner-Boore distance, R_{JB} [km]	27.83	69.94	46.34	25.30	4.26	6.37	57.17	43.24
Rupture distance, R_{RUP} [km]	27.83	72.28	46.34	25.30	9.97	6.37	60.01	46.93
Site coordinate, R_X [km]	−10.99	82.24	−7.54	−23.48	10.87	−6.37	54.52	55.54
Seismogenic distance, R_{SEIS} [km]	28.85	72.28	46.81	27.35	9.97	8.92	60.01	46.93
Source-to-site azimuth, α [deg]	−156.75	90.00	−170.64	−111.87	111.40	−90.00	54.74	90.00
Hanging wall indicator, F_{HW}	0	1	0	0	1	0	1	1
Site parameters								
Geologic symbol	KJf	Qal, thin	Tss	QT	QT	Qal, thin	Qal, deep	Tsh
V_{S30} [m/sec] *	712.82	338.54	477.00	438.34	438.34	338.54	271.44	376.07
Site class dummy variable, S (AS97, SCE97)	0	1	0	1	1	1	1	0
Soft rock dummy variable, S_{SR} (C97)	0	0	1	0	0	0	0	1
Hard rock dummy variable, S_{HR} (C97)	1	0	0	0	0	0	0	0
Assumed depth to bedrock, D [km] (C97)	0	5	1	5	5	5	5	1

NOTE:
* All shear wave velocity data for the San Simeon earthquake are inferred from surficial geology. No estimates for the depth parameters ($Z_{1.0}$ and $Z_{2.5}$) are available.

Table B.3. Response variables for the Parkfield earthquake (Page 1 of 11)

	1		2		3		4		5		6		7		8	
Station information																
Station no. / code	1083		1747		35219		36138		36153		36176		36177		36227	
Owner	USGS		USGS		CSMIP		CSMIP		CSMIP		CSMIP		CSMIP		CSMIP	
Station location and name	San Luis Obispo – Rec Center		Coalinga – Fire Station 39		Buttonwillow – Hwy 58 & Wasco		Parkfield – Fault Zone 12		San Luis Obispo – Lopez Lake Grounds		Parkfield – Vineyard Canyon 3W		Parkfield – Vineyard Canyon 2E		Parkfield – Cholame 5W	
Maximum useable period, T_{high} [sec]	10.000		10.000		2.667		6.667		2.667		5.714		5.000		4.000	
Ground motion parameter [g]	GMxy	GMrotI50	GMxy	GMrotI50	GMxy	GMrotI50	GMxy	GMrotI50	GMxy	GMrotI50	GMxy	GMrotI50	GMxy	GMrotI50	GMxy	GMrotI50
PGA	1.188E-2	1.252E-2	5.949E-2	5.877E-2	7.964E-3	7.926E-3	2.894E-1	2.859E-1	1.582E-2	1.735E-2	2.824E-1	3.106E-1	2.868E-1	2.557E-1	2.408E-1	2.412E-1
Sa (T = 0.05 sec)	1.244E-2	1.308E-2	6.217E-2	6.243E-2	8.059E-3	8.057E-3	2.959E-1	2.909E-1	2.045E-2	2.188E-2	4.443E-1	3.737E-1	2.942E-1	2.652E-1	2.586E-1	2.469E-1
Sa (T = 0.075 sec)	1.599E-2	1.682E-2	6.638E-2	7.043E-2	8.127E-3	8.212E-3	3.046E-1	3.112E-1	3.035E-2	2.980E-2	7.030E-1	6.103E-1	3.396E-1	2.964E-1	3.024E-1	3.074E-1
Sa (T = 0.10 sec)	2.249E-2	2.274E-2	8.245E-2	8.870E-2	8.898E-3	9.224E-3	3.273E-1	3.187E-1	4.148E-2	4.634E-2	8.479E-1	8.441E-1	4.684E-1	4.191E-1	4.709E-1	4.608E-1
Sa (T = 0.15 sec)	2.583E-2	2.586E-2	1.535E-1	1.611E-1	1.119E-2	1.299E-2	3.795E-1	3.899E-1	5.714E-2	6.263E-2	7.478E-1	7.610E-1	7.245E-1	7.441E-1	5.796E-1	5.938E-1
Sa (T = 0.20 sec)	2.536E-2	2.569E-2	1.360E-1	1.428E-1	1.682E-2	1.798E-2	4.734E-1	5.022E-1	4.164E-2	3.882E-2	8.199E-1	9.342E-1	6.975E-1	6.908E-1	6.475E-1	6.584E-1
Sa (T = 0.30 sec)	2.884E-2	2.955E-2	1.212E-1	1.131E-1	1.989E-2	1.933E-2	4.020E-1	3.694E-1	2.410E-2	2.060E-2	6.137E-1	6.993E-1	5.591E-1	5.771E-1	3.965E-1	4.114E-1
Sa (T = 0.40 sec)	2.905E-2	2.973E-2	1.477E-1	1.438E-1	1.699E-2	1.768E-2	5.747E-1	5.332E-1	2.334E-2	2.225E-2	4.401E-1	4.580E-1	6.603E-1	6.289E-1	4.341E-1	4.423E-1
Sa (T = 0.50 sec)	2.946E-2	2.856E-2	1.246E-1	1.441E-1	1.839E-2	1.785E-2	5.385E-1	5.258E-1	1.685E-2	1.759E-2	3.852E-1	3.497E-1	4.360E-1	4.287E-1	4.751E-1	4.741E-1
Sa (T = 0.75 sec)	2.346E-2	2.348E-2	1.049E-1	1.116E-1	2.132E-2	2.139E-2	7.692E-1	7.847E-1	1.235E-2	1.198E-2	3.474E-1	3.788E-1	2.839E-1	2.827E-1	3.106E-1	3.015E-1
Sa (T = 1.0 sec)	1.270E-2	1.218E-2	9.547E-2	8.232E-2	1.516E-2	1.549E-2	7.382E-1	6.858E-1	1.054E-2	1.055E-2	2.091E-1	2.222E-1	1.828E-1	1.649E-1	1.503E-1	1.432E-1
Sa (T = 1.5 sec)	4.794E-3	4.719E-3	3.915E-2	4.272E-2	1.501E-2	1.518E-2	3.351E-1	2.906E-1	5.068E-3	4.957E-3	1.425E-1	1.135E-1	1.345E-1	1.337E-1	5.258E-2	5.161E-2
Sa (T = 2.0 sec)	2.837E-3	2.717E-3	3.229E-2	3.243E-2	6.241E-3	6.356E-3	1.784E-1	1.530E-1	2.954E-3	2.860E-3	5.939E-2	6.968E-2	6.190E-2	5.875E-2	2.356E-2	2.391E-2
Sa (T = 3.0 sec)	1.114E-3	1.142E-3	2.423E-2	2.030E-2			6.336E-2	5.952E-2			4.149E-2	3.936E-2	3.314E-2	4.311E-2	1.350E-2	1.226E-2
Sa (T = 4.0 sec)	7.617E-4	7.765E-4	1.241E-2	1.042E-2			3.624E-2	3.118E-2			1.967E-2	2.245E-2	1.741E-2	1.923E-2	8.084E-3	7.550E-3
Sa (T = 5.0 sec)	4.844E-4	4.557E-4	5.028E-3	5.194E-3			2.294E-2	1.914E-2			1.352E-2	1.230E-2	1.009E-2	1.006E-2		
Sa (T = 7.5 sec)	2.099E-4	2.011E-4	2.564E-3	2.982E-3												
Sa (T = 10.0 sec)	1.167E-4	9.853E-5	1.449E-3	1.624E-3												

Table B.3 Continued. Response variables for the Parkfield earthquake (Page 2 of 11)

	9		10		11		12		13		14		15		16	
Station information																
Station no. / code	36228		36229		36230		36407		36408		36410		36411		36412	
Owner	CSMIP		CSMIP		CSMIP		CSMIP		CSMIP		CSMIP		CSMIP		CSMIP	
Station location and name	Parkfield – Cholame 2WA		Parkfield – Cholame 12W		Parkfield – Cholame 2E		Parkfield – Fault Zone 1		Parkfield – Fault Zone 3		Parkfield – Cholame 3W		Parkfield – Cholame 4W		Parkfield – Cholame 4AW	
Maximum useable period, T_{high} [sec]	5.714		4.000		5.000		5.714		6.667		5.714		5.000		5.000	
Ground motion parameter [g]	GMxy	GMrotI50	GMxy	GMrotI50	GMxy	GMrotI50	GMxy	GMrotI50	GMxy	GMrotI50	GMxy	GMrotI50	GMxy	GMrotI50	GMxy	GMrotI50
PGA	4.726E-1	4.838E-1	7.990E-2	8.589E-2	4.690E-1	4.451E-1	6.963E-1	6.902E-1	3.801E-1	3.625E-1	4.255E-1	4.024E-1	5.438E-1	5.235E-1	2.892E-1	2.735E-1
Sa (T = 0.05 sec)	4.916E-1	4.830E-1	1.111E-1	1.061E-1	6.053E-1	4.815E-1	7.470E-1	7.163E-1	4.215E-1	3.972E-1	4.564E-1	4.129E-1	5.607E-1	5.439E-1	3.007E-1	2.777E-1
Sa (T = 0.075 sec)	6.963E-1	7.094E-1	1.837E-1	1.585E-1	6.587E-1	6.120E-1	8.825E-1	8.700E-1	6.365E-1	6.458E-1	5.525E-1	4.555E-1	5.887E-1	6.222E-1	3.507E-1	3.286E-1
Sa (T = 0.10 sec)	6.327E-1	6.652E-1	2.045E-1	1.780E-1	7.579E-1	7.325E-1	1.099E+0	1.083E+0	8.695E-1	9.061E-1	7.406E-1	6.083E-1	5.947E-1	6.189E-1	5.610E-1	5.757E-1
Sa (T = 0.15 sec)	5.987E-1	5.695E-1	1.800E-1	1.847E-1	1.834E+0	1.578E+0	8.510E-1	8.366E-1	1.059E+0	9.390E-1	8.313E-1	6.794E-1	7.172E-1	7.576E-1	5.950E-1	5.725E-1
Sa (T = 0.20 sec)	7.782E-1	7.300E-1	1.505E-1	1.591E-1	1.590E+0	1.590E+0	9.222E-1	9.008E-1	9.860E-1	9.113E-1	6.849E-1	7.215E-1	9.972E-1	1.004E+0	7.363E-1	7.523E-1
Sa (T = 0.30 sec)	1.040E+0	9.600E-1	1.171E-1	1.312E-1	7.533E-1	6.319E-1	1.059E+0	1.044E+0	8.903E-1	8.426E-1	6.771E-1	6.248E-1	9.284E-1	9.250E-1	5.471E-1	5.340E-1
Sa (T = 0.40 sec)	8.929E-1	9.880E-1	9.988E-2	1.131E-1	4.711E-1	4.896E-1	1.557E+0	1.539E+0	8.030E-1	7.565E-1	7.083E-1	7.349E-1	9.126E-1	8.625E-1	5.699E-1	5.548E-1
Sa (T = 0.50 sec)	9.653E-1	1.065E+0	9.729E-2	1.051E-1	2.647E-1	2.907E-1	1.054E+0	1.064E+0	7.755E-1	8.422E-1	6.611E-1	5.801E-1	8.053E-1	7.167E-1	4.915E-1	5.056E-1
Sa (T = 0.75 sec)	9.151E-1	9.502E-1	8.102E-2	8.523E-2	2.722E-1	2.428E-1	9.737E-1	9.852E-1	2.877E-1	2.812E-1	5.374E-1	5.483E-1	4.775E-1	4.309E-1	2.790E-1	2.637E-1
Sa (T = 1.0 sec)	5.799E-1	6.361E-1	5.898E-2	5.454E-2	1.541E-1	1.634E-1	8.649E-1	8.508E-1	2.126E-1	2.080E-1	3.436E-1	3.490E-1	2.541E-1	1.992E-1	2.074E-1	1.861E-1
Sa (T = 1.5 sec)	2.774E-1	2.521E-1	3.992E-2	4.240E-2	7.106E-2	7.513E-2	3.937E-1	3.892E-1	1.259E-1	1.226E-1	1.506E-1	1.320E-1	1.049E-1	8.552E-2	9.364E-2	8.171E-2
Sa (T = 2.0 sec)	1.628E-1	1.422E-1	2.425E-2	2.366E-2	4.103E-2	4.095E-2	2.127E-1	2.120E-1	4.209E-2	4.507E-2	7.512E-2	6.442E-2	5.904E-2	5.519E-2	5.280E-2	4.515E-2
Sa (T = 3.0 sec)	5.078E-2	5.206E-2	6.929E-3	6.819E-3	1.691E-2	1.418E-2	8.251E-2	7.846E-2	2.175E-2	2.266E-2	3.297E-2	2.526E-2	2.802E-2	2.451E-2	1.984E-2	1.769E-2
Sa (T = 4.0 sec)	2.898E-2	2.809E-2	5.519E-3	5.363E-3	1.033E-2	8.159E-3	3.777E-2	3.728E-2	1.282E-2	1.071E-2	2.006E-2	1.459E-2	1.590E-2	1.336E-2	1.287E-2	1.111E-2
Sa (T = 5.0 sec)	1.994E-2	1.857E-2			6.653E-3	5.516E-3	2.177E-2	2.103E-2	7.281E-3	6.536E-3	1.351E-2	9.400E-3	1.032E-2	7.910E-3	9.085E-3	7.974E-3
Sa (T = 7.5 sec)																
Sa (T = 10.0 sec)																

Table B.3 Continued. Response variables for the Parkfield earthquake (Page 3 of 11)

	17		18		19		20		21		22		23		24	
Station information																
Station no. / code	36414		36415		36416		36419		36420		36421		36422		36427	
Owner	CSMIP		CSMIP		CSMIP		CSMIP		CSMIP		CSMIP		CSMIP		CSMIP	
Station location and name	Parkfield – Fault Zone 4		Parkfield – Gold Hill 1W		Parkfield – Gold Hill 2W		Parkfield – Stone Corral 1E		Parkfield – Gold Hill 3W		Parkfield – Gold Hill 2E		Parkfield – Stone Corral 2E		Point Buchon – Los Osos	
Maximum useable period, T_{high} [sec]	5.000		5.000		4.000		5.714		5.714		5.000		5.000		2.667	
Ground motion parameter [g]	GMxy	GMrotI50	GMxy	GMrotI50	GMxy	GMrotI50	GMxy	GMrotI50	GMxy	GMrotI50	GMxy	GMrotI50	GMxy	GMrotI50	GMxy	GMrotI50
PGA	1.191E-1	1.180E-1	1.452E-1	1.327E-1	2.080E-1	2.164E-1	7.402E-1	7.842E-1	5.319E-1	5.538E-1	1.838E-1	2.008E-1	1.821E-1	1.712E-1	1.155E-2	1.175E-2
Sa (T = 0.05 sec)	1.332E-1	1.285E-1	1.915E-1	1.689E-1	2.553E-1	2.524E-1	1.011E+0	9.928E-1	6.618E-1	5.953E-1	2.860E-1	2.171E-1	2.614E-1	2.457E-1	1.306E-2	1.247E-2
Sa (T = 0.075 sec)	1.565E-1	1.535E-1	3.117E-1	3.014E-1	4.723E-1	4.769E-1	9.977E-1	1.014E+0	7.940E-1	8.376E-1	4.370E-1	3.730E-1	4.031E-1	3.134E-1	1.728E-2	1.787E-2
Sa (T = 0.10 sec)	1.519E-1	1.575E-1	2.637E-1	2.513E-1	6.418E-1	6.254E-1	1.235E+0	1.204E+0	1.034E+0	1.052E+0	4.183E-1	4.244E-1	5.554E-1	5.247E-1	2.992E-2	2.981E-2
Sa (T = 0.15 sec)	1.790E-1	1.786E-1	1.944E-1	1.962E-1	4.041E-1	4.155E-1	1.459E+0	1.274E+0	1.238E+0	1.165E+0	2.794E-1	2.897E-1	6.879E-1	5.152E-1	4.706E-2	4.751E-2
Sa (T = 0.20 sec)	1.951E-1	2.034E-1	1.753E-1	1.956E-1	4.674E-1	4.652E-1	1.575E+0	1.316E+0	9.893E-1	1.066E+0	3.693E-1	3.436E-1	2.935E-1	2.844E-1	2.774E-2	2.358E-2
Sa (T = 0.30 sec)	2.229E-1	2.141E-1	1.967E-1	1.912E-1	3.516E-1	3.522E-1	1.169E+0	1.027E+0	4.357E-1	4.392E-1	2.824E-1	3.076E-1	2.387E-1	2.652E-1	2.023E-2	1.891E-2
Sa (T = 0.40 sec)	2.726E-1	2.746E-1	2.306E-1	2.251E-1	2.744E-1	2.640E-1	9.945E-1	7.831E-1	4.197E-1	4.809E-1	3.705E-1	4.604E-1	2.415E-1	2.439E-1	1.984E-2	1.795E-2
Sa (T = 0.50 sec)	3.193E-1	3.363E-1	2.350E-1	2.342E-1	2.415E-1	2.391E-1	9.164E-1	7.826E-1	3.100E-1	3.911E-1	3.300E-1	2.943E-1	1.786E-1	1.656E-1	2.376E-2	2.479E-2
Sa (T = 0.75 sec)	3.177E-1	2.933E-1	1.768E-1	1.640E-1	1.174E-1	1.154E-1	5.025E-1	5.284E-1	1.596E-1	1.559E-1	9.700E-2	9.412E-2	1.025E-1	1.107E-1	1.491E-2	1.342E-2
Sa (T = 1.0 sec)	1.999E-1	1.953E-1	1.162E-1	1.271E-1	8.818E-2	8.608E-2	3.022E-1	2.702E-1	1.239E-1	1.046E-1	5.316E-2	4.703E-2	1.011E-1	1.118E-1	1.199E-2	1.221E-2
Sa (T = 1.5 sec)	7.085E-2	7.002E-2	5.080E-2	5.327E-2	4.724E-2	4.645E-2	1.248E-1	1.164E-1	5.689E-2	4.971E-2	2.171E-2	2.235E-2	7.749E-2	7.622E-2	7.464E-3	7.063E-3
Sa (T = 2.0 sec)	4.888E-2	5.101E-2	3.543E-2	3.256E-2	3.453E-2	3.393E-2	6.697E-2	5.511E-2	3.250E-2	2.512E-2	1.533E-2	1.505E-2	3.521E-2	3.533E-2	3.584E-3	4.096E-3
Sa (T = 3.0 sec)	1.889E-2	1.881E-2	1.780E-2	1.706E-2	1.696E-2	1.658E-2	2.917E-2	2.321E-2	1.951E-2	1.584E-2	1.170E-2	1.039E-2	1.154E-2	1.164E-2		
Sa (T = 4.0 sec)	1.013E-2	1.071E-2	1.070E-2	9.986E-3	8.494E-3	8.385E-3	1.637E-2	1.335E-2	1.220E-2	1.071E-2	7.271E-3	6.742E-3	6.635E-3	6.283E-3		
Sa (T = 5.0 sec)	5.202E-3	5.310E-3	6.407E-3	6.623E-3			1.083E-2	8.848E-3	9.961E-3	8.921E-3	5.264E-3	4.420E-3	4.393E-3	3.681E-3		
Sa (T = 7.5 sec)																
Sa (T = 10.0 sec)																

Table B.3 Continued. Response variables for the Parkfield earthquake (Page 4 of 11)

	25		26		27		28		29		30		31		32	
Station information																
Station no. / code	36431		36432		36433		36434		36437		36439		36440		36441	
Owner	CSMIP		CSMIP		CSMIP		CSMIP		CSMIP		CSMIP		CSMIP		CSMIP	
Station location and name	Parkfield – Fault Zone 7		Parkfield – Gold Hill 6W		Parkfield – Gold Hill 4W		Parkfield – Gold Hill 5W		Parkfield – Stone Corral 3E		Parkfield – Gold Hill 3E		Parkfield – Vineyard Canyon 5W		Parkfield – Vineyard Canyon 6W	
Maximum useable period, T_{high} [sec]	5.714		3.333		4.000		5.000		5.000		5.000		5.000		5.000	
Ground motion parameter [g]	GMxy	GMrotI50	GMxy	GMrotI50	GMxy	GMrotI50	GMxy	GMrotI50	GMxy	GMrotI50	GMxy	GMrotI50	GMxy	GMrotI50	GMxy	GMrotI50
PGA	2.408E-1	2.382E-1	1.023E-1	1.031E-1	3.458E-1	3.533E-1	2.075E-1	2.095E-1	1.952E-1	1.990E-1	1.460E-1	1.593E-1	1.696E-1	1.669E-1	1.068E-1	1.083E-1
Sa (T = 0.05 sec)	2.740E-1	2.606E-1	1.190E-1	1.098E-1	6.309E-1	5.226E-1	3.316E-1	2.765E-1	2.279E-1	2.357E-1	2.064E-1	2.053E-1	2.016E-1	1.852E-1	1.185E-1	1.305E-1
Sa (T = 0.075 sec)	4.619E-1	3.983E-1	2.109E-1	1.939E-1	1.075E+0	9.854E-1	4.549E-1	4.932E-1	4.147E-1	3.855E-1	2.717E-1	3.343E-1	2.868E-1	3.060E-1	2.108E-1	2.396E-1
Sa (T = 0.10 sec)	5.547E-1	5.001E-1	2.145E-1	1.998E-1	1.112E+0	1.071E+0	4.334E-1	4.297E-1	4.925E-1	4.542E-1	3.166E-1	3.280E-1	4.006E-1	3.640E-1	3.558E-1	3.130E-1
Sa (T = 0.15 sec)	6.015E-1	5.025E-1	1.799E-1	1.681E-1	6.152E-1	6.672E-1	4.724E-1	4.487E-1	6.385E-1	6.029E-1	3.500E-1	3.868E-1	4.853E-1	4.790E-1	3.195E-1	3.333E-1
Sa (T = 0.20 sec)	4.443E-1	4.867E-1	2.541E-1	2.498E-1	6.583E-1	5.896E-1	3.777E-1	3.733E-1	3.983E-1	3.677E-1	3.569E-1	3.439E-1	3.305E-1	3.326E-1	2.747E-1	2.836E-1
Sa (T = 0.30 sec)	5.312E-1	5.313E-1	2.358E-1	2.289E-1	2.715E-1	2.715E-1	3.748E-1	4.432E-1	2.440E-1	2.405E-1	2.365E-1	2.565E-1	3.778E-1	3.903E-1	1.902E-1	2.032E-1
Sa (T = 0.40 sec)	6.126E-1	6.408E-1	1.347E-1	1.280E-1	1.397E-1	1.314E-1	2.686E-1	2.694E-1	1.688E-1	1.698E-1	2.525E-1	3.052E-1	1.959E-1	1.968E-1	2.218E-1	2.116E-1
Sa (T = 0.50 sec)	6.440E-1	6.470E-1	7.902E-2	7.906E-2	1.072E-1	1.158E-1	1.672E-1	1.612E-1	1.000E-1	9.722E-2	1.670E-1	1.781E-1	2.134E-1	2.063E-1	1.505E-1	1.500E-1
Sa (T = 0.75 sec)	3.730E-1	3.768E-1	3.953E-2	3.939E-2	9.604E-2	1.101E-1	8.760E-2	8.937E-2	1.010E-1	9.353E-2	1.423E-1	1.191E-1	2.503E-1	2.312E-1	1.159E-1	1.093E-1
Sa (T = 1.0 sec)	2.758E-1	2.607E-1	3.064E-2	2.938E-2	6.060E-2	5.962E-2	7.861E-2	7.532E-2	1.204E-1	1.105E-1	6.028E-2	5.327E-2	1.179E-1	1.072E-1	9.441E-2	9.054E-2
Sa (T = 1.5 sec)	1.375E-1	1.321E-1	1.699E-2	1.620E-2	2.554E-2	2.504E-2	2.735E-2	2.803E-2	7.611E-2	6.761E-2	2.528E-2	2.392E-2	6.540E-2	7.131E-2	4.924E-2	4.977E-2
Sa (T = 2.0 sec)	7.873E-2	7.433E-2	1.263E-2	1.206E-2	2.598E-2	2.436E-2	2.379E-2	2.238E-2	4.198E-2	3.443E-2	2.175E-2	1.870E-2	4.329E-2	4.073E-2	3.374E-2	3.448E-2
Sa (T = 3.0 sec)	3.024E-2	2.926E-2	8.860E-3	8.617E-3	1.754E-2	1.626E-2	1.220E-2	1.169E-2	1.519E-2	1.220E-2	1.593E-2	1.398E-2	2.259E-2	2.460E-2	1.800E-2	1.736E-2
Sa (T = 4.0 sec)	1.639E-2	1.382E-2			8.920E-3	8.255E-3	7.233E-3	7.165E-3	8.467E-3	6.944E-3	9.935E-3	9.142E-3	1.999E-2	1.752E-2	1.843E-2	1.730E-2
Sa (T = 5.0 sec)	1.002E-2	8.283E-3					4.275E-3	4.300E-3	5.593E-3	4.740E-3	5.841E-3	4.915E-3	1.038E-2	9.344E-3	1.430E-2	1.078E-2
Sa (T = 7.5 sec)																
Sa (T = 10.0 sec)																

Table B.3 Continued. Response variables for the Parkfield earthquake (Page 5 of 11)

	33		34		35		36		37		38		39		40	
Station information																
Station no. / code	36443		36445		36446		36447		36448		36449		36450		36451	
Owner	CSMIP		CSMIP		CSMIP		CSMIP		CSMIP		CSMIP		CSMIP		CSMIP	
Station location and name	Parkfield – Fault Zone 9		Parkfield – Fault Zone 15		Parkfield – Vineyard Canyon 4W		Parkfield – Vineyard Canyon 2W		Parkfield – Vineyard Canyon 1W		Parkfield – Fault Zone 8		Parkfield – Cholame 3E		Parkfield – Cholame 6W	
Maximum useable period, T_{high} [sec]	5.714		6.667		5.714		5.714		6.667		5.000		5.000		4.000	
Ground motion parameter [g]	GMxy	GMrotI50	GMxy	GMrotI50	GMxy	GMrotI50	GMxy	GMrotI50	GMxy	GMrotI50	GMxy	GMrotI50	GMxy	GMrotI50	GMxy	GMrotI50
PGA	1.203E-1	1.254E-1	1.798E-1	2.045E-1	9.388E-2	1.060E-1	4.450E-1	4.278E-1	1.484E-1	1.483E-1	5.208E-1	4.720E-1	6.198E-1	5.578E-1	2.958E-1	3.143E-1
Sa (T = 0.05 sec)	1.321E-1	1.316E-1	1.868E-1	2.113E-1	1.175E-1	1.161E-1	4.720E-1	4.755E-1	1.720E-1	1.765E-1	6.760E-1	6.170E-1	7.019E-1	6.382E-1	3.256E-1	3.156E-1
Sa (T = 0.075 sec)	1.808E-1	1.744E-1	2.171E-1	2.468E-1	1.878E-1	1.827E-1	5.723E-1	5.234E-1	2.675E-1	2.169E-1	8.078E-1	7.346E-1	1.108E+0	1.052E+0	4.580E-1	4.249E-1
Sa (T = 0.10 sec)	2.237E-1	1.998E-1	2.663E-1	3.131E-1	2.343E-1	2.474E-1	7.454E-1	6.969E-1	2.624E-1	2.570E-1	9.865E-1	9.725E-1	1.327E+0	1.242E+0	4.488E-1	4.521E-1
Sa (T = 0.15 sec)	2.275E-1	2.357E-1	4.427E-1	5.236E-1	2.127E-1	2.136E-1	7.642E-1	8.673E-1	4.887E-1	4.609E-1	1.126E+0	1.294E+0	1.055E+0	1.164E+0	7.398E-1	7.059E-1
Sa (T = 0.20 sec)	2.207E-1	2.748E-1	5.096E-1	4.760E-1	2.488E-1	2.344E-1	7.282E-1	7.202E-1	4.885E-1	4.583E-1	1.017E+0	9.246E-1	9.984E-1	1.195E+0	8.863E-1	8.303E-1
Sa (T = 0.30 sec)	2.189E-1	1.952E-1	3.184E-1	3.505E-1	2.379E-1	2.153E-1	1.388E+0	1.389E+0	3.022E-1	2.840E-1	9.761E-1	9.919E-1	1.011E+0	8.661E-1	5.704E-1	7.363E-1
Sa (T = 0.40 sec)	2.575E-1	2.845E-1	4.698E-1	5.177E-1	1.891E-1	2.106E-1	7.675E-1	8.552E-1	1.952E-1	2.048E-1	8.742E-1	7.974E-1	9.734E-1	9.280E-1	5.676E-1	5.550E-1
Sa (T = 0.50 sec)	2.240E-1	2.386E-1	3.613E-1	3.803E-1	2.037E-1	1.897E-1	3.634E-1	3.567E-1	2.011E-1	1.969E-1	4.385E-1	4.908E-1	7.415E-1	7.457E-1	5.487E-1	6.218E-1
Sa (T = 0.75 sec)	2.901E-1	2.631E-1	3.052E-1	2.836E-1	8.606E-2	9.823E-2	1.179E-1	1.210E-1	2.436E-1	2.186E-1	1.919E-1	1.998E-1	2.630E-1	2.660E-1	2.260E-1	2.189E-1
Sa (T = 1.0 sec)	2.736E-1	3.078E-1	3.398E-1	2.850E-1	7.101E-2	7.397E-2	8.557E-2	9.872E-2	2.372E-1	2.293E-1	1.185E-1	1.108E-1	1.530E-1	1.558E-1	1.190E-1	1.076E-1
Sa (T = 1.5 sec)	1.378E-1	1.585E-1	1.535E-1	1.509E-1	5.707E-2	5.848E-2	6.971E-2	7.428E-2	1.168E-1	1.167E-1	4.655E-2	4.558E-2	6.295E-2	6.018E-2	5.546E-2	5.054E-2
Sa (T = 2.0 sec)	7.939E-2	7.748E-2	9.285E-2	8.776E-2	2.739E-2	2.686E-2	3.988E-2	4.796E-2	5.577E-2	6.215E-2	2.660E-2	2.806E-2	3.927E-2	3.336E-2	2.428E-2	2.018E-2
Sa (T = 3.0 sec)	3.211E-2	2.840E-2	4.972E-2	4.767E-2	1.919E-2	1.945E-2	2.287E-2	1.994E-2	3.463E-2	3.468E-2	1.521E-2	1.501E-2	1.456E-2	1.118E-2	1.282E-2	1.145E-2
Sa (T = 4.0 sec)	1.878E-2	1.495E-2	3.033E-2	3.072E-2	1.070E-2	1.123E-2	1.750E-2	1.562E-2	2.519E-2	2.474E-2	9.287E-3	8.509E-3	8.062E-3	6.759E-3	8.764E-3	7.151E-3
Sa (T = 5.0 sec)	1.180E-2	9.056E-3	1.928E-2	1.859E-2	6.913E-3	6.180E-3	1.021E-2	8.669E-3	1.480E-2	1.333E-2	6.033E-3	5.456E-3	5.655E-3	4.452E-3		
Sa (T = 7.5 sec)																
Sa (T = 10.0 sec)																

Table B.3 Continued. Response variables for the Parkfield earthquake (Page 6 of 11)

	41		42		43		44		45		46		47		48	
Station information																
Station no. / code	36452		36453		36454		36455		36456		36510		36518		36519	
Owner	CSMIP		CSMIP		CSMIP		CSMIP		CSMIP		CSMIP		CSMIP		CSMIP	
Station location and name	Parkfield – Cholame 1E		Parkfield – Fault Zone 11		Parkfield – Fault Zone 6		Parkfield – Vineyard Canyon 1E		Parkfield – Fault Zone 14		Parkfield – Temblor		Parkfield – Turkey Flat 4		Parkfield – Turkey Flat 3	
Maximum useable period, T_{high} [sec]	5.714		5.714		5.000		5.714		6.667		5.000		6.154		6.154	
Ground motion parameter [g]	GMxy	GMrotI50	GMxy	GMrotI50	GMxy	GMrotI50	GMxy	GMrotI50	GMxy	GMrotI50	GMxy	GMrotI50	GMxy	GMrotI50	GMxy	GMrotI50
PGA	3.828E-1	3.721E-1	6.501E-1	7.226E-1	1.779E-1	2.116E-1	2.767E-1	3.090E-1	8.401E-1	8.794E-1	8.869E-2	1.005E-1	1.054E-1	9.276E-2	2.468E-1	2.456E-1
Sa (T = 0.05 sec)	4.600E-1	4.556E-1	1.022E+0	9.629E-1	2.645E-1	2.609E-1	3.269E-1	3.386E-1	9.871E-1	1.054E+0	9.457E-2	1.021E-1	1.250E-1	1.163E-1	3.679E-1	3.286E-1
Sa (T = 0.075 sec)	4.572E-1	4.494E-1	1.446E+0	1.614E+0	3.508E-1	3.302E-1	4.752E-1	4.811E-1	1.305E+0	1.135E+0	1.185E-1	1.105E-1	1.622E-1	1.471E-1	6.674E-1	6.390E-1
Sa (T = 0.10 sec)	4.835E-1	4.879E-1	1.814E+0	1.745E+0	5.993E-1	5.970E-1	5.144E-1	5.381E-1	1.632E+0	1.634E+0	1.801E-1	1.605E-1	2.934E-1	2.520E-1	8.994E-1	9.617E-1
Sa (T = 0.15 sec)	7.560E-1	7.336E-1	1.356E+0	1.614E+0	5.731E-1	4.971E-1	9.342E-1	9.878E-1	2.001E+0	1.990E+0	2.242E-1	2.451E-1	1.936E-1	1.738E-1	5.353E-1	4.945E-1
Sa (T = 0.20 sec)	7.237E-1	7.088E-1	1.326E+0	1.423E+0	3.009E-1	3.222E-1	7.151E-1	6.606E-1	1.944E+0	1.777E+0	3.289E-1	3.002E-1	1.960E-1	2.228E-1	4.155E-1	4.073E-1
Sa (T = 0.30 sec)	5.947E-1	5.960E-1	1.216E+0	1.115E+0	3.434E-1	3.334E-1	7.148E-1	6.362E-1	1.649E+0	1.600E+0	2.071E-1	2.189E-1	2.213E-1	2.104E-1	2.828E-1	2.773E-1
Sa (T = 0.40 sec)	5.304E-1	5.480E-1	4.839E-1	4.687E-1	2.210E-1	2.125E-1	8.894E-1	9.267E-1	1.810E+0	1.946E+0	2.036E-1	1.845E-1	1.784E-1	1.614E-1	1.878E-1	1.798E-1
Sa (T = 0.50 sec)	5.941E-1	6.216E-1	3.092E-1	2.942E-1	1.789E-1	1.770E-1	5.063E-1	5.303E-1	1.606E+0	1.894E+0	1.548E-1	1.542E-1	1.454E-1	1.344E-1	1.373E-1	1.339E-1
Sa (T = 0.75 sec)	5.684E-1	5.770E-1	1.992E-1	1.862E-1	1.909E-1	1.988E-1	3.943E-1	4.254E-1	1.316E+0	1.293E+0	1.172E-1	1.228E-1	9.298E-2	8.952E-2	9.334E-2	9.803E-2
Sa (T = 1.0 sec)	4.707E-1	4.392E-1	1.439E-1	1.330E-1	1.881E-1	1.601E-1	3.612E-1	3.194E-1	5.990E-1	5.589E-1	7.766E-2	7.743E-2	5.259E-2	4.902E-2	5.050E-2	4.945E-2
Sa (T = 1.5 sec)	2.260E-1	2.058E-1	5.686E-2	5.529E-2	9.799E-2	8.982E-2	1.424E-1	1.570E-1	2.548E-1	2.634E-1	3.684E-2	3.427E-2	3.633E-2	3.587E-2	3.367E-2	3.525E-2
Sa (T = 2.0 sec)	1.308E-1	1.115E-1	2.889E-2	2.716E-2	5.331E-2	6.062E-2	9.713E-2	1.077E-1	1.500E-1	1.787E-1	3.111E-2	2.811E-2	2.435E-2	2.385E-2	2.589E-2	2.614E-2
Sa (T = 3.0 sec)	4.678E-2	4.150E-2	1.281E-2	1.438E-2	2.103E-2	2.062E-2	5.418E-2	4.954E-2	7.365E-2	8.534E-2	9.129E-3	8.675E-3	9.571E-3	8.078E-3	1.049E-2	9.657E-3
Sa (T = 4.0 sec)	2.437E-2	2.164E-2	7.842E-3	8.295E-3	1.283E-2	1.254E-2	3.015E-2	2.618E-2	3.994E-2	4.489E-2	3.740E-3	3.647E-3	5.462E-3	5.195E-3	5.935E-3	5.584E-3
Sa (T = 5.0 sec)	1.632E-2	1.395E-2	4.956E-3	4.295E-3	8.065E-3	6.967E-3	1.598E-2	1.372E-2	2.835E-2	2.829E-2	2.540E-3	2.354E-3	3.394E-3	3.480E-3	3.696E-3	3.463E-3
Sa (T = 7.5 sec)																
Sa (T = 10.0 sec)																

Table B.3 Continued. Response variables for the Parkfield earthquake (Page 7 of 11)

	49		50		51		52		53		54		55		56	
Station information																
Station no. / code	36520		36529		36531		36535		36712		37737		46174		46175	
Owner	CSMIP		CSMIP		CSMIP		CSMIP		CSMIP		CSMIP		CSMIP		CSMIP	
Station location and name	Parkfield – Turkey Flat 2		Parkfield – Turkey Flat 1		Parkfield – 1-Story School Building		Shandon – 1-Story High School Bldg.		Templeton – Hospital Grounds		Cambria – Hwy 1 Caltrans Bridge Grnds		Coalinga – Priest Valley		Coalinga – Slack Canyon	
Maximum useable period, T_{high} [sec]	6.154		6.154		4.706		4.000		2.667		2.667		5.000		5.714	
Ground motion parameter [g]	GMxy	GMrotI50	GMxy	GMrotI50	GMxy	GMrotI50	GMxy	GMrotI50	GMxy	GMrotI50	GMxy	GMrotI50	GMxy	GMrotI50	GMxy	GMrotI50
PGA	2.921E-1	2.719E-1	2.178E-1	2.132E-1	2.594E-1	2.580E-1	1.751E-1	1.847E-1	3.601E-2	3.790E-2	9.536E-3	9.145E-3	2.486E-2	2.401E-2	2.706E-1	2.835E-1
Sa (T = 0.05 sec)	3.725E-1	3.472E-1	2.351E-1	2.299E-1	3.001E-1	2.645E-1	2.090E-1	2.128E-1	4.286E-2	4.423E-2	9.949E-3	9.734E-3	2.741E-2	2.509E-2	2.765E-1	2.891E-1
Sa (T = 0.075 sec)	7.892E-1	7.703E-1	3.053E-1	2.995E-1	3.235E-1	2.779E-1	2.817E-1	2.857E-1	5.683E-2	5.537E-2	1.036E-2	1.139E-2	2.617E-2	2.679E-2	2.932E-1	3.012E-1
Sa (T = 0.10 sec)	7.793E-1	7.672E-1	3.147E-1	3.155E-1	3.709E-1	3.458E-1	3.685E-1	3.102E-1	6.544E-2	6.919E-2	1.386E-2	1.534E-2	3.180E-2	3.554E-2	3.229E-1	3.259E-1
Sa (T = 0.15 sec)	7.144E-1	7.313E-1	3.702E-1	3.624E-1	5.125E-1	3.870E-1	4.334E-1	4.872E-1	8.213E-2	8.902E-2	2.149E-2	1.969E-2	4.104E-2	3.758E-2	3.444E-1	3.490E-1
Sa (T = 0.20 sec)	6.671E-1	6.027E-1	3.544E-1	3.560E-1	8.235E-1	4.931E-1	3.538E-1	4.276E-1	9.419E-2	1.008E-1	2.468E-2	2.470E-2	6.473E-2	6.111E-2	3.642E-1	3.871E-1
Sa (T = 0.30 sec)	2.579E-1	2.421E-1	3.851E-1	3.756E-1	3.948E-1	3.355E-1	2.193E-1	2.236E-1	9.339E-2	8.842E-2	2.325E-2	2.283E-2	5.410E-2	4.924E-2	4.852E-1	4.784E-1
Sa (T = 0.40 sec)	1.142E-1	1.127E-1	4.092E-1	3.987E-1	5.861E-1	5.215E-1	1.551E-1	1.581E-1	7.107E-2	7.102E-2	2.138E-2	2.063E-2	4.816E-2	4.911E-2	5.565E-1	5.510E-1
Sa (T = 0.50 sec)	1.120E-1	1.116E-1	4.012E-1	3.946E-1	5.368E-1	5.240E-1	1.439E-1	1.240E-1	9.777E-2	9.427E-2	2.000E-2	1.819E-2	6.484E-2	6.741E-2	8.556E-1	8.574E-1
Sa (T = 0.75 sec)	1.010E-1	9.805E-2	1.674E-1	1.645E-1	6.999E-1	7.440E-1	7.459E-2	6.893E-2	4.025E-2	3.884E-2	2.213E-2	2.248E-2	5.469E-2	4.896E-2	9.120E-1	9.522E-1
Sa (T = 1.0 sec)	4.911E-2	4.857E-2	7.595E-2	7.557E-2	6.626E-1	6.159E-1	4.858E-2	5.408E-2	2.199E-2	2.231E-2	9.940E-3	1.033E-2	4.863E-2	4.934E-2	5.630E-1	5.352E-1
Sa (T = 1.5 sec)	2.943E-2	2.888E-2	3.963E-2	3.806E-2	2.824E-1	2.822E-1	4.326E-2	3.728E-2	1.719E-2	1.676E-2	3.679E-3	3.840E-3	3.486E-2	3.919E-2	1.780E-1	1.728E-1
Sa (T = 2.0 sec)	2.310E-2	2.323E-2	2.489E-2	2.458E-2	1.675E-1	1.458E-1	1.994E-2	2.000E-2	2.031E-2	2.025E-2	2.595E-3	2.803E-3	3.393E-2	3.231E-2	1.193E-1	1.185E-1
Sa (T = 3.0 sec)	1.105E-2	1.006E-2	1.141E-2	1.112E-2	5.389E-2	5.762E-2	5.568E-3	5.169E-3					1.367E-2	1.464E-2	6.163E-2	6.144E-2
Sa (T = 4.0 sec)	5.612E-3	5.284E-3	6.857E-3	6.318E-3	3.420E-2	3.034E-2	4.288E-3	3.615E-3					6.230E-3	6.179E-3	3.426E-2	3.423E-2
Sa (T = 5.0 sec)	3.473E-3	3.103E-3	4.303E-3	3.645E-3									5.137E-3	5.112E-3	1.823E-2	1.784E-2
Sa (T = 7.5 sec)																
Sa (T = 10.0 sec)																

Table B.3 Continued. Response variables for the Parkfield earthquake (Page 8 of 11)

	57		58		59		60		61		62		63		64	
Station information																
Station no. / code	47231		47232		47236		47460		61022		DFU		EFU		FFU	
Owner	CSMIP		CSMIP		CSMIP		CSMIP		BDSN		USGS		USGS		USGS	
Station location and name	King City – 2-Story Hospital		King City – Canal & Reich		San Benito – Bear Valley CDF		Greenfield – Police Station		Parkfield – Bear Valley Ranch		Parkfield – Donna Lee		Parkfield – Eades		Parkfield – Froelich	
Maximum useable period, T_{high} [sec]	8.000		2.667		2.667		2.667		10.000		10.000		10.000		8.000	
Ground motion parameter [g]	GMxy	GMrotI50	GMxy	GMrotI50	GMxy	GMrotI50	GMxy	GMrotI50	GMxy	GMrotI50	GMxy	GMrotI50	GMxy	GMrotI50	GMxy	GMrotI50
PGA	3.642E-2	3.823E-2	5.193E-2	5.090E-2	1.527E-2	1.718E-2	2.795E-2	2.836E-2	1.556E-1	1.518E-1	3.313E-1	3.151E-1	3.525E-1	3.316E-1	4.169E-1	4.092E-1
Sa (T = 0.05 sec)	4.260E-2	4.259E-2	8.765E-2	8.580E-2	1.674E-2	1.803E-2	3.372E-2	3.340E-2	1.705E-1	1.512E-1	3.949E-1	3.760E-1	5.133E-1	5.235E-1	6.773E-1	7.245E-1
Sa (T = 0.075 sec)	4.850E-2	4.813E-2	1.133E-1	9.991E-2	2.043E-2	2.017E-2	5.426E-2	5.222E-2	2.653E-1	2.534E-1	5.631E-1	5.675E-1	9.381E-1	8.669E-1	9.248E-1	8.851E-1
Sa (T = 0.10 sec)	5.477E-2	5.937E-2	1.338E-1	1.183E-1	2.140E-2	2.155E-2	7.992E-2	8.035E-2	4.020E-1	3.569E-1	8.051E-1	9.404E-1	1.145E+0	1.069E+0	1.032E+0	1.041E+0
Sa (T = 0.15 sec)	8.006E-2	9.266E-2	1.508E-1	1.365E-1	2.469E-2	2.566E-2	6.449E-2	6.434E-2	3.734E-1	3.726E-1	7.090E-1	7.671E-1	9.076E-1	9.213E-1	1.149E+0	1.164E+0
Sa (T = 0.20 sec)	9.263E-2	8.760E-2	1.327E-1	1.285E-1	4.043E-2	3.795E-2	6.566E-2	6.455E-2	5.176E-1	5.433E-1	7.832E-1	6.974E-1	8.193E-1	7.253E-1	7.380E-1	7.866E-1
Sa (T = 0.30 sec)	9.811E-2	8.668E-2	1.120E-1	1.143E-1	4.311E-2	4.590E-2	6.222E-2	6.092E-2	3.064E-1	3.128E-1	3.668E-1	3.829E-1	4.188E-1	3.953E-1	3.586E-1	3.906E-1
Sa (T = 0.40 sec)	1.013E-1	1.135E-1	1.222E-1	1.215E-1	4.626E-2	4.316E-2	5.086E-2	5.048E-2	2.091E-1	2.147E-1	4.169E-1	3.715E-1	4.629E-1	4.459E-1	2.491E-1	2.629E-1
Sa (T = 0.50 sec)	6.517E-2	5.922E-2	6.816E-2	5.969E-2	4.552E-2	5.302E-2	6.182E-2	6.180E-2	2.139E-1	2.202E-1	2.522E-1	2.440E-1	3.219E-1	3.406E-1	1.783E-1	1.796E-1
Sa (T = 0.75 sec)	3.867E-2	4.429E-2	4.340E-2	4.138E-2	2.960E-2	2.861E-2	4.402E-2	4.411E-2	1.099E-1	1.144E-1	1.857E-1	2.046E-1	4.539E-1	4.404E-1	1.788E-1	1.863E-1
Sa (T = 1.0 sec)	2.500E-2	2.617E-2	3.598E-2	3.518E-2	1.702E-2	1.650E-2	3.558E-2	3.500E-2	6.416E-2	6.575E-2	1.146E-1	1.016E-1	3.876E-1	3.376E-1	1.238E-1	1.259E-1
Sa (T = 1.5 sec)	1.998E-2	2.108E-2	2.264E-2	2.269E-2	1.100E-2	1.352E-2	1.311E-2	1.317E-2	5.182E-2	5.378E-2	6.704E-2	5.419E-2	1.822E-1	1.505E-1	8.201E-2	8.786E-2
Sa (T = 2.0 sec)	1.502E-2	1.466E-2	1.200E-2	1.170E-2	6.410E-3	7.079E-3	8.163E-3	8.165E-3	4.787E-2	5.170E-2	3.678E-2	3.516E-2	9.760E-2	7.855E-2	5.788E-2	5.739E-2
Sa (T = 3.0 sec)	5.876E-3	5.839E-3							2.192E-2	2.067E-2	1.916E-2	1.992E-2	3.761E-2	3.580E-2	2.243E-2	2.204E-2
Sa (T = 4.0 sec)	2.849E-3	2.895E-3							1.449E-2	1.382E-2	1.239E-2	1.195E-2	1.984E-2	1.674E-2	1.369E-2	1.298E-2
Sa (T = 5.0 sec)	1.918E-3	1.974E-3							8.514E-3	8.125E-3	6.816E-3	7.069E-3	1.228E-2	9.890E-3	8.787E-3	7.914E-3
Sa (T = 7.5 sec)	8.939E-4	8.131E-4							3.866E-3	3.807E-3	2.646E-3	2.908E-3	5.636E-3	3.924E-3	3.479E-3	2.951E-3
Sa (T = 10.0 sec)									1.909E-3	1.784E-3	1.654E-3	1.334E-3	3.413E-3	2.060E-3		

Table B.3 Continued. Response variables for the Parkfield earthquake (Page 9 of 11)

	65		66		67		68		69		70		71	
Station information														
Station no. / code	GFU		JFU		KFU		MFU		PHOB		RFU		SFU	
Owner	USGS		USGS		USGS		USGS		NCSN		USGS		USGS	
Station location and name	Parkfield – Gold Hill		Parkfield – Joaquin Canyon		Parkfield – Jack Canyon		Parkfield – Middle Mountain		Hog Canyon		Parkfield – Red Hills		Parkfield – Stockdale Mtn	
Maximum useable period, T_{high} [sec]	8.000		8.000		8.000		8.000		10.000		8.000		8.000	
Ground motion parameter [g]	GMxy	GMrotI50	GMxy	GMrotI50	GMxy	GMrotI50	GMxy	GMrotI50	GMxy	GMrotI50	GMxy	GMrotI50	GMxy	GMrotI50
PGA	1.542E-1	1.527E-1	5.552E-1	5.596E-1	1.577E-1	1.562E-1	2.749E-1	2.815E-1	2.646E-1	2.604E-1	4.649E-2	4.425E-2	2.875E-1	2.924E-1
Sa (T = 0.05 sec)	2.750E-1	2.799E-1	8.733E-1	8.772E-1	2.719E-1	2.746E-1	2.950E-1	3.119E-1	N/A	3.428E-1	5.930E-2	6.799E-2	4.012E-1	3.840E-1
Sa (T = 0.075 sec)	3.898E-1	3.363E-1	1.289E+0	1.381E+0	3.205E-1	2.976E-1	3.696E-1	3.339E-1	N/A	4.068E-1	6.801E-2	7.200E-2	5.288E-1	5.004E-1
Sa (T = 0.10 sec)	3.770E-1	4.277E-1	1.488E+0	1.414E+0	3.666E-1	3.669E-1	3.587E-1	3.554E-1	5.252E-1	5.429E-1	1.018E-1	9.079E-2	7.334E-1	7.417E-1
Sa (T = 0.15 sec)	4.203E-1	4.159E-1	2.133E+0	2.064E+0	3.763E-1	3.850E-1	5.222E-1	4.771E-1	6.257E-1	6.592E-1	1.493E-1	1.460E-1	8.722E-1	8.090E-1
Sa (T = 0.20 sec)	3.756E-1	4.058E-1	1.339E+0	1.347E+0	4.187E-1	4.358E-1	5.141E-1	4.974E-1	5.507E-1	6.051E-1	1.345E-1	1.372E-1	4.927E-1	5.274E-1
Sa (T = 0.30 sec)	1.449E-1	1.588E-1	9.539E-1	9.370E-1	2.104E-1	2.073E-1	7.416E-1	8.227E-1	4.751E-1	5.464E-1	7.495E-2	7.727E-2	2.713E-1	2.848E-1
Sa (T = 0.40 sec)	1.472E-1	1.336E-1	5.313E-1	5.570E-1	2.181E-1	2.313E-1	6.414E-1	6.089E-1	6.803E-1	6.629E-1	4.923E-2	4.481E-2	1.245E-1	1.221E-1
Sa (T = 0.50 sec)	8.200E-2	8.370E-2	5.369E-1	5.309E-1	1.691E-1	1.860E-1	4.535E-1	5.686E-1	7.776E-1	8.071E-1	3.419E-2	3.716E-2	8.279E-2	8.485E-2
Sa (T = 0.75 sec)	3.544E-2	4.376E-2	3.710E-1	3.748E-1	1.345E-1	1.016E-1	1.876E-1	1.992E-1	4.691E-1	4.592E-1	3.506E-2	3.715E-2	4.611E-2	4.229E-2
Sa (T = 1.0 sec)	3.352E-2	3.061E-2	1.999E-1	2.009E-1	7.292E-2	7.361E-2	1.911E-1	2.024E-1	2.471E-1	2.774E-1	2.481E-2	2.729E-2	4.109E-2	4.431E-2
Sa (T = 1.5 sec)	1.872E-2	2.163E-2	9.872E-2	9.968E-2	3.319E-2	3.040E-2	1.352E-1	1.425E-1	1.274E-1	1.289E-1	9.127E-3	1.079E-2	5.089E-2	4.009E-2
Sa (T = 2.0 sec)	1.579E-2	1.601E-2	6.167E-2	5.871E-2	2.032E-2	1.763E-2	1.007E-1	1.125E-1	7.267E-2	6.143E-2	4.856E-3	5.406E-3	2.216E-2	2.168E-2
Sa (T = 3.0 sec)	8.052E-3	7.775E-3	2.797E-2	2.866E-2	6.630E-3	5.514E-3	6.583E-2	5.785E-2	3.231E-2	3.172E-2	1.850E-3	2.025E-3	7.121E-3	7.327E-3
Sa (T = 4.0 sec)	4.694E-3	4.315E-3	1.575E-2	1.604E-2	4.265E-3	3.375E-3	3.680E-2	3.519E-2	2.125E-2	2.150E-2	1.079E-3	1.023E-3	3.981E-3	3.846E-3
Sa (T = 5.0 sec)	3.093E-3	2.988E-3	9.217E-3	9.100E-3	3.053E-3	2.446E-3	2.222E-2	2.024E-2	1.255E-2	1.191E-2	6.817E-4	6.134E-4	2.706E-3	2.176E-3
Sa (T = 7.5 sec)	1.280E-3	9.485E-4	4.405E-3	3.760E-3	1.635E-3	1.206E-3	8.427E-3	6.505E-3	4.789E-3	4.144E-3	3.623E-4	2.720E-4	1.231E-3	9.773E-4
Sa (T = 10.0 sec)									2.625E-3	2.105E-3				

Table B.3 Continued. Response variables for the Parkfield earthquake (Page 10 of 11)

	72		73		74		75		76		77		78	
Station information														
Station no. / code	UPSAR01		UPSAR02		UPSAR03		UPSAR05		UPSAR06		UPSAR07		UPSAR08	
Owner	USGS		USGS		USGS		USGS		USGS		USGS		USGS	
Station location and name	Parkfield – USGS Parkfield Dense Seismograph Array 01		Parkfield – USGS Parkfield Dense Seismograph Array 02		Parkfield – USGS Parkfield Dense Seismograph Array 03		Parkfield – USGS Parkfield Dense Seismograph Array 05		Parkfield – USGS Parkfield Dense Seismograph Array 06		Parkfield – USGS Parkfield Dense Seismograph Array 07		Parkfield – USGS Parkfield Dense Seismograph Array 08	
Maximum useable period, T_{high} [sec]	10.000		10.000		10.000		10.000		10.000		10.000		10.000	
Ground motion parameter [g]	GMxy	GMrotI50	GMxy	GMrotI50	GMxy	GMrotI50	GMxy	GMrotI50	GMxy	GMrotI50	GMxy	GMrotI50	GMxy	GMrotI50
PGA	1.585E-1	1.694E-1	2.303E-1	2.530E-1	1.935E-1	2.022E-1	2.966E-1	3.049E-1	2.361E-1	2.374E-1	3.497E-1	3.774E-1	2.181E-1	2.059E-1
Sa (T = 0.05 sec)	1.944E-1	2.064E-1	2.846E-1	3.444E-1	2.094E-1	2.192E-1	3.291E-1	3.709E-1	2.754E-1	2.676E-1	4.946E-1	5.325E-1	2.484E-1	2.626E-1
Sa (T = 0.075 sec)	3.129E-1	3.118E-1	4.285E-1	3.953E-1	3.308E-1	3.373E-1	6.514E-1	6.551E-1	4.276E-1	3.881E-1	7.166E-1	7.374E-1	3.834E-1	3.943E-1
Sa (T = 0.10 sec)	3.165E-1	3.259E-1	4.565E-1	5.345E-1	3.402E-1	3.487E-1	4.321E-1	4.478E-1	3.638E-1	3.418E-1	7.049E-1	6.952E-1	3.189E-1	2.941E-1
Sa (T = 0.15 sec)	3.436E-1	3.523E-1	5.437E-1	5.447E-1	5.249E-1	5.352E-1	5.078E-1	4.845E-1	4.754E-1	5.215E-1	6.751E-1	7.025E-1	3.758E-1	3.964E-1
Sa (T = 0.20 sec)	4.327E-1	4.055E-1	5.158E-1	5.761E-1	4.811E-1	4.721E-1	6.937E-1	6.652E-1	5.563E-1	5.315E-1	6.263E-1	6.769E-1	4.530E-1	4.209E-1
Sa (T = 0.30 sec)	5.290E-1	4.689E-1	4.778E-1	5.858E-1	3.930E-1	3.807E-1	6.041E-1	6.460E-1	8.049E-1	7.139E-1	6.368E-1	6.969E-1	4.630E-1	4.913E-1
Sa (T = 0.40 sec)	3.284E-1	3.360E-1	4.983E-1	4.365E-1	6.063E-1	6.087E-1	5.671E-1	5.804E-1	6.986E-1	7.700E-1	8.676E-1	9.384E-1	4.820E-1	4.760E-1
Sa (T = 0.50 sec)	2.601E-1	2.804E-1	5.045E-1	4.486E-1	3.456E-1	3.439E-1	6.147E-1	6.610E-1	6.237E-1	6.172E-1	6.771E-1	7.016E-1	4.279E-1	3.935E-1
Sa (T = 0.75 sec)	3.661E-1	3.449E-1	4.377E-1	4.020E-1	2.484E-1	2.321E-1	5.419E-1	4.934E-1	5.193E-1	4.444E-1	5.500E-1	4.420E-1	4.447E-1	4.372E-1
Sa (T = 1.0 sec)	1.682E-1	1.646E-1	1.596E-1	1.468E-1	1.209E-1	1.213E-1	1.989E-1	2.000E-1	1.820E-1	2.058E-1	2.044E-1	1.983E-1	1.754E-1	1.929E-1
Sa (T = 1.5 sec)	6.633E-2	6.093E-2	6.611E-2	6.726E-2	5.801E-2	5.528E-2	7.328E-2	6.646E-2	6.846E-2	6.372E-2	6.691E-2	6.384E-2	6.431E-2	5.920E-2
Sa (T = 2.0 sec)	3.314E-2	2.929E-2	3.543E-2	4.035E-2	2.906E-2	2.876E-2	4.066E-2	4.186E-2	3.836E-2	4.039E-2	4.015E-2	4.163E-2	3.242E-2	3.207E-2
Sa (T = 3.0 sec)	1.509E-2	1.489E-2	1.580E-2	1.342E-2	1.400E-2	1.375E-2	1.613E-2	1.523E-2	1.650E-2	1.576E-2	1.715E-2	1.535E-2	1.667E-2	1.457E-2
Sa (T = 4.0 sec)	9.380E-3	9.223E-3	9.396E-3	1.019E-2	9.126E-3	8.802E-3	1.059E-2	1.064E-2	1.012E-2	1.071E-2	1.073E-2	1.032E-2	9.455E-3	9.734E-3
Sa (T = 5.0 sec)	7.015E-3	7.441E-3	7.647E-3	7.973E-3	7.317E-3	7.396E-3	8.178E-3	8.767E-3	7.640E-3	8.173E-3	7.719E-3	8.600E-3	7.675E-3	8.242E-3
Sa (T = 7.5 sec)	3.275E-3	2.985E-3	3.630E-3	2.879E-3	3.444E-3	2.954E-3	3.884E-3	3.211E-3	3.678E-3	3.011E-3	3.841E-3	3.057E-3	3.370E-3	2.941E-3
Sa (T = 10.0 sec)	1.645E-3	1.319E-3	1.798E-3	1.525E-3	1.573E-3	1.331E-3	2.007E-3	1.549E-3	1.758E-3	1.401E-3	1.905E-3	1.442E-3	1.700E-3	1.288E-3

Table B.3 Continued. Response variables for the Parkfield earthquake (Page 11 of 11)

	79		80		81		82		83		84		85	
Station information														
Station no. / code	UPSAR09		UPSAR10		UPSAR11		UPSAR12		UPSAR13		VFU		WFU	
Owner	USGS		USGS		USGS		USGS		USGS		USGS		USGS	
Station location and name	Parkfield – USGS Parkfield Dense Seismograph Array 09		Parkfield – USGS Parkfield Dense Seismograph Array 10		Parkfield – USGS Parkfield Dense Seismograph Array 11		Parkfield – USGS Parkfield Dense Seismograph Array 12		Parkfield – USGS Parkfield Dense Seismograph Array 13		Parkfield – Vineyard Canyon		Parkfield – Work Ranch	
Maximum useable period, T_{high} [sec]	10.000		10.000		10.000		10.000		10.000		8.000		8.000	
Ground motion parameter [g]	GMxy	GMrotI50	GMxy	GMrotI50	GMxy	GMrotI50	GMxy	GMrotI50	GMxy	GMrotI50	GMxy	GMrotI50	GMxy	GMrotI50
PGA	2.388E-1	2.465E-1	2.931E-1	2.455E-1	4.075E-1	3.942E-1	2.352E-1	2.628E-1	2.605E-1	2.457E-1	2.213E-1	2.398E-1	2.522E-1	2.942E-1
Sa (T = 0.05 sec)	2.648E-1	2.714E-1	3.737E-1	3.898E-1	5.289E-1	5.170E-1	2.659E-1	3.162E-1	3.267E-1	3.034E-1	2.938E-1	3.019E-1	4.893E-1	5.432E-1
Sa (T = 0.075 sec)	3.114E-1	3.203E-1	4.063E-1	4.347E-1	5.240E-1	5.236E-1	3.532E-1	3.694E-1	3.610E-1	3.432E-1	3.551E-1	3.452E-1	6.996E-1	7.562E-1
Sa (T = 0.10 sec)	3.349E-1	3.199E-1	4.139E-1	4.030E-1	6.267E-1	6.446E-1	3.966E-1	4.325E-1	3.783E-1	3.710E-1	4.742E-1	4.407E-1	7.285E-1	6.278E-1
Sa (T = 0.15 sec)	4.236E-1	4.432E-1	4.700E-1	4.107E-1	5.545E-1	5.538E-1	3.950E-1	4.553E-1	4.329E-1	4.431E-1	4.793E-1	4.894E-1	8.101E-1	8.768E-1
Sa (T = 0.20 sec)	4.759E-1	4.778E-1	5.367E-1	5.018E-1	8.143E-1	8.257E-1	5.464E-1	5.937E-1	6.340E-1	6.778E-1	5.219E-1	5.377E-1	4.399E-1	4.723E-1
Sa (T = 0.30 sec)	4.392E-1	4.287E-1	4.697E-1	4.292E-1	8.705E-1	8.631E-1	6.432E-1	6.106E-1	5.435E-1	5.146E-1	5.417E-1	5.092E-1	1.875E-1	2.228E-1
Sa (T = 0.40 sec)	5.416E-1	5.332E-1	7.098E-1	7.248E-1	1.104E+0	1.098E+0	5.632E-1	6.409E-1	4.480E-1	4.194E-1	5.309E-1	5.551E-1	1.561E-1	1.553E-1
Sa (T = 0.50 sec)	7.210E-1	7.173E-1	5.152E-1	5.591E-1	9.101E-1	9.164E-1	4.369E-1	4.783E-1	3.991E-1	3.857E-1	5.344E-1	6.391E-1	1.274E-1	1.166E-1
Sa (T = 0.75 sec)	7.180E-1	6.664E-1	4.061E-1	3.521E-1	4.129E-1	3.927E-1	3.038E-1	3.275E-1	6.253E-1	6.127E-1	3.660E-1	4.051E-1	9.372E-2	9.086E-2
Sa (T = 1.0 sec)	2.792E-1	2.787E-1	2.558E-1	2.231E-1	2.342E-1	2.269E-1	1.728E-1	1.644E-1	2.262E-1	2.412E-1	2.342E-1	2.479E-1	4.587E-2	4.370E-2
Sa (T = 1.5 sec)	7.096E-2	6.935E-2	7.011E-2	6.535E-2	6.818E-2	6.466E-2	8.103E-2	7.468E-2	1.049E-1	9.728E-2	1.512E-1	1.353E-1	2.561E-2	2.279E-2
Sa (T = 2.0 sec)	4.217E-2	4.105E-2	4.177E-2	3.807E-2	4.016E-2	3.871E-2	3.922E-2	3.722E-2	4.431E-2	4.723E-2	6.736E-2	6.907E-2	1.673E-2	1.618E-2
Sa (T = 3.0 sec)	2.046E-2	1.883E-2	1.665E-2	1.565E-2	1.745E-2	1.632E-2	1.819E-2	1.766E-2	1.977E-2	1.769E-2	3.129E-2	3.025E-2	8.510E-3	7.359E-3
Sa (T = 4.0 sec)	1.153E-2	1.045E-2	9.918E-3	1.066E-2	1.046E-2	9.934E-3	1.007E-2	9.479E-3	1.155E-2	1.059E-2	1.603E-2	1.444E-2	6.077E-3	4.899E-3
Sa (T = 5.0 sec)	9.625E-3	9.328E-3	7.619E-3	8.368E-3	9.340E-3	9.192E-3	7.158E-3	8.622E-3	7.775E-3	9.526E-3	9.714E-3	8.748E-3	3.780E-3	3.200E-3
Sa (T = 7.5 sec)	3.958E-3	3.371E-3	3.732E-3	3.273E-3	4.739E-3	3.781E-3	3.343E-3	3.056E-3	3.939E-3	3.830E-3	4.724E-3	3.587E-3	1.123E-3	8.710E-4
Sa (T = 10.0 sec)	2.078E-3	1.617E-3	1.954E-3	1.609E-3	2.191E-3	1.533E-3	2.027E-3	1.340E-3	1.990E-3	1.528E-3				

Table B.4. Response variables for the San Simeon earthquake

	1		2		3		4		5		6		7		8	
Station information																
Station no. / code	1083		1747		36153		36427		36695		37737		47460		61022	
Owner	USGS		USGS		CSMIP		CSMIP		CSMIP		CSMIP		CSMIP		BDSN	
Station location and name	San Luis Obispo – Rec Center		Coalinga – Fire Station 39		San Luis Obispo – Lopez Lake Grounds		Point Buchon – Los Osos		Templeton – 1 Story Hospital		Cambria – Hwy 1 Caltrans Bridge Grnds		Greenfield – Police Station		Parkfield – Bear Valley Ranch	
Maximum useable period, T_{high} [sec]	4.800		4.800		8.000		8.000		6.000		9.600		4.800		10.000	
Ground motion parameter [g]	GMxy	GMrotI50	GMxy	GMrotI50	GMxy	GMrotI50	GMxy	GMrotI50	GMxy	GMrotI50	GMxy	GMrotI50	GMxy	GMrotI50	GMxy	GMrotI50
PGA	1.392E-1	1.278E-1	2.616E-2	2.553E-2	1.224E-1	1.209E-1	7.177E-2	7.160E-2	4.479E-1	4.396E-1	1.502E-1	1.513E-1	1.863E-2	1.950E-2	2.826E-2	2.799E-2
Sa (T = 0.05 sec)	1.524E-1	1.426E-1	2.661E-2	2.581E-2	1.271E-1	1.235E-1	7.719E-2	7.469E-2	5.140E-1	5.628E-1	2.407E-1	2.278E-1	1.948E-2	2.100E-2	2.874E-2	2.803E-2
Sa (T = 0.075 sec)	1.785E-1	1.790E-1	2.761E-2	2.717E-2	1.517E-1	1.493E-1	9.105E-2	8.415E-2	8.025E-1	7.361E-1	2.620E-1	2.629E-1	2.636E-2	2.831E-2	3.454E-2	3.222E-2
Sa (T = 0.10 sec)	2.777E-1	2.806E-1	2.962E-2	2.946E-2	2.111E-1	2.122E-1	1.340E-1	1.348E-1	1.021E+0	1.055E+0	3.253E-1	3.220E-1	3.796E-2	3.515E-2	4.395E-2	4.431E-2
Sa (T = 0.15 sec)	4.103E-1	4.273E-1	4.242E-2	4.176E-2	3.856E-1	4.149E-1	1.994E-1	2.059E-1	1.152E+0	1.143E+0	3.561E-1	3.565E-1	3.630E-2	3.529E-2	8.347E-2	7.797E-2
Sa (T = 0.20 sec)	4.372E-1	4.536E-1	3.937E-2	4.242E-2	3.029E-1	3.046E-1	1.575E-1	1.792E-1	1.275E+0	1.189E+0	4.255E-1	4.127E-1	4.331E-2	4.456E-2	5.663E-2	5.648E-2
Sa (T = 0.30 sec)	2.453E-1	2.216E-1	4.707E-2	4.894E-2	1.885E-1	1.902E-1	1.085E-1	1.068E-1	1.202E+0	1.040E+0	3.394E-1	3.398E-1	4.962E-2	4.987E-2	4.952E-2	4.699E-2
Sa (T = 0.40 sec)	1.601E-1	1.591E-1	6.565E-2	6.854E-2	2.012E-1	1.955E-1	1.018E-1	9.995E-2	8.871E-1	8.432E-1	3.608E-1	3.684E-1	6.265E-2	6.077E-2	4.511E-2	4.203E-2
Sa (T = 0.50 sec)	1.547E-1	1.517E-1	7.820E-2	7.642E-2	1.270E-1	1.304E-1	1.246E-1	1.089E-1	7.198E-1	8.154E-1	2.408E-1	2.260E-1	5.143E-2	4.935E-2	5.554E-2	5.447E-2
Sa (T = 0.75 sec)	9.575E-2	1.092E-1	6.625E-2	6.534E-2	1.443E-1	1.410E-1	1.159E-1	1.115E-1	4.045E-1	3.687E-1	1.911E-1	1.855E-1	4.021E-2	3.508E-2	8.198E-2	7.793E-2
Sa (T = 1.0 sec)	8.676E-2	7.844E-2	4.753E-2	5.345E-2	1.050E-1	1.035E-1	7.389E-2	7.753E-2	2.799E-1	3.376E-1	1.550E-1	1.549E-1	3.649E-2	3.572E-2	4.568E-2	4.297E-2
Sa (T = 1.5 sec)	7.716E-2	8.722E-2	3.127E-2	3.280E-2	7.669E-2	7.367E-2	6.044E-2	5.764E-2	2.307E-1	2.458E-1	7.155E-2	7.190E-2	2.723E-2	2.833E-2	2.289E-2	2.368E-2
Sa (T = 2.0 sec)	4.750E-2	5.473E-2	1.473E-2	1.484E-2	5.707E-2	5.333E-2	7.753E-2	7.951E-2	1.693E-1	1.533E-1	4.770E-2	4.908E-2	2.139E-2	1.956E-2	1.107E-2	1.056E-2
Sa (T = 3.0 sec)	3.474E-2	3.865E-2	9.911E-3	9.907E-3	4.096E-2	4.208E-2	4.500E-2	4.172E-2	6.018E-2	6.268E-2	2.784E-2	2.683E-2	2.136E-2	2.065E-2	7.976E-3	8.358E-3
Sa (T = 4.0 sec)	3.400E-2	2.814E-2	6.161E-3	6.043E-3	6.305E-2	6.181E-2	3.747E-2	5.013E-2	6.103E-2	5.603E-2	2.600E-2	2.416E-2	1.100E-2	1.115E-2	3.706E-3	3.813E-3
Sa (T = 5.0 sec)					3.627E-2	3.562E-2	2.676E-2	2.639E-2	4.153E-2	3.593E-2	1.826E-2	1.754E-2			4.169E-3	4.268E-3
Sa (T = 7.5 sec)					1.142E-2	1.130E-2	1.407E-2	1.487E-2			5.385E-3	4.920E-3			2.600E-3	2.597E-3
Sa (T = 10.0 sec)															1.558E-3	1.406E-3

Appendix C:
R CODE FOR IMPLEMENTATION OF THE NGA RELATIONS

In this appendix, we present our *R* code for the numerical implementation of the five NGA models explored in this study. To implement any of these GMPEs using the open-source statistical language and environment *R*, the user should simply cut and paste the code for that particular GMPE into the *R* console. Because the models have similar notations, please do not mix the code from different GMPEs within the same *R* console. Users may compare the results of different models simultaneously by using multiple *R* consoles simultaneously. The code for each model begins with the definitions of the model coefficients, is followed by the necessary background calculations, and ends with the function for spectral acceleration (*Sa*).

After the code has been entered into *R*, the user should type the desired explanatory variables within the function Sa and then press `Enter` to obtain a result. For example, to obtain the BA08 median estimate of *Sa* at 1.0 second for a strike-slip *M* 6.5 earthquake at a site with R_{JB} = 20 km and V_{S30} = 500 m/sec, the user would type

```
Sa(M = 6.5, Rjb = 20, RS = 0, NS = 0, SS = 1, U = 0, Vs30 = 500, T = 1)
```

into the *R* console, with the code for BA08 already entered. As long as the variable names are entered into the parentheses, the order of the variables does not matter. For example, the function call

```
Sa(T = 1, M = 6.5, Rjb = 20, RS = 0, NS = 0, SS = 1, U = 0, Vs30 = 500)
```

which has the period first (rather than last) would yield the same result as the previous call. If the variable names are *not* entered into the parentheses, the order of the variables must be identical to the order in the function definition. For example, typing

```
Sa(6.5, 20, 0, 0, 1, 0, 500, 1)
```

would yield the same result as the two function calls above. Because this thesis has focused upon the median estimates of earthquake ground motion, only the median ground motion prediction equations are currently implemented. Future work will involve the implementation of the equations for the uncertainties of the models' median estimates.

To evaluate spectral acceleration at a given period, the appropriate period should be entered for *T* within the parentheses of the *R* function Sa. As presented in Table 2.5, each model has a specified allowable range of *T*; values of *T* without defined model coefficients will not yield a result. To evaluate *PGA* or *PGV*, the user should enter "−1" or "−2" for *T*, respectively. Details on the explanatory variables for each model are presented in Appendix A, but there are brief comments in the code as well. Comments in *R* are specified with the number sign, #. The specified equations and tables in the code refer to the original papers in which the models were published.

Information about *R* and its internal functions may be obtained at the website of the *R* Project for Statistical Computing, <http://www.r-project.org/>. For a simple understanding of *R* when reading the code, the following tips might be useful:

- Assignment in *R* is specified with the following arrow-like symbol: <-
- A list or vector **x** composed of *n* elements (x_1, x_2, . . . , x_n) is specified using the "c" function in R:

  ```
  x <- c(x1, x2, ... , xn)
  ```

  To access any element *i* of the vector **x**, use brackets: `x[i]`
- For example, a function $z(x, y) = 2x + 2y$ with input parameters *x* and *y* would be defined as:

  ```
  z <- function(x, y)  {return(2*x + 2*y)}
  ```

  Of course, the definitions of more complicated functions may require several lines. It is not absolutely necessary to use `return()` at the bottom of the function, but it is good form to do so.
- The naming of intrinsic functions in *R* is generally intuitive (such as `sqrt` and `exp`), but the intrinsic function `log` refers to the natural logarithm, not the base 10 logarithm.

Future work will involve the creation of a fully documented *R* package for implementing the NGA relations, which will be publicly available for download. In addition to the Excel and FORTRAN implementations currently available on the PEER web site, the *R* package will be a useful addition to the scientific community for performing calculations with the NGA relations.

C.1 Abrahamson and Silva (2008)

```
# 1. MODEL COEFFICIENTS

# a. List of periods with defined coefficients (PGA is -1 and PGV is -2)
Period.list <- c(-1.0, 0.01, 0.02, 0.03, 0.04, 0.05, 0.075, 0.10, 0.15, 0.20, 0.25,
                 0.30, 0.40, 0.50, 0.75, 1.0, 1.5, 2.0, 3.0, 4.0, 5.0, 7.5, 10.0, -2.0)


# b. Define list of coefficients (Tables 4, 5a, and 5b)

Vlin.list <- c(865.1, 865.1, 865.1, 907.8, 994.5, 1053.5, 1085.7, 1032.5, 877.6, 748.2,
               654.3, 587.1, 503.0, 456.6, 410.5, 400.0, 400.0, 400.0, 400.0, 400.0,
               400.0, 400.0, 400.0, 400.0)

b.list <- c(-1.186, -1.186, -1.219, -1.273, -1.308, -1.346, -1.471, -1.624, -1.931,
            -2.188, -2.381, -2.518, -2.657, -2.669, -2.401, -1.955, -1.025, -0.299,
            0.000, 0.000, 0.000, 0.000, 0.000, -1.955)

a1.list <- c(0.804, 0.811, 0.855, 0.962, 1.037, 1.133, 1.375, 1.563, 1.716, 1.687,
             1.646, 1.601, 1.511, 1.397, 1.137, 0.915, 0.510, 0.192, -0.280, -0.639,
             -0.936, -1.527, -1.993, 5.7578)

a2.list <- c(-0.9679, -0.9679, -0.9774, -1.0024, -1.0289, -1.0508, -1.0810, -1.0833,
             -1.0357, -0.9700, -0.9202, -0.8974, -0.8677, -0.8475, -0.8206, -0.8088,
             -0.7995, -0.7960, -0.7960, -0.7960, -0.7960, -0.7960, -0.7960, -0.9046)

a3.list <- c(0.265, 0.265, 0.265, 0.265, 0.265, 0.265, 0.265, 0.265, 0.265, 0.265,
             0.265, 0.265, 0.265, 0.265, 0.265, 0.265, 0.265, 0.265, 0.265, 0.265,
             0.265, 0.265, 0.265, 0.265)

a4.list <- c(-0.231, -0.231, -0.231, -0.231, -0.231, -0.231, -0.231, -0.231, -0.231,
             -0.231, -0.231, -0.231, -0.231, -0.231, -0.231, -0.231, -0.231, -0.231,
             -0.231, -0.231, -0.231, -0.231, -0.231, -0.231)

a5.list<- c(-0.398, -0.398, -0.398, -0.398, -0.398, -0.398, -0.398, -0.398, -0.398,
            -0.398, -0.398, -0.398, -0.398, -0.398, -0.398, -0.398, -0.398, -0.398,
            -0.398, -0.398, -0.398, -0.398, -0.398, -0.398)

a8.list <- c(-0.0372, -0.0372, -0.0372, -0.0372, -0.0315, -0.0271, -0.0191, -0.0166,
             -0.0254, -0.0396, -0.0539, -0.0656, -0.0807, -0.0924, -0.1137, -0.1289,
             -0.1534, -0.1708, -0.1954, -0.2128, -0.2263, -0.2509, -0.2683, -0.1200)

a10.list <- c(0.9445, 0.9445, 0.9834, 1.0471, 1.0884, 1.1333, 1.2808, 1.4613, 1.8071,
              2.0773, 2.2794, 2.4201, 2.5510, 2.5395, 2.1493, 1.5705, 0.3991, -0.6072,
              -0.9600, -0.9600, -0.9208, -0.7700, -0.6630, 1.5390)

a12.list <- c(0.0000, 0.0000, 0.0000, 0.0000, 0.0000, 0.0000, 0.0000, 0.0000, 0.0181,
              0.0309, 0.0409, 0.0491, 0.0619, 0.0719, 0.0800, 0.0800, 0.0800, 0.0800,
              0.0800, 0.0800, 0.0800, 0.0800, 0.0800, 0.0800)

a13.list <- c(-0.0600, -0.0600, -0.0600, -0.0600, -0.0600, -0.0600, -0.0600, -0.0600,
              -0.0600, -0.0600, -0.0600, -0.0600, -0.0600, -0.0600, -0.0600, -0.0600,
              -0.0600, -0.0600, -0.0600, -0.0600, -0.0600, -0.0600, -0.0600, -0.0600)

a14.list <- c(1.0800, 1.0800, 1.0800, 1.1331, 1.1708, 1.2000, 1.2000, 1.2000, 1.1683,
              1.1274, 1.0956, 1.0697, 1.0288, 0.9971, 0.9395, 0.8985, 0.8409, 0.8000,
              0.4793, 0.2518, 0.0754, 0.0000, 0.0000, 0.7000)

a15.list <- c(-0.3500, -0.3500, -0.3500, -0.3500, -0.3500, -0.3500, -0.3500, -0.3500,
              -0.3500, -0.3500, -0.3500, -0.3500, -0.3500, -0.3500, -0.3191, -0.2629, -0.2230,
              -0.1668, -0.1270, -0.0708, -0.0309, 0.0000, 0.0000, 0.0000, -0.3900)

a16.list <- c(0.9000, 0.9000, 0.9000, 0.9000, 0.9000, 0.9000, 0.9000, 0.9000,
              0.9000, 0.9000, 0.9000, 0.9000, 0.8423, 0.7458, 0.5704, 0.4460, 0.2707,
              0.1463, -0.0291, -0.1535, -0.2500, -0.2500, -0.2500, 0.6300)
```

```
a18.list <- c(-0.0067, -0.0067, -0.0067, -0.0067, -0.0067, -0.0076, -0.0093, -0.0093,
              -0.0093, -0.0083, -0.0069, -0.0057, -0.0039, -0.0025, 0.0000, 0.0000,
              0.0000, 0.0000, 0.0000, 0.0000, 0.0000, 0.0000, 0.0000, 0.0000)


# c. Assign coefficients using the intrinsic R "match" function;
#    this matches the period with the appropriate coefficient for that period
Vlin <- function(T) {Vlin.list[match(T, Period.list)]}
b <- function(T) {b.list[match(T, Period.list)]}
a1 <- function(T) {a1.list[match(T, Period.list)]}
a2 <- function(T) {a2.list[match(T, Period.list)]}
a3 <- function(T) {a3.list[match(T, Period.list)]}
a4 <- function(T) {a4.list[match(T, Period.list)]}
a5 <- function(T) {a5.list[match(T, Period.list)]}
a8 <- function(T) {a8.list[match(T, Period.list)]}
a10 <- function(T) {a10.list[match(T, Period.list)]}
a12 <- function(T) {a12.list[match(T, Period.list)]}
a13 <- function(T) {a13.list[match(T, Period.list)]}
a14 <- function(T) {a14.list[match(T, Period.list)]}
a15 <- function(T) {a15.list[match(T, Period.list)]}
a16 <- function(T) {a16.list[match(T, Period.list)]}
a18 <- function(T) {a18.list[match(T, Period.list)]}


# d. Assign coefficients that are constants, i.e. period independent (Table 4)
c <- 1.88
c1 <- 6.75
c2 <- 50
c4 <- 4.5
n <- 1.18




# 2. FUNCTIONS FOR INTERPOLATION (need for constant displacement model)

# a. Write interpolation function (log-linear space)
interpolation <- function(x1, x2, y1, y2, x)
{
  # Interpolate for intermediate values
  if(x > x1) {approx(c(log(x1), log(x2)), c(y1, y2), log(x))$y} else

  # No interpolation necessary
  {y1}
}


# b. Given a period T*, find the index of the first period T1
#    BELOW T* that has defined model coefficients
lowerbound <- function(T)
{
  i <- 2
  for(i in 2:22)
    {if(T >= Period.list[i] & T <= Period.list[i+1] & T > 0)  {return(i)}}
}


# c. Given a period T*, find the index of the first period T2
#    ABOVE T* that has defined model coefficients
upperbound <- function(T)
{
  i <- 2
  for(i in 2:22)
    {if(T >= Period.list[i] & T <= Period.list[i+1] & T > 0)  {return(i + 1)}}
}
```

```
# 3. BACKGROUND FUNCTIONS FOR CALCULATING MEDIAN GROUND MOTION

# a. Base Model
f1 <- function(M, Rrup, T)
  {

    # Calculate R (Eqn 3)
    R <- sqrt(Rrup^2 + c4^2)

    # Return f1 (Eqn 2)
    if(M <= c1)
      {return(a1(T) + a4(T)*(M - c1) + a8(T)*(8.5 - M)^2 +
       (a2(T) + a3(T)*(M - c1))*log(R))} else
    if(M > c1)
      {return(a1(T) + a5(T)*(M - c1) + a8(T)*(8.5 - M)^2 +
       (a2(T) + a3(T)*(M - c1))*log(R))}
  }


# b. Site Response Model
f5 <- function(PGA1100, Vs30, T)
  {

    # Calculate V1 (Eqn 6)
    if(T == -2) {V1 <- 862} else  #PGV
    if(T <= 0.5) {V1 <- 1500} else
    if(T > 0.5 & T <= 1) {V1 <- exp(8 - 0.795*log(T/0.21))} else
    if(T > 1 & T < 2) {V1 <- exp(6.76 - 0.297*log(T))} else
    if(T >= 2) V1 <- 700

    # Calculate Vs30star (Eqn 5)
    if(Vs30 < V1) {Vs30star <- Vs30} else
    if(Vs30 >= V1) {Vs30star <- V1}

    # Return f5 (Eqn 4)
    if(Vs30 < Vlin(T))
      {return(a10(T)*log(Vs30star/Vlin(T)) - b(T)*log(PGA1100 + c) +
              b(T)*log(PGA1100 + c*(Vs30star/Vlin(T))^n))} else
    if(Vs30 >= Vlin(T))
      {return((a10(T) + b(T)*n)*log(Vs30star/Vlin(T)))}
  }


# c. Hanging Wall Model
f4 <- function(Rjb, Rx, dip, Ztor, M, W, T)
  {

    # Calculate tapers

    # T1 (Eqn 8)
    if(Rjb < 30) {T1 <- 1 - Rjb/30} else
    if(Rjb >= 30) {T1 <- 0}

    # T2 (Eqn 9)
    if(Rx > W*cos(dip*pi/180) | dip == 90) {T2 <- 1} else
    T2 <- 0.5 + Rx/(2*W*cos(dip*pi/180))

    # T3 (Eqn 10)
    if(Rx >= Ztor) {T3 <- 1} else
    if(Rx < Ztor) {T3 <- Rx/Ztor}

    # T4 (Eqn 11)
    if(M <= 6) {T4 <- 0} else
    if(M > 6 & M < 7) {T4 <- M - 6} else
    if(M >= 7) {T4 <- 1}

    # T5 (Eqn 12)
    if(dip >= 70) {T5 <- 1 - (dip - 70)/20} else
    if(dip < 70) {T5 <- 1}
```

```
    # Return f4 (Eqn 7)
    return(a14(T)*T1*T2*T3*T4*T5)
  }


# d. Depth to Top of Rupture Model (Eqn 13)
f6 <- function(Ztor, T)
  {
    if(Ztor < 10) {return(a16(T)*Ztor/10)} else
    if(Ztor >= 10) {return(a16(T))}
  }


# e. Large Distance Model
f8 <- function(Rrup, M, T)
  {

    # Calculate Taper 6 (Eqn 15)
    if(M < 5.5) {T6 <- 1} else
    if(M >= 5.5 & M <= 6.5) {T6 = 0.5*(6.5 - M) + 0.5} else
    if(M > 6.5) {T6 <- 0.5}

    # Return f8 (Eqn 14)
    if(Rrup < 100) {return(0)}  else
    if(Rrup >=100) {return(a18(T)*(Rrup - 100)*T6)}
  }


# f. Soil Depth Model
f10 <- function(Z1.0, Vs30, T)
  {

    # Calculate V1 (Eqn 6)
    if(T == -2) {V1 <- 862} else  #PGV
    if(T <= 0.5) {V1 <- 1500} else
    if(T > 0.5 & T <= 1) {V1 <- exp(8 - 0.795*log(T/0.21))} else
    if(T > 1 & T < 2) {V1 <- exp(6.76 - 0.297*log(T))} else
    if(T >= 2) V1 <- 700

    # Calculate Vs30star (Eqn 5)
    if(Vs30 < V1) {Vs30star <- Vs30} else {Vs30star <- V1}

    # Obtain Ln of Median Z1.0 (Eqn 17)
    if(Vs30 < 180) {LnMedianZ1.0 <- 6.745} else
    if(Vs30 >= 180 & Vs30 <= 500) {LnMedianZ1.0 <- 6.745 - 1.35*log(Vs30/180)} else
    if(Vs30 > 500) {LnMedianZ1.0 <- 5.394 - 4.48*log(Vs30/500)}

    # Obtain Median Z1.0
    MedianZ1.0 <- exp(LnMedianZ1.0)

    # Calculate e2 (Eqn 19)
    if(T == -2) {e2 <- -0.25 * log(Vs30/1000) * log(1/0.35)} else  #PGV
    if(T < 0.35 | Vs30 > 1000) {e2 <- 0} else
    if(T >= 0.35 & T <= 2) {e2 <- -0.25 * log(Vs30/1000) * log(T/0.35)} else
    if(T > 2) {e2 <- -0.25 * log(Vs30/1000) * log(2/0.35)}

    # Calculate a21 (Eqn 18)
    if(Vs30 >= 1000) {a21 <- 0} else
    if((a10(T) + b(T)*n)*log(Vs30star / min(V1, 1000)) +
         e2*log((Z1.0 + c2)/(MedianZ1.0 + c2)) < 0)
       {a21 <- -(a10(T) + b(T)*n)*log(Vs30star / min(V1, 1000)) /
                     log((Z1.0 + c2)/(MedianZ1.0 + c2))} else
    {a21 <- e2}

    # Calculate a22 (Eqn 20)
    if(T < 2) {a22 <- 0} else
    if(T >= 2) {a22 <- 0.0625*(T - 2)}
```

```
    # Return f10 (Eqn 16)
    if(Z1.0 >= 200)
      {return(a21*log((Z1.0 + c2) / (MedianZ1.0 + c2)) + a22*log(Z1.0/200))} else
    if(Z1.0 < 200)
      {return(a21*log((Z1.0 + c2) / (MedianZ1.0 + c2)))}
  }


# 4. FINAL FUNCTION FOR CALCULATING Sa, PGA, and PGV  (Eqn 1)
Sa <- function(M, Rrup, Rjb, Rx, Ztor, Frv, Fnm, Fas, Fhw, dip, Vs30, Z1.0, W, T)
  {

    # a. Calculation of PGA1100, the median PGA when Vs30 = 1100 m/s
    Vs30.rock <- 1100
    Z1.0.rock <- exp(5.394 - 4.48*log(Vs30.rock/500))   # 6.43 m
    PGA1100.rock <- 0
    LnSa.rock <- f1(M, Rrup, T = -1) + a12(T = -1)*Frv + a13(T = -1)*Fnm +
      a15(T = -1)*Fas + f5(PGA1100.rock, Vs30.rock, T = -1) +
      Fhw*f4(Rjb, Rx, dip, Ztor, M, W, T = -1) + f6(Ztor, T = -1) + f8(Rrup, M, T = -1) +
      f10(Z1.0.rock, Vs30.rock, T = -1)
    PGA1100 <- exp(LnSa.rock)

    # b. Calculate cutoff period for constant displacement Model (Eqn 21)
    LogTd <- -1.25 + 0.3*M
    Td <- min(10^(LogTd), 10)

    # c. Do not apply constant displacement model for T <= Td
    if(T <= Td)
      {
        LnSa <- f1(M, Rrup, T) + a12(T)*Frv + a13(T)*Fnm + a15(T)*Fas +
          f5(PGA1100, Vs30, T) + Fhw*f4(Rjb, Rx, dip, Ztor, M, W, T) +
          f6(Ztor, T) + f8(Rrup, M, T) + f10(Z1.0, Vs30, T)

        return(exp(LnSa))

      }  else

    # d. Apply constant displacement model for T > Td
    #    (modification of Eqn 22 to fix an error in the printed equation)
      {
        # Calculate LnSa.rock.Td (Rock Sa at Td for Vs30 = 1100 m/s)
        # Lower bound Td for interpolation
        Td1 <- Period.list[lowerbound(Td)]
        LnSa.rock.Td1 <- f1(M, Rrup, T = Td1) + a12(T = Td1)*Frv +
          a13(T = Td1)*Fnm + a15(T = Td1)*Fas + f5(PGA1100,Vs30.rock, T = Td1) +
          Fhw*f4(Rjb, Rx, dip, Ztor, M, W, T = Td1) +
          f6(Ztor, T = Td1) + f8(Rrup, M, T = Td1) + f10(Z1.0.rock, Vs30.rock, T = Td1)
        # Upper bound Td for interpolation
        Td2 <- Period.list[upperbound(Td)]
        LnSa.rock.Td2 <- f1(M, Rrup, T = Td2) + a12(T = Td2)*Frv +
          a13(T = Td2)*Fnm + a15(T = Td2)*Fas + f5(PGA1100, Vs30.rock, T = Td2) +
          Fhw*f4(Rjb, Rx, dip, Ztor, M, W, T = Td2) +
          f6(Ztor, T = Td2) + f8(Rrup, M, T = Td2) + f10(Z1.0.rock, Vs30.rock, T = Td2)
        # Actual Td, computed by interpolation
        LnSa.rock.Td <- interpolation(Td1, Td2, LnSa.rock.Td1, LnSa.rock.Td2, Td)

        # Calculate LnSa.rock.T (scale the Rock Sa to the spectral period T)
        LnSa.rock.T <- LnSa.rock.Td + log((Td/T)^2)

        # Calculate soil amplification
        SiteResponse.soil <- f5(PGA1100, Vs30, T) + f10(Z1.0, Vs30, T)
        SiteResponse.rock <- f5(PGA1100, Vs30.rock, T) + f10(Z1.0.rock, Vs30.rock, T)
        Soil.amp <- SiteResponse.soil - SiteResponse.rock

        # Calculate final spectral acceleration
        LnSaConstDisp <- LnSa.rock.T + Soil.amp

        return(exp(LnSaConstDisp))
      }
  }
```

```
# REQUIRED INPUTS TO THE Sa FUNCTION:
#   M = Moment magnitude
#   Rrup = Rupture distance (km)
#   Rjb = Joyner-Boore distance (km)
#   Rx = Site coordinate (km)
#   Ztor = Depth to top of rupture (km)
#   Frv = Reverse style-of-faulting flag (0 or 1)
#   Fnm = Normal style-of-faulting flag (0 or 1)
#   Fas = Aftershock flag (0 or 1)
#   Fhw = Hanging wall flag (0 or 1)
#   dip = Fault dip (deg)
#   Vs30 = Time-averaged shear wave velocity over 30 m subsurface depth  (m/sec)
#   Z1.0 = Depth to Vs = 1.0 km/sec  (m)
#   W = Down-dip rupture width (km)
#   T = Spectral period, sec (-1 for PGA; -2 for PGV)
```

C.2 Boore and Atkinson (2008)

```
# 1. MODEL COEFFICIENTS

# a. List of periods with defined coefficients (PGA is -1; PGV is -2)
Period.list <- c(-2.0, -1.0, 0.01, 0.02, 0.03, 0.05, 0.075, 0.10, 0.15, 0.20, 0.25,
                 0.30, 0.40, 0.50, 0.75, 1.0, 1.5, 2.0, 3.0, 4.0, 5.0, 7.5, 10.0)


# b. List of distance-scaling coefficients (Table 6)
c1.list <- c(-0.87370, -0.66050, -0.66220, -0.66600, -0.69010, -0.71700, -0.72050,
             -0.70810, -0.69610, -0.58300, -0.57260, -0.55430, -0.64430, -0.69140,
             -0.74080, -0.81830, -0.83030, -0.82850, -0.78440, -0.68540, -0.50960,
             -0.37240, -0.09824)

c2.list <- c(0.10060, 0.11970, 0.12000, 0.12280, 0.12830, 0.13170, 0.12370, 0.11170,
             0.09884, 0.04273, 0.02977, 0.01955, 0.04394, 0.06080, 0.07518, 0.10270,
             0.09793, 0.09432, 0.07282, 0.03758, -0.02391, -0.06568, -0.13800)

c3.list <- c(-0.00334, -0.01151, -0.01151, -0.01151, -0.01151, -0.01151, -0.01151,
             -0.01151, -0.01113, -0.00952, -0.00837, -0.00750, -0.00626, -0.00540,
             -0.00409, -0.00334, -0.00255, -0.00217, -0.00191, -0.00191, -0.00191,
             -0.00191, -0.00191)

h.list <- c(2.54, 1.35, 1.35, 1.35, 1.35, 1.35, 1.55, 1.68, 1.86, 1.98, 2.07, 2.14,
            2.24, 2.32, 2.46, 2.54, 2.66, 2.73, 2.83, 2.89, 2.93, 3.00, 3.04)


# c. List of magnitude-scaling coefficients (Table 7)
e1.list <- c(5.00121, -0.53804, -0.52883, -0.52192, -0.45285, -0.28476, 0.00767,
             0.20109, 0.46128, 0.57180, 0.51884, 0.43825, 0.39220, 0.18957, -0.21338,
             -0.46896, -0.86271, -1.22652, -1.82979, -2.24656, -1.28408, -1.43145,
             -2.15446)

e2.list <- c(5.04727, -0.50350, -0.49429, -0.48508, -0.41831, -0.25022, 0.04912,
             0.23102, 0.48661, 0.59253, 0.53496, 0.44516, 0.40602, 0.19878,
             -0.19496, -0.43443, -0.79593, -1.15514, -1.74690, -2.15906, -1.21270,
             -1.31632, -2.16137)

e3.list <- c(4.63188, -0.75472, -0.74551, -0.73906, -0.66722, -0.48462, -0.20578,
             0.03058, 0.30185, 0.4086, 0.3388, 0.25356, 0.21398, 0.00967, -0.49176,
             -0.78465, -1.20902, -1.57697, -2.22584, -2.58228, -1.50904, -1.81022,
             -2.53323)

e4.list <- c(5.0821, -0.5097, -0.49966, -0.48895, -0.42229, -0.26092, 0.02706, 0.22193,
             0.49328, 0.61472, 0.57747, 0.5199, 0.4608, 0.26337, -0.10813, -0.3933,
             -0.88085, -1.27669, -1.91814, -2.38168, -1.41093, -1.59217, -2.14635)

e5.list <- c(0.18322, 0.28805, 0.28897, 0.25144, 0.17976, 0.06369, 0.0117, 0.04697,
             0.1799, 0.52729, 0.6088, 0.64472, 0.7861, 0.76837, 0.75179, 0.6788,
             0.70689, 0.77989, 0.77966, 1.24961, 0.14271, 0.52407, 0.40387)

e6.list <- c(-0.12736, -0.10164, -0.10019, -0.11006, -0.12858, -0.15752, -0.17051,
             -0.15948, -0.14539, -0.12964, -0.13843, -0.15694, -0.07843, -0.09054,
             -0.14053, -0.18257, -0.2595, -0.29657, -0.45384, -0.35874, -0.39006,
             -0.37578, -0.48492)

e7.list <- c(0, 0, 0, 0, 0, 0, 0, 0, 0, 0.00102, 0.08607, 0.10601, 0.02262, 0,
             0.10302, 0.05393, 0.19082, 0.29888, 0.67466, 0.79508, 0, 0, 0)

Mh.list <- c(8.5, 6.75, 6.75, 6.75, 6.75, 6.75, 6.75, 6.75, 6.75, 6.75, 6.75, 6.75,
             6.75, 6.75, 6.75, 6.75, 6.75, 6.75, 6.75, 6.75, 8.5, 8.5, 8.5)

Mref <- 4.5

Rref <- 1.0
```

```
# d. List of site-amplification coefficients (period-dependent), Table 3
blin.list <- c(-0.6, -0.36, -0.36, -0.34, -0.33, -0.29, -0.23, -0.25, -0.28, -0.31,
               -0.39, -0.44, -0.5, -0.6, -0.69, -0.7, -0.72, -0.73, -0.74, -0.75,
               -0.75, -0.692, -0.65)

b1.list <- c(-0.5, -0.64, -0.64, -0.63, -0.62, -0.64, -0.64, -0.6, -0.53, -0.52,
             -0.52, -0.52, -0.51, -0.5, -0.47, -0.44, -0.4, -0.38, -0.34, -0.31,
             -0.291, -0.247, -0.215)

b2.list <- c(-0.06, -0.14, -0.14, -0.12, -0.11, -0.11, -0.11, -0.13, -0.18,
             -0.19, -0.16, -0.14, -0.1, -0.06, 0 , 0, 0, 0, 0, 0, 0, 0, 0)


# e. List of site-amplification coefficients (period-independent), Table 4
a1 <- 0.03
pga.low <- 0.06
a2 <- 0.09
V1 <- 180
V2 <- 300
Vref <- 760


# f. Assign coefficients using the intrinsic R "match" function;
#    this matches the period with the appropriate coefficient for that period
c1 <- function(T) {c1.list[match(T, Period.list)]}
c2 <- function(T) {c2.list[match(T, Period.list)]}
c3 <- function(T) {c3.list[match(T, Period.list)]}
h <- function(T) {h.list[match(T, Period.list)]}
e1 <- function(T) {e1.list[match(T, Period.list)]}
e2 <- function(T) {e2.list[match(T, Period.list)]}
e3 <- function(T) {e3.list[match(T, Period.list)]}
e4 <- function(T) {e4.list[match(T, Period.list)]}
e5 <- function(T) {e5.list[match(T, Period.list)]}
e6 <- function(T) {e6.list[match(T, Period.list)]}
e7 <- function(T) {e7.list[match(T, Period.list)]}
Mh <- function(T) {Mh.list[match(T, Period.list)]}
blin <- function(T) {blin.list[match(T, Period.list)]}
b1 <- function(T) {b1.list[match(T, Period.list)]}
b2 <- function(T) {b2.list[match(T, Period.list)]}



# 2. FUNCTIONS FOR DUMMY VARIABLES FOR DIFFERENT FAULT TYPES (Table 2).
#     The user only needs to input the fault type ("unspecified," "strike slip",
#     "normal", or "reverse"), instead of manually inputting all the dummy
#     variables U, SS, NS, and RS.  These functions determine the values of the
#     dummy variables from the fault type that the user enters.

U <- function(Fault.Type)
  {
    Fault.Type <- toupper(Fault.Type)
    if(Fault.Type == "UNSPECIFIED" | Fault.Type == "U") {1} else {0}
  }

SS <- function(Fault.Type)
  {
    Fault.Type <- toupper(Fault.Type)
    if(Fault.Type == "STRIKE-SLIP" | Fault.Type == "STRIKE SLIP" |
       Fault.Type == "SS" | Fault.Type == "S") {1} else {0}
  }

NS <- function(Fault.Type)
  {
    Fault.Type <- toupper(Fault.Type)
    if(Fault.Type == "NORMAL" | Fault.Type == "N" |
       Fault.Type == "NM" | Fault.Type == "NS") {1} else {0}
  }
```

```
RS <- function(Fault.Type)
  {
    Fault.Type <- toupper(Fault.Type)
    if(Fault.Type == "THRUST" | Fault.Type == "REVERSE" | Fault.Type == "R" |
       Fault.Type == "RV" | Fault.Type == "RS") {1} else {0}
  }



# 3. BACKGROUND FUNCTIONS FOR CALCULATING MEDIAN GROUND MOTION

# a. Distance Function
Fd <- function(M, Rjb, T)
  {
    # Calculate R (Eqn 3)
    R <- sqrt(Rjb^2 + (h(T))^2)

    # Return Fd (Eqn 4)
    return((c1(T) + c2(T)*(M - Mref))*log(R / Rref) + c3(T)*(R - Rref))
  }


# b. Magnitude Function
Fm <- function(M, FT, T)
  {
    if(M <= Mh(T))  # Eqn 5A
      {
        return( e1(T)*U(FT) + e2(T)*SS(FT) + e3(T)*NS(FT) + e4(T)*RS(FT) +
                e5(T)*(M - Mh(T)) + e6(T)*(M - Mh(T))^2 )
      } else
    if(M > Mh(T))  # Eqn 5B
      {
        return( e1(T)*U(FT) + e2(T)*SS(FT) + e3(T)*NS(FT) + e4(T)*RS(FT) +
                 e7(T)*(M - Mh(T)))
      }
  }


# c. Site Amplification Function
Fs <- function(M, Rjb, Vs30, FT, T)
  {
    # i. LINEAR TERM (Eqn 7)
    Flin <- blin(T)*log(Vs30 / Vref)


    # ii. NONLINEAR TERM

    # Calculate pga4nl, the median PGA when Vs30 = Vref = 760 m/s
    R <- sqrt(Rjb^2 + (h(-1))^2)
    pga4nl <- exp(Fm(M, FT, -1) + (c1(-1) + c2(-1)*(M - Mref))*log(R / Rref) +
       c3(-1)*(R - Rref))

    # Calculate Nonlinear slope, bnl (Eqns 13a, 13b, and 13c)
    if(Vs30 <= V1)
      {bnl <- b1(T)} else
    if(Vs30 > V1 & Vs30 <= V2)
      {bnl <- (b1(T) - b2(T))*log(Vs30/V2) / log(V1/V2) + b2(T)} else
    if(Vs30 > V2 & Vs30 < Vref)
      {bnl <- b2(T)*log(Vs30/Vref) / log(V2/Vref)} else
    if(Vref <= Vs30)
      {bnl <- 0}

    # Calculate smoothing constants (Eqns 9, 10, 11, and 12)
    dx <- log(a2/a1)
    dy <- bnl*log(a2/pga.low)
    c <- (3*dy - bnl*dx)/(dx^2)
    d <- -(2*dy - bnl*dx)/(dx^3)
```

```
    # Final equation for nonlinear term (Eqns 8a, 8b, and 8c)
    if(pga4nl <= a1)
      {Fnl <- bnl*log(pga.low/0.1)} else
    if(pga4nl > a1 & pga4nl <= a2)
      {Fnl <- bnl*log(pga.low/0.1) + c*(log(pga4nl/a1))^2 + d*(log(pga4nl/a1))^3} else
    if(pga4nl > a2)
      {Fnl <- bnl*log(pga4nl/0.1)}

    # Return Fs (Eqn 6)
    return(Flin + Fnl)
  }



# 4. FINAL FUNCTION FOR CALCULATING Sa, PGA, and PGV  (Eqn 1)
Sa <- function(M, Rjb, Vs30, FT, T)
  {
    exp(Fm(M, FT, T) + Fd(M, Rjb, T) + Fs(M, Rjb, Vs30, FT, T))
  }


# REQUIRED INPUTS TO THE Sa FUNCTION:
#   M = Moment magnitude
#   Rjb = Joyner-Boore distance (km)
#   Vs30 = Time-averaged shear wave velocity over 30 m subsurface depth  (m/sec)
#   FT = Fault type ("unspecified", "strike-slip", "normal", or "reverse")
#   T = Spectral period, sec (-1 for PGA; -2 for PGV)
```

C.3 Campbell and Bozorgnia (2008)

```
# 1. MODEL COEFFICIENTS

# a. List of periods with defined coefficients (PGA is -1; PGV is -2)
Period.list <- c(0.01, 0.02, 0.03, 0.05, 0.075, 0.10, 0.15, 0.20, 0.25, 0.30, 0.40,
                 0.50, 0.75, 1.0, 1.5, 2.0, 3.0, 4.0, 5.0, 7.5, 10.0, -1.0, -2.0)


# b. Define list of period-dependent coefficients (Table 2)

c0.list <- c(-1.715, -1.68, -1.552, -1.209, -0.657, -0.314, -0.133, -0.486, -0.89,
             -1.171, -1.466, -2.569, -4.844, -6.406, -8.692, -9.701, -10.556, -11.212,
             -11.684, -12.505, -13.087, -1.715, 0.954)

c1.list <- c(0.5, 0.5, 0.5, 0.5, 0.5, 0.5, 0.5, 0.5, 0.5, 0.5, 0.5, 0.656, 0.972,
             1.196, 1.513, 1.6, 1.6, 1.6, 1.6, 1.6, 1.6, 0.5, 0.696)

c2.list <- c(-0.53, -0.53, -0.53, -0.53, -0.53, -0.53, -0.53, -0.446, -0.362, -0.294,
             -0.186, -0.304, -0.578, -0.772, -1.046, -0.978, -0.638, -0.316, -0.07,
             -0.07, -0.07, -0.53, -0.309)

c3.list <- c(-0.262, -0.262, -0.262, -0.267, -0.302, -0.324, -0.339, -0.398, -0.458,
             -0.511, -0.592, -0.536, -0.406, -0.314, -0.185, -0.236, -0.491, -0.77,
             -0.986, -0.656, -0.422, -0.262, -0.019)

c4.list <- c(-2.118, -2.123, -2.145, -2.199, -2.277, -2.318, -2.309, -2.22, -2.146,
             -2.095, -2.066, -2.041, -2, -2, -2, -2, -2, -2, -2, -2, -2, -2.118, -2.016)

c5.list <- c(0.17, 0.17, 0.17, 0.17, 0.17, 0.17, 0.17, 0.17, 0.17, 0.17, 0.17, 0.17,
             0.17, 0.17, 0.17, 0.17, 0.17, 0.17, 0.17, 0.17, 0.17, 0.17, 0.17)

c6.list <- c(5.6, 5.6, 5.6, 5.74, 7.09, 8.05, 8.79, 7.6, 6.58, 6.04, 5.3, 4.73, 4,
             4, 4, 4, 4, 4, 4, 4, 4, 5.6, 4)

c7.list <- c(0.28, 0.28, 0.28, 0.28, 0.28, 0.28, 0.28, 0.28, 0.28, 0.28, 0.28, 0.28,
             0.28, 0.255, 0.161, 0.094, 0, 0, 0, 0, 0, 0.28, 0.245)

c8.list <- c(-0.12, -0.12, -0.12, -0.12, -0.12, -0.099, -0.048, -0.012, 0, 0, 0, 0,
             0, 0, 0, 0, 0, 0, 0, 0, 0, -0.12, 0)

c9.list <- c(0.49, 0.49, 0.49, 0.49, 0.49, 0.49, 0.49, 0.49, 0.49, 0.49, 0.49, 0.49,
             0.49, 0.49, 0.49, 0.371, 0.154, 0, 0, 0, 0, 0.49, 0.358)

c10.list <- c(1.058, 1.102, 1.174, 1.272, 1.438, 1.604, 1.928, 2.194, 2.351, 2.46,
              2.587, 2.544, 2.133, 1.571, 0.406, -0.456, -0.82, -0.82, -0.82, -0.82,
              -0.82, 1.058, 1.694)

c11.list <- c(0.04, 0.04, 0.04, 0.04, 0.04, 0.04, 0.04, 0.04, 0.04, 0.04, 0.04, 0.04,
              0.077, 0.15, 0.253, 0.3, 0.3, 0.3, 0.3, 0.3, 0.3, 0.04, 0.092)

c12.list <- c(0.61, 0.61, 0.61, 0.61, 0.61, 0.61, 0.61, 0.61, 0.7, 0.75, 0.85, 0.883,
              1, 1, 1, 1, 1, 1, 1, 1, 1, 0.61, 1)

k1.list <- c(865, 865, 908, 1054, 1086, 1032, 878, 748, 654, 587, 503, 457, 410, 400,
             400, 400, 400, 400, 400, 400, 865, 400)

k2.list <- c(-1.186, -1.219, -1.273, -1.346, -1.471, -1.624, -1.931, -2.188, -2.381,
             -2.518, -2.657, -2.669, -2.401, -1.955, -1.025, -0.299, 0, 0, 0, 0, 0,
             -1.186, -1.955)

k3.list <- c(1.839, 1.84, 1.841, 1.843, 1.845, 1.847, 1.852, 1.856, 1.861, 1.865, 1.874,
             1.883, 1.906, 1.929, 1.974, 2.019, 2.11, 2.2, 2.291, 2.517, 2.744, 1.839,
             1.929)
```

```
# c. Define list of period-independent coefficients (Table 2)
c <- 1.88
n <- 1.18


# d. Assign coefficients using the intrinsic R "match" function;
#    this matches the period with the appropriate coefficient for that period
c0 <- function(T) {c0.list[match(T, Period.list)]}
c1 <- function(T) {c1.list[match(T, Period.list)]}
c2 <- function(T) {c2.list[match(T, Period.list)]}
c3 <- function(T) {c3.list[match(T, Period.list)]}
c4 <- function(T) {c4.list[match(T, Period.list)]}
c5 <- function(T) {c5.list[match(T, Period.list)]}
c6 <- function(T) {c6.list[match(T, Period.list)]}
c7 <- function(T) {c7.list[match(T, Period.list)]}
c8 <- function(T) {c8.list[match(T, Period.list)]}
c9 <- function(T) {c9.list[match(T, Period.list)]}
c10 <- function(T) {c10.list[match(T, Period.list)]}
c11 <- function(T) {c11.list[match(T, Period.list)]}
c12 <- function(T) {c12.list[match(T, Period.list)]}
k1 <- function(T) {k1.list[match(T, Period.list)]}
k2 <- function(T) {k2.list[match(T, Period.list)]}
k3 <- function(T) {k3.list[match(T, Period.list)]}



# 2. BACKGROUND FUNCTIONS FOR CALCULATING MEDIAN GROUND MOTION

# a. Magnitude Term (Eqn 2)
Fmag <- function(M, T)
  {
    if(M <= 5.5)
      {return(c0(T) + c1(T)*M)} else
    if(M > 5.5 & M <= 6.5)
      {return(c0(T) + c1(T)*M + c2(T)*(M - 5.5))} else
    if(M > 6.5)
      {return(c0(T) + c1(T)*M + c2(T)*(M - 5.5) + c3(T)*(M - 6.5))}
  }


# b. Distance Term (Eqn 3)
Fdist <- function(M, Rrup, T)
  {
    return((c4(T) + c5(T)*M)*log(sqrt(Rrup^2 + c6(T)^2)))
  }


# c. Fault Mechanism Term
Fflt <- function(Ztor, Frv, Fnm, T)
  {
    # Calculate Fflt.z (Eqn 5)
    if(Ztor < 1) {Fflt.z <- Ztor} else
    if(Ztor >= 1) {Fflt.z <- 1}

    # Return Fflt (Eqn 4)
    return(c7(T)*Frv*Fflt.z + c8(T)*Fnm)
  }


# d. Hanging-Wall Term
Fhng <- function(M, Rrup, Rjb, Ztor, dip, T)
  {

    # Calculate Fhng.R (Rupture Distance), Eqn 7
    if(Rjb == 0)
      {Fhng.R <- 1} else
    if(Rjb > 0 & Ztor < 1)
      {Fhng.R <- (max(Rrup, sqrt(Rjb^2 + 1)) - Rjb) / max(Rrup, sqrt(Rjb^2 + 1))} else
    if(Rjb > 0 & Ztor >= 1)
      {Fhng.R <- (Rrup - Rjb)/Rrup}
```

```
    # Calculate Fhng.M (Magnitude), Eqn 8
    if(M <= 6)
      {Fhng.M <- 0} else
    if(M > 6 & M < 6.5)
      {Fhng.M <- 2*(M - 6)} else
    if(M >= 6.5)
      {Fhng.M <- 1}

    # Calculate Fhng.Z (Depth to Top of Rupture), Eqn 9
    if(Ztor >= 20)
      {Fhng.Z <- 0} else
    if(Ztor >= 0 & Ztor < 20)
      {Fhng.Z <- (20 - Ztor)/20}

    # Calculate Fhng.dip (Dip Angle), Eqn 10
    if(dip <= 70)
      {Fhng.dip <- 1} else
    if(dip > 70)
      {Fhng.dip <- (90 - dip)/20}

    # Return Fhng, Eqn 6
    return( c9(T) * Fhng.R * Fhng.M * Fhng.Z * Fhng.dip )
  }


# e. Shallow Site Response Term
Fsite <- function(M, Rrup, Rjb, Ztor, Frv, Fnm, dip, Vs30, Z2.5,  T)
  {

    # Calculate A1100, the median PGA when Vs30 = 1100 m/s
    A1100 <- exp(Fmag(M, T = -1) + Fdist(M, Rrup, T = -1) +
       Fflt(Ztor, Frv, Fnm, T = -1) + Fhng(M, Rrup, Rjb, Ztor, dip, T = -1) +
       Fsed(Z2.5, T = -1) + (c10(T = -1) + k2(T = -1)*n)*log(1100/k1(T = -1)))

    # Return Fsite (Eqn 11)
    if(Vs30 < k1(T))
      {return(c10(T)*log(Vs30/k1(T)) +
        k2(T)*(log(A1100 + c*(Vs30/k1(T))^n) - log(A1100 + c)))} else
    if(Vs30 >= k1(T) & Vs30 < 1100)
      {return((c10(T) + k2(T)*n)*log(Vs30/k1(T)))} else
    if(Vs30 > 1100)
      {return((c10(T) + k2(T)*n)*log(1100/k1(T)))}
  }


# f. Basin Response Term (Eqn 12)
Fsed <- function(Z2.5, T)
  {
    if(Z2.5 < 1)
      {return(c11(T)*(Z2.5 - 1))} else
    if(Z2.5 >= 1 & Z2.5 <= 3)
      {return(0)} else
    if(Z2.5 > 3)
      {return(c12(T)*k3(T)*exp(-0.75)*(1 - exp(-0.25*(Z2.5-3))))}
  }




# 3. FINAL FUNCTION FOR CALCULATING Sa, PGA, and PGV  (Eqn 1)
Sa <- function(M, Rrup, Rjb, Ztor, Frv, Fnm, dip, Vs30, Z2.5, T)
  {

   # Calculate spectral acceleration
    PSA <- (exp(Fmag(M, T) + Fdist(M, Rrup, T) + Fflt(Ztor, Frv, Fnm, T) +
                Fhng(M, Rrup, Rjb, Ztor, dip, T) +
                Fsite(M, Rrup, Rjb, Ztor, Frv, Fnm, dip, Vs30, Z2.5, T) + Fsed(Z2.5, T)))
```

```
    # Check for PSA < PGA at short periods (note on page 147 of CB08 paper)
    if(T <= 0.25)
      {
        PGA <- (exp(Fmag(M, T = -1) + Fdist(M, Rrup, T = -1) +
                  Fflt(Ztor, Frv, Fnm, T = -1) +  Fhng(M, Rrup, Rjb, Ztor, dip, T = -1) +
                  Fsite(M, Rrup, Rjb, Ztor, Frv, Fnm, dip, Vs30, Z2.5, T = -1) +
                  Fsed(Z2.5, T = -1)))
        if(PSA < PGA) {return(PGA)} else  {return(PSA)}
      } else

    return(PSA)
  }


# REQUIRED INPUTS TO THE Sa FUNCTION:
#   M = Moment magnitude
#   Rrup = Rupture distance (km)
#   Rjb = Joyner-Boore distance (km)
#   Ztor = Depth to top of rupture (km)
#   Frv = Reverse style-of-faulting flag (0 or 1)
#   Fnm = Normal style-of-faulting flag (0 or 1)
#   dip = Fault dip (deg)
#   Vs30 = Time-averaged shear wave velocity over 30 m subsurface depth  (m/sec)
#   Z2.5 = Depth to Vs = 2.5 km/sec  (km)
#   T = Spectral period, sec (-1 for PGA; -2 for PGV)
```

C.4 Chiou and Youngs (2008a)

```
# 1. MODEL COEFFICIENTS

# a. List of periods with defined coefficients (PGA is -1 and PGV is -2)
Period.list  <- c(-1, 0.01, 0.02, 0.03, 0.04, 0.05, 0.075, 0.10, 0.11, 0.15, 0.20, 0.25,
                  0.30, 0.40, 0.50, 0.75, 1.0, 1.5, 2.0, 3.0, 4.0, 5.0, 7.5, 10.0, -2.0)


# b. List of coefficients (Tables 1, 2, and 3)

c1.list <- c(-1.2687, -1.2687, -1.2515, -1.1744, -1.0671, -0.9464, -0.7051, -0.5747,
             -0.5453, -0.5309, -0.6352, -0.7766, -0.9278, -1.2176, -1.4695, -1.9278,
             -2.2453, -2.7307, -3.1413, -3.7413, -4.1814, -4.5187, -5.1224, -5.5872,
             2.2884)

c1a.list <- c(0.1, 0.1, 0.1, 0.1, 0.1, 0.1, 0.1, 0.1, 0.1, 0.1, 0.1, 0.1, 0.0999,
              0.0997, 0.0991, 0.0936, 0.0766, 0.0022, -0.0591, -0.0931, -0.0982,
              -0.0994, -0.0999, -0.1, 0.1094)

c1b.list <- c(-0.255, -0.255, -0.255, -0.255, -0.255, -0.255, -0.254, -0.253, -0.2529,
              -0.25, -0.2449, -0.2382, -0.2313, -0.2146, -0.1972, -0.162, -0.14,
              -0.1184, -0.11, -0.104, -0.102, -0.101, -0.101, -0.1, -0.0626)

c2.list <- c(1.06, 1.06, 1.06, 1.06, 1.06, 1.06, 1.06, 1.06, 1.06, 1.06, 1.06, 1.06,
             1.06, 1.06, 1.06, 1.06, 1.06, 1.06, 1.06, 1.06, 1.06, 1.06, 1.06, 1.06,
             1.06)

c3.list <- c(3.45, 3.45, 3.45, 3.45, 3.45, 3.45, 3.45, 3.45, 3.45, 3.45, 3.45, 3.45,
             3.45, 3.45, 3.45, 3.45, 3.45, 3.45, 3.45, 3.45, 3.45, 3.45, 3.45, 3.45,
             3.45)

cn.list <- c(2.996, 2.996, 3.292, 3.514, 3.563, 3.547, 3.448, 3.312, 3.255, 3.044, 2.831,
             2.658, 2.505, 2.261, 2.087, 1.812, 1.648, 1.511, 1.47, 1.456, 1.465, 1.478,
             1.498, 1.502, 1.648)

cM.list <- c(4.1840, 4.1840, 4.1879, 4.1556, 4.1226, 4.1011, 4.0860, 4.1030, 4.114,
             4.1717, 4.2476, 4.3184, 4.3844, 4.4979, 4.5881, 4.7571, 4.8820, 5.0697,
             5.2173, 5.4385, 5.5977, 5.7276, 5.9891, 6.1930, 4.2979)

c4.list <- c(-2.1, -2.1, -2.1, -2.1, -2.1, -2.1, -2.1, -2.1, -2.1, -2.1, -2.1, -2.1,
             -2.1, -2.1, -2.1, -2.1, -2.1, -2.1, -2.1, -2.1, -2.1, -2.1, -2.1, -2.1,
             -2.1)

c4a.list <- c(-0.5, -0.5, -0.5, -0.5, -0.5, -0.5, -0.5, -0.5, -0.5, -0.5, -0.5, -0.5,
              -0.5, -0.5, -0.5, -0.5, -0.5, -0.5, -0.5, -0.5, -0.5, -0.5, -0.5, -0.5,
              -0.5)

cRB.list <- c(50, 50, 50, 50, 50, 50, 50, 50, 50, 50, 50, 50, 50, 50, 50, 50, 50, 50,
              50, 50, 50, 50, 50, 50, 50)

c5.list <- c(6.16, 6.16, 6.158, 6.155, 6.1508, 6.1441, 6.12, 6.085, 6.0683, 5.9871,
             5.8699, 5.7547, 5.6527, 5.4997, 5.4029, 5.29, 5.248, 5.2194, 5.2099,
             5.204, 5.202, 5.201, 5.2, 5.2, 5.17)

c6.list <- c(0.4893, 0.4893, 0.4892, 0.489, 0.4888, 0.4884, 0.4872, 0.4854, 0.4846,
             0.4808, 0.4755, 0.4706, 0.4665, 0.4607, 0.4571, 0.4531, 0.4517, 0.4507,
             0.4504, 0.4501, 0.4501, 0.45, 0.45, 0.45, 0.4407)

cHM.list <- c(3, 3, 3, 3, 3, 3, 3, 3, 3, 3, 3, 3, 3, 3, 3, 3, 3, 3, 3, 3, 3, 3, 3, 3, 3)

c7.list <- c(0.0512, 0.0512, 0.0512, 0.0511, 0.0508, 0.0504, 0.0495, 0.0489, 0.0486,
             0.0479, 0.0471, 0.0464, 0.0458, 0.0445, 0.0429, 0.0387, 0.035, 0.028,
             0.0213, 0.0106, 0.0041, 0.001, 0, 0, 0.0207)
```

```
c7a.list <- c(0.0860, 0.0860, 0.0860, 0.0860, 0.0860, 0.0860, 0.0860, 0.0860,
              0.0860, 0.0860, 0.0860, 0.0860, 0.0860, 0.0850, 0.0830, 0.0690,
              0.0450, 0.0134, 0.0040, 0.0010, 0, 0, 0, 0, 0.0437)

c9.list <- c(0.79, 0.79, 0.8129, 0.8439, 0.874, 0.8996, 0.9442, 0.9677, 0.9718,
             0.966, 0.9334, 0.8946, 0.859, 0.8019, 0.7578, 0.6788, 0.6196, 0.5101,
             0.3917, 0.1244, 0.0086, 0, 0, 0, 0.3079)

c9a.list <- c(1.5005, 1.5005, 1.5028, 1.5071, 1.5138, 1.523, 1.5597, 1.6104,
              1.6384, 1.7549, 1.9157, 2.0709, 2.2005, 2.3886, 2.5, 2.6224, 2.669,
              2.6985, 2.7085, 2.7145, 2.7164, 2.7172, 2.7177, 2.718, 2.669)

c10.list <-  c(-0.3218, -0.3218, -0.3323, -0.3394, -0.3453, -0.3502, -0.3579, -0.3604,
               -0.3595, -0.3565, -0.3470, -0.3379, -0.3314, -0.3256, -0.3189, -0.2702,
               -0.2059, -0.0852, 0.0160, 0.1876, 0.3378, 0.4579, 0.7514, 1.1856, -0.1166)

# NOTE:  The "g" refers to "gamma."
cg1.list <- c(-0.00804, -0.00804, -0.008113, -0.008387, -0.008754, -0.009121, -0.009733,
              -0.009753, -0.009627, -0.008832, -0.007776, -0.006877, -0.006123, -0.00498,
              -0.004199, -0.003078, -0.002464, -0.001802, -0.001467, -0.001172,
              -0.001065, -0.001016, -0.000961, -0.000937, -0.00275)

cg2.list <- c(-0.00785, -0.00785, -0.007921, -0.008189, -0.008547, -0.008906, -0.009503,
              -0.009522, -0.0094, -0.008623, -0.007592, -0.006714, -0.005979, -0.004862,
              -0.0041, -0.003005, -0.002406, -0.001759, -0.001433, -0.001145, -0.00104,
              -0.000992, - 0.000938, -0.000914, -0.00625)

cg3.list <- c(4, 4, 4, 4, 4, 4, 4, 4, 4, 4, 4, 4, 4, 4, 4, 4, 4, 4, 4, 4, 4, 4, 4, 4, 4)

# NOTE:  The coefficient "f" means "phi."
f1.list <- c(-0.4417, -0.4417, -0.434, -0.4177, -0.4, -0.3903, -0.404, -0.4423, -0.4585,
             -0.5162, -0.5697, -0.6109, -0.6444, -0.6931, -0.7246, -0.7708, -0.799,
             -0.8382, -0.8663,  -0.9032, -0.9231, -0.9222, -0.8346, -0.7332, -0.7861)

f2.list <- c(-0.1417, -0.1417, -0.1364, -0.1403, -0.1591, -0.1862, -0.2538, -0.2943,
             -0.3025, -0.3113, -0.2927, -0.2662, -0.2405, -0.1975, -0.1633, -0.1028,
             -0.0699, -0.0425, -0.0302, -0.0129, -0.0016, 0, 0, 0, -0.0699)

f3.list <- c(-0.00701, -0.00701, -0.007279, -0.007354, -0.006977, -0.006467, -0.005734,
             -0.005604, -0.005644, -0.005845, -0.006141, -0.006439, -0.006704, -0.007125,
             -0.007435, -0.00812, -0.008444, -0.007707, -0.004792, -0.001828, -0.001523,
             -0.00144, -0.001369, -0.001361, -0.008444)

f4.list <- c(0.102151, 0.102151, 0.10836, 0.119888, 0.133641, 0.148927, 0.190596,
             0.230662, 0.243315, 0.266468, 0.255253, 0.231541, 0.207277, 0.165464,
             0.133828, 0.085153, 0.058595, 0.031787, 0.019716, 0.009643, 0.005379,
             0.003223, 0.001134, 0.000515, 5.41)

f5.list <- c(0.2289, 0.2289, 0.2289, 0.2289, 0.2289, 0.229, 0.2292, 0.2297, 0.2302,
             0.2326, 0.2386, 0.2497, 0.2674, 0.312, 0.361, 0.4353, 0.4629, 0.4756,
             0.4785, 0.4796, 0.4799, 0.4799, 0.48, 0.48, 0.2899)

f6.list <- c(0.014996, 0.014996, 0.014996, 0.014996, 0.014996, 0.014996, 0.014996,
             0.014996, 0.014994, 0.014988, 0.014964, 0.014881, 0.014639, 0.013493,
             0.011133, 0.006739, 0.005749, 0.005544, 0.005521, 0.005517, 0.005517,
             0.005517, 0.005517, 0.005517, 0.006718)

f7.list <- c(580, 580, 580, 580, 579.9, 579.9, 579.6, 579.2, 578.8, 577.2, 573.9,
             568.5, 560.5, 540, 512.9, 441.9, 391.8, 348.1, 332.5, 324.1, 321.7, 320.9,
             320.3, 320.1, 459)

f8.list <- c(0.07, 0.07, 0.0699, 0.0701, 0.0702, 0.0701, 0.0686, 0.0646, 0.0635, 0.0494,
             -0.0019, -0.0479, -0.0756, -0.096, -0.0998, -0.0765, -0.0412, 0.014, 0.0544,
             0.1232, 0.1859, 0.2295, 0.266, 0.2682, 0.1138)
```

```
# c. Assign coefficients using the intrinsic R "match" function;
#    this matches the period with the appropriate coefficient for that period
c1 <- function(T) {c1.list[match(T, Period.list)]}
c1a <- function(T) {c1a.list[match(T, Period.list)]}
c1b <- function(T) {c1b.list[match(T, Period.list)]}
c2 <- function(T) {c2.list[match(T, Period.list)]}
c3 <- function(T) {c3.list[match(T, Period.list)]}
cn <- function(T) {cn.list[match(T, Period.list)]}
cM <- function(T) {cM.list[match(T, Period.list)]}
c4 <- function(T) {c4.list[match(T, Period.list)]}
c4a <- function(T) {c4a.list[match(T, Period.list)]}
cRB <- function(T) {cRB.list[match(T, Period.list)]}
c5 <- function(T) {c5.list[match(T, Period.list)]}
c6 <- function(T) {c6.list[match(T, Period.list)]}
cHM <- function(T) {cHM.list[match(T, Period.list)]}
c7 <- function(T) {c7.list[match(T, Period.list)]}
c7a <- function(T) {c7a.list[match(T, Period.list)]}
c9 <- function(T) {c9.list[match(T, Period.list)]}
c9a <- function(T) {c9a.list[match(T, Period.list)]}
c10 <- function(T) {c10.list[match(T, Period.list)]}
cg1 <- function(T) {cg1.list[match(T, Period.list)]}
cg2 <- function(T) {cg2.list[match(T, Period.list)]}
cg3 <- function(T) {cg3.list[match(T, Period.list)]}
f1 <- function(T) {f1.list[match(T, Period.list)]}
f2 <- function(T) {f2.list[match(T, Period.list)]}
f3 <- function(T) {f3.list[match(T, Period.list)]}
f4 <- function(T) {f4.list[match(T, Period.list)]}
f5 <- function(T) {f5.list[match(T, Period.list)]}
f6 <- function(T) {f6.list[match(T, Period.list)]}
f7 <- function(T) {f7.list[match(T, Period.list)]}
f8 <- function(T) {f8.list[match(T, Period.list)]}



# 2. BACKGROUND FUNCTION FOR CALCULATING MEDIAN GROUND MOTION (Eqn 13a)

LnYref <-  function(M, Rrup, Rjb, Rx, Ztor, dip, Frv, Fnm, Fhw, AS, T)
  {

    # Line 1 of equation
    Line1 <- c1(T) + (c1a(T)*Frv + c1b(T)*Fnm + c7(T)*(Ztor - 4))*(1 - AS) +
             (c10(T) + c7a(T)*(Ztor - 4))*AS

    # Line 2 of equation
    Line2 <- c2(T)*(M - 6) + ((c2(T) - c3(T))/cn(T))*log(1 + exp(cn(T)*(cM(T) - M)))

    # Line 3 of equation
    Line3 <- c4(T)*log(Rrup + c5(T)*cosh(c6(T)*max((M - cHM(T)), 0)))

    # Line 4 of equation
    Line4 <- (c4a(T) - c4(T))*log(sqrt(Rrup^2 + cRB(T)^2))

    # Line 5 of equation
    Line5 <- (cg1(T) + cg2(T) / (cosh(max((M - cg3(T)), 0))))*Rrup

    # Line 6 of equation
    Line6 <- c9(T) * Fhw * tanh(Rx*(cos(dip*pi/180)^2)/c9a(T)) *
             (1 - sqrt(Rjb^2 + Ztor^2) / (Rrup + 0.001))

    return(Line1 + Line2 + Line3 + Line4 + Line5 + Line6)
  }
```

```
# 3.  FINAL FUNCTION FOR CALCULATING Sa, PGA, and PGV  (Eqn 13b)
Sa <- function(M, Rrup, Rjb, Rx, Ztor, dip, Frv, Fnm, Fhw, AS, Vs30, Z1.0, T)
  {

    # Sa on reference site
    LnYref.value <- LnYref(M, Rrup, Rjb, Rx, Ztor, dip, Frv, Fnm, Fhw, AS, T)

    # Line 1 of equation
    Line1 <- LnYref.value + f1(T)*min(log(Vs30/1130), 0)

    # Line 2 of equation
    Line2 <- f2(T) * (exp(f3(T)*(min(Vs30,1130) - 360)) - exp(f3(T)*(1130-360))) *
               log((exp(LnYref.value) + f4(T)) / f4(T))

    # Line 3 of equation
    Line3 <- f5(T) * (1 - 1 /(cosh(f6(T) * max(0, (Z1.0 - f7(T)))))) +
               f8(T) / cosh(0.15*max(0, (Z1.0 - 15)))

   return(exp(Line1 + Line2 + Line3))
  }


# REQUIRED INPUTS TO THE Sa FUNCTION:
#   M = Moment magnitude
#   Rrup = Rupture distance (km)
#   Rjb = Joyner-Boore distance (km)
#   Rx = Site coordinate (km)
#   Ztor = Depth to top of rupture (km)
#   dip = Fault dip (deg)
#   Frv = Reverse style-of-faulting flag (0 or 1)
#   Fnm = Normal style-of-faulting flag (0 or 1)
#   Fhw = Hanging wall flag (0 or 1)
#   AS = Aftershock flag (0 or 1)
#   Vs30 = Time-averaged shear wave velocity over 30 m subsurface depth  (m/sec)
#   Z1.0 = Depth to Vs = 1.0 km/sec  (m)
#   T = Spectral period, sec (-1 for PGA; -2 for PGV)
```

C.5 Idriss (2008)

```
# 1. DEFINE LISTS OF MODEL COEFFICIENTS

# a. List of periods with defined coefficients (PGA is -1; there is no model for PGV)
Period.list <- c(-1, 0.01, 0.02, 0.03, 0.04, 0.05, 0.06, 0.08, 0.1, 0.15, 0.2, 0.25, 0.3,
                 0.35, 0.4, 0.45, 0.5, 0.6, 0.7, 0.8, 0.9, 1, 1.5, 2, 3, 4, 5, 6, 7, 8,
                 9, 10)


# b. Define list of coefficients for low magnitude (4.5 <= M <= 6.75), Table 6

alpha1.Mlow.list <- c(3.7066, 3.7066, 3.7066, 3.7566, 3.8066, 4.1248, 4.4681, 4.4853,
                      4.4592, 3.4793, 3.2354, 2.7628, 2.3813, 2.0302, 1.7037, 1.394,
                      1.0893, 0.5308, 0.024, -0.4141, -0.8184, -1.229, -2.9168, -4.2783,
                      -6.2431, -7.6967, -8.811, -9.7232, -10.4706, -11.0814, -11.5896,
                      -12.0149)

alpha2.Mlow.list <- c(-0.1252, -0.1252, -0.1252, -0.1252, -0.1252, -0.1781, -0.2228,
                      -0.1949, -0.1624, -0.0188, 0.0346, 0.0791, 0.1187, 0.1545, 0.1873,
                      0.2177, 0.2461, 0.2979, 0.3443, 0.3866, 0.4255, 0.4615, 0.6103,
                      0.7246, 0.8935, 1.0137, 1.1027, 1.1696, 1.2197, 1.2566, 1.2826,
                      1.2995)

beta1.Mlow.list <- c(2.9832, 2.9832, 2.9832, 2.9832, 2.9832, 3.0156, 3.0708, 3.1071,
                     3.1212, 2.8609, 2.8739, 2.8203, 2.8126, 2.8056, 2.7992, 2.7932,
                     2.7876, 2.7772, 2.7677, 2.759, 2.751, 2.7434, 2.7112, 2.6851,
                     2.6437, 2.611, 2.5839, 2.5607, 2.5406, 2.5228, 2.507, 2.4928)

beta2.Mlow.list <- c(-0.2339, -0.2339, -0.2339, -0.2339, -0.2339, -0.2445, -0.2536,
                     -0.2576, -0.257, -0.2267, -0.2282, -0.2292, -0.2301, -0.2309,
                     -0.2317, -0.2324, -0.233, -0.2342, -0.2353, -0.2363, -0.2373,
                     -0.2381, -0.2418, -0.2447, -0.2493, -0.2529, -0.2558, -0.2582,
                     -0.2603, -0.2621, -0.2636, -0.265)


# c. Define list of coefficients for high magnitude (6.75 < M <= 8.0), Table 7

alpha1.Mhigh.list <- c(5.6315, 5.6315, 5.6315, 5.6815, 5.7315, 5.8447, 6.0362, 6.4307,
                       6.3053, 5.0845, 5.0842, 4.5453, 4.2719, 4.0174, 3.7792, 3.5519,
                       3.3235, 2.9047, 2.5222, 2.1972, 1.8971, 1.5822, 0.2888, -0.7737,
                       -2.3037, -3.4564, -4.3563, -5.1145, -5.7538, -6.2921, -6.7588,
                       -7.1679)

alpha2.Mhigh.list <- c(-0.4104, -0.4104, -0.4104, -0.4104, -0.4104, -0.4329, -0.4551,
                       -0.4831, -0.4359, -0.2566, -0.2393, -0.185, -0.1614, -0.1399,
                       -0.1202, -0.102, -0.0849, -0.0538, -0.0258, -0.0003, 0.0232,
                       0.045, 0.1354, 0.2054, 0.3099, 0.3855, 0.4427, 0.4868, 0.5209,
                       0.5471, 0.5669, 0.5814)

beta1.Mhigh.list <- c(2.9832, 2.9832, 2.9832, 2.9832, 2.9832, 2.9487, 2.9494, 2.9788,
                      2.9153, 2.4829, 2.5066, 2.3687, 2.3475, 2.3284, 2.3105, 2.2937,
                      2.2793, 2.2507, 2.225, 2.2014, 2.1786, 2.1588, 2.072, 2.0027,
                      1.8938, 1.8091, 1.7401, 1.6825, 1.6327, 1.59, 1.5532, 1.5201)

beta2.Mhigh.list <- c(-0.2339, -0.2339, -0.2339, -0.2339, -0.2339, -0.2346, -0.2356,
                      -0.2386, -0.2265, -0.1707, -0.1738, -0.1623, -0.1612, -0.1602,
                      -0.1593, -0.1584, -0.1577, -0.1562, -0.1549, -0.1537, -0.1525,
                      -0.1515, -0.1471, -0.1436, -0.1382, -0.1341, -0.1308, -0.1281,
                      -0.1258, -0.1239, -0.1223, -0.1209)
```

```
# d. Define list of coefficients that are magnitude-independent, Tables 6 and 7

gamma.list <- c(0.00047, 0.00047, 0.00047, 0.00047, 0.00047, 0, 0, 0, 0, 0, 0, -0.00049,
                0.00052, 0.00099, 0.00112, 0.00114, 0.00132, 0.00154, 0.0017, 0.00152,
                0.00157, 0.00188, 0.0025, 0.00268, 0.0005, -0.00248, -0.00453, -0.00566,
                -0.00633, -0.00671, -0.00689, -0.00709)

phi.list <- c(0.12, 0.12, 0.12, 0.12, 0.12, 0.12, 0.12, 0.12, 0.12, 0.12, 0.12, 0.12,
              0.12, 0.12, 0.12, 0.12, 0.12, 0.12, 0.12, 0.12, 0.11, 0.1, 0.06, 0.04, 0,
              0, 0, 0, 0, 0, 0, 0)



# 2. ASSIGN MODEL COEFFICIENTS USING FUNCTIONS

alpha1 <- function(T, M, Vs30)
  {
    # Compute alpha1 initial
    if(M <= 6.75)
      {alpha1.initial <- alpha1.Mlow.list[match(T, Period.list)]} else
    if(M > 6.75)
      {alpha1.initial <- alpha1.Mhigh.list[match(T, Period.list)]}

    # Return alpha1 for 450 <= Vs30 <= 900
    if(Vs30 >= 450 & Vs30 <= 900)
      {return(alpha1.initial)} else

    # Correct alpha1 for Vs30 > 900  (Eqn 3)
    if(Vs30 > 900)
      {
        # Calculate d.alpha (constant to be added if Vs30 > 900)
        if(T <= 0.05)
          {d.alpha <- -0.1492} else
        if(T > 0.05 & T <= 10)
          {d.alpha <- log((1 + 11*T + 0.27*T^2)/(1 + 16*T + 0.08*T^2))}
        # Add d.alpha
        return(alpha1.initial + d.alpha)
      }
  }

alpha2 <- function(T, M)
  {
    if(M <= 6.75)
      {return(alpha2.Mlow.list[match(T, Period.list)])} else
    if(M > 6.75)
      {return(alpha2.Mhigh.list[match(T, Period.list)])}
  }

beta1 <- function(T, M)
  {
    if(M <= 6.75)
      {return(beta1.Mlow.list[match(T, Period.list)])} else
    if(M > 6.75)
      {return(beta1.Mhigh.list[match(T, Period.list)])}
  }

beta2 <- function(T, M)
  {
    if(M <= 6.75)
      {return(beta2.Mlow.list[match(T, Period.list)])} else
    if(M > 6.75)
      {return(beta2.Mhigh.list[match(T, Period.list)])}
  }

gamma <- function(T)
  {return(gamma.list[match(T, Period.list)])}

phi <- function(T)
  {return(phi.list[match(T, Period.list)])}
```

```
# 3.  FINAL FUNCTION FOR CALCULATING Sa and PGA  (Eqn 1)
Sa <- function(M, Rrup, F, Vs30, T)
  {
    return(exp(alpha1(T, M, Vs30) + alpha2(T, M)*M - (beta1(T, M) +
           beta2(T, M)*M)*log(Rrup + 10) + gamma(T)*Rrup + phi(T)*F))
  }


# REQUIRED INPUTS TO THE Sa FUNCTION:
#   M = Moment magnitude
#   Rrup = Rupture distance (km)
#   F = Reverse style-of-faulting flag (0 or 1)
#   Vs30 = Time-averaged shear wave velocity over 30 m subsurface depth  (m/sec)
#     (Vs30 is not quantitatively incorporated into I08; it just defines the category
#     for the coefficient alpha1.)
#   T = Spectral period, sec (-1 for PGA)
```

Appendix D:
EXTENDED TABLES AND FIGURES OF RESULTS

In this appendix, we present additional tables and figures of the goodness-of-fit measures for each testing subset. The purposes of this appendix are to (1) present additional goodness-of-fit statistics besides *E*, and (2) disaggregate the "total" goodness-of-fit statistics into separate values for the seven individual ground motion parameters. In addition to the Nash-Sutcliffe model efficiency coefficient (*E*), we present the percent bias (*PB*), percent root mean square error (*PRMSE*), and correlation coefficient (*r*). The results are organized into one table per subset, as delineated in Figure 2.13. In the tables, the four goodness-of-fit statistics are first presented for each parameter (*PGA*, and *Sa* at 0.1, 0.2, 0.3, 0.5, 1.0, and 2.0 seconds), with the goodness-of-fit statistics calculated by a single-period analysis. Second, as a summary (in the "total" column), the four goodness-of-fit statistics are presented in the total sense; *i.e.*, calculated by a multiple period analysis, with the summation occurring across the whole matrix rather than for only one of the seven individual columns (Figure 3.1). The values for *E* in the "total" column have already been presented in the tables throughout the report, but they are replicated here for comparison with the other goodness-of-fit statistics and the single-period values.

For each subset, the distribution of the single-period E across the set of seven ground motion parameters {PGA, $Sa(T = 0.1$ s), $Sa(T = 0.2$ s), $Sa(T = 0.3$ s), $Sa(T = 0.5$ s), $Sa(T = 1.0$ s), $Sa(T = 2.0$ s)} is summarized in graphical form using a boxplot. For comparison, the "total" value of E (computed across all periods) is presented as a black circle on each boxplot. The model rankings based on the median E over the set {E_{PGA}, $E_{Sa(0.1)}$, $E_{Sa(0.2)}$, $E_{Sa(0.3)}$, $E_{Sa(0.5)}$, $E_{Sa(1.0)}$, $E_{Sa(2.0)}$} are typically identical to the model rankings based on the "total" value of E, but the "total" values of E are generally greater than the median. One of the benefits of a total analysis is that each data point influences the calculation once. When the goodness-of-fit statistics are calculated separately for each of the seven periods, and when the distribution of E across those seven periods is described with summary statistics (such as the mean or median), extreme data points may influence the conclusions twice—once in the calculation of the goodness-of-fit statistic, and once in the statistical summary of the goodness-of-fit statistics. With a total analysis, summary statistics are not necessary because a single goodness-of-fit statistic conveys the necessary information of model performance across periods. Nonetheless, the boxplots of E across the individual periods provides a nice visual summary of the conclusions we have already made about model performance.

Sometimes, especially for smaller datasets (such as the Parkfield and San Simeon datasets), the total value of E is greater than all the values of E for the individual periods. Graphically, this occurs when the black circle representing the total value of E is located above the boxplot for the set {E_{PGA}, $E_{Sa(0.1)}$, $E_{Sa(0.2)}$, $E_{Sa(0.3)}$, $E_{Sa(0.5)}$, $E_{Sa(1.0)}$, $E_{Sa(2.0)}$}. As mentioned in section 4.2, the "whole is greater than the sum of the parts" phenomenon occurs because of the relative influence of extreme observations, and the fact that E

compares alternative models to the mean of the observed values. Recall that when E is less than 0, the arithmetic mean of the observed values has greater prediction accuracy than the model itself. Consider the example of Table D.1, in which E is calculated for two artificial datasets x and y, each of size $n = 2$:

Table D.1. Example calculation of E for two datasets

	Dataset x		Dataset y	
	Observed, x_i	Predicted, $\hat{x}_i$	Observed, y_i	Predicted, $\hat{y}_i$
Data point 1	2	2.5	2	2.5
Data point 2	3	2.5	10	5
Mean of observed values	2.5	–	6.25	–
E for each subset	0.0		21.1	
Combined E	42.5			

The model predictions for both points in the first subset ($x_1 = 2$, $x_2 = 3$) are simply the mean of the observed values ($\hat{x}_1 = \hat{x}_2 = \bar{x} = 2.5$); as a result, the coefficient of efficiency is equal to zero, because the model gives predictions equal to that of the sample mean. For the second subset, the model again predicts $\hat{y}_1 = 2.5$ for the first point ($y_1 = 2$), but it predicts $\hat{y}_2 = 5$ for the second point ($y_2 = 10$), which is a much larger observation than the other values in the two subsets. In this case, because E is greater than zero, the model predictions ($\hat{y}_1 = 2.5$, $\hat{y}_2 = 5$) are better predictors than the mean of the observations ($\bar{y} = 6.25$). When subsets x and y are combined, E is larger for the combined dataset than for either of the individual subsets.

For an individual subset, there are fewer extreme values than when the subsets are combined into a composite dataset. Within an individual subset, especially if the observed values are numerically close to one another, the sample mean may do a reasonable job of predicting the values. However, when the subsets are combined, the sample mean performs much worse than it does for the separate subsets, because the mean is greatly affected by extreme observations. In order to make reasonable predictions when extreme observations are present, it is necessary to use the model; the mean of the observed values is no longer as useful as before. Because *E* compares model predictions to the mean of the observed values, and since the mean will be a better predictor in an individual subset than when the subsets are combined, the values of *E* may be smaller for the individual subsets than in the combined dataset. Nonetheless, *E* is still useful for assessing the relative performances of alternative models in subdivided datasets.

Table D.2. Goodness-of-fit measures for the mainshocks subset of the NGA flatfile

		PGA	Spectral acceleration (*Sa*)						**Total**
Period (*T*), sec		–	0.1	0.2	0.3	0.5	1.0	2.0	–
AS08	*PB*	2.2	–5.7	3.6	6.9	2.5	–2.5	0.6	1.7
	PRMSE	68.2	81.4	77.1	76.9	74.1	75.7	78.8	81.9
	r	77.8	72.9	71.7	70.3	70.8	72.6	75.2	74.9
	E	59.7	52.8	49.8	46.1	47.9	52.4	56.2	54.8
BA08	*PB*	2.9	2.2	–1.2	–4.5	–9.7	–15.6	–18.0	–5.0
	PRMSE	70.3	83.3	74.0	71.9	68.1	74.0	79.9	78.8
	r	75.7	71.3	73.4	73.1	75.4	75.8	77.4	76.4
	E	57.3	50.6	53.7	52.9	55.9	54.5	55.0	58.1
CB08	*PB*	–5.5	–1.1	–3.8	–9.3	–10.1	–13.1	–8.3	–7.1
	PRMSE	66.6	80.9	73.2	70.7	69.8	72.2	73.7	77.7
	r	78.6	73.0	74.1	74.3	74.3	76.3	79.1	77.2
	E	61.5	53.3	54.7	54.5	53.7	56.7	61.7	59.3
CY08	*PB*	12.1	20.5	12.9	5.1	–4.3	–10.8	–18.8	4.9
	PRMSE	78.6	101.5	90.8	83.3	76.5	78.2	83.4	92.1
	r	75.2	67.7	68.0	68.9	71.0	72.4	73.5	72.3
	E	46.4	26.6	30.3	36.9	44.5	49.2	51.0	42.7

NOTE: All values in the tables of this appendix are percents.

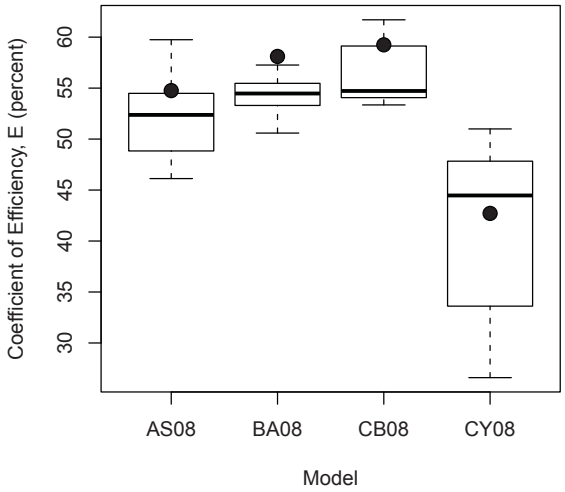

Figure D.1. Boxplots for *E* for the mainshocks subset of the NGA flatfile

Table D.3. Goodness-of-fit measures for the mainshocks—soil subdivision

		PGA	Spectral acceleration (*Sa*)						**Total**
	Period (*T*), sec	–	0.1	0.2	0.3	0.5	1.0	2.0	–
AS08	*PB*	–0.8	–10.2	–2.3	1.3	–0.8	–3.0	3.6	–2.1
	PRMSE	64.8	74.1	68.7	70.5	70.1	72.9	76.5	75.4
	r	77.3	75.2	74.4	71.4	70.2	70.7	74.9	76.0
	E	59.7	55.3	55.2	50.9	48.6	49.1	54.5	57.7
BA08	*PB*	1.3	–0.5	–4.5	–6.6	–9.1	–14.0	–17.4	–6.4
	PRMSE	67.4	75.7	68.3	69.0	64.9	68.1	74.5	73.7
	r	75.2	73.0	74.8	73.1	75.4	76.0	78.5	77.4
	E	56.5	53.3	55.7	53.0	56.0	55.5	56.9	59.5
CB08	*PB*	–8.3	–6.2	–9.1	–12.4	–11.1	–12.4	–7.6	–9.9
	PRMSE	63.7	73.8	67.8	68.5	65.6	66.8	70.6	72.9
	r	78.9	75.7	76.6	75.0	75.1	76.8	79.2	78.5
	E	61.1	55.6	56.4	53.6	55.1	57.2	61.3	60.4
CY08	*PB*	7.2	11.0	5.0	–0.4	–6.0	–9.5	–15.5	0.2
	PRMSE	69.7	78.8	72.9	73.4	70.9	75.9	80.9	78.8
	r	76.1	72.9	72.3	70.3	71.5	70.9	73.3	75.0
	E	53.3	49.4	49.6	46.7	47.5	44.7	49.2	53.7

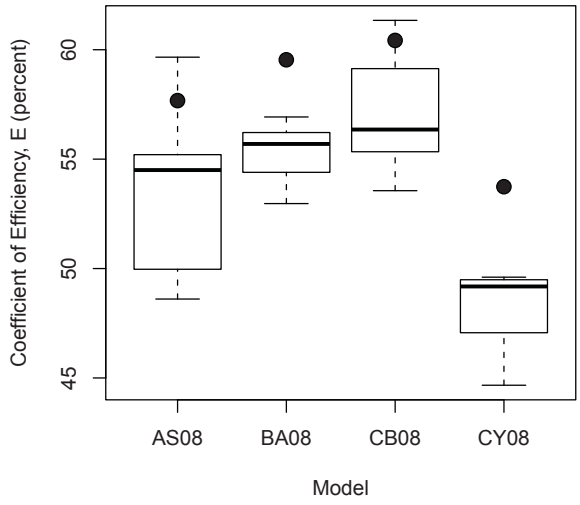

Figure D.2. Boxplots for *E* for the mainshocks—soil subdivision

Table D.4. Goodness-of-fit measures for the mainshocks—rock subdivision

		PGA	Spectral acceleration (*Sa*)						**Total**
	Period (*T*), sec	–	0.1	0.2	0.3	0.5	1.0	2.0	–
AS08	*PB*	9.1	4.9	18.1	21.0	10.9	–1.3	–7.1	11.0
	PRMSE	74.7	94.4	93.3	90.5	82.8	82.2	84.5	95.1
	r	79.1	71.6	71.5	72.5	73.0	75.9	78.1	74.9
	E	59.7	49.0	40.9	37.3	46.6	57.7	59.3	49.7
BA08	*PB*	6.6	8.3	6.7	0.7	–11.3	–19.7	–19.7	–1.7
	PRMSE	75.9	96.8	85.6	78.5	75.2	86.8	92.4	89.3
	r	76.7	69.0	72.4	73.9	75.4	76.1	75.2	75.0
	E	58.4	46.4	50.3	52.8	55.8	52.8	51.4	55.6
CB08	*PB*	1.1	10.6	9.2	–1.6	–7.5	–14.7	–10.1	–0.1
	PRMSE	72.5	93.7	84.1	75.7	79.1	83.8	81.3	87.7
	r	79.1	71.8	74.0	75.9	73.5	75.7	79.4	76.5
	E	62.1	49.8	52.0	56.1	51.1	56.0	62.4	57.2
CY08	*PB*	23.9	42.5	32.3	18.8	0.0	–14.1	–27.3	16.5
	PRMSE	94.9	136.6	122.2	103.1	88.4	83.3	89.5	117.2
	r	75.0	65.2	66.2	69.7	70.6	76.0	78.8	70.5
	E	35.0	–6.7	–1.4	18.6	39.0	56.5	54.5	23.5
I08	*PB*	2.6	2.3	6.8	5.2	–3.1	–10.0	–17.4	0.5
	PRMSE	87.4	106.8	99.3	89.5	85.0	92.2	95.0	100.8
	r	70.3	62.0	64.3	66.9	67.4	69.1	75.1	68.6
	E	44.9	34.7	33.1	38.7	43.6	46.7	48.6	43.4

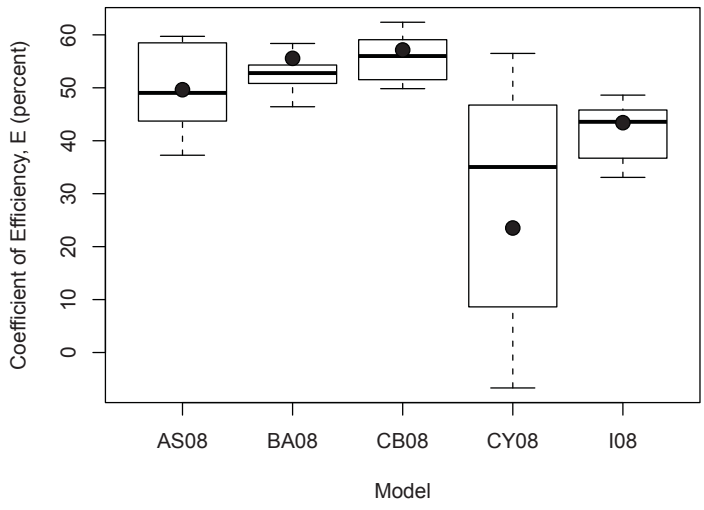

Figure D.3. Boxplots for *E* for the mainshocks—rock subdivision

Table D.5. Goodness-of-fit measures for the mainshocks—small distance subdivision

		PGA	Spectral acceleration (*Sa*)						**Total**
	Period (*T*), sec	–	0.1	0.2	0.3	0.5	1.0	2.0	–
AS08	*PB*	5.5	2.0	6.0	4.6	3.6	–9.3	–9.6	1.9
	PRMSE	47.9	57.8	60.1	56.9	55.5	54.9	60.4	60.6
	r	45.6	35.2	29.4	30.3	35.0	50.9	54.6	56.5
	E	12.0	5.7	–10.1	–22.1	–18.1	19.9	25.0	22.6
BA08	*PB*	–6.8	2.4	0.7	–4.2	–5.9	–20.5	–25.5	–5.8
	PRMSE	45.8	57.1	54.9	50.6	47.0	53.5	62.0	55.6
	r	47.6	34.9	36.5	37.4	47.4	59.5	59.3	61.7
	E	19.5	8.1	8.2	3.5	15.4	24.1	21.0	34.8
CB08	*PB*	0.7	0.0	–0.7	–4.8	6.0	–1.8	0.2	–0.2
	PRMSE	43.9	56.8	56.2	49.1	49.5	49.7	54.3	55.3
	r	52.7	36.1	34.3	42.3	48.5	61.1	64.7	61.9
	E	25.8	9.0	3.9	8.8	6.0	34.3	39.4	35.4
CY08	*PB*	25.0	35.1	29.3	21.1	17.6	6.3	–3.9	21.5
	PRMSE	59.3	81.3	75.8	64.8	58.8	57.7	64.6	72.8
	r	38.8	26.8	24.5	26.1	33.2	46.3	48.2	52.8
	E	–35.3	–86.5	–75.0	–58.4	–32.5	11.6	14.2	–11.8

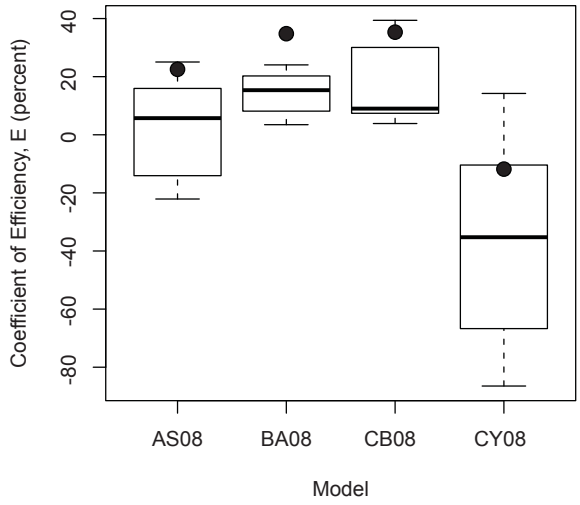

Figure D.4. Boxplots for *E* for the mainshocks—small distance subdivision

Table D.6. Goodness-of-fit measures for the mainshocks—medium distance subdivision

		PGA	Spectral acceleration (*Sa*)						**Total**
	Period (*T*), sec	–	0.1	0.2	0.3	0.5	1.0	2.0	–
AS08	*PB*	0.7	–9.2	1.2	5.7	0.2	0.4	6.7	0.5
	PRMSE	66.6	78.0	69.9	72.8	70.9	74.6	73.7	78.0
	r	67.4	65.1	63.7	58.7	61.4	59.9	69.6	68.5
	E	45.2	41.4	40.0	31.5	36.8	34.0	46.2	46.4
BA08	*PB*	6.8	1.8	–2.1	–4.8	–11.2	–12.0	–12.0	–4.4
	PRMSE	71.6	81.5	69.9	70.7	68.6	72.7	72.8	77.6
	r	61.3	60.0	63.3	60.1	65.2	62.5	70.8	68.7
	E	36.7	35.9	40.0	35.5	40.9	37.4	47.6	46.9
CB08	*PB*	–8.2	–2.3	–5.8	–12.2	–16.0	–15.3	–7.9	–9.8
	PRMSE	67.7	78.2	67.5	70.0	69.5	72.9	70.5	76.2
	r	67.8	64.7	67.3	62.9	66.9	63.4	71.8	71.2
	E	43.5	41.0	44.0	36.6	39.3	37.0	50.9	48.9
CY08	*PB*	9.1	15.5	7.1	–0.5	–11.2	–14.2	–21.1	0.1
	PRMSE	73.0	88.2	77.7	76.4	72.4	75.4	75.8	83.6
	r	63.0	58.2	57.7	54.9	60.4	59.7	69.5	64.8
	E	34.2	25.0	25.8	24.5	34.1	32.7	43.1	38.4

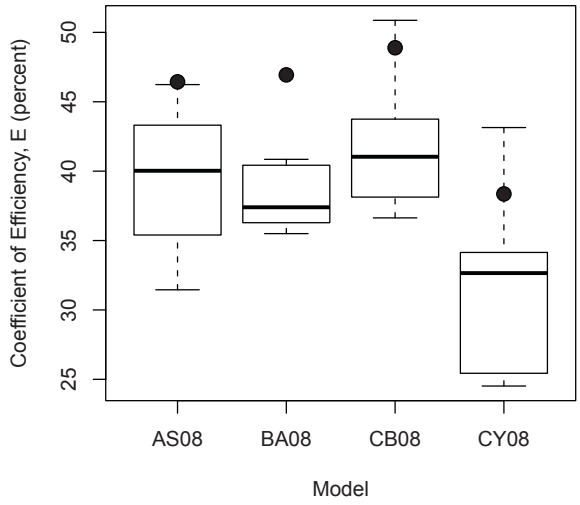

Figure D.5. Boxplots for *E* for the mainshocks—medium distance subdivision

Table D.7. Goodness-of-fit measures for the mainshocks—large distance subdivision

		PGA	Spectral acceleration (*Sa*)						**Total**
	Period (*T*), sec	–	0.1	0.2	0.3	0.5	1.0	2.0	–
AS08	*PB*	3.6	3.1	26.0	33.3	23.1	–2.5	–7.2	14.2
	PRMSE	57.8	62.9	79.4	82.0	75.8	68.7	66.0	77.3
	r	41.6	31.8	18.5	24.1	31.4	56.0	56.9	47.8
	E	3.0	–12.6	–83.2	–93.7	–42.5	30.8	28.3	–6.5
BA08	*PB*	1.4	6.6	1.0	–2.0	–8.8	–26.5	–31.7	–8.8
	PRMSE	61.8	68.3	64.6	62.4	63.4	73.1	72.2	68.9
	r	41.9	30.1	24.4	30.1	35.9	57.9	57.5	47.6
	E	–11.0	–32.9	–21.1	–12.1	0.1	21.6	14.2	15.3
CB08	*PB*	–3.0	10.0	9.1	5.2	–8.4	–29.9	–31.4	–6.6
	PRMSE	52.3	57.0	58.9	57.3	59.8	75.6	71.8	65.4
	r	45.4	35.6	27.5	32.8	37.9	57.2	56.7	50.7
	E	20.4	7.4	–0.9	5.7	11.1	16.1	15.3	23.8
CY08	*PB*	–13.1	8.9	9.4	0.1	–14.9	–36.1	–43.3	–12.0
	PRMSE	58.7	71.2	74.5	67.0	64.6	78.3	77.7	73.6
	r	40.0	26.6	15.7	23.9	33.4	57.8	62.2	41.8
	E	–0.3	–44.3	–61.5	–29.2	–3.7	10.1	0.7	3.5

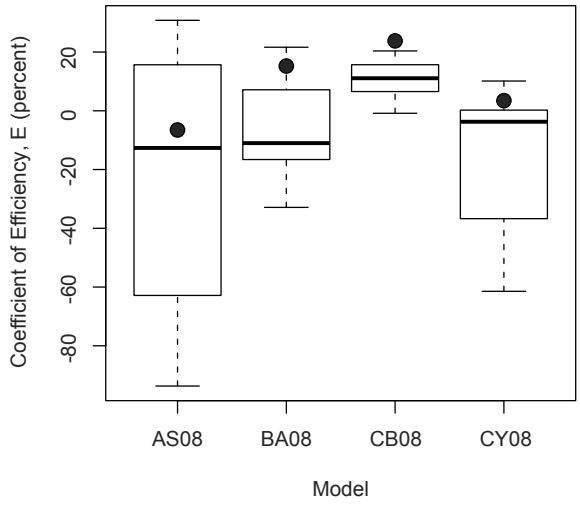

Figure D.6. Boxplots for *E* for the mainshocks—large distance subdivision

Table D.8. Goodness-of-fit measures for the aftershocks subset of the NGA flatfile

		PGA	Spectral acceleration (*Sa*)						**Total**
	Period (*T*), sec	–	0.1	0.2	0.3	0.5	1.0	2.0	–
AS08	*PB*	−6.6	−13.3	−7.1	−10.8	−18.2	−27.2	−37.2	−14.3
	PRMSE	97.5	115.9	105.4	103.3	95.2	93.4	106.0	112.0
	r	71.3	66.4	69.3	67.5	67.2	64.3	56.2	70.3
	E	50.2	42.6	46.7	43.8	42.4	35.9	20.8	47.9
BA08	*PB*	22.2	21.6	22.5	15.8	3.8	−7.4	−19.8	12.4
	PRMSE	101.3	114.5	106.2	102.2	97.1	95.8	108.0	112.4
	r	70.5	68.3	69.5	68.1	64.2	60.1	52.3	69.9
	E	46.2	44.0	45.9	45.0	40.2	32.6	17.8	47.6
CB08	*PB*	29.8	34.4	27.4	12.9	5.0	−10.1	−28.6	14.9
	PRMSE	107.8	124.8	111.6	105.9	103.5	104.4	117.1	119.0
	r	67.1	63.6	66.5	64.7	59.6	54.6	47.4	66.2
	E	39.0	33.5	40.2	41.0	32.0	19.9	3.4	41.2
CY08	*PB*	29.8	34.4	27.4	12.9	5.0	−10.1	−28.6	−26.7
	PRMSE	107.8	124.8	111.6	105.9	103.5	104.4	117.1	117.1
	r	67.1	63.6	66.5	64.7	59.6	54.6	47.4	68.4
	E	39.0	33.5	40.2	41.0	32.0	19.9	3.4	43.1

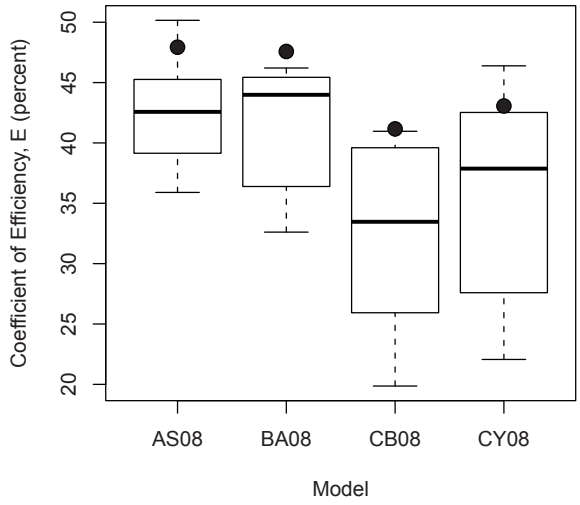

Figure D.7. Boxplots for *E* for the aftershocks subset of the NGA flatfile

Table D.9. Goodness-of-fit measures for the aftershocks—soil subdivision

		PGA	Spectral acceleration (*Sa*)						**Total**
	Period (*T*), sec	–	0.1	0.2	0.3	0.5	1.0	2.0	–
AS08	*PB*	26.1	14.4	24.2	21.7	12.6	−7.8	−28.0	14.1
	PRMSE	102.5	112.9	105.9	110.2	95.7	89.5	99.6	113.2
	r	74.6	72.1	73.9	69.0	68.5	64.6	56.5	72.4
	E	52.1	51.2	52.1	45.5	44.7	38.0	19.9	51.2
BA08	*PB*	22.9	20.1	21.4	17.8	10.1	−2.9	−20.2	13.7
	PRMSE	104.6	112.7	107.6	110.5	98.8	94.4	103.7	114.8
	r	72.7	72.9	72.4	68.3	65.8	60.5	51.9	71.3
	E	50.0	51.4	50.5	45.2	41.2	30.9	13.2	49.8
CB08	*PB*	22.4	23.9	18.9	9.1	6.0	−8.3	−29.6	10.1
	PRMSE	109.6	118.3	109.3	114.0	109.1	107.5	114.9	120.6
	r	69.0	69.7	71.3	64.9	58.0	52.3	46.1	67.3
	E	45.2	46.4	49.0	41.6	28.2	10.4	−6.6	44.6
CY08	*PB*	4.0	5.9	1.8	−6.3	−9.5	−19.1	−38.6	−5.6
	PRMSE	104.9	117.7	109.5	113.7	105.6	103.6	113.6	119.3
	r	71.6	69.6	70.1	65.1	60.4	54.1	44.5	68.5
	E	49.8	47.0	48.8	42.0	32.8	16.8	−4.3	45.8

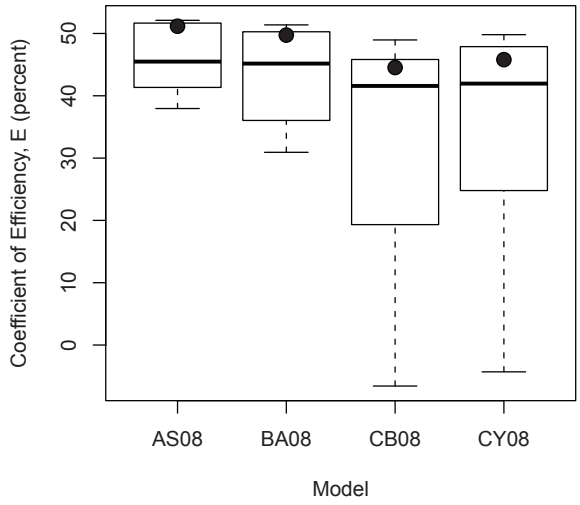

Figure D.8. Boxplots for *E* for the aftershocks—soil subdivision

Table D.10. Goodness-of-fit measures for the aftershocks—rock subdivision

		PGA	Spectral acceleration (*Sa*)						**Total**
	Period (*T*), sec	–	0.1	0.2	0.3	0.5	1.0	2.0	–
AS08	*PB*	37.0	26.5	35.8	29.2	9.3	−12.6	−30.7	20.9
	PRMSE	105.9	125.0	115.3	94.2	92.2	92.7	112.0	115.2
	r	61.6	52.4	56.4	62.5	60.9	61.1	47.2	63.3
	E	8.0	10.7	7.6	15.4	34.3	36.2	15.8	25.6
BA08	*PB*	21.1	24.1	24.4	12.2	−7.4	−16.0	−18.8	10.0
	PRMSE	92.2	117.0	101.3	77.9	91.3	95.2	110.4	104.1
	r	62.3	54.7	59.4	66.3	60.2	59.3	46.1	64.6
	E	30.3	21.9	28.7	42.2	35.7	32.7	18.2	39.2
CB08	*PB*	42.5	51.9	42.2	19.6	3.3	−13.5	−26.2	23.7
	PRMSE	102.4	135.6	114.7	82.1	87.6	90.4	109.8	112.8
	r	63.6	54.2	58.7	66.4	64.1	64.2	48.9	64.5
	E	13.9	−5.0	8.7	35.8	40.8	39.3	19.0	28.6
CY08	*PB*	18.7	21.8	10.7	−2.7	−15.5	−24.7	−36.6	0.2
	PRMSE	102.6	130.5	108.5	84.0	90.6	93.2	111.6	111.0
	r	62.0	52.8	57.5	64.6	62.6	63.3	50.5	63.3
	E	13.6	2.7	18.2	32.7	36.7	35.5	16.4	30.9
I08	*PB*	−7.7	−11.0	−12.4	−16.0	−22.5	−26.0	−32.5	−16.5
	PRMSE	92.0	116.8	100.9	80.7	94.7	99.3	114.4	105.7
	r	61.2	51.5	57.4	64.6	59.0	56.4	44.4	63.2
	E	30.6	22.1	29.3	37.8	30.8	26.8	12.1	37.4

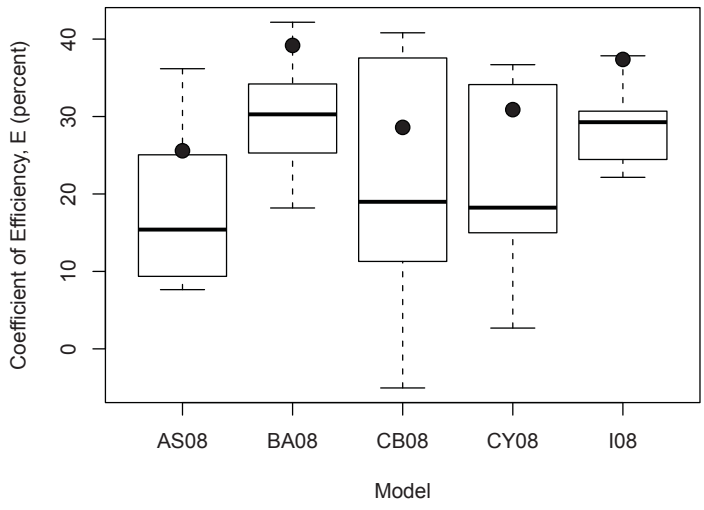

Figure D.9. Boxplots for *E* for the aftershocks—rock subdivision

Table D.11. Goodness-of-fit measures for the Parkfield dataset

		PGA	Spectral acceleration (*Sa*)						**Total**
Period (*T*), sec		–	0.1	0.2	0.3	0.5	1.0	2.0	–
AS08	*PB*	−11.1	−19.7	−11.4	−5.7	−18.1	−8.7	40.6	−11.9
	PRMSE	64.0	66.8	63.1	66.5	80.0	83.0	96.7	76.4
	r	48.7	51.1	45.7	45.8	39.9	50.4	58.0	63.2
	E	17.3	18.6	13.6	16.1	9.8	24.0	−27.5	38.1
BA08	*PB*	−7.8	−6.8	−9.1	−5.8	−13.0	1.7	55.6	−6.4
	PRMSE	67.9	69.2	63.1	66.0	79.3	83.1	95.5	77.1
	r	39.3	42.4	42.8	44.5	39.5	49.9	59.9	61.5
	E	7.0	12.5	13.8	17.3	11.3	23.8	−24.4	36.9
CB08	*PB*	−0.3	−14.5	−4.0	3.9	2.4	16.5	77.8	−0.2
	PRMSE	61.6	64.4	59.2	64.7	79.4	84.3	121.2	74.0
	r	50.5	53.6	49.8	47.7	39.9	53.3	64.3	64.8
	E	23.6	24.3	24.0	20.6	11.3	21.6	−100.4	42.0
CY08	*PB*	8.8	−2.9	10.0	23.9	14.1	36.8	111.3	14.4
	PRMSE	69.9	66.9	69.0	79.2	86.1	97.6	168.8	83.7
	r	45.1	48.2	43.1	43.9	40.7	55.3	64.8	60.4
	E	1.5	18.2	−3.2	−19.0	−4.5	−5.1	−288.9	25.8
AS97	*PB*	11.0	5.1	16.4	21.4	10.1	22.1	83.8	15.2
	PRMSE	67.8	71.0	72.5	74.0	73.3	80.4	118.6	81.4
	r	44.2	42.1	39.6	44.8	47.9	60.1	63.8	61.9
	E	7.0	8.5	−8.7	1.8	17.8	29.6	−89.3	30.4
BJF97	*PB*	−11.7	−14.9	0.3	16.2	12.2	16.4	84.7	3.6
	PRMSE	60.9	64.8	59.5	68.9	77.8	87.4	114.0	74.9
	r	52.7	52.8	52.4	49.2	44.3	51.9	62.2	64.8
	E	25.0	23.7	26.9	14.9	7.3	16.8	−74.8	41.1
C97	*PB*	17.1	−4.5	15.2	30.4	16.9	27.2	109.9	17.2
	PRMSE	70.5	68.2	68.2	78.1	77.5	88.6	143.6	81.5
	r	46.0	46.0	47.1	47.2	44.0	49.7	54.4	62.4
	E	−0.4	15.4	3.8	−9.3	8.0	14.3	−177.3	30.1
SCE97	*PB*	6.3	7.8	15.9	23.4	4.1	7.7	58.4	12.9
	PRMSE	69.7	73.1	71.9	77.4	73.5	76.4	94.6	82.5
	r	41.6	42.2	42.4	43.7	46.6	60.8	64.8	61.9
	E	1.7	2.9	−6.8	−7.4	17.3	36.4	−20.3	28.4

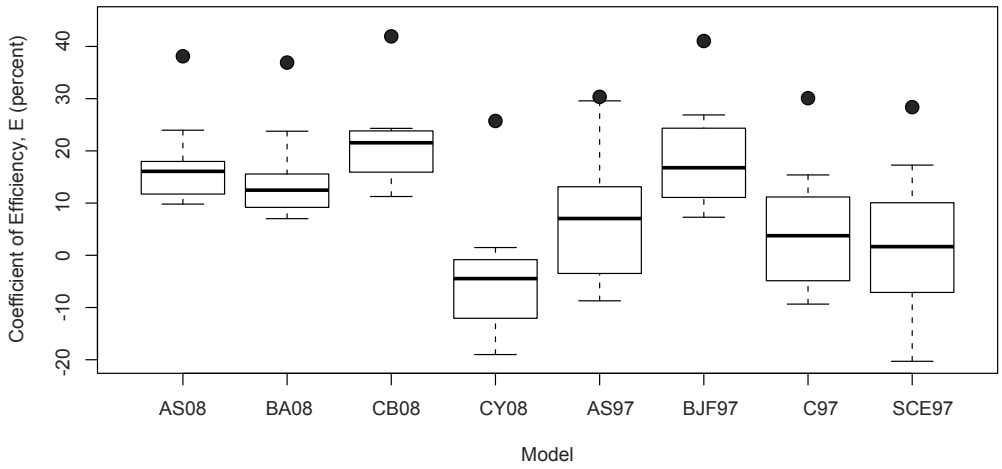

Figure D.10. Boxplots for *E* for the Parkfield dataset

Table D.12. Goodness-of-fit measures for the Parkfield—soil subdivision

		PGA	Spectral acceleration (*Sa*)						**Total**
Period (*T*), sec		–	0.1	0.2	0.3	0.5	1.0	2.0	–
AS08	*PB*	−11.7	−19.3	−12.2	−10.9	−23.1	−12.0	41.1	−14.1
	PRMSE	64.6	66.2	59.7	66.0	79.1	80.3	96.9	74.8
	r	47.5	50.5	48.5	44.9	37.8	49.1	56.7	62.6
	E	14.7	17.8	15.5	13.9	4.1	21.4	−34.6	36.6
BA08	*PB*	−5.4	−2.1	−6.7	−7.6	−15.6	−0.2	55.0	−5.5
	PRMSE	69.2	69.1	59.9	66.3	78.7	80.4	94.0	76.0
	r	36.3	42.2	44.3	41.2	34.6	47.7	58.8	60.0
	E	2.1	10.4	14.8	13.0	4.9	21.2	−26.6	34.7
CB08	*PB*	−2.9	−16.0	−6.9	−3.1	−4.5	12.4	77.6	−3.9
	PRMSE	61.4	64.0	55.1	62.6	76.7	80.4	120.3	71.6
	r	50.0	53.7	54.0	48.5	38.5	52.6	63.6	64.9
	E	23.0	23.1	28.1	22.4	9.8	21.2	−107.2	42.0
CY08	*PB*	7.8	−3.2	9.3	18.3	8.1	33.2	111.5	12.2
	PRMSE	70.6	66.5	66.0	77.0	83.7	93.8	168.5	81.8
	r	43.9	47.7	45.2	41.9	37.8	54.4	64.5	59.5
	E	−1.8	17.0	−3.3	−17.4	−7.3	−7.3	−306.5	24.3
AS97	*PB*	7.5	3.5	13.6	14.4	2.6	16.1	79.0	10.8
	PRMSE	66.9	68.4	67.6	69.2	69.3	73.8	111.6	76.5
	r	44.6	45.0	44.3	46.3	47.4	62.1	66.1	63.3
	E	10.8	13.1	0.6	9.8	19.1	34.7	−73.0	34.7
BJF97	*PB*	−8.6	−10.7	3.9	15.4	9.5	15.7	83.8	5.4
	PRMSE	61.5	63.0	57.2	68.4	76.4	84.9	111.9	73.3
	r	51.2	53.3	54.8	47.1	40.4	50.2	61.9	64.5
	E	24.7	26.3	28.9	11.9	1.9	13.5	−74.2	40.0
C97	*PB*	14.3	−4.6	14.5	24.3	8.7	19.7	101.9	13.8
	PRMSE	70.7	67.9	65.6	73.5	70.8	78.2	130.7	77.6
	r	44.6	45.9	49.7	47.8	46.6	56.3	60.2	63.3
	E	0.3	14.4	6.4	−1.6	15.7	26.6	−137.3	32.7
SCE97	*PB*	2.4	6.6	13.6	16.0	−3.5	2.1	53.5	8.6
	PRMSE	69.3	70.9	67.9	73.0	70.2	70.8	88.2	78.3
	r	41.9	44.9	46.6	44.5	46.3	63.1	67.0	62.8
	E	4.3	6.5	−0.3	−0.1	17.2	39.8	−8.2	31.6

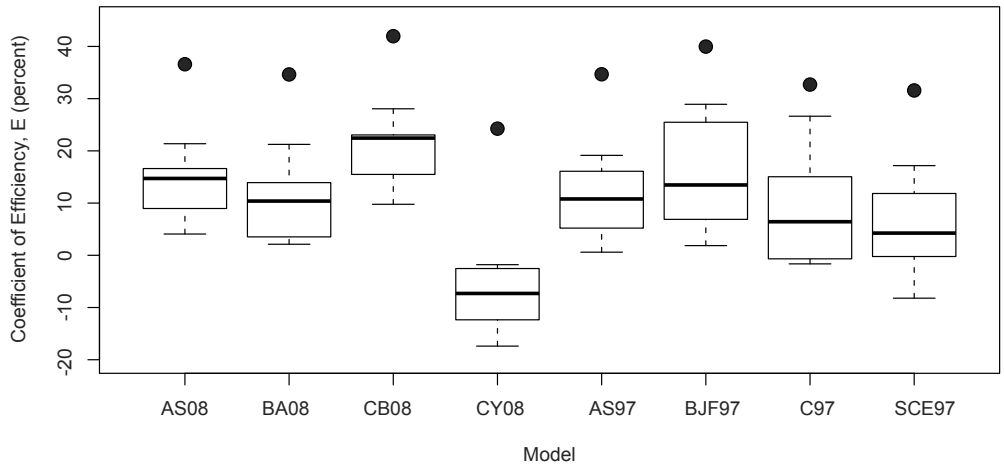

Figure D.11. Boxplots for *E* for the Parkfield—soil subdivision

Table D.13. Goodness-of-fit measures for the Parkfield—rock subdivision

		PGA	Spectral acceleration (*Sa*)						**Total**
	Period (*T*), sec	–	0.1	0.2	0.3	0.5	1.0	2.0	–
AS08	*PB*	−8.7	−21.2	−8.2	22.0	16.5	14.4	37.3	−2.0
	PRMSE	61.6	68.0	74.3	66.9	74.5	95.9	80.4	83.5
	r	54.4	51.6	37.6	56.4	52.1	45.6	52.9	65.8
	E	27.6	18.8	8.8	16.2	20.7	18.6	−3.0	43.1
BA08	*PB*	−17.5	−23.0	−18.4	3.8	5.2	14.3	58.9	−10.3
	PRMSE	62.1	69.2	73.4	60.4	69.8	96.4	97.4	82.3
	r	56.9	50.3	41.0	56.7	55.5	44.7	49.4	68.1
	E	26.3	15.9	11.1	31.8	30.3	17.8	−51.0	44.7
CB08	*PB*	10.4	−9.4	7.2	41.4	49.8	44.9	79.2	16.7
	PRMSE	62.3	65.1	72.4	75.5	92.7	108.3	114.3	84.9
	r	54.2	52.4	40.7	57.0	49.4	44.0	52.7	66.4
	E	25.9	25.7	13.5	−6.6	−23.0	−3.8	−108.1	41.1
CY08	*PB*	13.3	−2.2	12.9	54.5	54.7	62.1	109.8	24.6
	PRMSE	67.0	67.7	79.0	90.0	96.4	118.5	149.5	92.4
	r	50.8	47.8	37.1	57.5	55.2	47.9	51.0	64.1
	E	14.3	19.5	−3.1	−51.7	−32.9	−24.4	−256.0	30.3
I08	*PB*	−2.5	−27.1	−12.9	18.4	14.9	9.5	12.9	−5.6
	PRMSE	63.8	71.5	75.5	66.2	70.2	92.5	66.2	85.1
	r	49.6	48.2	34.7	53.5	57.4	50.3	57.4	64.1
	E	22.2	10.4	5.9	17.9	29.6	24.1	30.3	40.9
AS97	*PB*	25.3	8.4	24.7	55.7	60.7	63.1	110.4	33.2
	PRMSE	71.4	81.7	90.8	99.7	98.4	124.9	155.5	105.0
	r	45.1	23.6	19.6	40.2	53.8	38.8	35.7	55.7
	E	−9.9	−17.6	−43.4	−61.9	−38.4	−36.3	−317.3	8.7
BJF97	*PB*	−24.6	−29.8	−13.6	20.6	31.1	21.1	90.7	−4.9
	PRMSE	58.5	69.6	67.5	69.4	79.6	97.6	120.2	81.9
	r	67.7	59.5	49.2	53.9	51.7	46.3	46.8	67.3
	E	26.2	14.7	20.6	21.6	9.4	16.7	−149.6	44.4
C97	*PB*	28.5	−4.0	17.7	62.7	72.1	77.8	159.1	32.4
	PRMSE	69.3	68.8	77.5	102.1	123.3	157.1	221.8	98.8
	r	53.0	44.9	37.9	47.0	29.6	6.8	10.2	59.5
	E	−3.5	16.7	−4.5	−69.8	−117.3	−115.8	−750.0	19.1
SCE97	*PB*	22.2	12.1	24.7	61.9	55.2	45.5	88.6	32.9
	PRMSE	71.4	79.0	85.3	100.7	94.2	113.7	133.5	101.2
	r	42.8	31.8	28.1	46.5	53.0	37.6	35.1	59.9
	E	−10.1	−9.8	−26.7	−65.0	−27.0	−12.9	−207.7	15.1
I91	*PB*	−38.5	−43.3	−32.6	−10.4	−12.4	−33.4	−23.6	−30.0
	PRMSE	71.6	78.7	77.6	78.6	94.5	120.3	88.5	94.0
	r	46.8	53.4	37.1	25.6	−6.7	−19.0	−9.6	59.5
	E	−10.7	−8.9	−4.7	−0.5	−27.8	−26.5	−35.2	26.8

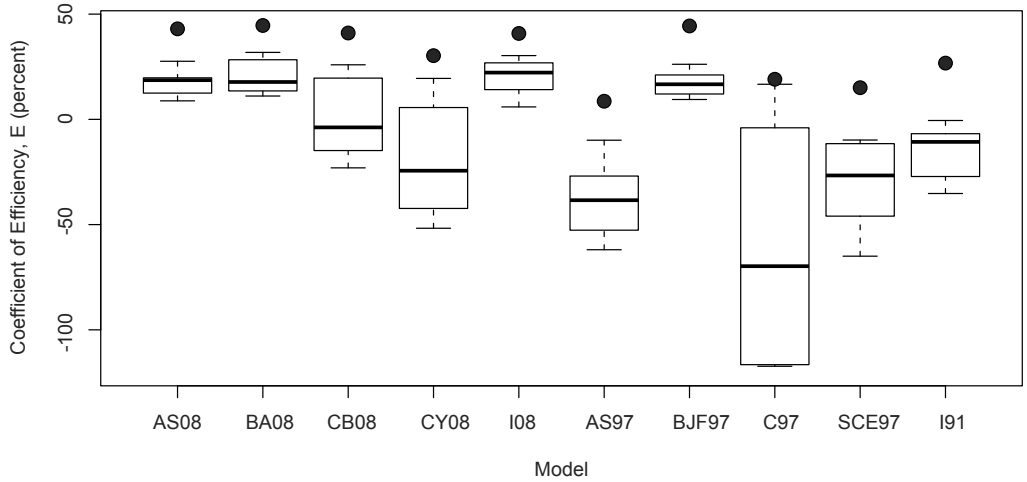

Figure D.12. Boxplots for *E* for the Parkfield—rock subdivision

Table D.14. Goodness-of-fit measures for the Parkfield—small distance subdivision

		PGA	Spectral acceleration (*Sa*)						**Total**
Period (*T*), sec		–	0.1	0.2	0.3	0.5	1.0	2.0	–
AS08	*PB*	–9.2	–18.1	–8.2	–3.5	–17.2	–9.9	41.7	–10.1
	PRMSE	60.3	62.7	59.9	62.9	74.9	77.2	90.6	71.8
	r	0.6	8.7	–4.7	–0.3	0.7	27.4	41.9	50.9
	E	–28.4	–19.1	–29.0	–22.8	–20.6	2.2	–65.2	23.0
BA08	*PB*	–8.9	–7.3	–9.2	–7.1	–13.9	–1.0	53.5	–7.2
	PRMSE	64.3	65.6	60.2	62.5	74.5	77.3	88.1	72.9
	r	–12.1	–4.0	–10.6	–1.0	2.8	26.2	42.2	48.7
	E	–46.0	–30.4	–30.4	–21.2	–19.4	2.1	–56.2	20.7
CB08	*PB*	–1.0	–17.5	–4.9	3.3	2.8	15.5	80.2	–1.1
	PRMSE	58.3	61.0	56.7	61.5	74.7	78.4	113.1	70.1
	r	–5.1	4.6	–9.5	–5.8	–2.4	31.4	49.8	52.1
	E	–20.0	–12.9	–15.6	–17.1	–20.1	–0.8	–157.6	26.7
CY08	*PB*	11.5	–1.4	14.6	28.3	17.6	39.0	119.1	17.9
	PRMSE	66.5	63.5	66.5	76.1	81.4	90.9	158.8	79.7
	r	–5.1	3.3	–6.8	0.3	6.1	36.0	51.2	46.9
	E	–56.3	–22.0	–59.4	–79.4	–42.7	–35.5	–407.6	5.2
AS97	*PB*	10.9	6.0	19.7	21.5	9.6	18.5	78.5	15.6
	PRMSE	64.2	67.5	70.0	70.4	68.7	73.9	107.7	77.2
	r	–22.5	–10.7	–20.6	–9.4	11.1	43.8	49.9	49.0
	E	–50.1	–36.6	–66.6	–44.7	–13.2	12.2	–128.8	11.6
BJF97	*PB*	–14.9	–16.5	–0.7	14.1	12.6	15.7	77.6	2.1
	PRMSE	57.4	61.3	56.9	65.2	73.6	81.4	102.1	70.8
	r	2.9	6.3	3.3	4.6	9.0	31.4	47.2	52.7
	E	–19.9	–12.7	–10.2	–24.4	–29.8	–6.6	–105.4	25.6
C97	*PB*	18.6	–2.1	19.5	32.1	17.7	23.9	106.1	19.0
	PRMSE	66.9	64.6	65.7	74.3	73.0	81.5	129.9	77.3
	r	–15.2	–2.9	–6.1	–5.9	–3.9	22.5	32.4	49.3
	E	–62.5	–25.1	–46.8	–61.6	–27.8	–6.8	–232.5	11.4
SCE97	*PB*	7.5	10.2	19.8	24.6	4.2	4.1	54.4	14.4
	PRMSE	66.0	69.5	69.2	73.6	68.9	70.5	86.0	78.3
	r	–18.2	–6.3	–9.5	–5.1	11.1	45.2	51.1	49.6
	E	–58.5	–44.7	–63.2	–58.6	–13.9	20.0	–45.7	9.1

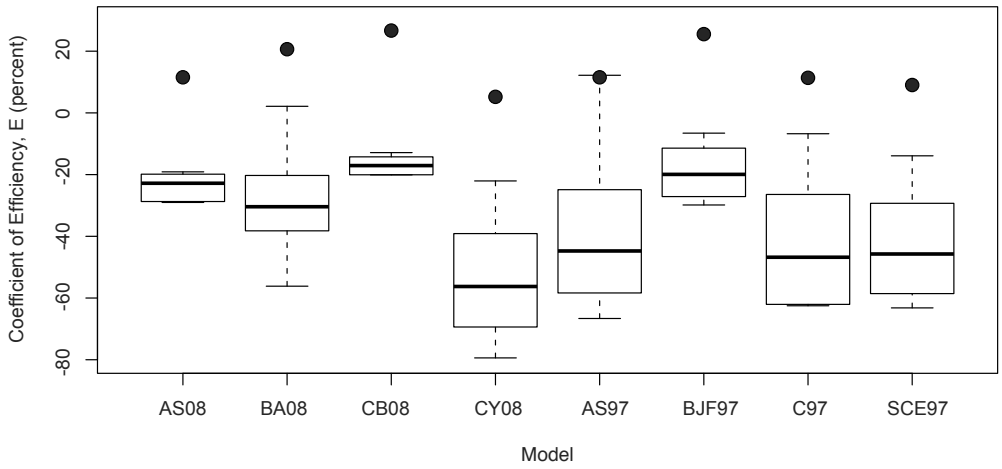

Figure D.13. Boxplots for *E* for the Parkfield—small distance subdivision

Table D.15. Goodness-of-fit measures for the Parkfield—medium distance subdivision

		PGA	Spectral acceleration (*Sa*)						**Total**
	Period (*T*), sec	–	0.1	0.2	0.3	0.5	1.0	2.0	–
AS08	*PB*	−22.5	−29.6	−28.1	−17.8	−23.4	0.6	33.1	−22.2
	PRMSE	52.8	57.7	59.9	59.0	73.9	44.8	68.8	69.2
	r	90.0	90.0	87.9	84.8	79.1	82.6	69.8	89.0
	E	63.3	55.8	53.6	59.1	46.3	67.9	−20.5	65.0
BA08	*PB*	−1.3	−3.9	−8.7	1.4	−7.0	21.7	69.5	−1.4
	PRMSE	48.8	47.6	54.8	57.8	68.8	48.4	98.4	63.5
	r	87.0	87.6	84.8	82.5	79.2	83.7	68.5	86.8
	E	68.6	70.0	61.1	60.7	53.5	62.5	−146.6	70.5
CB08	*PB*	3.7	3.7	1.1	7.3	0.5	23.9	62.1	5.5
	PRMSE	43.6	43.7	49.4	53.8	65.2	48.2	97.6	58.5
	r	88.8	88.1	84.6	83.3	78.9	85.4	68.8	87.6
	E	75.0	74.7	68.4	66.0	58.2	62.8	−142.6	74.9
CY08	*PB*	−7.3	−12.5	−13.5	−0.3	−−7.2	21.1	59.3	−5.7
	PRMSE	42.1	44.5	49.7	50.2	62.8	47.8	102.6	57.4
	r	89.7	89.7	86.4	84.8	80.7	86.4	68.0	88.8
	E	76.6	73.8	68.0	70.4	61.3	63.5	−167.9	75.9
AS97	*PB*	12.0	−0.1	−0.7	20.8	13.3	49.2	118.9	12.4
	PRMSE	39.7	43.0	48.0	48.4	66.8	75.9	151.2	57.6
	r	90.2	88.4	85.4	86.5	75.2	79.1	72.3	87.7
	E	78.8	75.6	70.7	69.2	54.6	14.4	−451.6	75.2
BJF97	*PB*	8.2	−5.1	6.1	28.9	10.0	21.7	132.2	12.2
	PRMSE	43.5	46.7	47.7	51.2	59.3	49.5	164.6	57.2
	r	90.1	87.9	86.3	87.5	82.5	84.1	69.7	88.0
	E	74.6	71.3	71.0	65.6	64.3	63.6	−554.4	75.6
C97	*PB*	8.0	−18.8	−7.9	20.2	12.2	51.2	135.2	6.3
	PRMSE	38.6	48.6	48.2	48.2	65.0	84.3	190.1	59.3
	r	90.0	88.9	85.1	87.3	76.7	78.6	66.9	86.2
	E	80.0	68.9	70.5	69.4	57.1	−5.5	−772.5	73.8
SCE97	*PB*	−1.5	−6.5	−4.9	15.7	3.1	34.3	84.8	4.4
	PRMSE	42.4	45.8	49.7	48.6	67.1	64.8	119.1	58.6
	r	88.6	87.5	84.8	85.0	74.2	78.9	74.8	86.9
	E	75.9	72.4	68.6	69.0	54.3	37.5	−242.6	74.3

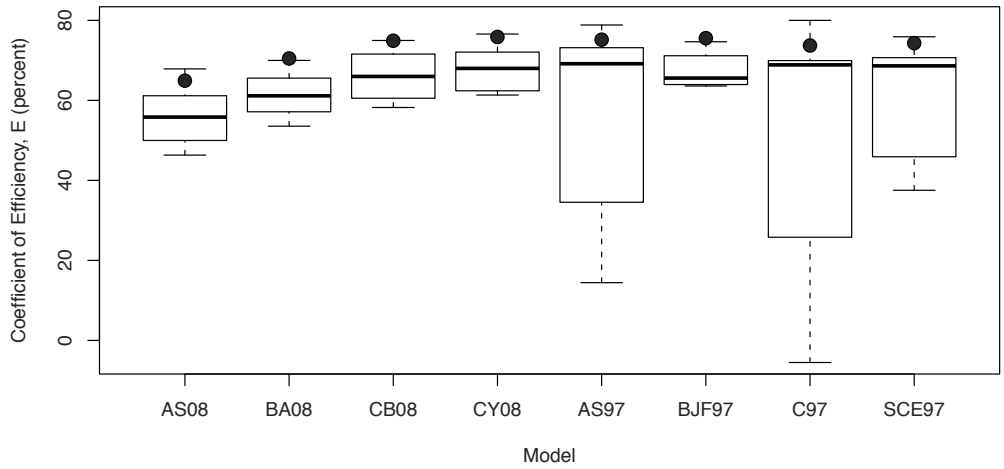

Figure D.14. Boxplots for *E* for the Parkfield—medium distance subdivision

Table D.16. Goodness-of-fit measures for the San Simeon dataset

		PGA	Spectral acceleration (*Sa*)						**Total**
	Period (*T*), sec	–	0.1	0.2	0.3	0.5	1.0	2.0	–
AS08	*PB*	−2.7	−24.6	−19.1	4.3	6.4	9.1	−5.0	−7.5
	PRMSE	63.3	78.2	68.1	68.7	73.1	55.7	76.4	78.5
	r	79.8	81.9	80.2	83.4	78.7	80.9	55.0	82.2
	E	63.5	57.6	59.2	68.3	61.7	56.1	8.8	66.2
BA08	*PB*	17.2	−5.2	0.4	27.1	24.2	20.4	−5.1	10.9
	PRMSE	63.2	72.7	64.8	74.5	76.5	53.3	63.6	77.4
	r	82.0	84.5	82.0	83.7	79.0	84.1	65.2	83.0
	E	63.6	63.3	63.1	62.8	58.1	59.9	36.8	67.0
CB08	*PB*	13.2	−2.0	−2.5	18.3	20.0	8.8	−7.8	7.1
	PRMSE	67.1	71.6	63.9	74.3	82.5	61.3	79.6	78.4
	r	78.1	82.6	80.9	81.0	74.2	76.8	50.8	81.7
	E	59.0	64.4	64.1	63.0	51.3	46.9	1.0	66.2
CY08	*PB*	22.4	4.9	0.4	21.4	14.1	11.2	−17.0	9.5
	PRMSE	70.3	59.3	59.8	70.8	80.8	70.5	83.3	73.5
	r	82.6	87.1	83.1	84.1	76.0	77.2	49.3	84.7
	E	55.0	75.6	68.5	66.4	53.3	29.7	−8.4	70.3
AS97	*PB*	49.2	22.2	22.4	41.4	59.6	72.2	39.9	38.5
	PRMSE	88.0	72.6	72.0	89.4	98.5	120.5	97.8	92.4
	r	79.5	81.1	79.6	79.7	81.9	85.5	63.8	81.1
	E	29.5	62.0	59.0	52.8	14.7	−172.6	−29.8	55.5
BJF97	*PB*	35.7	14.0	19.7	46.7	61.4	39.2	10.9	32.7
	PRMSE	75.4	67.4	71.0	91.6	99.5	76.7	71.7	88.9
	r	78.8	82.9	79.6	80.4	82.6	87.8	65.2	81.9
	E	48.1	67.3	60.2	50.5	12.9	−10.5	30.4	58.8
C97	*PB*	25.8	−4.7	−4.6	15.0	38.1	61.2	51.2	15.6
	PRMSE	88.2	77.1	78.5	92.7	103.9	135.6	136.3	98.7
	r	73.9	75.8	73.4	74.0	76.1	82.8	64.7	74.9
	E	29.1	57.1	51.2	49.3	5.1	−245.1	−151.9	49.2
SCE97	*PB*	32.5	22.9	17.7	40.1	56.7	74.0	44.9	35.6
	PRMSE	93.7	92.8	88.6	110.9	116.6	135.3	117.0	112.5
	r	67.1	68.2	67.4	66.6	69.0	77.8	59.0	70.9
	E	19.9	38.0	37.9	27.4	−19.5	−243.7	−85.7	34.0

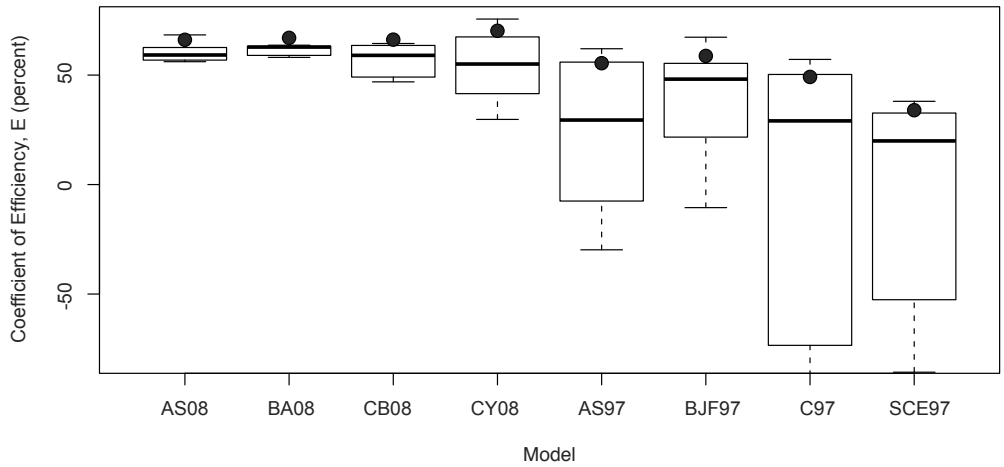

Figure D.15. Boxplots for *E* for the San Simeon dataset

List of References

Abrahamson, N. A. (2009). Clarifications to the AS08 NGA Model. Personal communication.

Abrahamson, N., G. Atkinson, D. Boore, Y. Bozorgnia, K. Campbell, B. Chiou, I. M. Idriss, W. Silva, R. Youngs (2008). Comparisons of the NGA Ground-Motion Relations, *Earthquake Spectra* **24**, 45–66.

Abrahamson, N. A., and K. M. Shedlock (1997). Overview, *Seismological Research Letters* **68**, 9–23.

Abrahamson, N. A., and W. J. Silva (1997). Empirical Response Spectral Attenuation Relations for Shallow Crustal Earthquakes, *Seismological Research Letters* **68**, 94–127.

—— (2008). Summary of the Abrahamson & Silva NGA Ground-Motion Relations, *Earthquake Spectra* **24**, 67–97.

Abrahamson, N. A., and P. G. Somerville (1996). Effects of the Hanging Wall and Footwall on Ground Motions Recorded during the Northridge Earthquake, *Bulletin of the Seismological Society of America* **86**, S93–S99.

Ambraseys, N. N., J. Douglas, J., S. K. Sarma, and P. M. Smit (2005). Equations for the Estimation of Strong Ground Motions from Shallow Crustal Earthquakes Using Data from Europe and the Middle East: Horizontal Peak Ground Acceleration and Spectral Acceleration, *Bulletin of Earthquake Engineering* **3**, 1–53.

Anderson, J. G., Y. Lee, Y. Zeng, and S. Day (1996). Control of Strong Motion by the Upper 30 Meters, *Bulletin of the Seismological Society of America* **86,** 1749–1759.

Atkinson, G. M. (1993). Earthquake Source Spectra in Eastern North America, *Bulletin of the Seismological Society of America* **83**, 1778–1798.

Atkinson, G. M., and D. M. Boore (2006). Earthquake Ground-Motion Prediction Equations for Eastern North America, *Bulletin of the Seismological Society of America* **96**, 2181–2205.

Berkeley Digital Seismic Network [BDSN] (2004). Seismic Recording Station Information for the Parkfield 2004-09-28 and San Simeon 2003-12-22 Earthquakes, University of California, Berkeley, <http://seismo.berkeley.edu /bdsn/>.

Beyer, K., and J. J. Bommer (2006). Relationships between Median Values and between Aleatory Variables for Different Definitions of the Horizontal Component of Motion, *Bulletin of the Seismological Society of America* **96**, 1512–1522.

Bommer, J. J., and N. A. Abrahamson (2006). Why Do Modern Probabilistic Seismic-Hazard Analyses Often Lead to Increased Hazard Estimates? *Bulletin of the Seismological Society of America* **96,** 1967–1977.

Bommer, J. J., J. Douglas, and F. O. Strasser (2003). Style-of-Faulting in Ground-Motion Prediction Equations, *Bulletin of Earthquake Engineering* **1**, 171–203.

Boore, D. M. (2008). TSPP—A Collection of FORTRAN Programs for Processing and Manipulating Time Series, Version 1.5, *U.S. Geological Survey Open-File Report 2008–1111*.

Boore, D. M., and G. M. Atkinson (1989). Spectral Scaling of the 1985 to 1988 Nahanni, Northwest Territories, Earthquakes, *Bulletin of the Seismological Society of America* **79**, 1736–1761.

—— (2007). Boore-Atkinson NGA Ground Motion Relations for the Geometric Mean Horizontal Component of Peak and Spectral Ground Motion Parameters, *PEER Report No. 2007/01*, Pacific Earthquake Engineering Research Center, University of California, Berkeley.

—— (2008). Ground-Motion Prediction Equations for the Average Horizontal Component of PGA, PGV, and 5%-Damped PSA at Spectral Periods between 0.01 s and 10.0 s, *Earthquake Spectra* **24**, 99–138.

Boore, D. M., W. B. Joyner, and T. E. Fumal (1997). Equations for Estimating Horizontal Response Spectra and Peak Acceleration from Western North American Earthquakes: A Summary of Recent Work, *Seismological Research Letters* **68**, 128–153.

Boore, D. M., J. Watson-Lamprey, and N. A. Abrahamson (2006). Orientation-Independent Measures of Ground Motion, *Bulletin of the Seismological Society of America* **96,** 1502–1511.

Building Seismic Safety Council [BSSC] (1998), NEHRP Recommended Provisions for Seismic Regulations for New Buildings and Other Structures, 1997 edition, *FEMA 303 Report*, Federal Emergency Management Agency, Washington, D. C.

California Geological Survey (2007). 1:250,000 Scale Regional Geologic Map Series; Monterrey, Fresno, San Luis Obispo, and Bakersfield quadrangles, <http://www.conservation.ca.gov/cgs/rghm/rgm/250k_index/Pages/250k_index.aspx>.

California Strong Motion Instrumentation Program [CSMIP] (2004). Seismic Recording Station Information for the Parkfield 2004-09-28 and San Simeon 2003-12-22 Earthquakes, California Geological Survey, <http://www.conservation.ca.gov/CGS/smip/Pages/Index.aspx>.

Campbell, K. W. (1989). Empirical Prediction of Near-Source Ground Motion for the Diablo Canyon Power Plant Site, San Luis Obispo County, California, *U.S. Geological Survey Open-File Report 89-484*.

—— (1997). Empirical Near-Source Attenuation Relationships for Horizontal and Vertical Components of Peak Ground Acceleration, Peak Ground Velocity, and Pseudo-Absolute Acceleration Response Spectra, *Seismological Research Letters* **68**, 154–179.

—— (2000). Erratum to "Empirical Near-Source Attenuation Relationships for Horizontal and Vertical Components of Peak Ground Acceleration, Peak Ground Velocity, and Pseudo-Absolute Acceleration Response Spectra," *Seismological Research Letters* **71**, 352–354.

—— (2009). Campbell's NGA Test Files, Open Seismic Hazard Analysis (OpenSHA.org), Southern California Earthquake Center and United States Geological Survey, <http://www.opensha.org/documentation/modelsImplemented/attenRel/Campbell_NGA_Test_Files/index.html>.

Campbell, K. W., and Y. Bozorgnia (2003). Updated Near-Source Ground Motion (Attenuation) Relations for the Horizontal and Vertical Components of Peak Ground Acceleration and Acceleration Response Spectra, *Bulletin of the Seismological Society of America* **93**, 314–331.

—— (2007). Campbell-Bozorgnia NGA Ground Motion Relations for the Geometric Mean Horizontal Component of Peak and Spectral Ground Motion Parameters, *PEER Report No. 2007/02*, Pacific Earthquake Engineering Research Center, University of California, Berkeley.

—— (2008). NGA Ground Motion Model for the Geometric Mean Horizontal Component of PGA, PGV, PGD and 5% Damped Linear Elastic Response Spectra for Periods Ranging from 0.01 to 10 s, *Earthquake Spectra* **24**, 139–171.

Castellaro, S., F. Mulargia, and P. L. Rossi (2008). Vs30: Proxy for Seismic Amplification? *Seismological Research Letters* **79**, 540–543.

Center for Engineering Strong Motion Data [CESMD] (2004). Earthquake Ground Motion Records for the Parkfield 2004-09-28 and San Simeon 2003-12-22 Earthquakes, <http://strongmotioncenter.org/>.

Chiou, B. S.-J. (2005). Documentation for NGA Flatfile Used for Development of NGA Models, Pacific Earthquake Engineering Research Center, University of California, Berkeley, <http://peer.berkeley.edu/assets/NGA_Documentation.pdf>.

—— (2009). Clarifications to the CY08 NGA Model. Personal communication.

Chiou, B. S.-J., R. Darragh, N. Gregor, and W. Silva (2008). NGA Project Strong-Motion Database, *Earthquake Spectra* **24**, 23–44.

Chiou, B. S.-J., and R. R. Youngs (2008a). An NGA Model for the Average Horizontal Component of Peak Ground Motion and Response Spectra, *Earthquake Spectra* **24,** 173–215.

—— (2008b). NGA Model for the Average Horizontal Component of Peak Ground Motion and Response Spectra, *PEER Report No. 2008/09*, Pacific Earthquake Engineering Research Center, University of California, Berkeley.

Consortium of Organizations for Strong-Motion Observation Systems [COSMOS] (2004). Earthquake Ground Motion Records for the Parkfield 2004-09-28 and San Simeon 2003-12-22 Earthquakes, available at the COSMOS Virtual Data Center, <http://db.cosmos-eq.org>.

Cornell, C. A. (1968). Engineering Seismic Hazard Analysis, *Bulletin of the Seismological Society of America* **59**, 1583–1606.

Cramer, C., J. Kutliroff, and D. Dangkua (2009). Next Generation Attenuation (NGA) East Ground Motion Database: Issues and Initial Effort, *Eastern Section of the Seismological Society of America, 2009 Meeting*, Palisades, N.Y.

Douglas, J. (2003). Earthquake Ground Motion Estimation Using Strong-Motion Records: A Review of Equations for the Estimation of Peak Ground Acceleration and Response Spectral Ordinates, *Earth-Science Reviews* **61**, 43–104.

Dreger, D. (2004). 09/28/2004 Preliminary Slip Model, Berkeley Seismological Laboratory, University of California, Berkeley. Accessed at *Finite-Source Rupture Model Database*, M. Mai, <http://www.seismo.ethz.ch/srcmod/>.

Field, E. H., K. R. Milner, and the 2007 Working Group on California Earthquake Probabilities (2008). Forecasting California's Earthquakes—What Can We Expect in the Next 30 Years? *U.S. Geological Survey Fact Sheet 2008-3027*.

Ghasemi, H., M. Zare, and Y. Fukushima (2008). Ranking of Several Ground-Motion Models for Seismic Hazard Analysis in Iran, *Journal of Geophysics and Engineering* **5**, 301–310.

Hanks, T. C., and H. Kanamori (1979). A Moment Magnitude Scale, *Journal of Geophysical Research* **84**, 2348–2350.

Helsel, D. R., and R. M. Hirsch (2002). *Statistical Methods in Water Resources*, Techniques of Water-Resources Investigations Book 4, Chapter A3, United States Geological Survey, <http://water.usgs.gov/pubs/twri/twri4a3/>.

Idriss, I. M. (1991). Selection of Earthquake Ground Motions at Rock Sites, Report prepared for the Structures Division, Building and Fire Research Laboratory, National Institute of Standards and Technology, Department of Civil Engineering, University of California, Davis.

—— (2002). Attenuation Relationship Derived by I. M. Idriss in 2002, Reported in "Empirical Model for Estimating the Average Horizontal Values of Pseudo-Absolute Spectral Accelerations Generated by Crustal Earthquakes" (2007), Interim Report Issued for USGS Review, Pacific Earthquake Engineering Research Center, University of California, Berkeley, <http://peer.berkeley.edu /products/Idriss_NGA.html>.

—— (2007). Empirical Model for Estimating the Average Horizontal Values of Pseudo-Absolute Spectral Accelerations Generated by Crustal Earthquakes, Interim Report Issued for USGS Review, Pacific Earthquake Engineering Research Center, University of California, Berkeley, <http://peer.berkeley.edu/products /Idriss_NGA.html>.

—— (2008). An NGA Empirical Model for Estimating the Horizontal Spectral Values Generated by Shallow Crustal Earthquakes, *Earthquake Spectra* **24,** 217–242.

Jennings, C. W. (compiler) (1977). *Geologic Map of California*, Geologic Data Map Series No. 2, California Department of Conservation, California Geological Survey.

Joyner, W. B., and T. E. Fumal (1984). Use of Measured Shear-Wave Velocity for Predicting Geologic Site Effects on Strong Ground Motion, *Proceedings of the Eighth World Conference on Earthquake Engineering* (San Francisco, Calif.) **2**, 777–783.

Kanamori, H. (1977). The Energy Release in Great Earthquakes, *Journal of Geophysical Research* **82**, 2981–2987.

Kayen, R. (2007). Shear Wave Velocity Data from the Parkfield, California, Area. Personal communication.

Kramer, S. L. (1996). *Geotechnical Earthquake Engineering*, Prentice Hall, Upper Saddle River, N.J.

Kuehn, N. M., F. Scherbaum, and C. Riggelsen (2009). Deriving Empirical Ground-Motion Models: Balancing Data Constraints and Physical Assumptions to Optimize Prediction Capability, *Bulletin of the Seismological Society of America* **99,** 2335–2347.

Legates, D. R. and G. J. McCabe Jr. (1999). Evaluating the Use of "Goodness-of-Fit" Measures in Hydrologic and Hydroclimatic Model Validation, *Water Resources Research* **35**, 233–241.

Louie, J. N. (2001). Faster, Better: Shear-Wave Velocity to 100 Meters Depth from Refraction Microtremor Arrays, *Bulletin of the Seismological Society of America* **91,** 347–364.

Nash, J. E. and J. V. Sutcliffe (1970). River Flow Forecasting Through Conceptual Models; Part I, A Discussion of Principles. *Journal of Hydrology* **10**, 282–290.

National Strong Motion Program [NSMP] (2004). Earthquake Ground Motion Records for the Parkfield 2004-09-28 and San Simeon 2003-12-22 Earthquakes, United States Geological Survey, <http://nsmp.wr.usgs.gov/>.

Northern California Seismic Network [NCSN] (2004). Seismic Recording Station Information for the Parkfield 2004-09-28 and San Simeon 2003-12-22 Earthquakes, United States Geological Survey, <http://www.ncedc.org/ncsn/>.

Pacific Earthquake Engineering Research Center (2008a). NGA Flatfile Used for Development of NGA Models, <http://peer.berkeley.edu/products/nga_flatfiles_dev.html>.

Pacific Earthquake Engineering Research Center (2008b). Next Generation Attenuation of Ground Motions (NGA) Project, <http://peer.berkeley.edu/products/nga_project.html>.

Park, C. B., R. D. Miller, and J. Xia (1999). Multi-channel Analysis of Surface Waves, *Geophysics* **64**, 800–808.

Petersen, M. D., A. D. Frankel, S. C. Harmsen, C. S. Mueller, K. M. Haller, R. L. Wheeler, R. L. Wesson, Y. Zeng, O. S. Boyd, D. M. Perkins, N. Luco, E. H. Field, C. J. Wills, and K. S. Rukstales (2008). Documentation for the 2008 Update of the United States National Seismic Hazard Maps, *U.S. Geological Survey Open-File Report 2008–1128*.

Power M., B. Chiou, N. Abrahamson, Y. Bozorgnia, T. Shantz, C. Roblee (2008). An Overview of the NGA Project, *Earthquake Spectra* **24**, 3–21.

R Development Core Team (2009). R: A Language and Environment for Statistical Computing, R Foundation for Statistical Computing, Vienna, Austria, ISBN 3-900051-07-0, <http://www.R-project.org>.

Real, C. R. (1988). Turkey Flat, USA, Site Effects Test Area, *Technical Report No. 88-2*, California Department of Conservation, Division of Mines and Geology, Earthquake Shaking Assessment Unit.

Reiter, L. (1990). *Earthquake Hazard Analysis – Issues and Insights*, Columbia University Press, New York.

Rolandone, F., R. Burgmann, D. Dreger, and M. Murray (2004). Coseismic Slip Distribution of the 22 December 2003 San Simeon Earthquake, *Annual Report 2003-2004*, Berkeley Seismological Laboratory, University of California, Berkeley, <http://seismo.berkeley.edu/annual_report/ar03_04/node19.html>.

Sadigh, K., C. Y. Chang, J. A. Egan, F. Makdisi, and R. R. Youngs (1997). Attenuation Relationships for Shallow Crustal Earthquakes Based on California Strong Motion Data, *Seismological Research Letters* **68**, 180–189.

Scott, J. B., M. Clark, C. Lopez, A. Pancha, T. Rasmussen, S. B. Smith, W. Thelen, and J. N. Louie (2006). Three Urban Transects of Shallow Shear-Velocity Using the Refraction Microtremor Method, *Proceedings of the Managing Risk in Earthquake Country 100th Anniversary Earthquake Conference Commemorating the 1906 San Francisco Earthquake*, San Francisco, Calif.

Shakal, A., V. Graizer, M. Huang, R. Borcherdt, H. Haddadi, K. Lin, C. Stephens, and P. Roffers (2005). Preliminary Analysis of Strong-Motion Recordings from the 28 September 2004 Parkfield, California Earthquake, *Seismological Research Letters* **76**, 27–39.

Shakal, A., H. Haddadi, V. Graizer, K. Lin, and M. Huang (2006). Some Key Features of the Strong-Motion Data from the M 6.0 Parkfield, California, Earthquake of 28 September 2004, *Bulletin of the Seismological Society of America* **96,** S90–S118.

Snyder, J. P. (1987). Map Projections: A Working Manual, *U. S. Geological Survey Professional Paper 1395*, U. S. Government Printing Office, Washington, D.C.

Somerville, P. G., N. F. Smith, R. W. Graves, and N. A. Abrahamson (1995). Representation of Near-Fault Directivity Effects in Design Ground Motions, and Application to Caltrans Bridges, *Proceedings of the National Seismic Conference on Bridges and Highways*, San Diego, Calif.

Somerville, P. G., N. F. Smith, R. W. Graves, and N. A. Abrahamson (1997). Modification of Empirical Strong Ground Motion Attenuation Relations to Include Amplitude and Duration Effects of Rupture Directivity, *Seismological Research Letters* **68**, 199–222.

Spudich, P., and B. S.-J. Chiou (2008). Directivity in NGA Earthquake Ground Motions: Analysis Using Isochrone Theory, *Earthquake Spectra* **24**, 279–298.

Spudich, P., W. B. Joyner, A. G. Lindh, D. M. Boore, B. M. Margaris, J. B. Fletcher (1999). SEA99: A Revised Ground Motion Prediction Relation for Use in Extensional Tectonic Regimes, *Bulletin of the Seismological Society of America* **89,** 1156–1170.

Stafford, P. J., F. O. Strasser, and J. J. Bommer (2008). An Evaluation of the Applicability of the NGA Models to Ground-Motion Prediction in the Euro-Mediterranean Region, *Bulletin of Earthquake Engineering* **6**, 149–177.

Star, L. M., J. P. Stewart, R. W. Graves, K. W. Hudnut (2008). Validation Against NGA Empirical Model of Simulated Motions for M 7.8 Rupture of San Andreas Fault, *The 14th World Conference on Earthquake Engineering*, Beijing, China.

Stewart, J. P., L. M. Star, and R. W. Graves (2008). Validation Against NGA Empirical Model of Simulated Motions for M 7.15 Rupture of Puente Hills Fault, *Final Report*, Pacific Earthquake Engineering Research Center, University of California, Berkeley, <http://peer.berkeley.edu/tbi/pdf-ppt/PuenteHills_Synthetic _Ground_Motion_rpt3.pdf>.

Stokoe II, K. H., S. G. Wright, J. A. Bay, and J. M. Roesset (1994). Characterization of Geotechnical Sites by SASW method, in *Geophysical Characterization of Sites,* ISSMFE Technical Committee #10, edited by R.D. Woods, Oxford & IBH Publishing Co., New Delhi, India, 15–25.

Strasser, F. O., N. A. Abrahamson, and J. J. Bommer (2009). Sigma: Issues, Insights, and Challenges, *Seismological Research Letters* **80**, 40–56.

United States Geological Survey [USGS] (2004). Seismic Recording Station Information for the Parkfield 2004-09-28 and San Simeon 2003-12-22 Earthquakes, <http ://earthquake.usgs.gov/>.

Wills, C. J., and K. B. Clahan (2006). Developing a Map of Geologically Defined Site-Condition Categories for California, *Bulletin of the Seismological Society of America* **96,** 1483–1501.